MODEL-BASED CO-DESIGN OF SENSING AND CONTROL SYSTEMS FOR TURBO-CHARGED, EGR UTILIZING SPARK-IGNITED ENGINES

by

Xu Zhang

A Dissertation

Submitted to the Faculty of Purdue University

In Partial Fulfillment of the Requirements for the degree of

Doctor of Philosophy

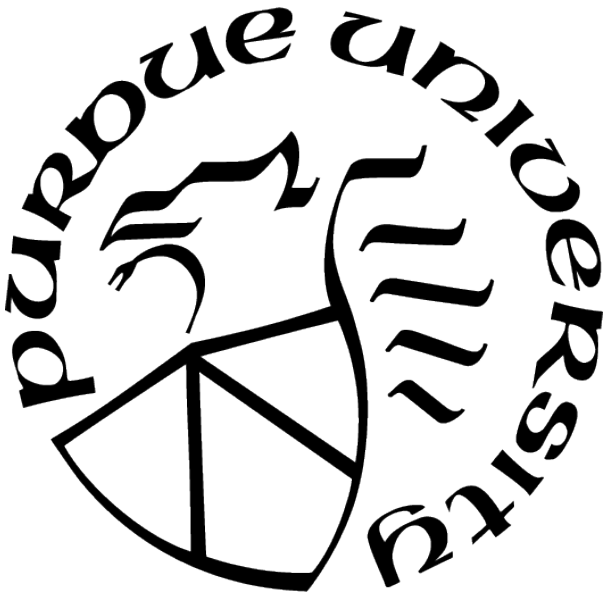

School of Mechanical Engineering

West Lafayette, Indiana

May 2021

THE PURDUE UNIVERSITY GRADUATE SCHOOL
STATEMENT OF COMMITTEE APPROVAL

Dr. Gregory M. Shaver, Chair

School of Mechanical Engineering

Dr. Peter H. Meckl

School of Mechanical Engineering

Dr. Neera Jain

School of Mechanical Engineering

Dr. Oleg Wasynczuk

School of Electrical and Computer Engineering

Approved by:

Dr. Nicole L. Key

To my dad Zhihua Zhang and mom Minzhi Liu,
and my beloved partner, Meng Liu.

ACKNOWLEDGMENTS

The study at Purdue is a wonderful journey for me. There are many who helped me along the way on this journey. This thesis would not have been possible without their help.

I would like to express my deepest appreciation to my advisor, Prof. Gregory M. Shaver, for your guidance and support throughout my PhD study and research, for your patience, encouragement and enthusiasm. Your advise and help on both my research as well as on my career have been invaluable. I could not have imagined having a better advisor for my Ph.D study. I would also like to thank my committee members, Prof. Peter H. Meckl, Prof. Neera Jain and Prof. Oleg Wasynczuk, for your brilliant comments and suggestions to help me reach my goal.

It's an honor for me to work with extremely motivated and reliable team members, Yunpeng Xu and Michael Robert Anthony, for all the time we spent on our project and each time we shared our accomplishments. You are ever-reliable teammates and with your help we keep our project making progress. I would also like to express sincere gratitude to my collaborators in Cummins Inc, Dr. Dheeraj Gosala, Dr. Carlos A Lana, Dr. Dat D Le, Dr. Bijesh M Shakya, David Langenderfer and Saradhi Rengarajan, your insightful and constructive feedback played a key role in preparing all the challenges in my research work. Special thanks go to Dr. Dheeraj Gosala, the supportive discussions pushed me to sharpen my thinking and brought my work to a higher level.

There is no way to express how much it meant to me to have been a member of Shaver group. These brilliant friends and colleagues inspired me over my PhD study. I would like to thank Dr. Dheeraj Gosala, Dr. Mrunal Joshi, Sree Harsha Rayasam, Dr. Vaidehi Hoshing, and Chaitu Panuganti, whom I had an opportunity of working with on one major project, for the stimulating discussions and all the fun we have had from our research work. I am so lucky to have met such great friends and research companions along the way as Chufan Jiang, Weijin Qiu, Ziping Liu, with whom I talked about the research and life during our weekly Friday afternoon tea break. I also greatly enjoyed working with Chisom, Miles, Vrushali, Shveta, Tyler, Shubham Ashta, Shubham Pradeep Agnihotri, John, Brady, Doni, Preston, Eric, Ryan, Dr. Xing Jin, Dr. Aswin Ramesh, Dr. Cody Allen, Dr. Kalen Vos, Dr. Alex

Taylor, Ife, Troy, Matt, and I learned a lot from. I also would like to thank Prof. Patricia Davies, Prof. Eckhard Groll, Cindy Sue Cory, Donna Cackley and Robin Sipes and all the staff at Herrick Labs, for providing us with a warm and pleasant working environment. Big thanks go to Sylvia Lu, who introduced me with Shaver group when I came to Purdue. Special thanks must go to Dr. Xing Jin, who has been a mentor and friend, helps and guides me to become better in my research and life.

I also thank all my friends at Purdue for providing support and friendship that I needed. My sincerest thanks to Dr. Xiaorong Cai, Haitian Hao, Dr. Xinye Zhang, Zechao Lu, Yongjie Zhuang, Haotian Liu, Kairui Hao, Zhuang Mo, Guochenhao Song, Clare, Ang Li, Wei Ding, Jianxiong Feng, Dr. Tongyang Shi, Dr. Yingying Xiao, Weimin Thor, Jiacheng Ma, Hongcheng Tao, Huanyu Liao, Tony, Jie Ma, Prof. Yangfan Liu, Dr. Li Cheng, Dr. Zhu Shi, for keeping great company outside the research. I would never forget our fun lunchbox time and life pieces we shared together.

I would like to express my gratitude to Martin T. Books for your excellent mentorship during my internship at Cummins Inc, for lending me your expertise and being patient for my never ending questions. I also want to thank Beth Lageveen and Katherine Bolte for helping me improve my presentation and communication skills.

I deeply thank my parents, my dad Zhihua Zhang and my mom Minzhi Liu, for your endless love and unconditional support throughout my life. Thank you both for giving me strength to reach for the stars and chase my dreams. Most of all, to the most special person in my life, my beloved partner, Meng Liu - you are always there to support and encourage me, and share all the happiness with me. You make every day a special day for me.

TABLE OF CONTENTS

LIST OF TABLES

LIST OF FIGURES

LIST OF SYMBOLS

P_{bm}	Boost manifold pressure
P_{im}	Intake manifold pressure
P_{em}	Exhaust manifold pressure
T_{bm}	Boost manifold temperature
T_{im}	Intake manifold temperature
T_{em}	Exhaust manifold temperature
ω_{tc}	Turbocharger speed
$F_{ub,bm}$	Boost manifold unburnt gas mass fraction
$F_{b,bm}$	Boost manifold burnt gas mass fraction
$F_{ub,im}$	Intake manifold unburnt gas mass fraction
$F_{b,im}$	Intake manifold burnt gas mass fraction
$F_{ub,em}$	Exhaust manifold unburnt gas mass fraction
$F_{b,em}$	Exhaust manifold burnt gas mass fraction
P	Pressure
V	Volume
T	Temperature
R	Mass-specific gas constant
W	Mass flow rate
bm	Boost manifold
im	Intake manifold
em	Exhaust manifold
$comp$	Compressor
thr	Throttle
cac	Charge air cooler
byp	Bypass
$egrh$	High pressure EGR
$egrl$	Low pressure EGR
cyl	Cylinder

$cyl-out$	Cylinder-out
$turb$	Turbine
wg	Waste-gate
γ	Gas specific heat ratio
F	Mass fraction
A_{eff}	Valve effective area
P_{out}	Downstream pressure
P_{in}	Upstream pressure
T_{in}	Upstream temperature
E_{ivc}	Cylinder gas energy at IVC
$E_{residual}$	Residual exhaust gas energy at IVO
$E_{backflow}$	Back flow exhaust gas energy from IVO to EVC
$E_{freshcharge}$	Fresh charge gas energy from intake manifold to cylinder during IVO to IVC
E_{piston}	Piston work energy done by cylinder gas from IVO to IVC
$E_{heattransfer}$	Heat transfer to cylinder gas from IVO to IVC
γ_{ivc}	Gas specific heat ratio at IVC
$h_{ivo-ivc}$	Heat transfer coefficient
N	Engine speed
B	Cylinder bore
S	Cylinder stroke
SA_{ivoivc}	Integrated surface area from IVO to IVC
v_{ivo}	Cylinder volume at IVO
v_{ivc}	Cylinder volume at IVC
v_{evo}	Cylinder volume at EVO
v_{evc}	Cylinder volume at EVC
A_{cyl}	Cross-section area of cylinder
$l_{ivo-ivc}$	Integrated cylinder height change
m_{charge}	Mass of cylinder charged gas
W_{charge}	Cylinder charge mass flow rate

$F_{ub,cylout}$	Cylinder-out unburnt gas mass fraction
$F_{b,cylout}$	Cylinder-out burnt gas mass fraction
$F_{uhc,cylout}$	Cylinder-out unburnt hydrocarbon mass fraction
AFR_{st}	Stoichiometric air-to-fuel ratio
m_{fuel}	Mass of the directly injected fuel per cycle
m_{res}	Residual gas mass
ϵ_{comb}	Combustion level
r_c	Compression ratio
Q_{LHV}	Lower heating value of the fuel
c_v	Constant volume specific heat of the air-fuel mixture
X_{eff}	Tuning parameter to reflect the energy conversion inefficiency
T_{evo}	EVO temperature
T_{evc}	EVC temperature
T_{bd}	Blowdown gas temperature
T_{cylout}	Cylinder-out exhaust gas temperature
T_{wall}	Cylinder wall temperature
h	Heat transfer coefficient
$m_{cyl,total}$	Total cylinder gas mass
$m_{backflow}$	Exhaust back flow mass
$m_{rev,\mathrm{ivo}}$	In-cylinder burnt gas mass at IVO
OLV	Valve overlap volume
A_{flow}	Cylinder valve effective area
I_{tc}	Turbo-charger inertia
Z_{turb}	Turbine power
Z_{comp}	Compressor power
P_a	Ambient pressure
$P_{turb,out}$	Turbine out pressure
W_{comp}	Compressor mass flow
$W_{comp,up}$	Upstream compressor mass flow
η_{comp}	Compressor efficiency

W_{turb}	Turbine mass flow
η_{turb}	Turbine efficiency
PR_c	Compressor pressure ratio
ρ_a	Compressor Inlet Air Density
d_c	Compressor blade tip diameter
T_a	Compressor inlet air temperature
$C_{p,a}$	Compressor inlet air specific heat
$W_{turb,red}$	Reduced turbine mass flow rate
N_{red}	Reduced turbine speed
PR_t	Pressure ratio across the turbine
W_{fuel}	Fueling rate
$A_{cmd,thr}$	Commanded effective throttle area
A_{thr}	Effective throttle area
A_{byp}	Effective bypass valve area
$D_{cmd,wg}$	Commanded waste-gate diameter
D_{wg}	Waste-gate diameter
$A_{\mathrm{egr}h}$	Effective HP EGR valve area
$A_{\mathrm{egr}l}$	Effective LP EGR valve area
$A_{cmd,egrl}$	Commanded effective LP EGR valve area
$\tilde{W}_{\mathrm{inlet}}$	Inlet air flow measurement
$\tilde{W}_{comp}$	CAC downstream flow measurement
$\tilde{W}_{\mathrm{egr}l}$	LP EGR valve flow measurement
$\tilde{W}_{comp,up}$	Compressor upstream flow measurement
δW_{max}	Maximum flowrate deviation with respect to its linearization point
G_u	Transfer function matrix between the normalized state and input
G_d	Transfer function matrix between the normalized state and disturbance input
Δ	Model uncertainty
P_{eng}	Generalized engine model plant
P_{flow}	Flow sensor model

K_{FF}	Feedforward controller
K_{FB}	Feedback controller
w	Exogenous inputs
u	Control signals
z	Exogenous outputs
v_{eng}	Feedback controller inputs for the general configuration
u_{FF}	Feedforward command
u_{FB}	Feedback command
y_{Δ}	Output perturbations
u_{Δ}	Input perturbations
δ	Variable change
Δ_{full}	Full-block perturbation uncertainty
Δ_{diag}	Block-diagonal uncertainty
$\bar{\sigma}\left(\Delta_{diag}\right)$	Maximum singular value of Δ_{diag}
Δ_P	Uncertainty block from performance specifications
D_f	Designed matrix which commutes with the uncertainty Δ
$\mathcal{D}$	Set of all matrices commute with Δ
μ	The structured singular value
$W_{FF,fuel}$	Feedforward fuel command
$W_{FB,fuel}$	Feedback fuel command
$\delta\bar{r}_{AFR}$	Nominalized AFR reference
$\delta\bar{r}_f$	Nominalized flow reference
$\delta\bar{u}_d$	Nominalized engine speed
$\delta\bar{u}_{FB,3}$	Feedback fueling command
$\delta\bar{u}_{FF,3}$	Feedforward fueling command
$\delta\bar{u}_3$	Total fueling command
$\delta\bar{u}_f$	Flow actuators' commands
n	Sensor noise
$Z_{p,AFR}$	Weighted control output of AFR
$Z_{p,f}$	Weighted control output of flows

$Z_{u,f}$	Weighted flows actuators' commands
$Z_{u,3}$	Weighted fueling rate command
$\delta\bar{y}_m$	Normalized sensor measurements
$\delta\bar{y}_{m,f}$	Normalized flow sensor measurements
$\delta\bar{y}_{m,AFR}$	Normalized UEGO sensor measurement
$\delta\bar{y}_{t,AFR}$	Normalized AFR control target
$\delta\bar{y}_{t,f}$	Normalized flow control target
$\delta\bar{W}_{u,3}$	Normalized feedforward fueling command
$\delta\bar{u}$	Normalized total actuator input
$\delta\bar{x}_0$	Normalized model states (nominal)
$\delta\bar{y}_0$	Normalized model output (nominal)
$\delta\bar{y}$	Normalized model output (with uncertainty)
G_u, G_d	Normalized system plants
W_d	Disturbance weighting function
W_{y_f}	Shaping function of measured flow modeling uncertainty
W_{y_ft}	Shaping function of target modeling uncertainty
W_{y_AFR}	Shaping function of AFR modeling uncertainty
$\Delta_{y,f}, \Delta_{y,AFR}, \Delta_{y,ft}$	Modeling uncertainty
Δ_s	Sensor bias error
M^*	maximum error at high frequencies
A^*	steady-state error
ω^*	frequency where error reaches 100%
τ	Time constant
δ_{si}	Percent bias error
W_n	Noise shaping function
Δ_y	Scaled diagonal uncertainty block
W_{air}	Engine-out mass air flow rate
f_{sat}	Saturation function of W_{air}
C	Effective TWC oxygen capacity
λ_{up}	TWC upstream λ (engine-out λ)

ρ	Exchange of oxygen between the engine-out exhaust and the TWC
α_L	Adsorption rate of oxygen
α_R	Desorption rate of oxygen
f_L	Fraction of oxygen from the engine-out exhaust gas sticking to a site in the TWC
f_R	Fraction of oxygen being released by the TWC and recombining with the engine-out exhaust gas
M_{O_2}	Molar mass of O_2
M_{exh}	Molar mass of the engine-out exhaust gas
W_{exh}	Engine-out mass flow rate
$C_{O_2,in}$ O_2	mole fraction in the TWC inlet flow
$C_{O_2,out}$ O_2	mole fraction in the TWC outlet flow
$\lambda_{dn,\tau}$	Modeled TWC outlet λ sensor measurement
$\delta\bar{u}_{d0}$	The normalized disturbance input
τ_{u_d}	The time constant for disturbance input

ABBREVIATIONS

AFFC	Adaptive feed-forward controller
AFR	Air-to-fuel ratio
APC	Adaptive posicast control
BDC	Bottom dead center
BMEP	Brake Mean Effective Pressure
BMI	Bilinear matrix inequalities
BSFC	Brake-specific fuel consumption
CAC	Charge air cooler
ChgVS	Virtual charge flow sensor
CI	Compression ignition
CMD.	Commanded
DISI	Direct injection spark-ignited
ECU	Engine control unit
EGO	Exhaust-gas oxygen
EGR	Exhaust gas recirculation
EGR DP	EGR delta pressure sensor (measuring EGR mass flow rate)
EKF	Extended Kalman-filter
EVC	Exhaust valve close
EVO	Exhaust valve open
FFT	Fast Fourier Analysis
FOS	Fractional oxygen state
GTDI	Gasoline turbocharged direct injection
HCCI	Homogeneous charge compression ignition
HP	Low pressure
IMEP	Indicated mean effective pressure
IVC	Intake valve close
IVO	intake valve open
LFTs	Linear fractional transformations

LMI	Linear matrix inequality
LP	Low pressure
LQG	Linear quadratic Gaussian
LTI	Linear time-invariant
LTV-MPC	Linear time-varying model predictive controller
MAF	Mass air flow sensor downstream of the air and LP EGR confluence point
MAFh	Mass air flow sensor for high pressure flow (charge air cooler downstream)
MAP	manifold absolute pressure
MIMO	Multiple-input multiple-output
MIMO	Multiple-input single-output
MPC	Model predictive control
MVM	Mean-value model
NS	Nominal stable
NVO	Negative valve overlap
OEM	Original equipment manufacturers
PDE	Partial differential equation
PI	Proportional-integral
PVO	Positive valve overlap
RGA	Relative gain array
RMSE	Expected root-mean-square error
RP	Robust performance
RS	Robust stability
SDP	Semi-definite programming
SI	Spark-ignited
SMC	Sliding mode control
STC	Self-tuning control
TDC	Top dead center
TWC	Three-way-catalyst
UEGO	Universal exhaust-gas oxygen
VVA	Variable valve actuation

VVT	Variable valve timing

ABSTRACT

Stoichiometric air-fuel ratio (AFR) and air/EGR flow control are essential control problems in today's advanced spark-ignited (SI) engines to enable effective application of the three-way-catalyst (TWC) and generation of required torque. External exhaust gas recirculation (EGR) can be used in SI engines to help mitigate knock, reduce enrichment and improve efficiency[1]. However, the introduction of the EGR system increases the complexity of stoichiometric engine-out lambda and torque management, particularly for high BMEP commercial vehicle applications. This thesis develops advanced frameworks for sensing and control architecture designs to enable robust air handling system management, stoichiometric cylinder air-fuel ratio (AFR) control and three-way-catalyst emission control.

The first work in this thesis derives a physically-based, control-oriented model for turbocharged SI engines utilizing cooled EGR and flexible VVA systems. The model includes the impacts of modulation to any combination of 11 actuators, including the throttle valve, bypass valve, fuel injection rate, waste-gate, high-pressure (HP) EGR, low-pressure (LP) EGR, number of firing cylinders, intake and exhaust valve opening and closing timings. A new cylinder-out gas composition estimation method, based on the inputs' information of cylinder charge flow, injected fuel amount, residual gas mass and intake gas compositions, is proposed in this model. This method can be implemented in the control-oriented model as a critical input for estimating the exhaust manifold gas compositions. A new flow-based turbine-out pressure modeling strategy is also proposed in this thesis as a necessary input to estimate the LP EGR flow rate. Incorporated with these two sub-models, the control-oriented model is capable to capture the dynamics of pressure, temperature and gas compositions in manifolds and the cylinder. Thirteen physical parameters, including intake, boost and exhaust manifolds' pressures, temperatures, unburnt and burnt mass fractions as well as the turbocharger speed, are defined as state variables. The outputs such as flow rates and AFR are modeled as functions of selected states and inputs. The control-oriented model is validated with a high fidelity SI engine GT-Power model for different operating conditions. The novelty in this physical modeling work includes the development and incorporation of the cylinder-out gas composition estimation method and the turbine-out pressure model in the control-oriented model.

The second part of the work outlines a novel sensor selection and observer design algorithm for linear time-invariant systems with both process and measurement noise based on H_2 optimization to optimize the tradeoff between the observer error and the number of required sensors. The optimization problem is relaxed to a sequence of convex optimization problems that minimize the cost function consisting of the H_2 norm of the observer error and the weighted l_1 norm of the observer gain. An LMI formulation allows for efficient solution via semi-definite programing. The approach is applied here, for the first time, to a turbo-charged spark-ignited (SI) engine using exhaust gas recirculation to determine the optimal sensor sets for real-time intake manifold burnt gas mass fraction estimation. Simulation with the candidate estimator embedded in a high fidelity engine GT-Power model demonstrates that the optimal sensor sets selected using this algorithm have the best H_2 estimation performance. Sensor redundancy is also analyzed based on the algorithm results. This algorithm is applicable for any type of modern internal combustion engines to reduce system design time and experimental efforts typically required for selecting optimal sensor sets.

The third study develops a model-based sensor selection and controller design framework for robust control of air-fuel-ratio (AFR), air flow and EGR flow for turbocharged stoichiometric engines using low pressure EGR, waste-gate turbo-charging, intake throttling and variable valve timing. Model uncertainties, disturbances, transport delays, sensor and actuator characteristics are considered in this framework. Based on the required control performance and candidate sensor sets, the framework synthesizes an H_∞ feedback controller and evaluates the viability of the candidate sensor set through analysis of the structured singular value μ of the closed-loop system in the frequency domain. The framework can also be used to understand if relaxing the controller performance requirements enables the use of a simpler (less costly) sensor set. The sensor selection and controller co-design approach is applied here, for the first time, to turbo-charged engines using exhaust gas circulation. High fidelity GT-Power simulations are used to validate the approach. The novelty of the work in this part can be summarized as follows: (1) A novel control strategy is proposed for the stoichiometric SI engines using low pressure EGR to simultaneously satisfy both the AFR and air/EGR-path control performance requirements; (2) A parametrical method to

simultaneously select the sensors and design the controller is first proposed for the internal combustion engines.

In the fourth part of the work, a novel two-loop estimation and control strategy is proposed to reduce the emission of the three-way-catalyst (TWC). In the outer loop, an FOS estimator consisting of a TWC model and an extended Kalman-filter is used to estimate the current TWC fractional oxygen state (FOS) and a robust controller is used to control the TWC FOS by manipulating the desired engine λ. The outer loop estimator and controller are combined with an existing inner loop controller. The inner loop controller controls the engine λ based on the desired λ value and the control inaccuracies are considered and compensated by the outer loop robust controller. This control strategy achieves good emission reduction performance and has advantages over the constant λ control strategy and the conventional two-loop switch-type control strategy.

1. INTRODUCTION

1.1 Motivation

Internal combustion engines are widely used in transport, power generation and other applications. Based on the difference of combination processes, the engine can be divided into two types: compression ignition (CI) engines and spark ignition (SI) engines. In CI engines, the air-fuel mixture is auto ignited by the heat of the compressed air. Fuel with low self-ignited temperatures, such as diesel, is the major power sources for the CI engine. In SI engines, the spark produced by the spark plug is used to ignite the mixture of air and fuel. SI engines take fuel with higher self-ignited temperatures such as gasoline and natural gas. Compared to the CI engines, the SI engines usually have lower costs and produce less noise. However, the lower brake mean effective pressure (BMEP) indicates less power generation from SI engines and the additional throttle brings in pumping losses which lowers down the engine efficiency.

The control of fuel and air in spark-ignited engines has increasingly became a challenge with the incorporation of turbo-charging, exhaust gas recirculation (EGR), valvetrain flexibility, and more stringent emission regulations. To enable effective stoichiometric air-to-fuel ratio control, the engine flow and composition must be accurately and robustly measured or estimated. The only viable option is to use algorithms to estimate the engine mass flow and composition. Five difficulties have to be taken into consideration for the engine air handling sensor and observer (i.e. estimator) design problem: (1) nonlinear system dynamics; (2) measurement uncertainties, including sensor delays and noise; (3) multivariate interactions; (4) engine variability for different operation conditions and (5) the trade-off between estimation accuracy and sensor costs.

Previous studies in the field of engine air handling system management have focused on the observer design based on pre-selected sensor sets [2][3][4][5]. However, considering the increasing complexity of today's engine systems and sensor characteristics, the choice of optimal air handling sensor set is not obvious; and it can be time-consuming and error prone if 'guess and check' experimental or simulation approaches are used. With the increasing variety of available sensors, the possible combinations of sensors will grow quickly. Brute-force

experimentation with different sensors is very expensive and time-consuming, and may need to be redone even when there are minor changes to the engine system or control strategies. In order to effectively solve the problem, an algorithm for optimal sensor selection and observer design for the engine air handling system is outlined and demonstrated in this work.

The sensor selection and controller design are also coupled problems since the control commands are always calculated based on sensor feedback signals. Proper sensor selection is critical for successful engine and control system designs. The most appropriate candidate control algorithms will depend on the sensing strategy selected. Ideally, sensor characteristics including noise, accuracy, dynamics, and delays would be taken into account when designing the controllers to achieve desired control performance. In the SI engine control problem, feedforward-feedback control is usually used for fast transient response and steady-state tracking performance. The sensor measurements can be used by the feedback controller or/and the feedforward controller. Experimental testing is one way to select sensor configurations and calibrate controller parameters. However, this method can be expensive and time-consuming, and may need to be redone even when there are minor changes to the engine system or the sensor/actuator characteristics. Therefore, a co-design strategy for both the sensing approach and control algorithm is desired to effectively select the acceptable sensor configurations and robustly design the controllers.

Emission control is also an essential control problem in today's advanced SI engines to meet the stringent emission regulations. The three-way-catalyst (TWC) is the most commonly used aftertreatment system in SI engines. TWC works as a buffer to store or release oxygen and increases the operating window about the stoichiometric air-to-fuel ratio (AFR). The fractional oxidation state (FOS) of TWC is a key control parameter for emission reductions. By manipulating the desired engine AFR, the TWC oxygen storage can be kept at the desired level to reduce emissions. Due to the lack of sensors, FOS is typically estimated by models. The model-based estimation can result in inaccurate estimations and thus limits the control performance. Some detailed chemical and thermodynamic-based models have been developed to describe the complex TWC chemical reactions by sets of partial differential equations (PDEs) in time and space[6][7]. Though such models could provide good estimations of FOS, they are not well-suited for controller designs. Moreover, the pre-existing

discrepancy between AFR command and actual AFR brings additional difficulties to the FOS controller. Considering all the challenges, a robust control strategy for the TWC FOS based on closed-loop FOS estimations is preferred for emission reductions.

1.2 Literature Review

1.2.1 Sensor Selection Algorithms

The sensor selection problem can be described as finding the sensor set which gives the best or acceptable performance over all possible sensor combinations.

As described in more detail in the following paragraphs, several mathematical methods have been developed to solve the sensor selection problem, including greedy algorithms and convex optimization. Greedy algorithms aim to find a global optimum by making the locally optimal choice at each stage. The solution computed by the greedy algorithm is not always globally optimum. Convex optimization problems have the property that any found local optimal will also be global. While most formulations are nonconvex, sometimes it is possible to convexify them with minimum or no impact on the solution to take advantage of the solution properties as well as of available solvers [8][9][10].

Sensor selection methods have been applied to various areas. In [11], the authors proposed three sensor selection algorithms for signal target tracking problems based on different resource and performance metrics. In another paper [12], the authors explored the use of randomization and a super-heuristic in multiple targets tracking problem to improve any given sensor set solution via random perturbation. That approach is more suitable for systems with little structure and for which the cost of solution evaluation is not high. In [13], the authors studied a randomized greedy algorithm for near-optimal sensor scheduling in large-scale sensor networks. In [14], a greedy algorithm based on two submodular cost functions, the weighted frame potential and the weighted log-det, was developed for the sensor selection problem in non-linear measurement models with additive normally distributed noise. Several sensor selection algorithms based on convex optimization or relaxation have also been applied to flexible structures. In [15][16][17] and [18], the weighed l_1 norm (without considering measurement noise) or l_2 norm of the observer gain was used to represent the sensor number,

and minimized along with the H_2 norm of the estimation error. The optimization problem was solved via SDP [15][16], alternating direction method of multipliers (ADMM) [17] and proximal methods [18]. In [19], several functions of the Cramer−Rao bound (CRB) were used as a performance measure and the sensor selection problem was formulated to minimize the CRB functions and a sparse selection vector. In [8], the authors computed the optimal sensor set among candidate linear measurements corrupted with normally distributed noises. The maximum-likelihood estimation errors were used as the performance evaluations.

In the application of engine sensor selection, methods include experimentation-based sensor selection and algorithm-based sensor selection. In [20], the best sensor configuration for a heavy-duty engine was found based on experimental results by testing each sensor design. In [21], the authors implemented a sensor selection algorithm for aircraft gas turbine engine healthy parameter estimation by minimizing the cost function of the estimation error and financial cost via a greedy algorithm. In [22], the authors determined the best sensor configurations among three candidate sensor configurations for air-fuel-ratio control in a spark ignited engine. Different controllers were designed for candidate sensor configurations. An objective function incorporating the overall system cost and controller performance as the optimization target was used, with solution via a genetic algorithm. In[23], the authors proposed a methodology for fault diagnosis sensor selection based on D_s-optimal FDI test design that maximized the sensitivity of outputs to anticipated faults and applied it in a diesel engine air handling system. The problem was solved using a heuristic method.

1.2.2 Air/EGR-Path Control

Several air-path control design studies have been done for SI engines with external EGR. In [24], the authors studied the charge control strategy for direct injection spark-ignited (DISI) engines with EGR. A nonlinear proportional-integral (PI) controller is combined with an adaptive burnt gas fraction observer to control the intake pressure and EGR flow based on the measurements of intake temperature sensor, intake pressure sensor, throttle flow sensor (MAF) and a universal exhaust-gas oxygen (UEGO) sensor. In [25], the authors developed an open-loop, linear time-varying model predictive controller (LTV-MPC) to track transient desired LP EGR rates for a gasoline turbocharged direct injection (GTDI) engine

with dual independent variable valve timing (VVT) by manipulating the LP EGR valve and modifying the VVT from an existing, baseline calibration. The MPC assumed a torque control strategy already existed to manage throttle, wastegate, fuel and spark timing. In [26], the authors proposed a fuel-efficient nonlinear model predictive control strategy with a disturbance observer to track an indicated mean effective pressure (IMEP) reference. The MPC was assumed to work with a perfect stoichiometric AFR controller. In[27], the author utilized the relative gain array (RGA) method to analyze the cross connections between air-path control inputs (throttle position, EGR valve position, waste-gate position) and outputs (intake pressure, intake EGR ratio) and proposed three candidate decentralized control strategies. All three controllers were assumed to work with a perfect fuel controller which ensured the engine was always running at the stoichiometric condition.

The above mentioned research focused on air-path or EGR flow control. The effort described in this thesis focuses instead on the development and validation of coordinated air flow, EGR flow and AFR control for stoichiometric engines using EGR, waste-gate turbocharging, intake throttling and variable valve timing (VVT). As of result of air/EGR-path dynamics and measurement inaccuracy, there are always some flow control errors during steady-state or transient conditions. Considering the interactions between the air/EGR-path control performance and the AFR control performance, the flow control inaccuracy will further result in errors in AFR control, which has a very tight control target for the stoichiometric SI engines. Previous research has studied the air-path and AFR control strategies for other types of engines with EGR, including diesel engines[28][29] and homogeneous charge compression ignition (HCCI) engines[30], but did not consider stoichiometric SI engines. Considering the different AFR control accuracy requirements and significant combustion differences, these control strategies are not expected to be suitable for stoichiometric SI engines.

1.2.3 Air-to-fuel Ratio Control

Many strategies for SI engine AFR control have been developed. These include open-loop feedforward control, closed-loop feedback control, and feedforward-feedback control[31]. Typical feedforward controllers rely on fast table look-up, estimation, and measurements of

mass air flow (MAF) or manifold absolute pressure (MAP) to calculate a first estimation of the desirable fueling amount. As a result, the feedforward control performance highly depends on the estimation and measurement accuracy, and the look-up table calibration. Typical feedback controllers rely on oxygen sensors– narrow-band exhaust-gas oxygen (EGO) or wide-band universal exhaust-gas oxygen (UEGO) sensors placed in the exhaust system. EGO sensors can only provide the information about whether the combustion is lean, rich or stoichiometric. Alternatively, the output voltage of wide range oxygen sensor UEGO depends on λ nonlinearly. AFR feedback controllers are therefore quite a bit different depending on the type of oxygen sensor(s) used. A significant benefit of the feedforward-feedback combination is that the feedforward controller can quickly respond to the transient operation and help the combustion maintain near stoichiometric operation while the feedback control actions are inherently slower due to the transport delay and chemical characteristic of the exhaust oxygen sensor[32]. In best practice, the feedback controller can compensate for feedforward fueling errors during closer to steady-state operations.

In this application area, many controllers have been developed, including PID control, robust control, linear quadratic Gaussian (LQG) control, adaptive control, fuzzy control, sliding mode control (SMC) and model predictive control (MPC). In [33], an adaptive delay-compensated PID feedback controller based on UEGO signal was applied to an SI engine for AFR control. In [34], a gain-scheduled H_∞ controller was designed to track reference AFR and minimize the effects of disturbances on the AFR for an SI engine based on the UEGO sensor measurement. In [35], an LQG controller was designed based on the linear model of the engine system to maintain the AFR in an allowable range. In [36], two adaptive controllers, adaptive feed-forward controller (AFFC) and adaptive posicast control (APC) were designed and tested on a vehicle for AFR control. In [37], a cost-effective fuzzy control system was applied to a small SI engine to regulate fuel injectors. Based on the engine speed and intake manifold pressure, the system determined the required fuel amount from a fuzzy algorithm and the parameters of the fuzzy control paradigm was a collection of rules and fuzzy-set membership functions. In [38], a sliding mode controller was applied to improve the accuracy of the AFR feedback control loop and a self-tuning control (STC) was added to the SMC to optimize the SMC gains sequentially. In [39], a neural network model-based

MPC controller was applied to a mean-value SI engine model for stoichiometric control with throttle angle considered as the disturbance. The neural network model used information from multiple variables and considers engine dynamics to do multi-step ahead prediction.

For all of the above mentioned studies, the controllers are designed based on already-selected sensor sets.

1.2.4 Three-way-catalyst Emission Control

The three-way-catalyst (TWC) is the most commonly used aftertreatment system in SI engines now. TWC can be used to simultaneously reduce the three major pollutants in the engine-out exhaust, carbon monoxide (CO), unburnt hydrocarbons (HC) and nitrogen oxides (NO_x) for SI engines. The reductants HC and CO can be oxidized into carbon dioxide (CO_2) and water (H_2O) by oxygen while the oxidant NO can be converted into nitrogen (N_2) and CO_2 by CO. However, the relative AFR window for achieving both oxidation and reduction simultaneously is very narrow, bringing difficulties to the engine AFR control system.

Consisting of Cerium oxides and precious metals[32], the TWC has an ability to store oxygen in lean conditions and release oxygen in rich conditions. Therefore, TWC works as a buffer to store or release oxygen and increases the operating window about the stoichiometric AFR.

Several TWC control strategies have been developed. A conventional approach is to use a PI controller to correct the engine fueling command by a multiplicative factor based on a single switch-type λ sensor upstream of the TWC[40]. The controller parameters need to be experimentally identified for every operating point and the TWC oxygen storage dynamics are not considered in this method. A more advanced TWC control method is to use a cascade control structure based on both TWC upstream and downstream λ sensors. In [41], a fore controller is designed to respond relatively quickly to AFR disturbances on the basis of pre-catalyst UEGO sensor signal and an aft controller is developed to adjust the setpoint of the fore controller on the basis of both pre-catalyst and post-catalyst UEGO sensors' measurements. In [42], a model predictive controller was designed as the primary control loop within a multi-rate cascade control configuration that adapted the parameters of a post-catalyst HEGO relay controller in an optimal manner using a predictive functional

control approach. The relay controller adjusted the target of a delay-compensated feedback controller for the pre-catalyst AFR to maintain the post-catalyst HEGO sensor signal within a specified range of the desired target voltage. The cascade control structure can further be combined with TWC oxygen storage level estimators. In [43], a TWC model was developed based on detailed first-principles reaction kinetics, subsequent averaging and model reduction. An outer loop PI controller was designed to control the model predicted TWC oxygen storage level by correcting the engine λ set point and an inner controller was developed to control the engine λ based on the outer loop command.

1.3 Contributions

1.3.1 Nonlinear Control-oriented Spark Ignition Engine Model Development

A physically-based, control-oriented state-space model of a 2.8L turbo-charged SI engine was derived, and then implemented in SIMULINK. The model includes intake, exhaust and boost manifolds filling dynamics. The turbocharger dynamics were modeled using a map reduction method. Two cooled EGR loops, high pressure (HP) EGR and low pressure (LP) EGR, are included in this model. The model includes the impact of modulation to any combination of 11 actuators, including the throttle valve, compressor bypass valve, fueling rate, waste gate, HP EGR valve, LP EGR valve, number of firing cylinders, intake valve open (IVO) timing, intake valve close (IVC) timing, exhaust valve open (EVO) timing and exhaust valve close (EVC) timing. Valve flow rates were modeled based on orifice equations. The insights learned in this work contributed to future engine control-oriented modeling efforts.

1.3.2 Cylinder-out Composition Modeling

A new composition model for the cylinder was proposed in this thesis to track the cylinder-out flow gas compositions with the assistance of Dheeraj Bharadwaj Gosala, PhD. This model utilizes cylinder charge flow, injected fuel amount, residual gas mass and intake manifold gas mass fractions to estimate the cylinder-out gas compositions, which are key parameters to predict exhaust manifold gas compositions. The model is physically-based

and contains no tuning parameters, allowing it to be implemented in the SI engine control-oriented model. This model is one of the novel work done by this thesis.

1.3.3 Cylinder-Out Temperature Modeling

The cylinder-out temperature is a key parameter to predict the exhaust manifold conditions. The effects of residual gas and fuel mass on the cylinder-out temperature were investigated. The simulation results indicate that the accuracy of Otto cycle-based cylinder-out temperature estimation are sensitive to the residual gas mass prediction especially at low engine speeds and low throttle angle operating ranges while the fuel mass has few effects. The neglect of residual gas mass leads to large estimation errors of the cylinder-out temperature or even results in reverse trends of the estimation results. This investigation work is unique to illustrate the necessity of modeling the residual gas mass by comparison results. The insights discovered in this investigation contributed to improving the accuracy of the control-oriented model. To achieve better estimation accuracy, the proposed cylinder-out temperature model also considers the EGR effects and the heat transfer during the exhaust blowdown process, which are usually not modeled in other Otto cycle models. The model achieved good estimation results of the cylinder-out temperature with an error of 30K for different engine operating conditions.

1.3.4 Turbine-Out Pressure Modeling

The turbine-out pressure is a necessary parameter for the LP EGR flow estimation. For the turbo-charged engine utilizing LP EGR, the turbine-out pressure cannot be simply set as ambient or other constant pressure value. As the upstream pressure of LP EGR valve, the accuracy of turbine-out pressure modeling affects the EGR flow rate estimation and thus the air handling system control. Moreover, the turbine flow estimation usually requires the value of turbine-out pressure as an input. In this thesis, a new flow-based turbine-out pressure estimation method was proposed. The utilization of this method contributed to the predictions of turbine flow and LP EGR flow.

1.3.5 Detailed Spark Ignition Engine Model in GT-Power

A detailed 2.8L turbocharged direct injection SI engine model with VVA system and dual EGR loops including HP EGR and LP EGR was developed in GT-Power software. The GT-Power model was used as the truth-reference and provided key parameters for the development and validation of the control-oriented model. This model was also used as a virtual test bench to test the designed observers and controllers. The insights learned in this work contributed to future SI engine modeling and validation work.

1.3.6 Spark Ignition Engine Model Linearization and Validation

The control-oriented nonlinear model was linearized based on the first-order Taylor expansion at the equilibrium point. Analysis was performed before the linearization to select proper sets of equations built for different conditions and deal with cycle-related terms. The linear state space model was used to perform control analysis. Both of the nonlinear and linear models were validated with a high fidelity SI engine GT-Power model for different engine operating conditions and achieved good estimation performance. The utilization of this model would allow for the implementation of the sensor selection frameworks to design optimal sensing architectures of the SI engine air handling system.

1.3.7 Model Uncertainty Estimation

Two new estimation models to quantify the model uncertainties were proposed in this thesis. Both methods were developed based on the comparison results between the truth-reference data and the model outputs. The first method is to calculate the error covariance of the derivatives of the linear model states in time-domain simulations. This method can be implemented in the state-space form to account for model uncertainties. The second method is to calculate the maximum relative steady-state errors of the linear model states compared to the truth-reference data, estimate the high frequency errors, and formulate these two errors in the frequency domain. Both of these two estimation methods worked well in the two sensor selection frameworks. The utilization of these two novel methods enabled the application of

sensor selection frameworks on actual physical systems by reasonably quantifying the effects of modeling errors.

1.3.8 Sensor and Actuator Dynamics Modeling

To account for the effects of sensor and actuator characteristics, first-order expressions were used to formulate their delays. The measurement noise was modeled in two different ways. The first method is to model the measurement noise as a diagonal matrix in the state space model based on the sensor accuracy. The second method, which is novel, is to model the bias error and precision error separately in frequency domain based on sensor accuracy and Fast Fourier Analysis (FFT) of the steady state measurements. These modeling efforts introduced the dynamics of sensors and actuators, and thus was critical to sensor architecture designs of the SI engine air handling system. The insights learned in this work would also contribute to future modeling work of sensors and actuators.

1.3.9 Sensor System and Observer Co-Design Framework Development

A sensor system and observer co-design framework based on H_2 optimization was developed to optimize the tradeoff between the observer error and the number of required sensors. The optimization problem was relaxed to a sequence of convex optimization problems that minimize the cost function consisting of the H_2 norm of the observer error and the weighted l_1 norm of the observer gain. An LMI formulation allows for efficient solution via semi-definite programming. The approach was applied to a physical-based control-oriented turbo-charged SI engine model with EGR to determine the optimal sensor sets for real-time intake manifold burnt gas mass fraction estimations. Simulation demonstrated that the optimal sensor sets computed using this algorithm had the best H_2 estimation performance, as expected, and desired. Sensor redundancy was also analyzed based on the algorithm results. This approach reduced computation time and experimental efforts typically required for selecting optimal sensor sets for a complex engine system.

This framework is a novel sensor selection framework for the engine air handling system and it has the following potentials:

1. This framework allows for evaluating the sensor redundancy.

2. The estimation performance of different sensing architectures can be compared based on the framework computation results instead of a large amount of experimental work.

3. The computed observer gain can be integrated to the engine control unit (ECU) and capable for observer switch in case of sensor failure.

1.3.10 Robust Control Based Sensor System and Controller Co-Design Framework Development

A sensor system and controller co-design framework based on robust performance was developed. This algorithm decided whether the system could achieve the required robust performance with the given set of sensors. It computed the structured singular value μ of the closed-loop system while synthesizing an H_∞ controller based on the given set of sensor. If μ is less than 1, a linear controller can be found for the current sensor set to make the closed-loop system achieve performance objectives. The lower the μ is, the more robust the closed-loop system will be. In this way, the acceptable sensor sets could be found by this framework. The framework was applied to an SI engine utilizing LP EGR to select suitable sensor sets for stoichiometric AFR and air/EGR-path controls. The framework designed sensing and control strategies were tested on a high fidelity SI engine GT-Power model. The simulation results demonstrated that the designed strategies achieved the desired AFR and air/EGR path control performance.

This framework is a novel method to simultaneously co-design the sensing and control strategies for the engine system and it has the following potentials:

1. With this framework, alternative sensors can be analyzed for cost, redundancy and/or robust performance even with sensor failure in the set.

2. This framework allows for evaluating the tradeoff between sensor characteristics and performance requirements.

1.3.11 TWC Oxygen Storage Level Estimation and Control

A novel two-loop control stratagy was developed for the TWC oxygen storage level control to reduce the emissions. In the outer loop, an FOS estimator consisting of a TWC model and

an extended Kalman-filter was designed to estimate the current TWC fractional oxygen state (FOS) and a robust controller was developed to control the TWC FOS by manipulating the desired engine λ. The outer loop estimator and controller were combined with an existing inner loop controller which controlled the engine λ based on the λ set point. In this novel control strategy, the inner loop control inaccuracies are considered and compensated by the outer loop robust controller, which is different from the conventional TWC control strategies.

2. PHYSICALLY-BASED CONTROL-ORIENTED ENGINE MODELING

2.1 Motivation

The physically-based, control-oriented mean-value model (MVM), is a very useful tool for control and diagnostic analysis. Compared to crank angle based models, MVMs describe variations slower than an engine cycle, and as such, typically have a frequency range of about 0.1 - 50Hz[32]. Such a model can capture the vast majority of the engine and sensor dynamics. Unlike the 'data driven' black-box model, state variables usually represent physical quantities and the model does not generally require a large amount of data for model training/tuning. In this chapter, a control-oriented SI engine model which includes gas exchange process, cylinder combustion process and turbocharger dynamics is developed. The first principle approach is used to model key parameters for the engine systems and air handling sensors/actuators. The state-space model can be easily obtained by using the variables and equations defined in this chapter for further control analysis. In comparison to the open literature, novel contribution of effort described in this chapter includes in-cylinder gas composition modeling, cylinder-out temperature model sensitivity investigation and turbine-out pressure estimation.

2.2 Engine Architecture

The engine model architecture is shown in Fig. 2.1. The model is a mean-value engine model developed in MATLAB and SIMULINK based on [32][44][45] [46]. It is equipped with both HP EGR and LP EGR paths.

2.3 Gas Exchange Model Development

In this section, the gas exchange process of the SI engine is modeled. The gas exchange model is formulated as first derivatives of manifold pressures, temperatures and compositions based on manifold filling dynamics. Three manifolds, boost, intake and exhaust manifolds are considered in this model. The following variables are modeled in this section:

1. Boost Manifold Pressure P_{bm}

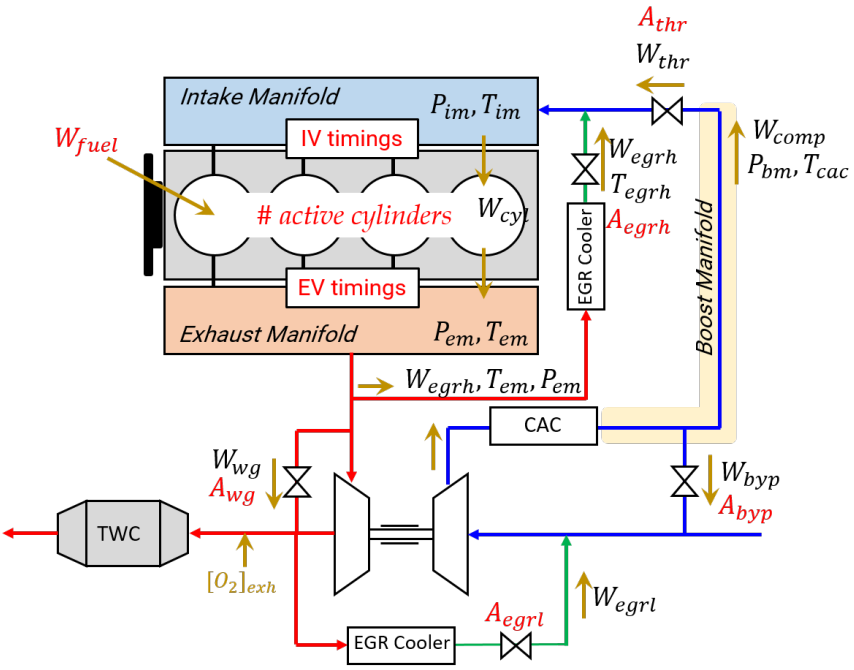

Figure 2.1. : Engine architecture.

2. Intake Manifold Pressure P_{im}
3. Exhaust Manifold Pressure P_{em}
4. Boost Manifold Temperature T_{bm}
5. Intake Manifold Temperature T_{im}
6. Exhaust Manifold Temperature T_{em}
7. Boost Manifold Unburnt Gas Mass Fraction $F_{ub,bm}$
8. Boost Manifold Burnt Gas Mass Fraction $F_{b,bm}$
9. Intake Manifold Unburnt Gas Mass Fraction $F_{ub,im}$
10. Intake Manifold Burnt Gas Mass Fraction $F_{b,im}$
11. Exhaust Manifold Unburnt Gas Mass Fraction $F_{ub,em}$
12. Exhaust Manifold Burnt Gas Mass Fraction $F_{b,em}$

2.3.1 Manifold Pressure

The manifold pressures are modeled as following:

$$\begin{aligned}
\dot{P}_{bm} &= \frac{\gamma_{bm} R_{bm}}{V_{bm}} [W_{comp} T_{cac} - W_{thr} T_{bm} - W_{byp} T_{bm}] \\
\dot{P}_{\mathrm{im}} &= \frac{\gamma_{\mathrm{im}} R_{\mathrm{im}}}{V_{\mathrm{im}}} [W_{thr} T_{bm} + W_{egrh} T_{\mathrm{egrh}} - W_{cyl} T_{\mathrm{im}}] \\
\dot{P}_{em} &= \frac{\gamma_{\mathrm{em}} R_{\mathrm{em}}}{V_{em}} [W_{cylout} T_{cylout} - W_{turb} T_{\mathrm{em}} - W_{wg} T_{\mathrm{em}} - W_{egrh} T_{\mathrm{em}}]
\end{aligned} \tag{2.1}$$

where P, V, T, R, W denote the pressure, volume, temperature, mass-specific gas constant, mass flow rate, respectively. Subscripts of bm, $\mathrm{i}m$, $\mathrm{e}m$, $comp$, thr, cac, byp, $\mathrm{e}grh$, cyl, $cylout$, $turb$, wg denote boost manifold, intake manifold, exhaust manifold, compressor, throttle, charge air cooler, bypass, high pressure EGR, cylinder, cylinder-out, turbine, waste-gate, respectively.

2.3.2 Manifold Temperature

The manifold temperatures are modeled as following:

$$\begin{aligned}
\dot{T}_{bm} &= \frac{R_{bm} T_{bm}}{P_{bm} V_{bm}} [W_{comp}(\gamma_{cac} T_{cac} - T_{bm}) - (W_{thr} + W_{byp})(\gamma_{bm} T_{bm} - T_{bm})] \\
\dot{T}_{\mathrm{im}} &= \frac{R_{\mathrm{im}} T_{\mathrm{im}}}{P_{\mathrm{im}} V_{\mathrm{im}}} [W_{thr}(\gamma_{bm} T_{bm} - T_{\mathrm{im}}) + W_{\mathrm{egrh}}(\gamma_{\mathrm{egrh}} T_{\mathrm{egrh}} - T_{\mathrm{im}}) - W_{cyl}(\gamma_{\mathrm{im}} T_{\mathrm{im}} - T_{\mathrm{im}})] \\
\dot{T}_{em} &= \frac{R_{\mathrm{em}} T_{\mathrm{em}}}{P_{\mathrm{em}} V_{\mathrm{em}}} [W_{cylout}(\gamma_{cylout} T_{cylout} - T_{\mathrm{em}}) - (W_{turb} + W_{wg} + W_{egrh})(\gamma_{\mathrm{em}} T_{em} - T_{em})]
\end{aligned} \tag{2.2}$$

where γ denotes the gas specific heat ratio.

2.3.3 Manifold Composition

The manifold compositions are modeled as following:

$$\begin{aligned}
\dot{F}_{ub,bm} &= \frac{R_{bm}T_{bm}}{P_{bm}V_{bm}}[W_{\text{inlet}}(1-F_{ub,bm}) + W_{egrl}(F_{ub,em}-F_{ub,bm})] \\
\dot{F}_{b,bm} &= \frac{R_{bm}T_{bm}}{P_{bm}V_{bm}}[W_{\text{inlet}}(0-F_{b,bm}) + W_{egrl}(F_{b,em}-F_{b,bm})] \\
\dot{F}_{ub,\text{im}} &= \frac{R_{\text{im}}T_{\text{im}}}{P_{\text{im}}V_{\text{im}}}[W_{thr}(F_{ub,bm}-F_{ub,\text{im}}) + W_{\text{egrh}}(F_{ub,em}-F_{ub,\text{im}})] \\
\dot{F}_{b,\text{im}} &= \frac{R_{\text{im}}T_{\text{im}}}{P_{\text{im}}V_{\text{im}}}[W_{thr}(F_{b,bm}-F_{b,\text{im}}) + W_{egrh}(F_{b,em}-F_{b,\text{im}})] \\
\dot{F}_{ub,em} &= \frac{R_{\text{em}}T_{em}}{P_{\text{em}}V_{em}}[W_{cylout}(F_{ub,cylout}-F_{ub,em})] \\
\dot{F}_{b,em} &= \frac{R_{\text{em}}T_{em}}{P_{\text{em}}V_{em}}[W_{cylout}(F_{b,cylout}-F_{b,em})]
\end{aligned} \tag{2.3}$$

where F denotes the mass fraction. The subscripts ub and b stand for unburnt gas and burnt gas, respectively.

2.4 Flow Model

2.4.1 Valve Flow Model

The valve mass flow rates are modeled by the following orifice equation[32]:

$$\begin{aligned}
W &= A_{\text{e}ff}\frac{P_{\text{in}}\sqrt{\gamma}}{\sqrt{RT_{\text{in}}}}f(\frac{P_{out}}{P_{\text{in}}}) \\
f\left(\frac{P_{out}}{P_{\text{in}}}\right) &= \begin{cases} \sqrt{\frac{2}{\gamma-1}\left[\left(\frac{P_{out}}{P_{\text{in}}}\right)^{\frac{2}{\gamma}} - \left(\frac{P_{out}}{P_{\text{in}}}\right)^{\frac{\gamma+1}{\gamma}}\right]} & \text{if} \quad \left(\frac{P_{out}}{P_{\text{in}}}\right) \geq \left(\frac{2}{\gamma+1}\right)^{\frac{\gamma}{\gamma-1}} \\ \sqrt{\left(\frac{2}{\gamma+1}\right)^{\frac{\gamma+1}{\gamma-1}}} & \text{if} \quad \left(\frac{P_{out}}{P_{\text{in}}}\right) \leq \left(\frac{2}{\gamma+1}\right)^{\frac{\gamma}{\gamma-1}} \end{cases}
\end{aligned} \tag{2.4}$$

where γ is the gas specific heat ratio, $A_{\text{e}ff}$ is the valve effective area, P_{out} is the downstream pressure, P_{in} and T_{in} are the upstream pressure and temperature, respectively.

2.4.2 Cylinder Charge Flow Model

The cylinder is treated as an open system during the gas exchange process from IVO (intake valve open) to IVC (intake valve close). An energy balance equation based on the First Law is used to describe the process as shown in Fig. 2.2. This model is developed from a diesel engine volumetric efficiency model proposed in [44].

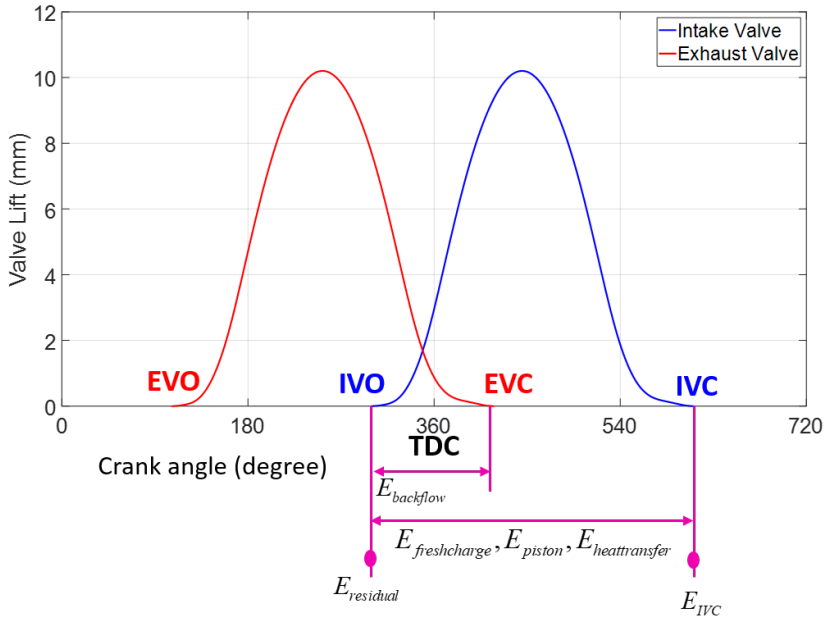

Figure 2.2. : Gas exchange process from IVO to IVC.

The energy balance equation is listed as following:

$$E_{ivc} = E_{residual} + E_{backflow} + E_{freshcharge} - E_{piston} + E_{heattransfer} \tag{2.5}$$

where E denotes energy.

The six energy terms in equation (2.5) are:

1. Cylinder gas energy at IVC, E_{ivc}
2. Residual exhaust gas energy at IVO, $E_{residual}$
3. Back flow exhaust gas energy from IVO to EVC (exhaust valve close), $E_{backflow}$
4. Fresh charge gas energy from intake manifold to cylinder during IVO to IVC, $E_{freshcharge}$
5. Piston work energy done by cylinder gas from IVO to IVC , E_{piston}

6. Heat transfer to cylinder gas from IVO to IVC, $E_{heattransfer}$

Cylinder gas energy at IVC E_{ivc} is calculated by:

$$E_{ivc} = P_{im}\left(\frac{V_{ivc_{eff}}}{V_{ivc}}\right)^{\gamma_{ivc}} V_{ivc}\frac{c_v}{R} \tag{2.6}$$

where γ_{ivc} is the gas specific heat ratio, specific heat (constant volume) and ideal gas constant for the gas trapped in cylinder at IVC. At IVC, the gas mixture trapped in cylinder consists of residual gas, external EGR and fresh charge. Since the major composition is the fresh charge, γ_{ivc} is assumed to be the same as the air specific heat ratio γ_{air}=1.35. $V_{ivc_{eff}}$ is the effective IVC volume defined as the volume of the point in the compression stroke (modeled as an isentropic process) whose pressure equals the intake manifold pressure. In this model, $V_{ivc_{eff}} = 16.9V_{ivc}$.

Residual exhaust gas energy at IVO $E_{residual}$ is calculated by:

$$E_{residual} = \begin{cases} \frac{P_{em}V_{ivo}c_{v,burnt}}{R_{burnt}} & if \quad (IVO < EVC) \\ P_{em}\left(\frac{V_{evc}}{V_{ivo}}\right)^{\gamma_{burnt}} V_{ivo}\frac{c_{v,burnt}}{R_{burnt}} & if \quad (IVO > EVC) \end{cases} \tag{2.7}$$

Back flow exhaust gas energy from IVO to EVC $E_{backflow}$ is calculated by:

$$E_{backflow} = \begin{cases} (P_{em}V_{evc} - P_{em}V_{ivo})\frac{c_{p,burnt}}{R_{burnt}} & if \quad (IVO < EVC) \\ 0 & if \quad (IVO > EVC) \end{cases} \tag{2.8}$$

Fresh charge gas energy from intake manifold to cylinder during IVO to IVC $E_{freshcharge}$ is calculated by:

$$E_{freshcharge} = m_{charge}c_{p,air}T_{im} \tag{2.9}$$

where the effects of exhaust recirculation gas on the gas constants are ignored.

Piston work energy done by cylinder gas from IVO to IVC E_{piston} is calculated by:

$$E_p = P_{im}\left(V_{ivc,eff} - V_{ivo}\right) \tag{2.10}$$

Heat transfer to cylinder gas from IVO to IVC $E_{heattransfer}$ is calculated by:

$$E_q = h_{ivo-ivc}\left(T_{wall} - T_{im}\right) SA_{ivo-ivc} \tag{2.11}$$

where T_{wall} is the cylinder temperature and is assumed as a constant value 400K. $h_{ivo-ivc}$ is heat transfer coefficient and is calculated by Woschni's correlation [47].

$$h_{ivo-ivc} = 3.26 \cdot B^{-0.2} \cdot {P_{im}}^{0.8} {T_{im}}^{-0.55} \cdot \left(6.18 \cdot 2 \cdot S \cdot \frac{N}{60}\right) \tag{2.12}$$

where N is the engine speed, B is the cylinder bore and S is the cylinder stroke. SA_{ivoivc} is the integrated surface area from IVO to IVC and is calculated by:

$$SA_{ivoivc} = \left(2\pi\left(\frac{B}{2}\right)^2 + \pi \cdot B \cdot l_{ivo-ivc}\right) \frac{IVC - IVO}{60N} \tag{2.13}$$

The cylinder volumes v_{ivo} (at IVO), v_{ivc} (IVC), v_{evo} (at EVO (exhaust valve open)) and v_{evc} (EVC) are calculated by:

$$\begin{aligned}
x_{ivo} &= x_{tdc} + (l_{rod} + r_{crk}) - r_{crk} \cdot cos(IVO) - \sqrt{l_{rod}^2 - \left(r_{crk} \cdot sin\left(IVO\right)\right)^2} \\
x_{ivc} &= x_{tdc} + (l_{rod} + r_{crk}) - r_{crk} \cdot cos(IVC) - \sqrt{l_{rod}^2 - \left(r_{crk} \cdot sin\left(IVC\right)\right)^2} \\
x_{evo} &= x_{tdc} + (l_{rod} + r_{crk}) - r_{crk} \cdot cos(EVO) - \sqrt{l_{rod}^2 - \left(r_{crk} \cdot sin\left(EVO\right)\right)^2} \\
x_{evc} &= x_{tdc} + (l_{rod} + r_{crk}) - r_{crk} \cdot cos(EVC) - \sqrt{l_{rod}^2 - \left(r_{crk} \cdot sin\left(EVC\right)\right)^2}
\end{aligned} \tag{2.14}$$

$$\begin{aligned}
V_{ivo} &= A_{cyl} x_{ivo} \\
V_{ivc} &= A_{cyl} x_{ivc} \\
V_{evo} &= A_{cyl} x_{evo} \\
V_{evc} &= A_{cyl} x_{evc}
\end{aligned} \tag{2.15}$$

where is A_{cyl} is the cross-section area of cylinder and $A_{cyl} = \frac{\pi B^2}{4}$.

The cylinder integrated cylinder height change from IVO to IVC $l_{ivo-ivc}$ is calculated by $l_{ivo} + l_{ivc}$ listed as following:

$$l_{\text{ivo}} = \begin{cases} x_{ivo} & \text{if} \quad (IVO < 360^\circ) \\ -x_{ivo} & \text{if} \quad (IVO > 360^\circ) \end{cases} \tag{2.16}$$

$$l_{\text{ivc}} = \begin{cases} 2 \cdot (x_{tdc} + S) - x_{\text{ivc}} & \text{if} \quad (IVO < 540^\circ) \\ -x_{\text{ivc}} & \text{if} \quad (IVC > 540^\circ) \end{cases} \tag{2.17}$$

The cylinder fresh charge mass over one cycle can be expressed by:

$$m_{charge} = \frac{(E_{IVC} - E_r - E_b + E_p - E_q)}{T_{\text{im}} c_{p,air}} \tag{2.18}$$

And the cylinder charge mass flow rate is:

$$W_{charge} = m_{charge} \frac{N}{120} \tag{2.19}$$

The final expression of the cylinder fresh charge mass flow rate for the positive valve overlap (PVO) case, i.e., $IVO < EVC$, is:

$$\begin{aligned} W_{charge} = & \frac{P_{\text{im}} V_{\text{ivc}} \left(\frac{V_{\text{ivc}_{eff}}}{V_{\text{ivc}}} \right)^{\gamma_{air}} c_{v,air} N}{120 c_{p,air} T_{\text{im}} R_{air}} \\ & - \frac{N \left(P_{em} V_{\text{ivo}} (c_{v,burnt} - c_{p,burnt}) + P_{em} V_{evc} c_{p,burnt} \right)}{120 c_{p,air} T_{\text{im}} R_{burnt}} \\ & + \frac{N \left(P_{\text{im}} \left(V_{\text{ivc},eff} - V_{ivo} \right) - h_{\text{ivo-ivc}} (T_{wall} - T_{\text{im}}) SA_{\text{ivo-ivc}} \right)}{120 c_{p,air} T_{\text{im}}} \end{aligned} \tag{2.20}$$

The final expression of the cylinder fresh charge mass flow rate for the negative valve overlap (NVO) case, i.e., $IVO > EVC$, is:

$$\begin{aligned} W_{charge} = & \frac{N}{120 T_{\text{im}} c_{p,air}} \left(P_{\text{im}} V_{\text{ivc}} \left(\frac{V_{\text{ivc}_{eff}}}{V_{\text{ivc}}} \right)^{\gamma_{air}} \frac{c_{v,air}}{R_{air}} - P_{em} V_{ivo} \left(\frac{V_{evc}}{V_{ivo}} \right)^{\gamma_{burnt}} \frac{c_{v,burnt}}{R_{burnt}} \right) \\ & + \frac{N}{120 T_{\text{im}} c_{p,air}} \left(P_{\text{im}} \left(V_{\text{ivc,e}ff} - V_{\text{ivo}} \right) - h_{ivo-ivc} (T_{wall} - T_{\text{im}}) SA_{\text{ivo}-ivc} \right) \end{aligned} \tag{2.21}$$

2.5 Combustion Model Development

2.5.1 Cylinder-out Composition

In this composition model, the cylinder-out gas mixture consists of the following three compositions:

1. Cylinder-out Unburnt Gas Mass Fraction, $F_{ub,cylout}$.
2. Cylinder-out Burnt Gas Mass Fraction, $F_{b,cylout}$.
3. Cylinder-out Unburnt Hydrocarbon Mass Fraction, $F_{uhc,cylout}$.

The modeling of in-cylinder composition before and after combustion considers two different cases: leaner than stoichiometry and richer than stoichiometry.

Leaner Combustion

For the leaner combustion case shown in Fig. 2.3, the condition and cylinder-out gas compositions are modeled as following:

$$\begin{aligned} & AFR_{st} \varepsilon_{comb} (m_{fuel} + F_{uhc,\text{im}} m_{charge}) \leq F_{b,\text{im}} m_{charge} \\ & F_{ub,cylout} = \frac{F_{ub,\text{im}} m_{charge} - AFR_{st} \varepsilon_{comb} \left(m_{fuel} + F_{uhc,\text{im}} m_{charge} \right)}{m_{charge} + m_{fuel} + m_{res}} \\ & F_{b,cylout} = \frac{\left(AFR_{st} + 1 \right) \varepsilon_{comb} \left(m_{fuel} + F_{uhc,\text{im}} m_{charge} \right) + F_{b,\text{im}} m_{charge} + m_{res}}{m_{charge} + m_{fuel} + m_{res}} \\ & F_{uhc,cylout} = 1 - F_{b,cylout} - F_{ub,cylout} \end{aligned} \tag{2.22}$$

where AFR_{st}, m_{fuel}, m_{charge}, m_{res} denote the stoichiometric AFR of the fuel, the mass of the directly injected fuel per cycle, the mass of total cylinder charged gas mixture per cycle, residual gas trapped in cylinder at intake valve close (IVC), respectively. The parameter

ε_{comb} is a factor between 0 and 1 to describe the combustion level. If $\varepsilon_{comb} = 1$, the air-fuel mixture is completely combusted. If $\varepsilon_{comb} = 0$, the air-fuel mixture is not burnt at all.

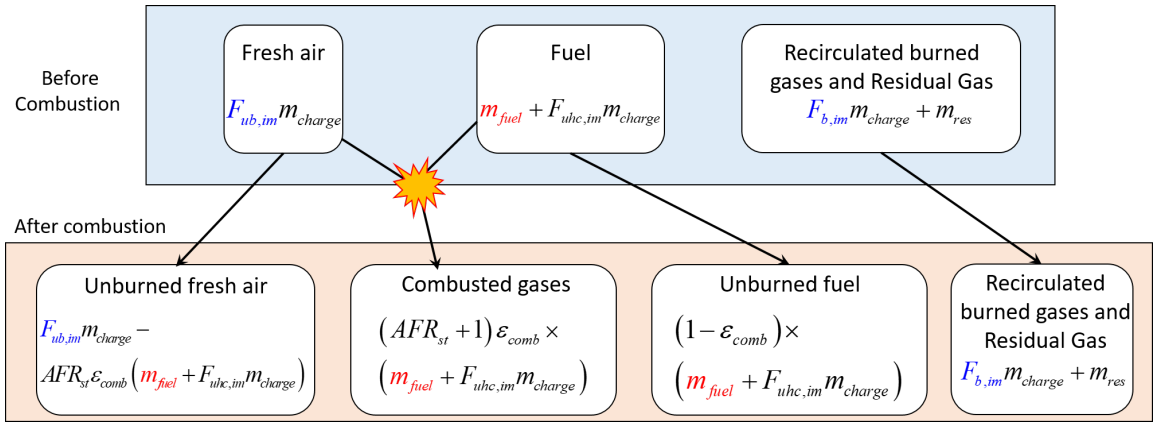

Figure 2.3. : Leaner than stoichiometry: in-cylinder composition.

In this case, the air in the cylinder charge goes into two parts after the combustion: unburnt fresh air and combusted gases. In the lean-burn mode, the fuel is burnt with an excess of air. Thus there is unburnt fresh air remained in the cylinder after the combustion. The mass of combusted gases is calculated based upon the amount of combusted fuel. Two possible fuel sources, the direct injected fuel and the port-injected fuel, are considered in this model. After combustion, the cylinder-out mixture consists of the unburnt air, combusted gases, unburnt fuel and recirculated burnt gases.

Richer Combustion

For the richer combustion case shown in Fig. 2.4, the condition and cylinder-out gas compositions are modeled as following:

$$
\begin{aligned}
& AFR_{st}\varepsilon_{comb}(m_{fuel} + F_{uhc,\mathrm{im}} m_{charge}) \geq F_{b,\mathrm{im}} m_{charge} \\
& F_{ub,cylout} = 0 \\
& F_{b,cylout} = \frac{F_{ub,\mathrm{im}} m_{charge} \left(1 + \frac{1}{AFR_{st}}\right) + F_{b,\mathrm{im}} m_{charge} + m_{res}}{m_{charge} + m_{fuel} + m_{res}} \\
& F_{uhc,cylout} = \frac{m_{fuel} + F_{ub,\mathrm{im}} m_{charge} - \frac{F_{ub,\mathrm{im}} m_{charge}}{AFR_{st}}}{m_{charge} + m_{fuel} + m_{res}}
\end{aligned}
\tag{2.23}
$$

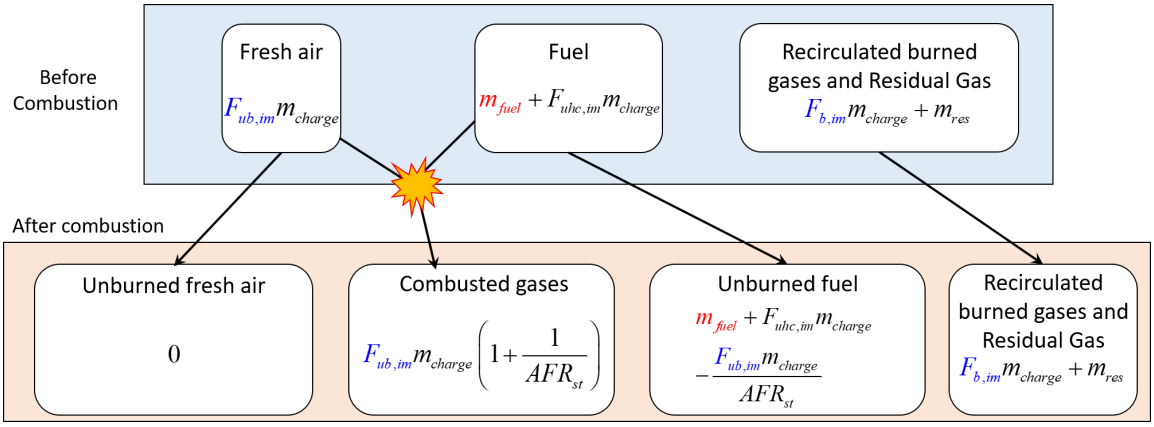

Figure 2.4. : Richer than stoichiometry: in-cylinder composition.

In this case, the fresh air is burnt with an excess of fuel. Complete combustion is assumed and thus there is no unburnt air remaining in the cylinder-out mixture. The mass of combusted gases is calculated based upon the combusted air. After the combustion, the cylinder-out mixture consists of the combusted gases, unburnt fuel and recirculated burnt gases.

2.5.2 Otto Cycle

For the combustion process, the Otto cycle as shown in Fig. 2.5 is modeled based on [32].

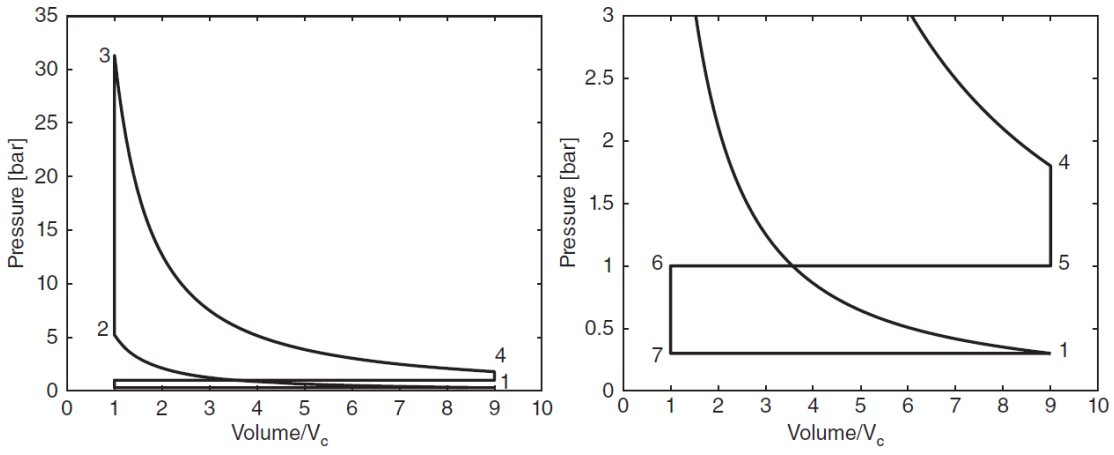

Figure 2.5. : P-V diagram of Otto cycle[32].

From 1 (bottom dead center (BDC)) to 2 (top dead center (TDC)), the compression stroke is modeled as the following isentropic process which is adiabatic and reversible:

$$T_2 = T_1(\frac{V_1}{V_2})^{\gamma_{im}-1} = T_1(r_c)^{\gamma_{im}-1} \tag{2.24}$$

where $r_c = \frac{V_1}{V_2}$ is the compression ratio.

From 2 (TDC) to 3 (peak temperature), the combustion process is modeled as a constant volume process. The heat generated by the chemical combustion is converted to the thermal energy. For the direct injection SI engine model, the unburnt hydrocarbons in the intake manifold is assumed to remain 0 and all the fuel comes from the cylinder direct injector. Therefore, the heat exchange process can be modeled as following:

$$m_{fuel}X_{eff}Q_{LHV} = (m_{res} + m_{charge} + m_{fuel})c_v(T_3 - T_2) \tag{2.25}$$

where Q_{LHV} is the lower heating value of the fuel, $c_v = \frac{R}{\gamma-1}$ (R is the gas specific heat) is the constant volume specific heat of the air-fuel mixture, m_{res} is the residual gas mass remaining in the cylinder from last cycle. m_{charge} is the total mass of charged gas. X_{eff} is a tuning parameter to reflect the energy conversion inefficiency which is primarily caused by heat loss. X_{eff} is modeled by a linear function of engine speed[48]:

$$X_{eff} = a \cdot N + b \tag{2.26}$$

where a and b are constant tuning parameters.

Therefore, the peak temperature T_3 during the combustion process can be calculated as:

$$T_3 = T_2 + \frac{m_{fuel}X_{eff}Q_{LHV}(\gamma - 1)}{(m_{res} + m_{charge} + m_{fuel})R} \tag{2.27}$$

For the stoichiometric operation, equation (2.27) can be further simplified by introducing a new parameter x_r, the residual gas mass fraction:

$$x_r = \frac{m_{res}}{m_{charge} + m_{res} + m_{fuel}} \tag{2.28}$$

and thus

$$m_{res} = \frac{x_r}{1 - x_r} \left(m_{charge} + m_{fuel} \right) \tag{2.29}$$

The relationship between the fuel mass and the total mass of cylinder gas m_{charge} can be formulated as following based on the assumption of stoichiometric operation with the existed of external exhaust gas recirculation:

$$m_{fuel} = \frac{m_{charge} F_{ub,im}}{AFR} \tag{2.30}$$

Substitute equations (2.29) and (2.30) into (2.27), the combustion peak temperature T_3 can be calculated by:

$$T_3 = T_2 + \frac{(1 - x_r) F_{ub,im} X_{eff} Q_{LHV} (\gamma - 1)}{(F_{ub,im} + AFR) R} \tag{2.31}$$

From 3 (peak temperature) to 4 (EVO), the expansion stroke is modeled as an isentropic process and the EVO temperature T_{evo} is expressed as:

$$T_{evo} = T_4 = T_3 \left(\frac{V_3}{V_4} \right)^{\gamma_{cyl} - 1} = T_3 \left(\frac{V_{tdc}}{V_{evo}} \right)^{\gamma_{cyl} - 1} \tag{2.32}$$

From 4 (EVO) to 5, the blowdown process is modeled as an isentropic process and the blowdown gas temperature is:

$$T_{bd} = T_4 \left(\frac{P_{em}}{P_4} \right)^{1 - \left(\frac{1}{\gamma_{cyl}} \right)} \tag{2.33}$$

Considering the heat transfer between the blowdown gas and the cylinder wall, the cylinder-out exhaust gas temperature T_{cylout} is:

$$T_{cylout} = T_{bd} - \frac{hSA \left(T_{bd} - T_{wall} \right) \frac{30}{N}}{c_p \left(m_{charge} + m_{fuel} + m_r \right)} \tag{2.34}$$

where T_{wall} is the cylinder wall temperature and is assumed as a constant value 400K, SA is the heat transfer surface area. The heat transfer coefficient h is calculated based on Woschni's correlation [47]:

$$h = 3.26 \cdot B^{-0.2} \cdot {P_{em}}^{0.8} {T_{bd}}^{-0.55} \cdot \left(6.18 \cdot 2 \cdot S \cdot \frac{N}{60}\right) \tag{2.35}$$

The temperature T_1 at 1 (TDC) is the temperature of the fresh charge mixed with the residual gas. The fresh charge temperature is assumed to be the same as the intake manifold temperature T_{im}. The residual gas temperature T_r is calculated as:

$$T_r = T_{evc} \left(\frac{P_{im}}{P_{em}}\right)^{1-\left(\frac{1}{\gamma_r}\right)} \tag{2.36}$$

where T_{evc} is the in-cylinder temperature at EVC and assumed as a constant value 500K.

The mixing is modeled as an adiabatic mixing between the fresh charge and the residual gas. Thus the TDC temperature T_1 is expressed as:

$$T_1 = T_{im}\left(1 - x_r\right) + x_r T_r \tag{2.37}$$

where γ_r is the gas specific heat ratio of the residual gas.

2.5.3 Effects of Residual Gas Mass on Cylinder-out Temperature Estimations

Based on the Otto cycle model developed in Section 2.5.2, the residual gas mass has three explicit effects on the temperature estimation:

1. The temperature at the beginning of the compression stroke, T_1, is the temperature of the charged gas mixed with the residual gas in equation (2.37). Due to the high temperature of the residual gas, T_1 is higher than the intake manifold temperature T_{im}.

2. The existence of residual gas increases the total mixture mass during the heat conversion process in equation (2.25).

3. The existence of residual gas increases the total mixture mass during the heat transfer process in equation (2.34).

In order to understand the sensitivity of the cylinder-out temperature model to the residual gas mass and determine the necessity of the residual gas modeling work, a unique investigation was performed to study the effects of different cylinder compositions on T_{evo} and T_{cylout} estimations.

Fig. 2.6 and 2.7 show the effects of gas composition on the EVO temperature T_{evo} estimation. The reference engine GT-Power model was run at 800rpm, 1600rpm, 2400rpm, 3200rpm and 4000rpm. For each speed, six throttle angle operating conditions, 5°, 10°, 20°, 40°, 60°, 90°, were tested. For all the operating conditions, the LP EGR valve and HP EGR valve remained closed and thus the trapped burnt gases at IVC given all came from the residual gas. The developed control-oriented model based on the equations in Section 2.5.2 was also run to estimate the EVO temperature. All the composition mass data was directly obtained from high fidelity GT-Power simulation results. Different compositions' mass terms were ignored in the total cylinder gas mass calculation $m_{cyl,total} = m_{charge} + m_{fuel} + m_{res}$: fuel and residual gas, fuel, residual gas, none. If the residual gas mass is ignored, the residual gas fraction x_r in equation (2.37) is also set as 0 and thus the TDC temperature equals the intake manifold temperature T_{im}. For each case, $X_{\text{e}ff}$ in equation (2.26) is re-tuned to best fit the temperature curve. Per Fig. 2.6b and 2.7b, the EVO temperature T_{evo} cannot be accurately calculated if the residual gas mass is neglected. Instead, ignoring the fuel mass m_{fuel} in $m_{cyl,total}$ has few effects on the EVO temperature estimation. The reason can be found in Fig. 2.8. The residual gas percentage is much higher than the fuel mass percentage at low engine speeds and low throttle angles.

Fig. 2.9 and 2.10 show the effects of gas composition mass on the cylinder-out temperature T_{cylout} estimation. Without considering the residual gas mass, the model estimated cylinder-out temperature has reverse trends against GT-Power reference data. Fuel mass, however, has few effects on the estimation accuracy of the cylinder-out temperature model. Similar to the EVO temperature estimation, the residual gas mass shouldn't be ignored when estimating the cylinder-out temperature.

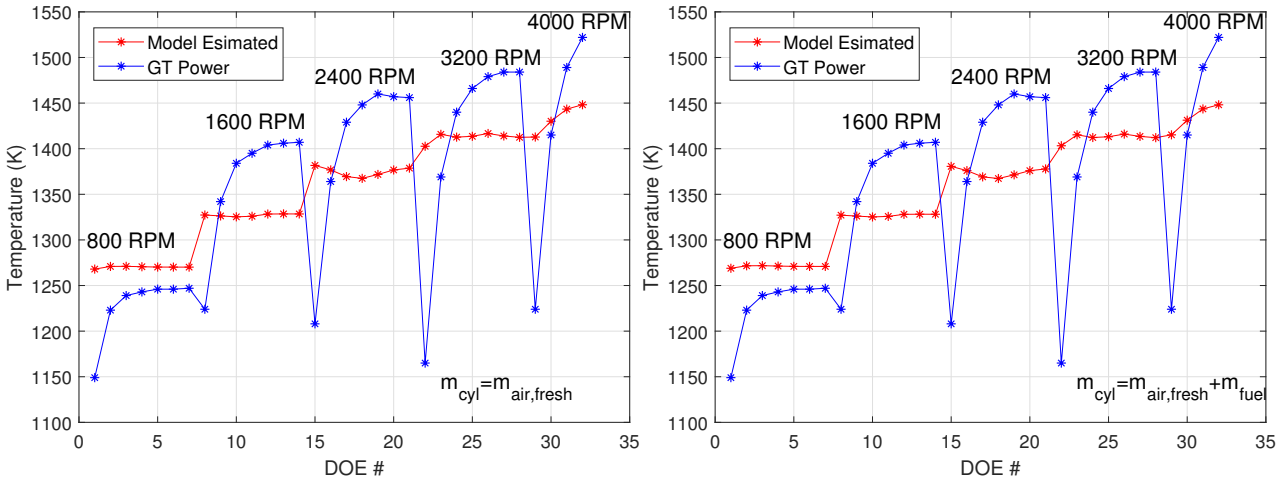

(a) No fuel or residual gas

(b) No residual gas

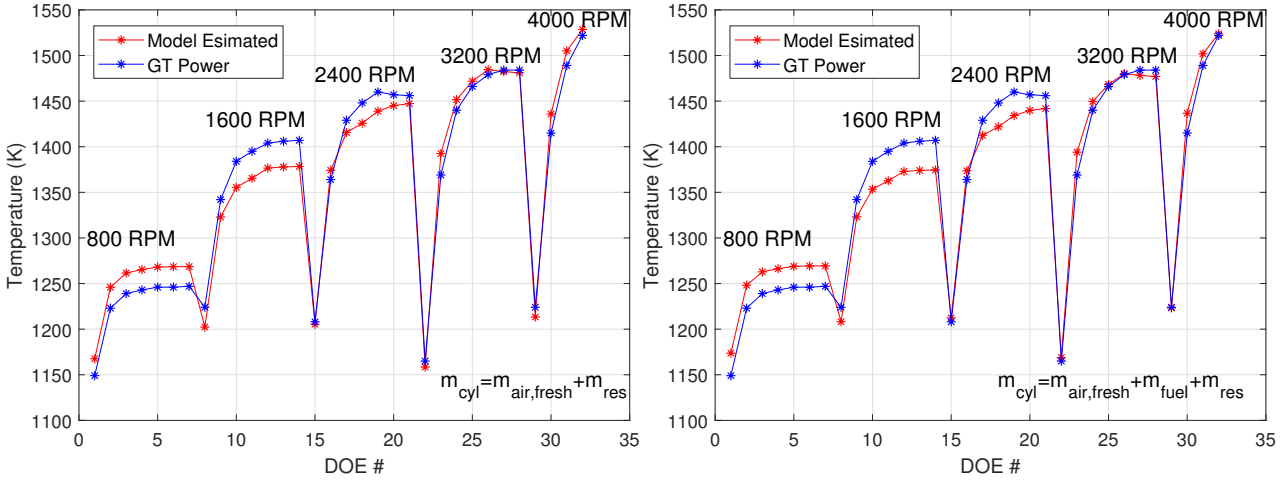

(c) No fuel

(d) All

Figure 2.6. : Effects of gas composition mass on the EVO temperature estimation.

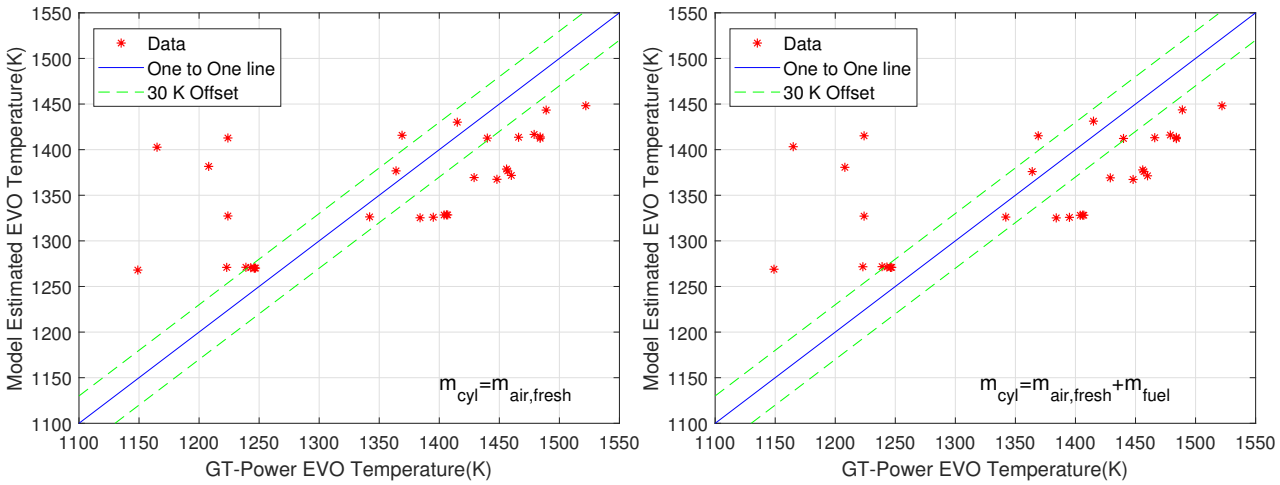

(a) No fuel or residual gas

(b) No residual gas

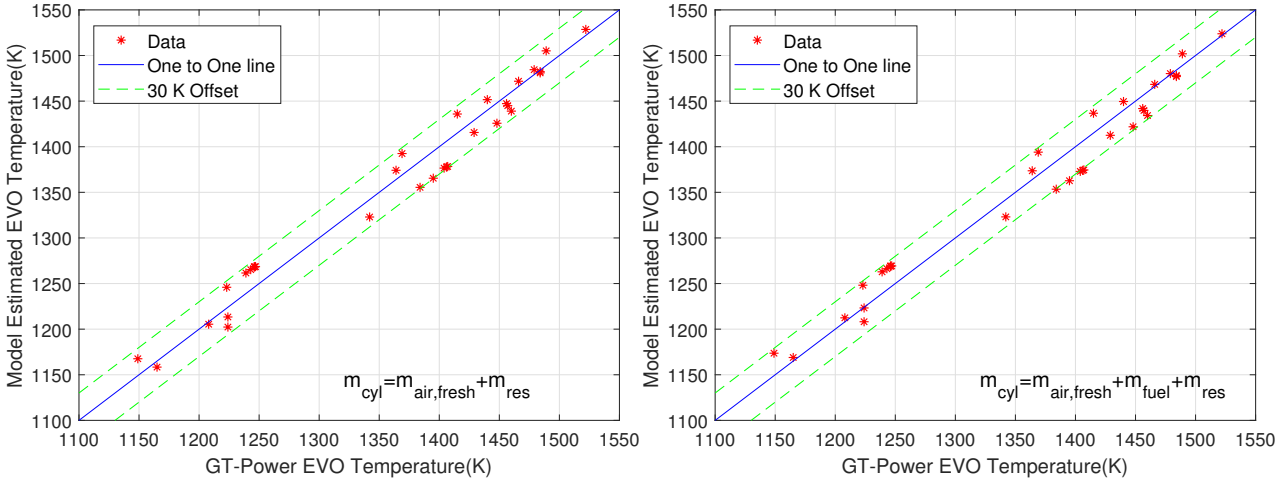

(c) No fuel

(d) All

Figure 2.7. : Estimation errors of EVO temperature.

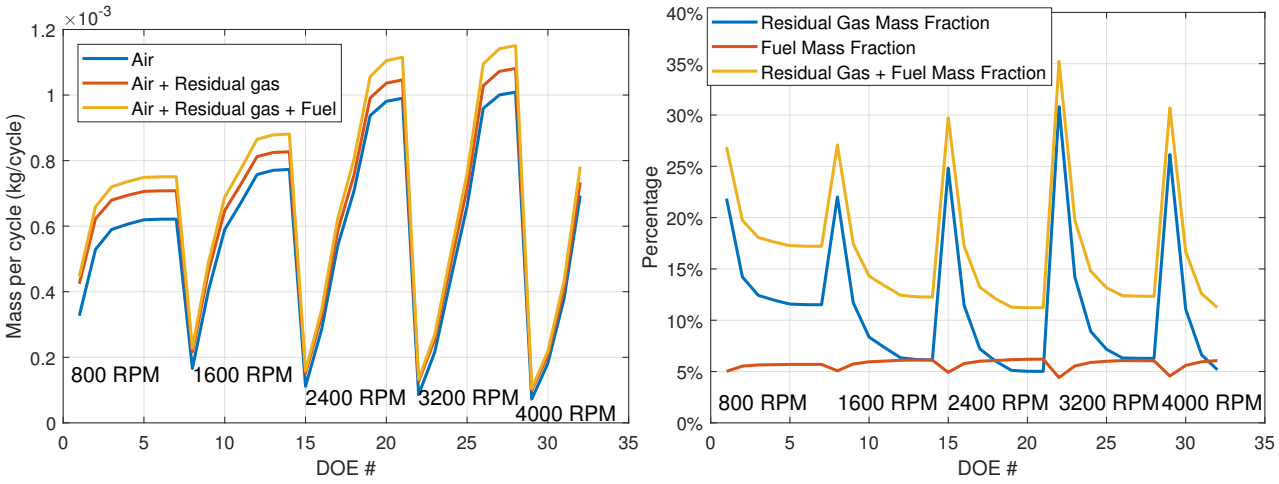

(a) In-cylinder composition mass

(b) In-cylinder residual gas and fuel mass fraction

Figure 2.8. : Cylinder gas compositions.

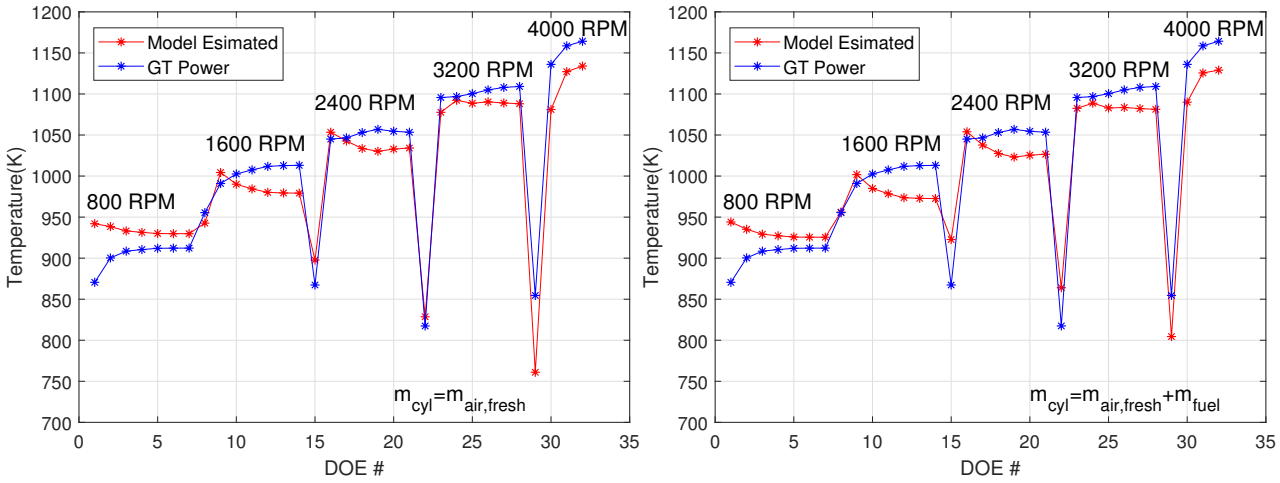

(a) No fuel or residual gas

(b) No residual gas

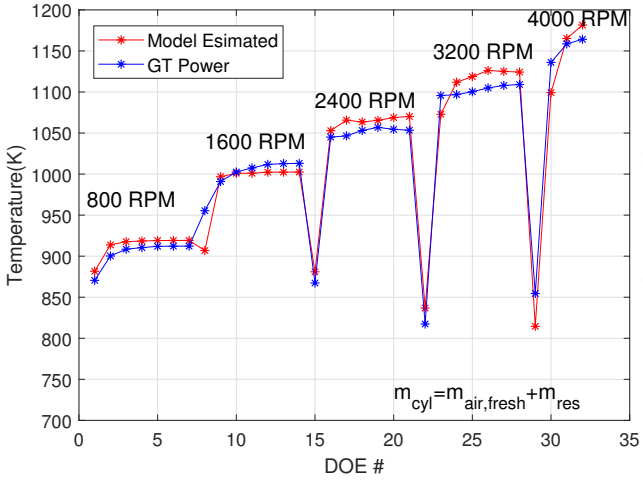

(c) No fuel

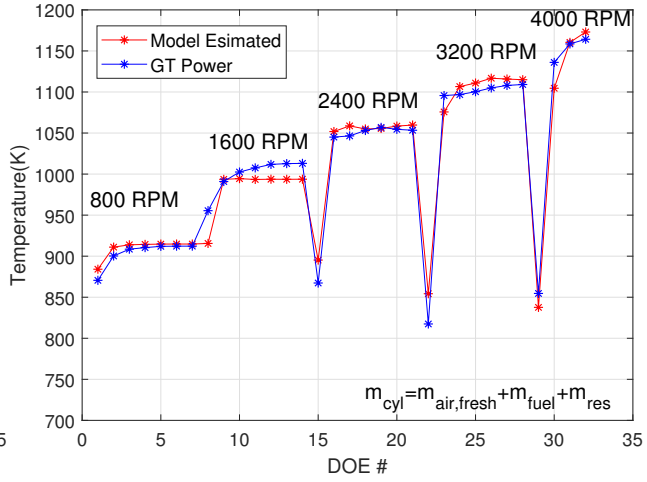

(d) All

Figure 2.9. : Effects of gas composition mass on the cylinder-out temperature estimation.

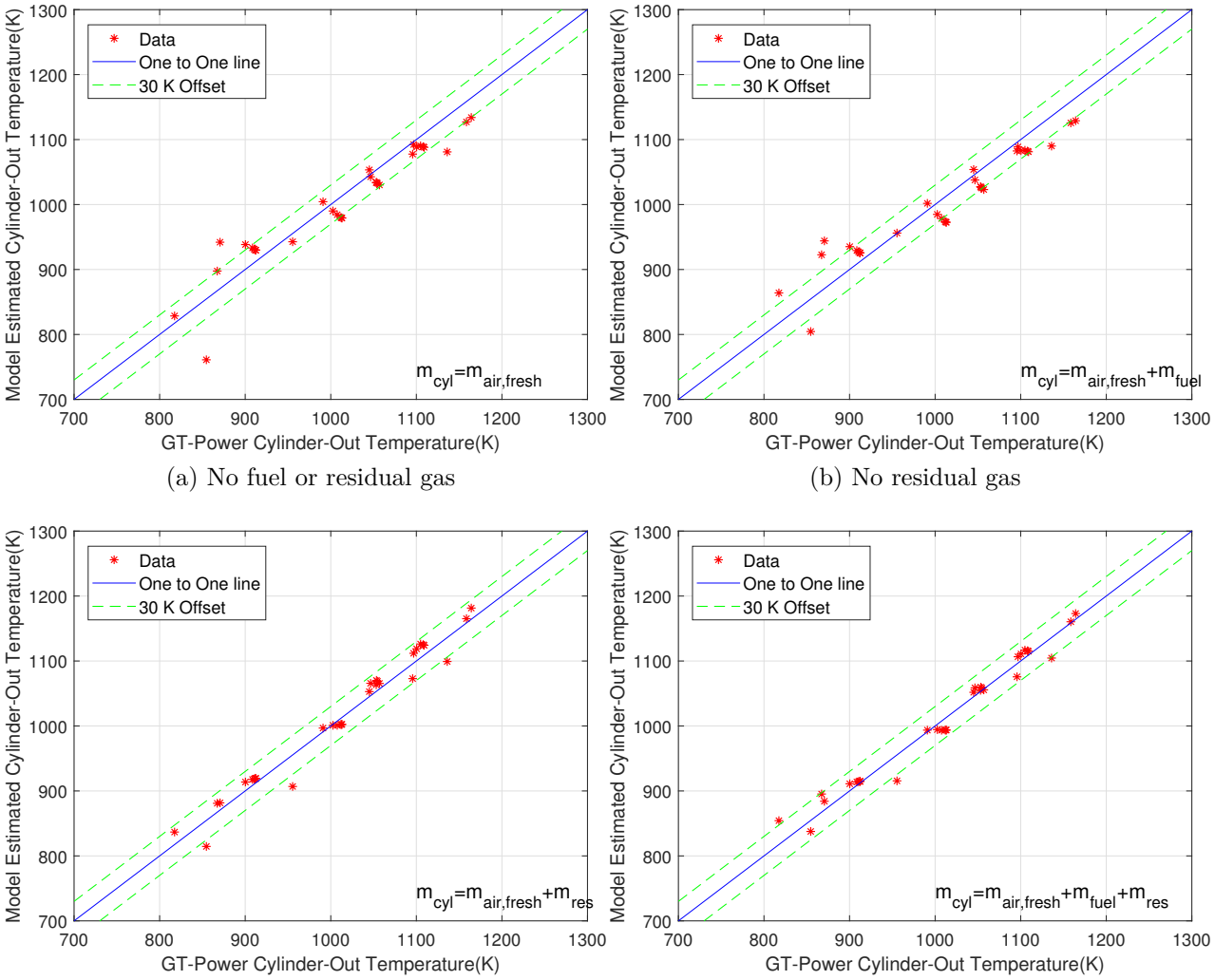

(a) No fuel or residual gas

(b) No residual gas

(c) No fuel

(d) All

Figure 2.10. : Estimation errors of cylinder-out temperature.

The investigation work shows the effects of residual gas mass on the EVO and cylinder-out temperature estimations. The work indicates that an estimation model of the residual gas mass is necessary in order to accurately predict the temperatures.

2.5.4 Residual Gas

The residual gas model is developed based on[49]. The total residual gas mass m_{res} consists of the exhaust back flow mass $m_{backflow}$ and the in-cylinder burnt gas mass $m_{rev,ivo}$ at IVO:

$$m_{res} = m_{backflow} + m_{rev,ivo} \tag{2.38}$$

The backflow mass $m_{backflow}$ can be calculated as:

$$m_{backflow} = C_1 \sqrt{\left(\frac{P_{em}}{RT_{em}} \left(P_{em} - P_{im} \right) \right)} A_{flow} \frac{OLV}{N} \tag{2.39}$$

where C_1 is a tunable parameter, N is the engine speed, OLV is the valve overlap volume and defined by the volume difference between exhaust valve close (EVC) and intake valve open (IVO) for positive valve overlap (PVO):

$$OLV = V_{evc} - V_{ivo} \tag{2.40}$$

and A_{flow} is the cylinder valve effective area. For the negative valve overlap (NVO) case, $OLV = 0$.

The trapped in-cylinder burnt gas mass at IVO $m_{rev,ivo}$ is calculated by:

$$m_{rev,ivo} = C_2 \frac{P_{em} V_{ivo}}{RT_{em}} \tag{2.41}$$

where C_2 is also a tunable parameter.

Fig. 2.11 shows the residual gas model estimation performance by setting $C_1 = 0.2$ and $C_2 = 0.83$. With this model, in-cylinder total mass error is within -13% to 7%.

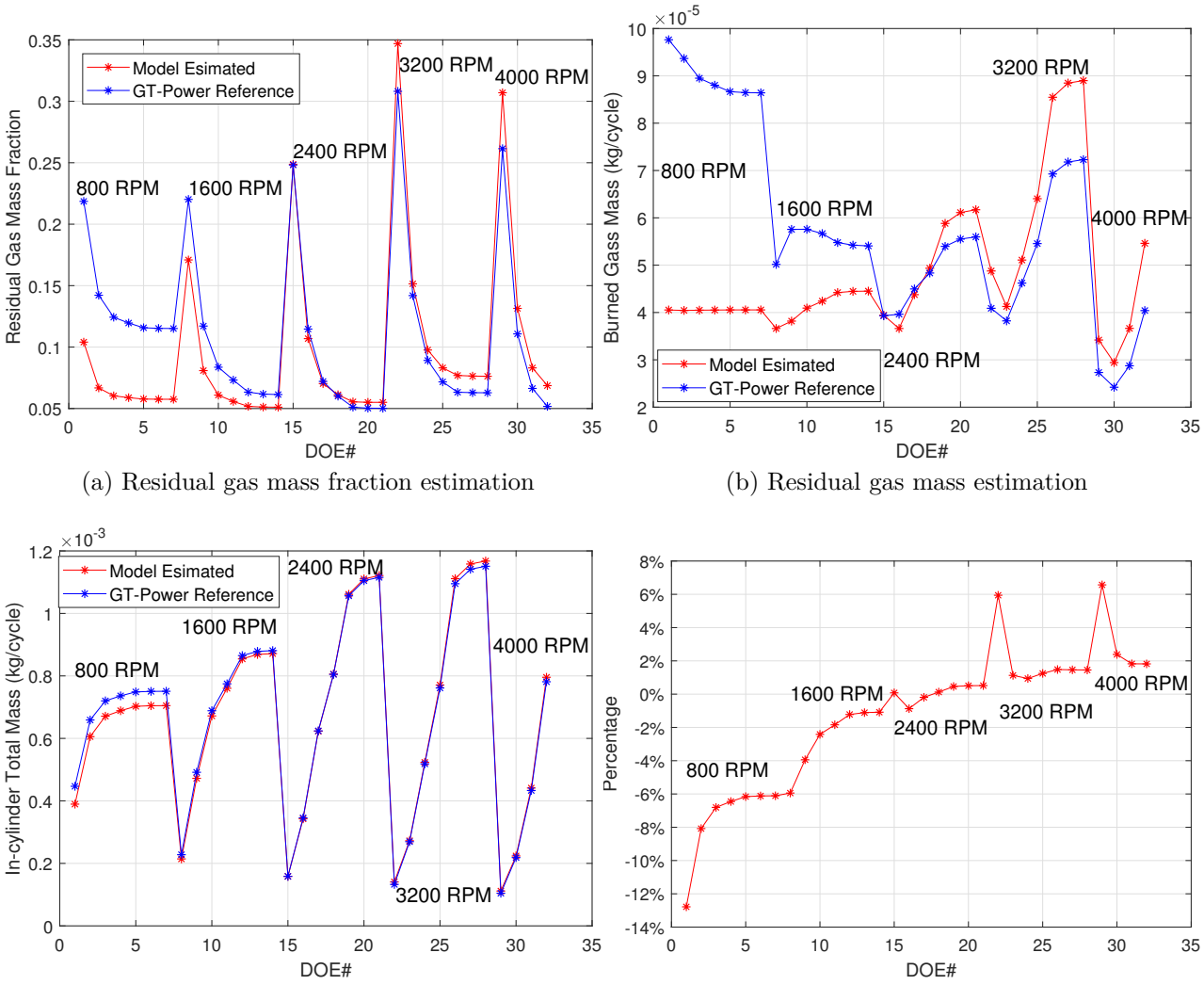

(a) Residual gas mass fraction estimation

(b) Residual gas mass estimation

(c) In-cylinder total mass

(d) In-cylinder mass estimation errors

Figure 2.11. : Residual gas model validation.

2.5.5 Model Validation

Fig. 2.12 shows the EVO temperature and cylinder-out temperature estimations based on the proposed residual gas model and Otto cycle model. 32 steady-state DOE cases were run in the reference engine GT-Power model. The engine speeds were set at 800rpm, 1600rpm, 2400rpm, 3200rpm and 4000rpm. For each speed, the throttle was operated at six different angles: 5°, 10°, 20°, 40°, 60° and 90° (fully open). For all of these cases, both LP EGR and HP EGR valves were left closed. The model estimated T_{evo} and T_{cylout} are within 30K range compared to GT-Power simulation results (per Fig. 2.12).

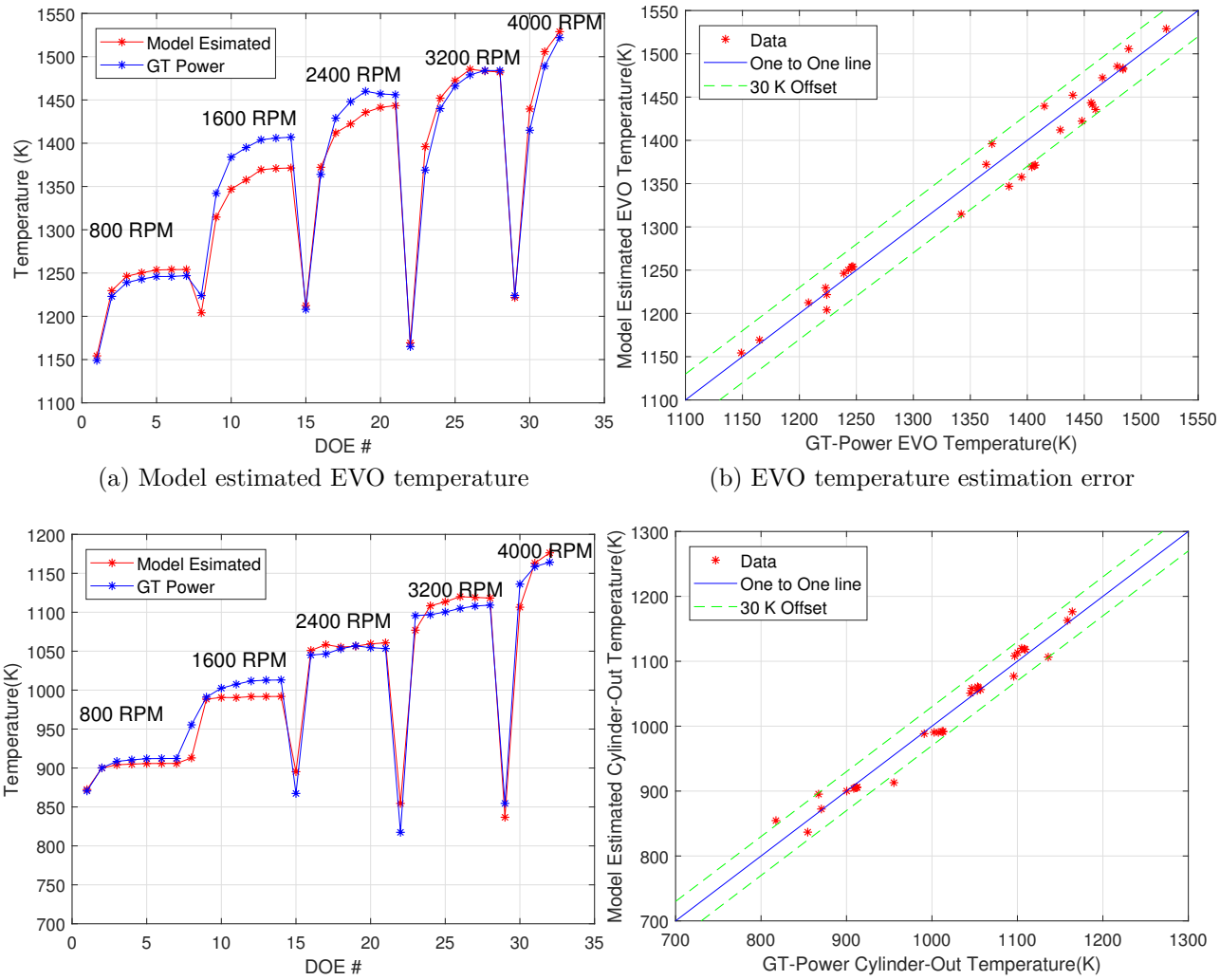

(a) Model estimated EVO temperature

(b) EVO temperature estimation error

(c) Model estimated cylinder-out temperature

(d) Cylinder-out temperature estimation error

Figure 2.12. : Model estimated EVO and cylinder-out temperatures.

Fig. 2.13 shows the cylinder-out temperature estimation based on the proposed residual gas model and Otto cycle model when the EGR flow is considered. 30 steady-state DOE cases were run in the reference engine GT-Power model. For each speed, LP EGR valve was operated at 0°, 18°, 36°, 54°, 72° and 90°. For all of these cases, throttle angle was fixed at 45°. Per Fig. 2.13, the model can well estimate the cylinder-out temperature when the EGR percentage varies within 0 to 25%.

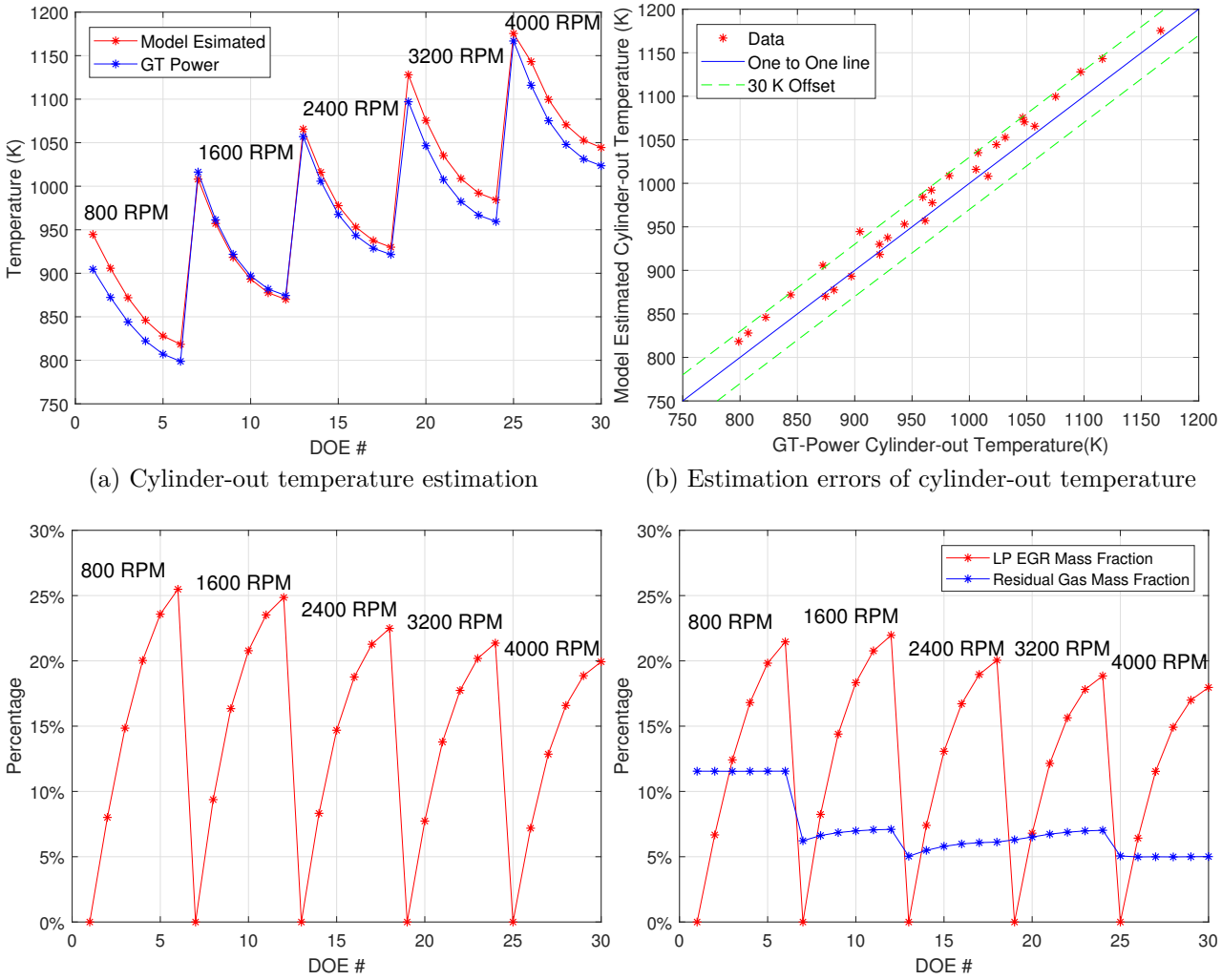

(a) Cylinder-out temperature estimation

(b) Estimation errors of cylinder-out temperature

(c) EGR fraction in the intake manifold

(d) In-cylinder burnt gas composition

Figure 2.13. : Cylinder-out temperature validation with LP EGR valve opens.

2.6 Turbocharger Model Development

2.6.1 Turbocharger Speed

The turbocharger speed ω_{tc} is modeled as following:

$$\dot{\omega}_{tc} = \frac{Z_{turb} - Z_{comp}}{I_{tc}\omega_{tc}} \tag{2.42}$$

where I_{tc} is the turbo-charger inertia. The turbine power Z_{turb} and compressor power Z_{comp} are modeled as following:

$$\begin{aligned} Z_{comp} &= \frac{W_{comp} C_{p,a} T_a}{\eta_{comp}} \left[\left(\frac{P_{bm}}{P_a} \right)^{\frac{\gamma_a - 1}{\gamma_a}} - 1 \right] \\ Z_{turb} &= W_{turb} C_{p,e} \eta_{turb} T_{em} \left[1 - \frac{P_{turb,out}}{P_{em}} \right]^{\frac{\gamma_e - 1}{\gamma_e}} \end{aligned} \tag{2.43}$$

where P_a is the ambient pressure and $P_a = 1\text{bar}$, $P_{turb,out}$ is the turbine out pressure, which is modeled is modeled in section 2.6.3.

The compressor mass flow W_{comp} and efficiency η_{comp} as well as turbine mass flow W_{turb} and efficiency η_{turb} are modeled based on the proposed method in [50] and polynomial fitting.

2.6.2 Compressor Mass Flow and Efficiency

The compressor mass flow rate W_{comp} and efficiency η_{comp} are modeled based on the non-dimensionalization strategy developed in [46]. W_{comp} is modeled as following:

$$W_{comp}\left(P_{\text{im}}, \omega_{tc}\right) = 2 \left[\frac{\pi}{4} \rho_a {d_c}^2 \left(\frac{1}{\gamma R T_a} \right)^{\frac{\gamma - 1}{2\gamma}} \left(\frac{\pi}{60} d_c \omega_{tc} \right)^{\frac{2\gamma - 1}{\gamma}} \right] \left(a_1 X^3 + a_2 X^2 + a_3 X + a_4 \right) \tag{2.44}$$

and the compressor efficiency η_{comp} can be modeled as following:

$$\eta_{comp}\left(P_{\text{im}}, \omega_{tc}\right) = \frac{\left(\frac{C_{p,a} T_a \left(PR_c{}^{\frac{\gamma - 1}{\gamma}} - 1 \right)}{\frac{1}{2}\left(\frac{\pi}{60} d_c \omega_{tc} \right)^2} \right)}{\left(c_1 \left(\frac{240 W_c}{\pi^2 \rho_a {d_c}^3 \rho_a {d_c}^2} \right) + c_2 \right)} \tag{2.45}$$

where the constant parameters used in equation (2.44) and (2.45) are shown in Table 2.1. C_1, C_2, a_1 , a_2 , a_3 and a_4 are constant tunable parameters which are obtained from linear regression to best fit the compressor flow and efficiency curves as shown in Table 2.2.

X is defined by:

$$X = \frac{C_{p,a} T_a \left(PR_c{}^{\frac{\gamma - 1}{\gamma}} - 1 \right)}{\frac{1}{2}\left(\frac{\pi}{60} d_c \omega_{tc} \right)^2} \tag{2.46}$$

The compressor pressure ratio PR_c across the compressor is defined as:

$$PR_c = \frac{P_{comp,out}}{P_{comp,in}} = \frac{P_{bm}}{P_a} \tag{2.47}$$

Table 2.1. : Constant parameters in compressor map modeling

Parameter	Description	Value	Unit
ρ_a	Compressor Inlet Air Density	1.161	kg/m^3
d_c	Compressor Blade Tip Diameter	55	mm
γ	Air Specific Heat Ratio	1.35	kg/s
R	Compressor Inlet Air Specific Heat	287	J/(kg·K)
T_a	Compressor Inlet Air Temperature	300	K
$C_{p,a}$	Compressor Inlet Air Specific Heat (Constant Pressure)	1107	J/(kg·K)

Table 2.2. : Constant tuning parameters in compressor map modeling

C_1	-6.8211
C_2	1.5145
a_1	-2.1882
a_2	3.3778
a_3	-1.7833
a_4	0.4278

Fig. 2.14 shows the modeled compressor map compared to the compressor table plot when the compressor speed varies within 90,000 to 200,000 rpm.

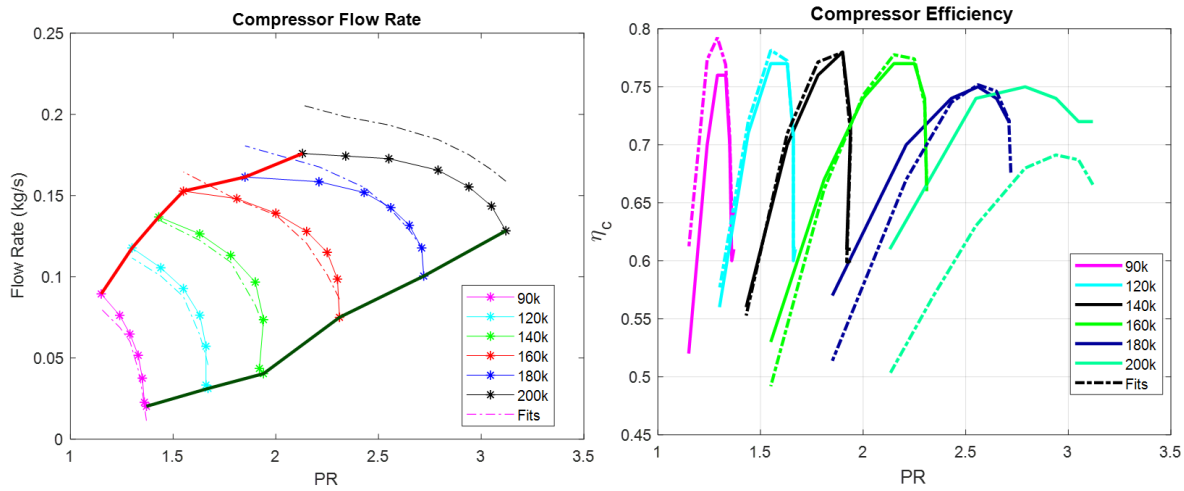

Figure 2.14. : Compressor map fitting.

2.6.3 Turbine Mass Flow and Efficiency

The turbine mass flow rate model is developed based on the map reduction method proposed in [46]:

$$W_{turb}\left(P_{em}, T_{em}, \omega_{tc}\right) = \frac{P_{em}}{\sqrt{T_{em}}} W_{turb,red}\left(P_{em}, T_{em}, \omega_{tc}\right) \tag{2.48}$$

where $W_{turb,red}$ is the reduced turbine mass flow rate.

$W_{turb,red}$ is fitted by using the following polynomial:

$$\begin{aligned} W_{turb,red} = &\left(a_1 N_{red}^3 + a_2 N_{red}^2 + a_3 N_{red} + a_4\right) \\ &\cdot \left(b_1 {PR_t}^7 + b_2 {PR_t}^6 + b_3 {PR_t}^5 + b_4 {PR_t}^4 + b_5 {PR_t}^3 + b_6 {PR_t}^2 + b_7 PR_t + b_8\right) \end{aligned} \tag{2.49}$$

where N_{red} is the reduced turbine speed:

$$N_{red} = \frac{\omega_{tc}}{\sqrt{T_{em}}} \tag{2.50}$$

and PR_t is the pressure ratio across the turbine:

$$PR_t = \frac{P_{turb,\text{in}}}{P_{turb,out}} = \frac{P_{em}}{P_{turb,out}} \tag{2.51}$$

Table 2.3. : Constant tuning parameters in turbine map modeling

a_1	-6.1137×10^{-12}
a_2	7.0948×10^{-8}
a_3	-2.6744×10^{-4}
a_4	1.3328
b_1	2.9968×10^{-2}
b_2	-0.4068
b_3	2.3341
b_4	-7.3410
b_5	13.6804
b_6	-15.13084
b_7	9.2253
b_8	-2.3895
b_9	0.4278

The parameters in equation (2.49) are shown in Table 2.3.

The turbine out pressure $P_{turb,out}$ (in bar) is modeled as a polynomial fitting of the cylinder-out mass flow rate and the comparison with GT-Power turbine out pressure is shown in Fig. 2.15.

$$P_{turb,out} = 9.51W_{cylout}^2 + 1.475W_{cylout} + 0.9853 \tag{2.52}$$

Fig. 2.16 shows the turbine out pressure modeling compared with GT-Power output.

Per Fig. 2.17, the reduced turbine mass flow rate fits the turbine map output well at different reduced turbine speeds. The turbine efficiency model was first developed as fitted polynomials (per Fig. 2.17). However, the fitted curves didn't match the turbine map plots well. Therefore, the turbine efficiency is set as a constant value 0.73.

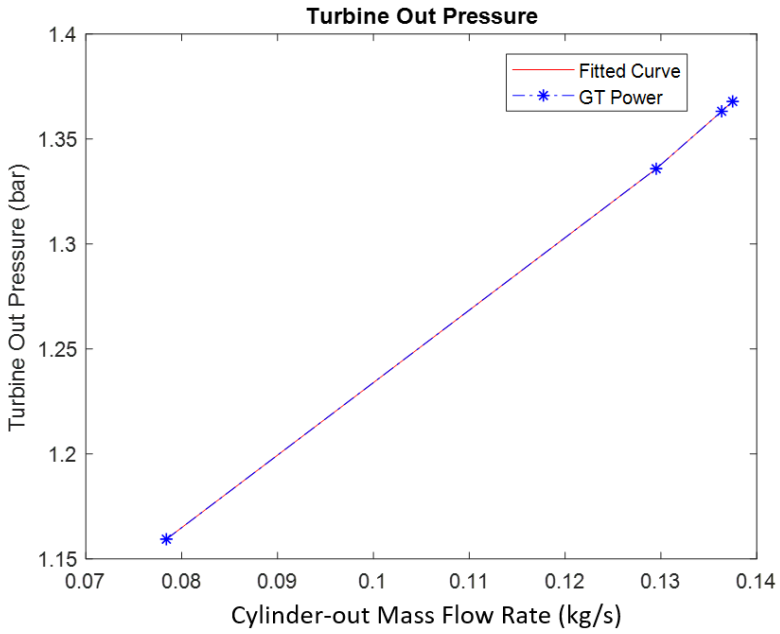

Figure 2.15. : Turbine out pressure versus cylinder-out mass flow rate.

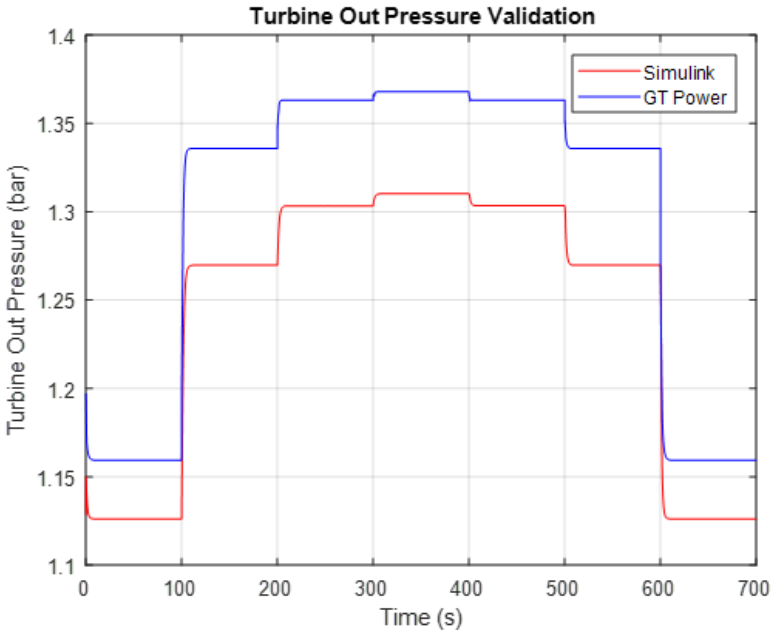

Figure 2.16. : Turbine out pressure.

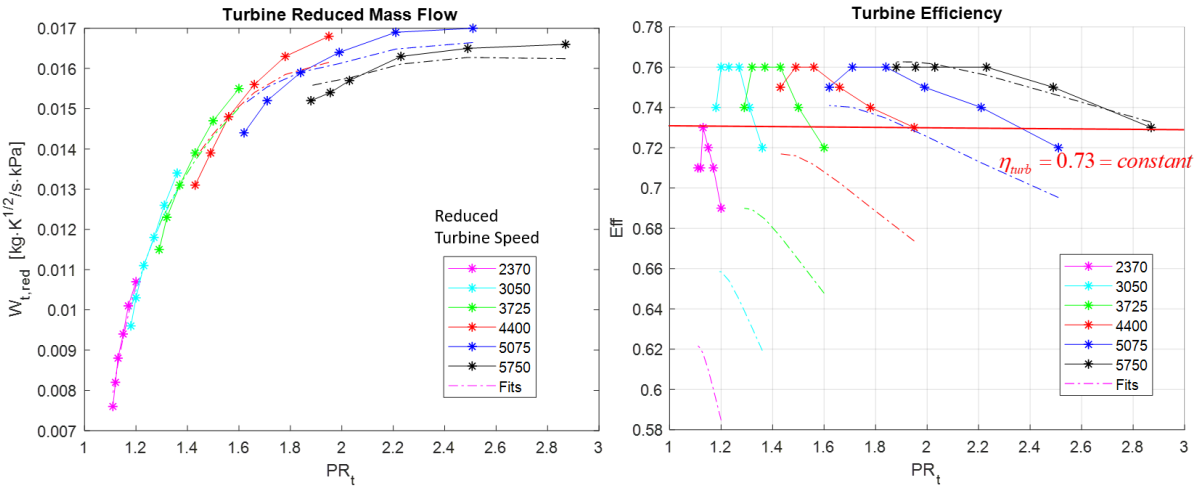

Figure 2.17. : Turbine map fitting.

2.7 Nonlinear Dynamic Model

The nonlinear dynamic model for the direct injection SI engine includes 13 states x, 11 inputs u and 1 disturbance input u_d as shown in Table 2.4, 2.5 and 2.6. It can be written as:

$$\dot{x} = f(x, u, u_d) \tag{2.53}$$

The model is expressed as:

$$\begin{aligned}
\dot{x_1} &= \dot{P}_{bm} = \frac{\gamma_{bm} R_{bm}}{V_{bm}} [W_{comp} T_{cac} - W_{thr} T_{bm} - W_{byp} T_{bm}] \\
\dot{x_2} &= \dot{P}_{\mathrm{im}} = \frac{\gamma_{\mathrm{im}} R_{\mathrm{im}}}{V_{\mathrm{im}}} [W_{thr} T_{bm} + W_{egrh} T_{egrh} - W_{cyl} T_{\mathrm{im}}] \\
\dot{x_3} &= \dot{P}_{em} = \frac{\gamma_{em} R_{em}}{V_{em}} [W_{cylout} T_{cylout} - W_{turb} T_{em} - W_{wg} T_{em} - W_{egrh} T_{em}] \\
\dot{x_4} &= \dot{T}_{bm} = \frac{R_{bm} T_{bm}}{P_{bm} V_{bm}} [W_{comp} (\gamma_{cac} T_{cac} - T_{bm}) - (W_{thr} + W_{byp})(\gamma_{bm} T_{bm} - T_{bm})] \\
\dot{x_5} &= \dot{T}_{\mathrm{im}} = \frac{R_{\mathrm{im}} T_{\mathrm{im}}}{P_{\mathrm{im}} V_{\mathrm{im}}} [W_{thr} (\gamma_{bm} T_{bm} - T_{\mathrm{im}}) + W_{egrh} (\gamma_{egrh} T_{egrh} - T_{\mathrm{im}}) - W_{cyl} (\gamma_{\mathrm{im}} T_{\mathrm{im}} - T_{\mathrm{im}})] \\
\dot{x_6} &= \dot{T}_{\mathrm{em}} = \frac{R_{\mathrm{em}} T_{\mathrm{em}}}{P_{\mathrm{em}} V_{\mathrm{em}}} [W_{cylout} (\gamma_{cylout} T_{cylout} - T_{\mathrm{em}}) - (W_{turb} + W_{wg} + W_{egrh})(\gamma_{\mathrm{em}} T_{\mathrm{em}} - T_{\mathrm{em}})] \\
\dot{x_7} &= \dot{\omega}_{tc} = \frac{Z_{turb} - Z_{comp}}{I_{tc} \omega_{tc}} \\
\dot{x_8} &= \dot{F}_{ub,bm} = \frac{R_{bm} T_{bm}}{P_{bm} V_{bm}} [W_{\mathrm{inlet}} (1 - F_{ub,bm}) + W_{egrl} (F_{ub,\mathrm{em}} - F_{ub,bm})] \\
\dot{x_9} &= \dot{F}_{b,bm} = \frac{R_{bm} T_{bm}}{P_{bm} V_{bm}} [W_{\mathrm{inlet}} (0 - F_{b,bm}) + W_{egrl} (F_{b,\mathrm{em}} - F_{b,bm})] \\
\dot{x_{10}} &= \dot{F}_{ub,\mathrm{im}} = \frac{R_{\mathrm{im}} T_{\mathrm{im}}}{P_{\mathrm{im}} V_{\mathrm{im}}} [W_{thr} (F_{ub,bm} - F_{ub,\mathrm{im}}) + W_{egrh} (F_{ub,\mathrm{em}} - F_{ub,\mathrm{im}})] \\
\dot{x_{11}} &= \dot{F}_{b,\mathrm{im}} = \frac{R_{\mathrm{im}} T_{\mathrm{im}}}{P_{\mathrm{im}} V_{\mathrm{im}}} [W_{thr} (F_{b,bm} - F_{b,\mathrm{im}}) + W_{egrh} (F_{b,\mathrm{em}} - F_{b,\mathrm{im}})] \\
\dot{x_{12}} &= \dot{F}_{ub,\mathrm{em}} = \frac{R_{\mathrm{em}} T_{\mathrm{em}}}{P_{\mathrm{em}} V_{\mathrm{em}}} [W_{cylout} (F_{ub,cylout} - F_{ub,\mathrm{em}})] \\
\dot{x_{13}} &= \dot{F}_{b,\mathrm{em}} = \frac{R_{\mathrm{em}} T_{\mathrm{em}}}{P_{\mathrm{em}} V_{\mathrm{em}}} [W_{cylout} (F_{b,cylout} - F_{b,\mathrm{em}})]
\end{aligned} \tag{2.54}$$

Table 2.4. : State variables for the engine model

State	Variable	Description	Units
x_1	P_{bm}	Boost Manifold Pressure	Pa
x_2	P_{im}	Intake Manifold Pressure	Pa
x_3	P_{em}	Exh. Manifold Pressure	Pa
x_4	T_{bm}	Boost Manifold Temperature	K
x_5	T_{im}	Intake Manifold Temperature	K
x_6	T_{em}	Exh. Manifold Temperature	K
x_7	ω_{tc}	Turbocharger Speed	rpm
x_8	$F_{ub,bm}$	Boost Manifold Unburnt Gas Fraction	/
x_9	$F_{b,bm}$	Boost Manifold Burnt Gas Fraction	/
x_{10}	$F_{ub,\text{im}}$	Intake Manifold Unburnt Gas Fraction	/
x_{11}	$F_{b,im}$	Intake Manifold Burnt Gas Fraction	/
x_{12}	$F_{ub,em}$	Exh. Manifold Unburnt Gas Fraction	/
x_{13}	$F_{b,em}$	Exh. Manifold Burnt Gas Fraction	/

All the flow rates used in the nonlinear model (2.4) can be expressed as nonlinear functions of the defined states, inputs and disturbance input:

$$y = g(x, u, u_d) \tag{2.55}$$

2.8 Model Linearization and Validation

The nonlinear dynamic model is linearized via the first-order approximation at the equilibrium points $(x_\text{e}, u_\text{e}, u_{de}, y_\text{e})$ to get the linear state space model which can be used for control analysis.

2.8.1 Pre-linearization Analysis

Before linearizing the nonlinear model, several questions need to be answered:

1. Which flow function should be used for linearization in orifice function (3.18) for each valve flow? Similarly, how to select the conditions for the in-cylinder composition model?

2. How to deal with compressor choke or surge conditions in the compressor efficiency or flow linearization?

Table 2.5. : Input variables for the engine model

Input	Variable	Description	Units
u_1	A_{thr}	Effective Throttle Area	m^2
u_2	A_{byp}	Effective Bypass Valve Area	m^2
u_3	W_{fuel}	Fueling Rate	kg/s
u_4	D_{wg}	Waste-gate Diameter	m
u_5	A_{egrh}	Effective HP EGR Valve Area	m^2
u_6	A_{egrl}	Effective LP EGR Valve Area	m^2
u_7	# firing	Number of Firing Cylinders	/
u_8	IVO	Intake Valve Open	CAD
u_9	IVC	Intake Valve Close	CAD
u_{10}	EVO	Exh.Valve Open	CAD
u_{11}	EVC	Exh.Valve Close	CAD

Table 2.6. : Disturbance input variables for the engine model

Disturbance Input	Variable	Description	Units
u_{d1}	ω	Engine Speed	rpm

3. The Otto cycle model needs T_1, the BDC temperature to start the calculation in equation (2.24). Per equation (2.36), the estimation of T_1 requires a known value of the residual gas temperature T_r from last cycle. Since the model is control-oriented mean-value model and T_r is not saved for cycle-by-cycle calculation, how to deal with the cycle-related term to start the Otto cycle calculation in the linear model?

For question 1, the nonlinear model was first run to compare with the high fidelity GT-Power model for the interested engine operation range ($1600 - 4000$ rpm). Condition terms for the valve choke in equation (3.18) and the combustion situation in equations (2.22) and (2.23) were created and checked. The intake throttle and LP EGR valve were operated in the unchoked condition except during some transient speed changes. Further, the in-cylinder composition model worked in leaner combustion condition for most of the time during the

simulation. Therefore, the unchoked orifice function and leaner combustion case are selected for the linearization.

For question 2, the equations of compressor boundary conditions are removed in the linear model. The resulting modeling errors should be taken into considerations when performing control analysis for the linear model.

For question 3, a constant T_r (= 70K) is used when calculating T_1 in the linear model instead of a recirculated calculation in the nonlinear model:

$$T_1 = T_{em} + 70K \tag{2.56}$$

2.8.2 Linear State-space Model

The linear state space model is expressed as:

$$\begin{aligned} \dot{x} &= A\delta x + B\delta u + B_d\delta u_d \\ \delta y &= C\delta x + D\delta u + D_d\delta u_d \end{aligned} \tag{2.57}$$

and the state matrices A, B, B_d, C, D, D_d are calculated as:

$$\begin{aligned} A^{13\times 13} &= \left[\begin{array}{ccc} \frac{\partial f_1}{\partial x_1} & \cdots & \frac{\partial f_1}{\partial x_n} \\ \vdots & \ddots & \vdots \\ \frac{\partial f_n}{\partial x_1} & \cdots & \frac{\partial f_n}{\partial x_n} \end{array}\right]\Bigg|_{(x,u,u_d)=(x_e,u_e,u_{de})} \\ B^{13\times 11} &= \left[\begin{array}{ccc} \frac{\partial f_1}{\partial u_1} & \cdots & \frac{\partial f_1}{\partial u_n} \\ \vdots & \ddots & \vdots \\ \frac{\partial f_n}{\partial u_1} & \cdots & \frac{\partial f_n}{\partial u_n} \end{array}\right]\Bigg|_{(x,u,u_d)=(x_e,u_e,u_{de})} \\ {B_d}^{13\times 1} &= \left[\begin{array}{ccc} \frac{\partial f_1}{\partial u_{d1}} & \cdots & \frac{\partial f_1}{\partial u_{dn}} \\ \vdots & \ddots & \vdots \\ \frac{\partial f_n}{\partial u_{d1}} & \cdots & \frac{\partial f_n}{\partial u_{dn}} \end{array}\right]\Bigg|_{(x,u,u_d)=(x_e,u_e,u_{de})} \end{aligned} \tag{2.58}$$

The nonlinear model is linearized at the steady-state (x_e, u_e, u_{de}, y_e) of 3200rpm engine speed, 60° throttle angle, 11.6mm waste-gate diameter, 10° LP EGR angle and four firing

cylinders. The equilibrium points of system states x_1 to x_{13} are directly obtained from GT-Power simulation results.

2.8.3 Model Validations

Fixed Valve Angle Testing

For the validation testing, the throttle angle is fixed at 60° and the LP EGR valve is fixed at 10°. The waste-gate and engine speed profiles are listed in Fig. 2.18. This testing is to investigate the model sensitivity to the disturbance input, engine speed.

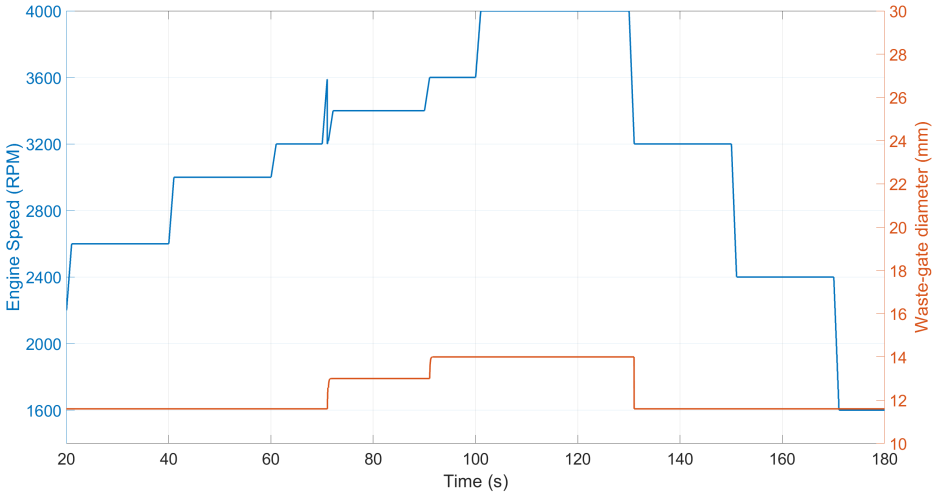

Figure 2.18. : Waste-gate and engine speed profiles for the validation.

The validations of boost, intake and exhaust manifold pressures x_1, x_2, x_3 are shown in Fig. 2.19. For boost and intake manifolds, the nonlinear model has higher estimations than the GT-Power reference but well captures the steady-state pressure changes at every step. The linear model, which is linearized at the GT-Power steady-state values, has better estimation performance than the nonlinear model when the engine speed is close to the linearization point 3200rpm. However, the linear model performs less well during the last step, where the operating point moves further from the linearization point. At 4000rpm, it has poor estimation performance as a result of the compressor limits being removed in the linear model. Both of the linear and nonlinear models predict the exhaust manifold pressure

well during 20 to 160s. However, when the engine speed decreases to 1600 rpm, the linear model has larger errors.

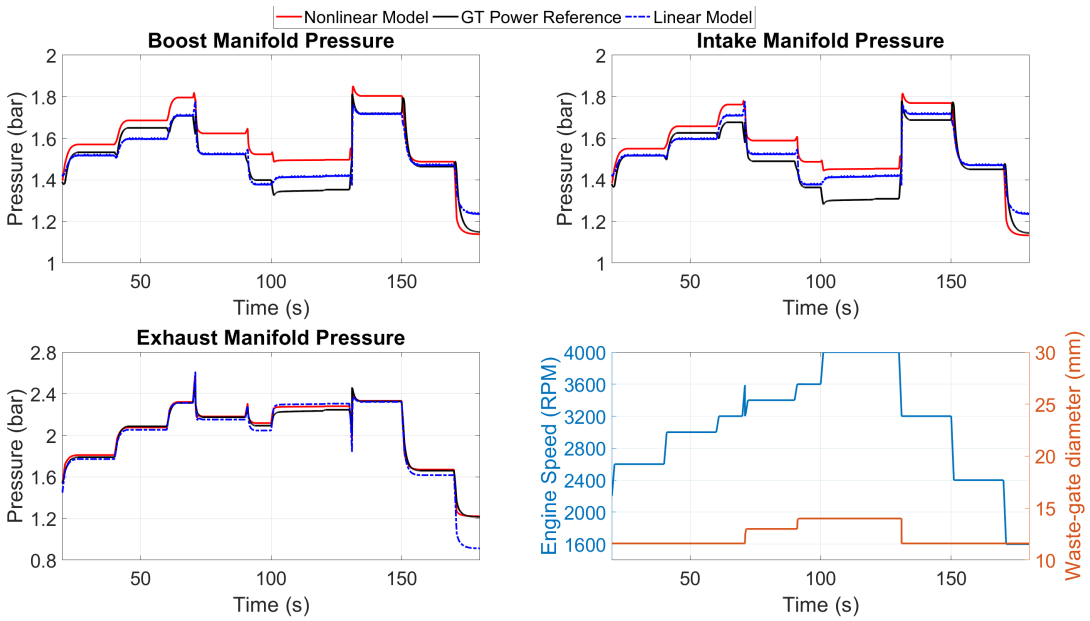

Figure 2.19. : Manifold pressure validation.

Fig. 2.20 shows the validation of boost, intake and exhaust manifolds temperatures x_4, x_5, x_6. For boost and intake manifolds, though the nonlinear model is around 6K higher than the GT-Power reference, it can capture the transient changes of the temperature at every step change. The linear model has undesirable increases from 70 to 130s when the engine speed changes from 3400 to 4000 rpm. For the exhaust manifold, the nonlinear model predicts the temperature within 45K error range for all steps. Though there exists a bias error, the nonlinear model captures the changes of exhaust manifold temperate well while the linear model fails to predict the trends of T_{em} for 3600 to 4000rpm during 90 to 130s.

Fig. 2.21 shows the validation of turbocharger speed x_7. It can be found that both linear and nonlinear model have good estimations from 20 to 170s. During the last step, the nonlinear model can still predict the turbocharger speed while the linear model has around 15K rpm estimation error.

The validations of boost, intake and exhaust manifold burnt mass fractions x_9, x_{11}, x_{13} are shown in Fig. 2.22. For boost and intake manifolds, both of the linear and nonlinear models have good estimation performance except the last step.

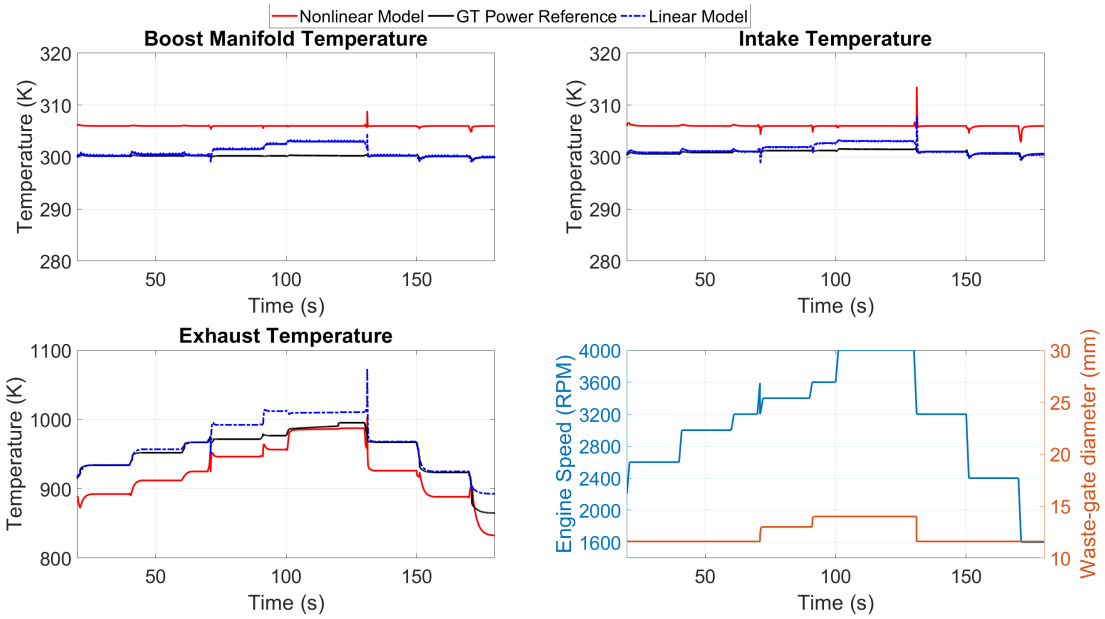

Figure 2.20. : Manifold temperature validation.

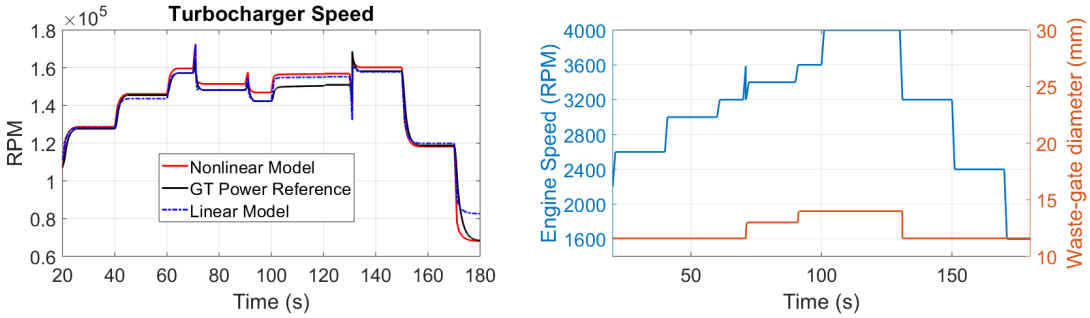

Figure 2.21. : Turbocharger speed validation.

Fig. 2.23 shows the validation results of different flow rates. There is a bias error between the nonlinear model estimation and the reference model. When the model is linearized at the steady-state of the reference model, the bias error is eliminated.

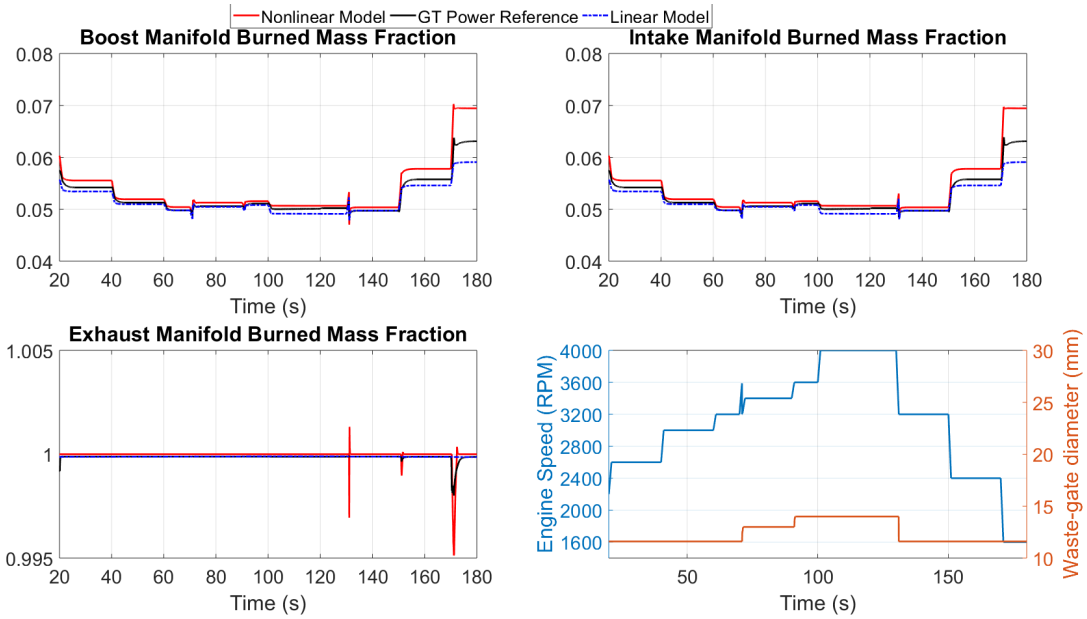

Figure 2.22. : Manifold burnt mass fraction validation.

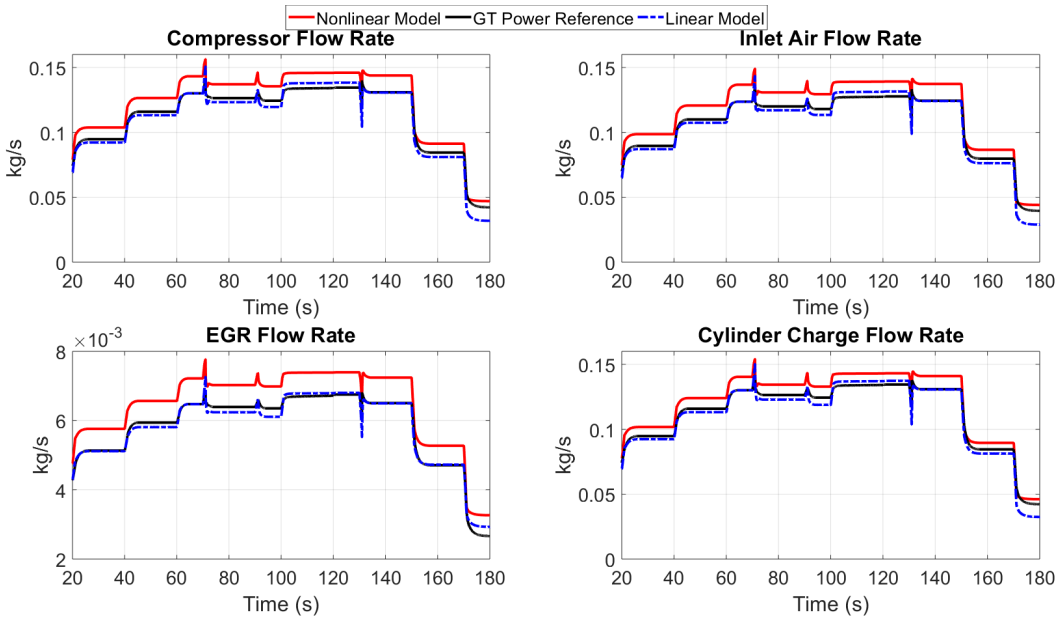

Figure 2.23. : Flow rate validation.

Aggressive Testing

A more aggressive testing is performed for both of the linear and nonlinear models.

The actuator profiles are shown in Fig. 2.24. The engine speed varies from 2400 to 4000rpm, every 100rpm. For each engine speed, the LP EGR valve is operated at 0°, 5°, 10°, 15° and 20°. For each EGR valve angle, the throttle valve is operated at 40°, 60°, 75° and 90°.

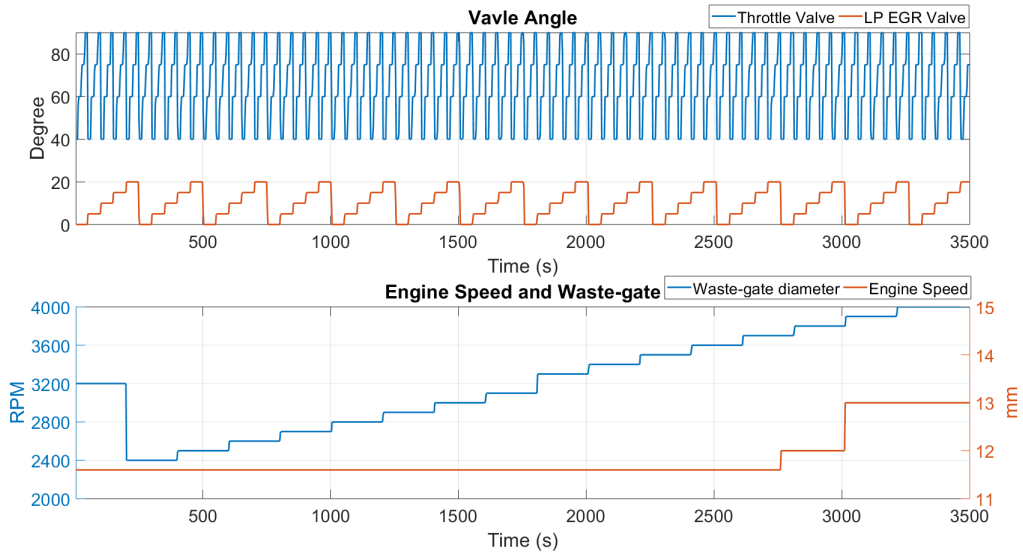

Figure 2.24. : Waste-gate and engine speed profiles for aggressive validation.

Fig. 2.25 to Fig. 2.31 show the model validation results of state variables and flow rates. Per Fig. 2.25, larger estimation errors for boost and intake manifold pressures are observed after 2000s, when the engine speed is higher than 3400rpm. Both linear and nonlinear models have very good tracking performance of the exhaust manifold pressure. A detailed comparison of the pressures during 1000 to 1500s is shown in Fig. 2.26. The nonlinear model can estimate the boost and intake manifold pressures within 0.06bar error. It can also track the pressure change when the throttle and LP EGR valves change. Compared with the nonlinear model, the linear model has larger errors when the EGR valve opens more.

Per Fig. 2.27, larger estimation errors are observed in the nonlinear model at lower engine speeds. The maximum estimation error of the nonlinear model is lower than 50K. Though

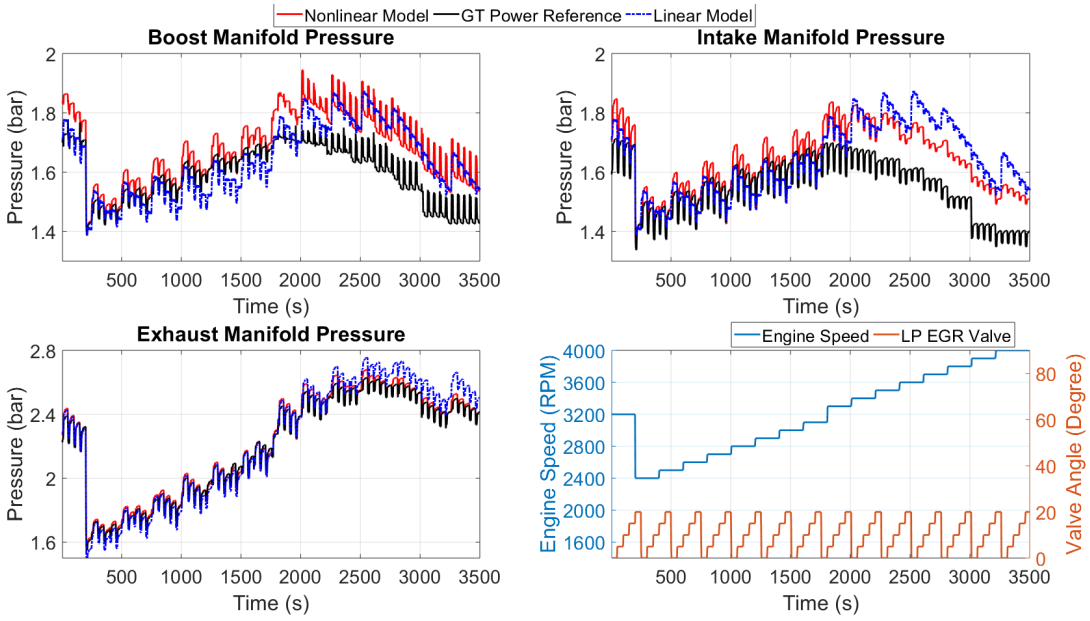

Figure 2.25. : Manifold pressure validation.

there are bias errors, the nonlinear model can well track the step changes of the exhaust temperature (per Fig. 2.28).

Per Fig. 2.29, both linear and nonlinear models can well estimate the turbocharger speed.

Per Fig. 2.30, both nonlinear and linear models have larger errors at lower engine speeds for the boost and intake manifold burnt gas estimation. The nonlinear model has worse estimation performance at high burnt gas levels while the linear model has larger errors at low burnt gas levels.

Fig. 2.31 shows the flow validation results. Larger estimation errors occur after 2000s in both models. Unexpected negative LP EGR flow is observed in the linear model, which is caused by the linearization. Per Fig. 2.32, though there are bias errors, the nonlinear model can well track the flow changes.

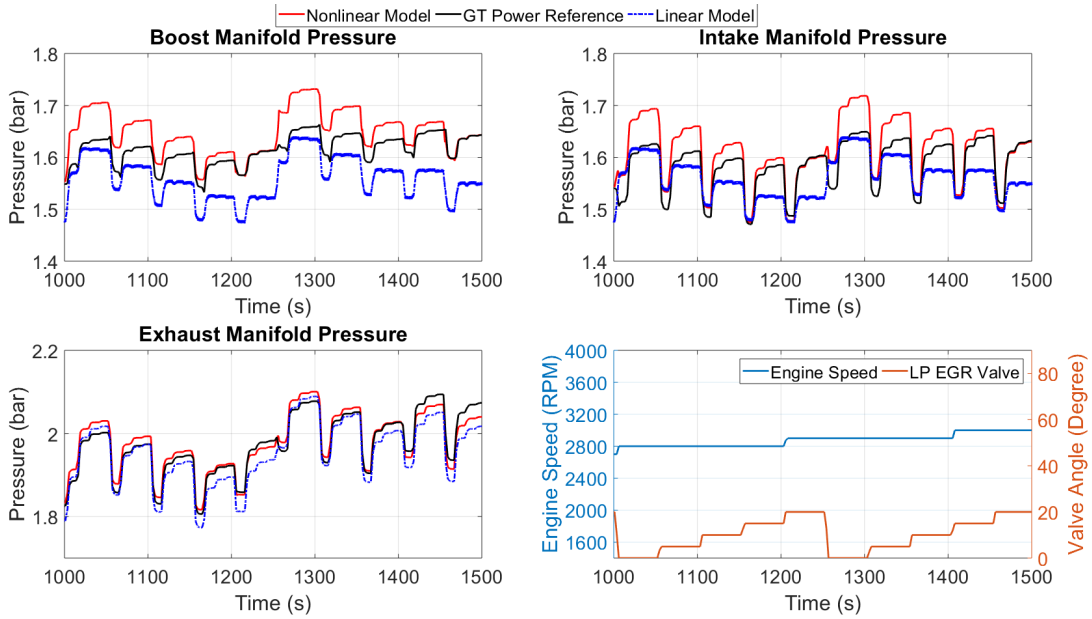

Figure 2.26. : Manifold pressure validation (1000-1500s).

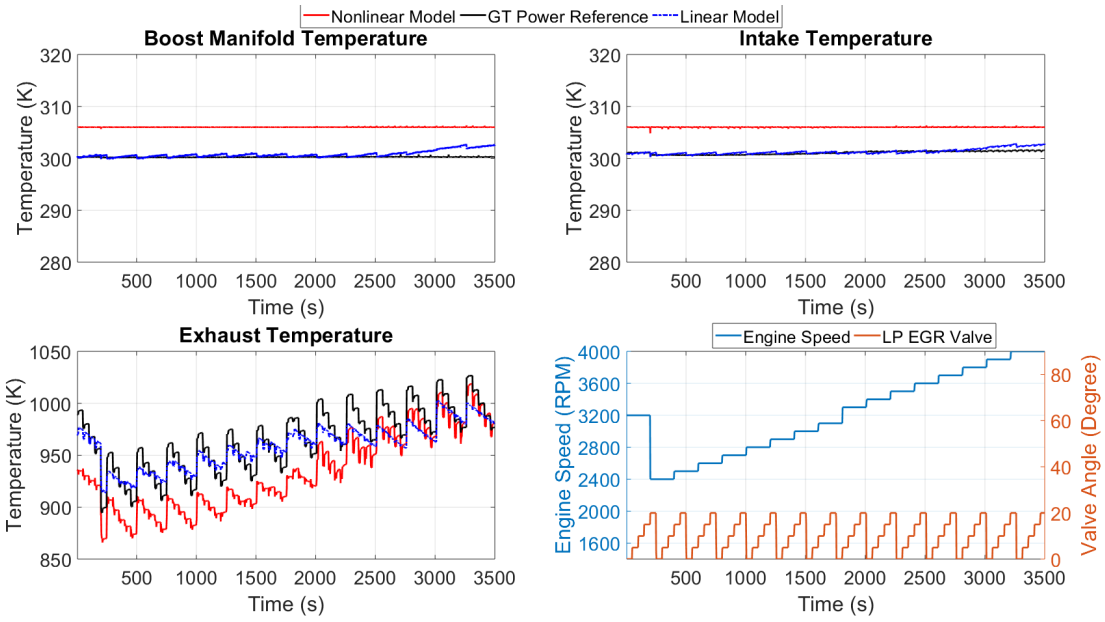

Figure 2.27. : Manifold temperature validation.

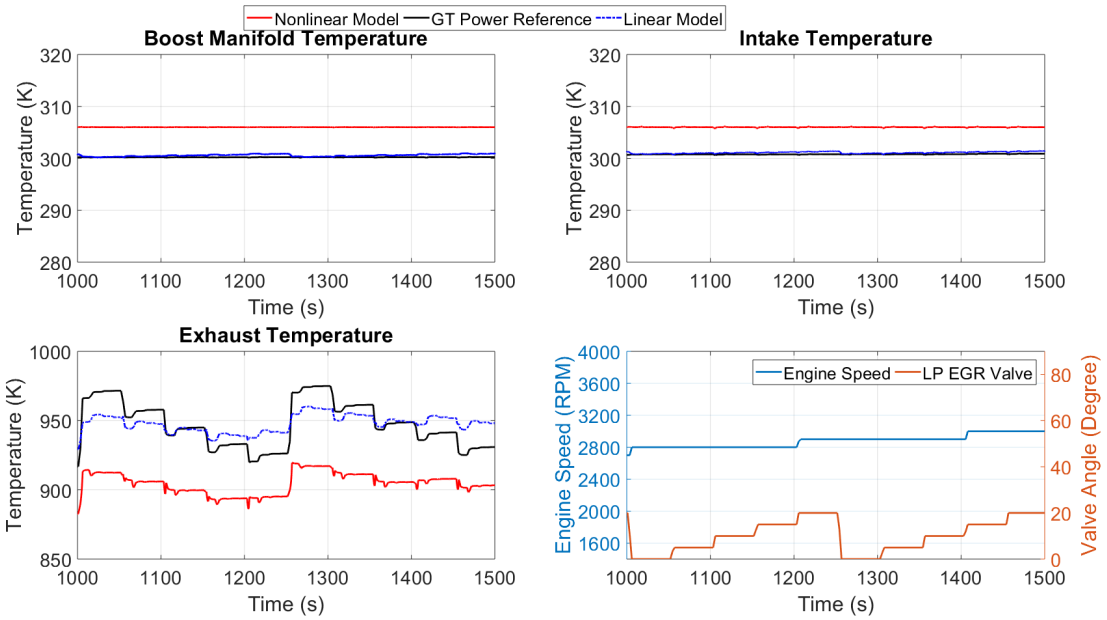

Figure 2.28. : Manifold temperature validation (1000-1500s).

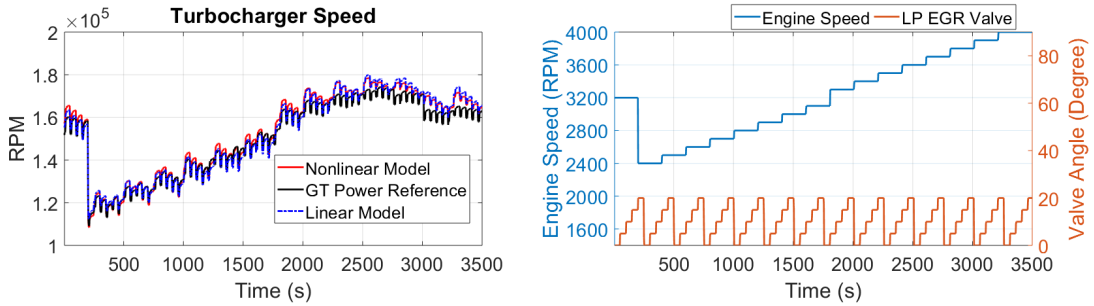

Figure 2.29. : Turbocharger speed validation.

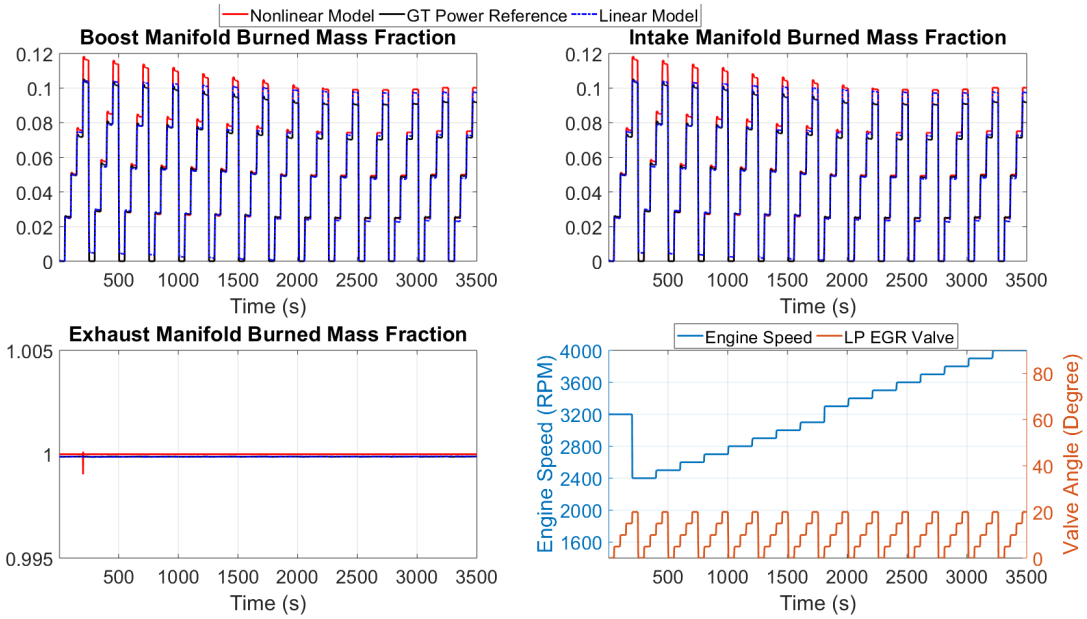

Figure 2.30. : Manifold burnt mass fraction validation.

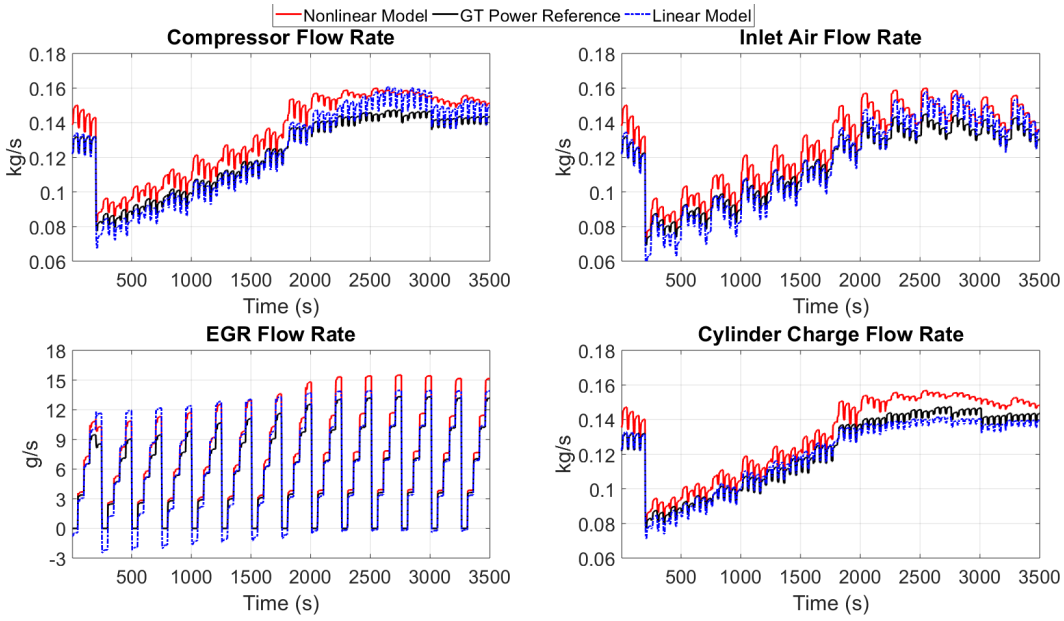

Figure 2.31. : Flow rate validation.

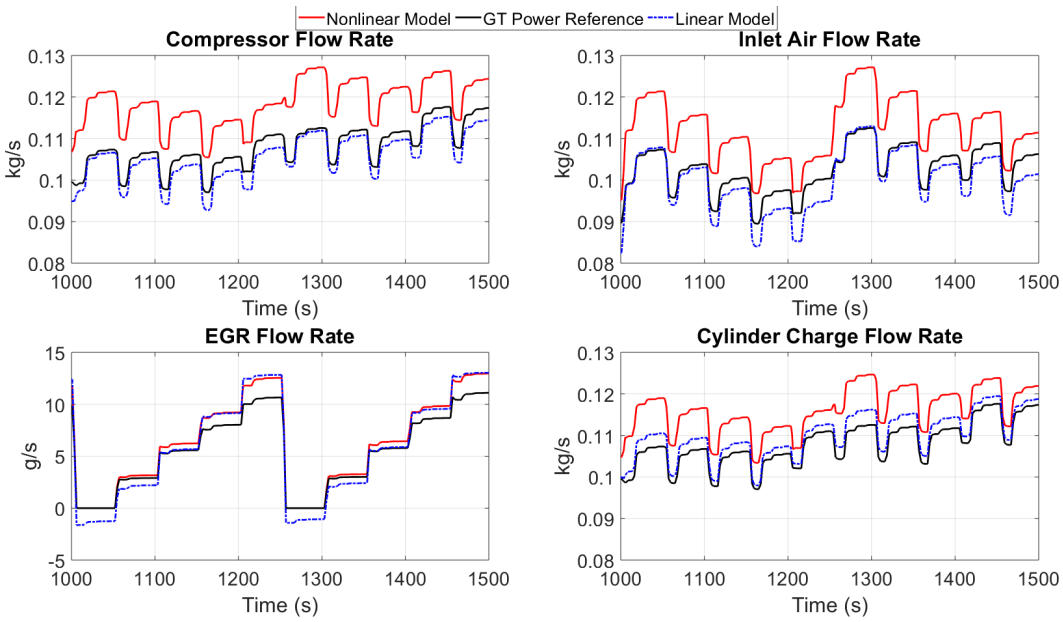

Figure 2.32. : Flow rate validation (1000-1500s).

2.9 Summary

In this chapter, a physically-based, control-oriented model was derived for turbo-charged SI engines utilizing cooled EGR and flexible VVA systems. The model includes the impacts of modulation to any combination of 11 actuators, including the throttle valve, bypass valve, fuel injection rate, waste gate, high-pressure (HP) EGR, LP EGR, number of firing cylinders, intake and exhaust valve opening and closing timings. An investigation based on comparison results was also done to evaluate the effects of residual gas mass on the model accuracy. This investigation work illustrated the necessity of modeling the residual gas mass and the insights discovered in this work contributed to the improvement of model accuracy. The control-oriented model incorporates two new sub-models to capture the dynamics of pressure, temperature and gas compositions in manifolds and the cylinder as well as different flow rates. The first sub-model is to estimate cylinder-out gas compositions based on the inputs' information of cylinder charge flow, injected fuel amount, residual gas mass and intake gas compositions. The second sub-model is to estimate the turbine-out pressure, which is a key input for LP EGR and turbine mass flow estimations. The control-oriented model was validated with a high fidelity SI engine GT-Power model for different operating conditions. The developed linear and nonlinear models achieved good steady-state and transient estimation performance. The control-oriented model is developed for control analysis and sensor framework applications.

3. H_2 OPTIMIZATION BASED SENSOR SYSTEM AND OBSERVER CO-DESIGN ALGORITHM

3.1 Motivation

Advanced SI engine architectures incorporate turbocharger, EGR and VVT to enable the improvements of fuel economy as well as engine performance. The increasing complexity of engine systems brings in more challenges for the design and control of the air handing systems. To enable stoichiometric air-to-fuel ratio control, the compositions of the gas in the intake manifold must be accurately and robustly measured or estimated. Unfortunately, there is currently no cost effective, production viable intake oxygen sensor for this purpose. Current approaches for the intake gas composition estimation are usually designing estimators based on already-selected sensors. However, considering the increasing complexity of today's engine systems and sensor characteristics, the choice of optimal air handling sensor set is not obvious. Traditional brute-force experimentation for sensor selection and estimator tuning can be expensive and time-consuming. Experiments may need to be redone even when there are minor changes to the engine system or sensor characteristics. To effectively solve the problem, an H_2 based, sensor system and observer co-design algorithm is proposed in this chapter. The goal of this algorithm is to definitively, and accurately, determine the tradeoff between the necessary sensor number and the estimation error. The sensor delay, measurement and process noise can be parametrically defined in this algorithm, allowing for the application across vehicle configurations, unique to each original equipment manufacturers (OEM). The implemented cost function consists of the H_2 norm of the observer error and the weighted l_1 norm of the observer gain. The problem, once formulated, can be solved efficiently via semi-definite programming (SDP). After selecting the optimal sensor set, the algorithm computes the corresponding Kalman-filter gain based on the selected sensor set. The method to estimate the modeling errors based on the comparison of reference data and modeling data is also developed in this chapter, enabling the application of the sensor selection framework on actual physical systems.

3.2 Sensor Selection Algorithm Based on H_2 Optimization

Considering the following linear continuous state space model:

$$\begin{aligned} \dot{x} &= Ax + Bu + B_d u_d + B_w w \\ y &= Cx + Du + D_d u_d + Hv \end{aligned} \tag{3.1}$$

with the state variables $x \in R^m$, measured outputs $y \in R^n$, control inputs $u \in R^p$, disturbance inputs $u_d \in R^s$, unknown disturbance related to model uncertainty $w \in R^m$, and sensor noise $v \in R^n$. Both w and v are modeled as white noise. $B_w \in R^{m\times m}$ and $H \in R^{n\times n}$ are diagonal magnitude matrices.

A Luenberger observer then takes the form:

$$\begin{aligned} \hat{\dot{x}} &= A\hat{x} + Bu + B_d u_d + L(y - \hat{y}) \\ \hat{y} &= C\hat{x} + Du + D_d u_d \\ z &= W\mathrm{e} = W(x - \hat{x}) \end{aligned} \tag{3.2}$$

where $L \in R^{m\times n}$ is the observer gain, $z \in R^q$ is the weighted error and $W \in R^{q\times m}$ is the weighting matrix to address some errors from all state errors.

By introducing the following two matrices:

$$\begin{aligned} \tilde{B}_w^{m\times(m+n)} &= \begin{bmatrix} {B_w}^{m\times m} & 0^{m\times n} \end{bmatrix} \\ \tilde{H}^{n\times(m+n)} &= \begin{bmatrix} 0^{n\times m} & H^{n\times n} \end{bmatrix} \end{aligned} \tag{3.3}$$

the weighted error z can be formulated as:

$$z = W(sI - A + LC)^{-1}(\tilde{B}_w - L\tilde{H}) \begin{bmatrix} w \\ v \end{bmatrix} = G \begin{bmatrix} w \\ v \end{bmatrix} \tag{3.4}$$

where the error system G is the transfer function matrix between $\begin{bmatrix} w \\ v \end{bmatrix}$ and z.

3.2.1 Cost Function

For multiple-input multiple-output (MIMO) systems, the H_2 norm is the impulse-to-energy gain or steady-state variance of outputs in response to white noise [51]. Therefore, by minimizing the H_2 norm of the error system (3.4), the expected root-mean-square error (RMSE) of the observer in response to white noise input excitation is minimized. The H_2 norm of the error system G in equation (3.4) is expressed as:

$$||G||_2 = \sqrt{\mathbb{E}\{\lim_{t\to\infty} \frac{1}{t}\int_0^t z^T(t)\, z(t)\, dt\}} \tag{3.5}$$

where $\mathbb{E}$ is the expectation operator.

Considering the observer gain matrix L, the corresponding j-th sensor measurement does not contribute to the state estimation results if every element in the j-th column of L is zero. In this case, the absolute sum of the elements in j-th column of L is also zero. The number of sensors can be reduced by minimizing the non-zero columns in L, which is the l_0 norm of the row vector $p \in R^{1\times n}$ of absolute column sum of L, i.e., $\|p\|_0 = \sum_{\mathrm{j}=1}^{n} \|\sum_{\mathrm{i}=1}^{m} |L_{\mathrm{ij}}|\|_0$.

In order to optimize the tradeoff between the observer estimation error and the number of required sensors, a cost function is defined as following:

$$J = (1-\alpha)||G||_2^2 + \alpha \sum_{\mathrm{j}=1}^{n} \left\| \sum_{\mathrm{i}=1}^{m} |L_{\mathrm{ij}}| \right\|_0 \tag{3.6}$$

where $\|G\|_2$ denotes the H_2 norm of the error system or the expected root-mean square weighted error, and α is the weighting factor between 0 and 1, balancing the effect of observer error and sensor number.

3.2.2 H_2 Norm of the Observer Error

From [52], for a linear time-invariant (LTI) system with a transfer function $G(s) = C(sI - A)^{-1}B$, the following statements are equivalent:

(1) A is Hurwitz and $||G||_2^2$ (the power of H_2 norm of the impulse response) $< \gamma^2$.

(2) There exists a positive definite matrix P (i.e., $P = P^T \succ 0$) such that

$$\begin{aligned} &A^T P + PA + C^T C \prec 0 \\ &trace(B^T PB) < \gamma^2 \end{aligned} \tag{3.7}$$

where the symbol $\prec$ in the first inequality of equation (3.7) denotes the negative definiteness of a matrix.

By applying equation (3.7) to system (3.4), the optimization problem for the first target $||G||_2^2$ in equation (3.6) can be formulated as following:

$$\begin{aligned} \min_{L,P} \quad & trace((\tilde{B}_w - L\tilde{H})^T P(\tilde{B}_w - L\tilde{H})) \\ \text{s.t.} \quad & (A - LC)^T P + P(A - LC) + W^T W \prec 0 \\ & P = P^T \succ 0 \end{aligned} \tag{3.8}$$

The optimization target and the first constraint in (3.8) are bilinear matrix inequalities (BMI) and thus this is not a convex optimization problem. Therefore, they need to be converted to linear matrix inequalities (LMI). A matrix $S = PL$ (thus $L = P^{-1}S$) is defined and the first constraint in equation (3.8) can be written as the following LMI:

$$A^T P + PA - C^T S^T - SC + W^T W \prec 0 \tag{3.9}$$

Via the Schur complement condition for positive semi-definiteness [53], the following two statements are equivalent:

(1) Symmetric matrix $\begin{bmatrix} \Delta_1 & \Delta_2 \\ \Delta_2^T & \Delta_3 \end{bmatrix} \succeq 0$

(2) $\Delta_3 = \Delta_3^T \succ 0$ and $\Delta_1 - \Delta_2 \Delta_3^{-1} \Delta_2^T \succeq 0$

To apply the Schur complement condition to the optimization target equation (3.8), we introduce a positive semi-definite matrix T, i.e., $T = T^T \succeq 0$. By substituting $\Delta_1 = T$, $\Delta_2 = (P\tilde{B}_w - S\tilde{H})^T$ and $\Delta_3 = P$, the following statement holds:

$$\begin{bmatrix} T & (P\tilde{B}_w - S\tilde{H})^T \\ P\tilde{B}_w - S\tilde{H} & P \end{bmatrix} \succeq 0, \quad P = P^T \succ 0 \tag{3.10}$$

iff

$$T - (P\tilde{B}_w - S\tilde{H})^T P^{-1}(P\tilde{B}_w - S\tilde{H}) \succeq 0, \quad P = P^T \succ 0 \tag{3.11}$$

The inequality in equation (3.11) can be rewritten as:

$$\begin{aligned} & T - (P\tilde{B}_w - S\tilde{H})^T P^{-1}(P\tilde{B}_w - S\tilde{H}) \\ =& T - (P\tilde{B}_w - S\tilde{H})^T P^{-1} P P^{-1}(P\tilde{B}_w - S\tilde{H}) \\ =& T - (P^{-1}P\tilde{B}_w - P^{-1}S\tilde{H})^T P(P^{-1}P\tilde{B}_w - P^{-1}S\tilde{H}) \\ =& T - (\tilde{B}_w - L\tilde{H})^T P(\tilde{B}_w - L\tilde{H}) \end{aligned} \tag{3.12}$$

Therefore, the following statement holds if condition (3.10) meets:

$$trace(T) \geq trace((\tilde{B}_w - L\tilde{H})^T P(\tilde{B}_w - L\tilde{H})) \tag{3.13}$$

Therefore, the optimization problem in (3.8) can be rewritten as:

$$\begin{aligned} \min_{L,P,T} \quad & trace(T) \\ \text{s.t.} \quad & A^T P + PA - C^T S^T - SC + W^T W \prec 0 \\ & \begin{bmatrix} T & (P\tilde{B}_w - S\tilde{H})^T \\ P\tilde{B}_w - S\tilde{H} & P \end{bmatrix} \succeq 0 \\ & P = P^T \succ 0 \\ & T = T^T \succeq 0 \end{aligned} \tag{3.14}$$

where the root of $trace(T)$ is the upper bound of the expected weighted root-mean-square error z. In equation (3.8), the optimization target is the H_2 norm of the error system. In equation (3.14), the optimization target is relaxed to the upper bound of the H_2 norm. Here the direct optimization target is $trace(T)$.

3.2.3 Weighted l_1 Norm of the Observer Gain Matrix

The second optimization target $\sum_{j=1}^{n} \|\sum_{i=1}^{m} |L_{ij}|\|_0$ in equation (3.6) is non-convex due to the existance of l_0 norm. For such l_0 norm optimization problem, it is generally impossible to solve as the solution usually requires an intractable combinatorial search [54]. As proposed in [54], the l_0 norm term $\|\sum_{i=1}^{m} |L_{ij}|\|_0$ can be relaxed to a convex target by using the weighted l_1 norm, $\mu_j^{(k)} \sum_{i=1}^{m} |L_{ij}|$, where $\mu_j^{(k)}$ is the weight of column j at iteration count k.

3.2.4 Optimization Problem

Using the lemma which is used and proved in [55]: given a matrix $L \in R^{m \times n}$, the following statements are equivalent:

(1) The j-th column of L is zero.

(2) The j-th column of $S = PL$ is zero for any $P \succ 0$.

Combining the above lemma with (3.14) and weighted l_1 norm, the optimization problem is formulated as following:

$$
\begin{aligned}
\min_{S,P,T} \quad & J = (1-\alpha) trace(T) + \alpha \sum_{j=1}^{n} \mu_j^{(k)} \sum_{i=1}^{m} |S_{ij}| \\
\text{s.t.} \quad & A^T P + PA - C^T S^T - SC + W^T W \prec 0 \\
& \begin{bmatrix} T & (P\tilde{B}_w - S\tilde{H})^T \\ P\tilde{B}_w - S\tilde{H} & P \end{bmatrix} \succeq 0 \\
& P = P^T \succ 0 \\
& T = T^T \succeq 0
\end{aligned}
\tag{3.15}
$$

The optimization problem (3.15) can be solved by the CVX toolbox [56] iteratively. At each iteration, the algorithm updates the weight factor $\mu_{\mathrm{j}}^{(k)} = \frac{1}{\epsilon+\sum_{\mathrm{i}=1}^{m}|S_{\mathrm{ij}}|}$. When $\mu_{\mathrm{j}}^{(k)}$ converges for all sensor j, i.e., $|\mu_{\mathrm{j}}^{(k+1)} - \mu_{\mathrm{j}}^{(k)}| < \epsilon$ where ϵ is a sufficiently small positive number, the iteration can be stopped.

Ideally, the j-th sensor signal is not utilized for the state estimation and should be removed if the j-th column of the observer gain matrix L is zero[16]. Similarly, for a properly scaled system, the signal from sensor(s) j with small $\sum_{\mathrm{i}=1}^{m}|L_{\mathrm{ij}}|$ will have very little impact on the estimation results and thus can be removed. However, it is hard to quantify the threshold of 'small' observer gain and decide the number of sensors that need to be removed. Instead of directly comparing the observer gain of the sensors, the value of $\sum_{\mathrm{j}=1}^{n}\mu_{\mathrm{j}}^{(k)}\sum_{\mathrm{i}=1}^{m}|S_{\mathrm{ij}}|$, representing the relaxed non-zero column number in the observer, is checked for every optimization result and used to decide the number of necessary sensors. $\sum_{\mathrm{j}=1}^{n}\mu_{\mathrm{j}}^{(k)}\sum_{\mathrm{i}=1}^{m}|S_{\mathrm{ij}}|$ is rounded to its nearest integer q, which is used as the number of selected sensors. For instance, if q is 3 for an optimization result, then the sensor(s) with the first three largest $\sum_{\mathrm{i}=1}^{m}|L_{\mathrm{ij}}|$ are the selected optimal sensors.

After computing the optimal sensor set, set α to 0 and remove the rows in C corresponding to unneeded sensors. Substitute $\alpha = 0$ and the modified C into the optimization algorithm (3.15) again to calculate the observer gain matrix $L = P^{-1}S$ based only on the selected optimal sensor combination.

3.3 Algorithm Application on a Turbo-charged SI Engine Model for Air Handling System Sensor Designs

In this section, the proposed sensor selection algorithm is applied to a turbo-charged SI engine utilizing EGR. The goal of the sensor design is to choose the optimal sensor combination for accurately estimating the intake manifold gas composition. More specifically, the desired outcome is to quickly be able to determine the tradeoff between estimated intake manifold gas composition estimation error and the number of sensors.

The engine architecture is shown in Fig. 3.1. For illustrative purposes, four available sensors are considered as candidates as shown in Table 3.1. A mass air flow sensor for inlet air (MAFa) can be placed upstream of the air and low pressure (LP) EGR confluence point,

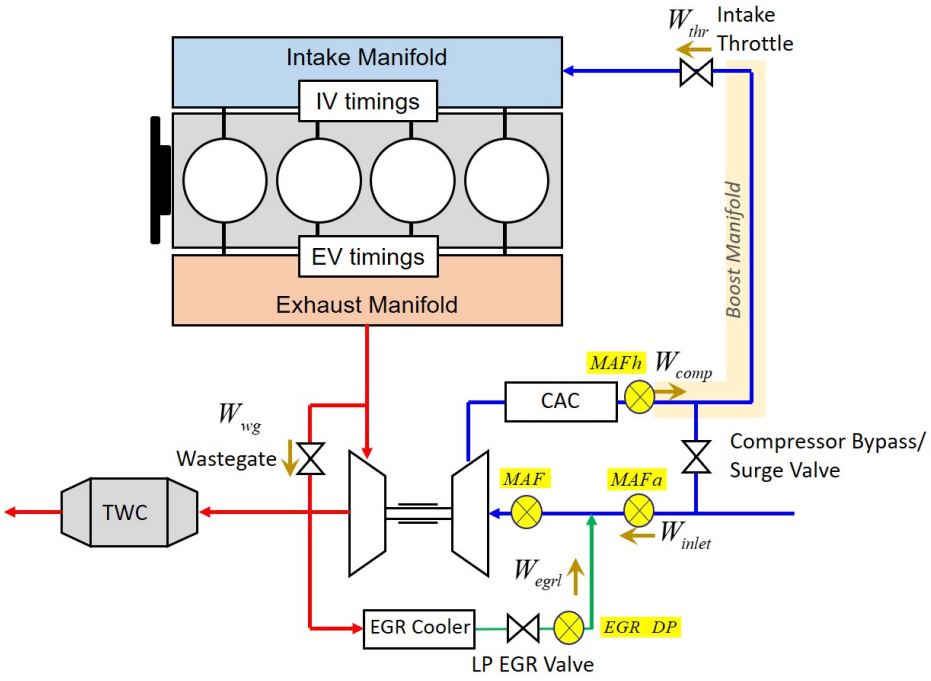

Figure 3.1. : Engine architecture and candidate sensor placements.

Table 3.1. : Available sensors

Sensor	Physical Quantity	Accuracy	Response Time
MAFa	Inlet Air Flow (EGR. Up)	4 %	30 ms
MAFh	Comp. Flow (CAC. Dn)	2 %	50 ms
EGR DP	EGR Flow	7 %	30ms (1000 rpm) 20ms (2000 rpm) 10ms (4000 rpm)
MAF	Comp. Flow (Comp. Up)	4%	30 ms

to measure the inlet air. A mass air flow sensor for high pressure flow (MAFh) can be placed downstream of the charge air cooler (CAC) to measure the cooled compressor mass flow rate. An EGR delta pressure sensor (EGR DP) can be located in the LP EGR valve to measure the LP EGR mass flow rate. Another option is a mass air flow sensor (MAF) put downstream of the air and LP EGR confluence point, but before the compressor, to measure total compressor inlet mass flow rate.

Table 3.2. : State variables for the engine model

State	Variable	Description	Units
x_1	P_{bm}	Boost Manifold Pressure	Pa
x_2	P_{im}	Intake Manifold Pressure	Pa
x_3	P_{em}	Exh. Manifold Pressure	Pa
x_4	T_{bm}	Boost Manifold Temperature	K
x_5	T_{im}	Intake Manifold Temperature	K
x_6	T_{em}	Exh. Manifold Temperature	K
x_7	ω_{tc}	Turbo-charger Speed	rpm
x_8	$F_{ub,bm}$	Boost Manifold Unburnt Gas Fraction	/
x_9	$F_{b,bm}$	Boost Manifold Burnt Gas Fraction	/
x_{10}	$F_{ub,im}$	Intake Manifold Unburnt Gas Fraction	/
x_{11}	$F_{b,im}$	Intake Manifold Burnt Gas Fraction	/
x_{12}	$F_{ub,em}$	Exh. Manifold Unburnt Gas Fraction	/
x_{13}	$F_{b,em}$	Exh. Manifold Burnt Gas Fraction	/
x_{14}	A_{thr}	Effective Throttle Valve Area	m^2
x_{15}	A_{egrl}	Effective LP EGR Valve Area	m^2
x_{16}	D_{wg}	Waste-gate Diameter	m
x_{17}	$\tilde{W}_{inlet}$	Inlet Air Flow Measurement	kg/s
x_{18}	$\tilde{W}_{comp}$	CAC Downstream Flow Measurement	kg/s
x_{19}	$\tilde{W}_{egrl}$	LP EGR Valve Flow Measurement	kg/s
x_{20}	$\tilde{W}_{comp,up}$	Comp. Upstream Flow Measurement	kg/s

3.3.1 Control-Oriented State-Space Engine Model

The model is a mean-value engine model based on [32][44][45] [46].

The model has 8 inputs, 1 disturbance input and 20 states as shown in Table 3.2, 3.3 and 3.4, respectively. The nonlinear dynamic model equations can be written as follows and the detailed governing equations are listed in Appendix A:

$$\dot{x} = f(x, u, u_d) \tag{3.16}$$

Taking the actuator and sensor response time into consideration, states x_{14} to x_{20} are added. First-order actuator responses are considered for the throttle valve, LP EGR valve

Table 3.3. : Input variables for the engine model

Input	Variable	Description	Units
u_1	$A_{cmd,thr}$	Cmd. Effective Throttle Area	m^2
u_2	W_{fuel}	Fueling Rate	kg/s
u_3	$D_{cmd,wg}$	Cmd. Waste-gate Diameter	m
u_4	$A_{cmd,egrl}$	Cmd. Effective LP EGR Valve Area	m^2
u_5	IVO	Intake Valve Open	CAD
u_6	IVC	Intake Valve Close	CAD
u_7	EVO	Exh.Valve Open	CAD
u_8	EVC	Exh.Valve Close	CAD

Table 3.4. : Disturbance input variables for the engine model

Disturbance Input	Variable	Description	Units
u_{d1}	ω	Engine Speed	rpm

and waste-gate. The following first-order approximation is used for the actuator and sensor dynamics:

$$\dot{x} = \frac{x_0 - x}{\tau} \tag{3.17}$$

where x_0 is the command actuator input or physical expressions of sensed variables without delay, and τ is the time constant.

In this engine model, the valve mass flow rate outputs are modeled by the following orifice equation[32]:

$$W = A_{eff} \frac{P_{in}\sqrt{\gamma}}{\sqrt{RT_{in}}} f(\frac{P_{out}}{P_{in}})$$

$$f\left(\frac{P_{out}}{P_{in}}\right) = \begin{cases} \sqrt{\frac{2}{\gamma-1}\left[\left(\frac{P_{out}}{P_{in}}\right)^{\frac{2}{\gamma}} - \left(\frac{P_{out}}{P_{in}}\right)^{\frac{\gamma+1}{\gamma}}\right]} \\ if \quad \left(\frac{P_{out}}{P_{in}}\right) \geq \left(\frac{2}{\gamma+1}\right)^{\frac{\gamma}{\gamma-1}} \\ \sqrt{\left(\frac{2}{\gamma+1}\right)^{\frac{\gamma+1}{\gamma-1}}} \\ if \quad \left(\frac{P_{out}}{P_{in}}\right) \leq \left(\frac{2}{\gamma+1}\right)^{\frac{\gamma}{\gamma-1}} \end{cases} \tag{3.18}$$

where γ is the gas specific heat ratio, A_{eff} is the effective valve area, P_{out} is the downstream pressure, P_{in} and T_{in} are the upstream pressure and temperature. A virtual flow sensor, which is developed based on speed-density equation, can be used for estimating the cylinder charge flow rate. Fig. 3.2 shows the comparison of the linear model estimated charge mass flow rate and the GT-Power reference. The maximum error for the virtual flow sensor is within $\pm 5.1\%$.

The nonlinear model is linearized at the steady-state (x_e, u_e, u_{de}, y_e) of 3200rpm engine speed, 60° throttle valve angle, 11.6mm waste-gate diameter and 10° LP EGR valve angle. All of the valves are butterfly valves. The equilibrium points of system states x_1 to x_{20} are directly obtained from GT-Power simulation results.

The nominal model is linearized into the following format:

$$\begin{aligned} \dot{x} &= A\delta x + B\delta u + F\delta u_d \\ \delta y &= C\delta x + D\delta u + G\delta u_d \end{aligned} \tag{3.19}$$

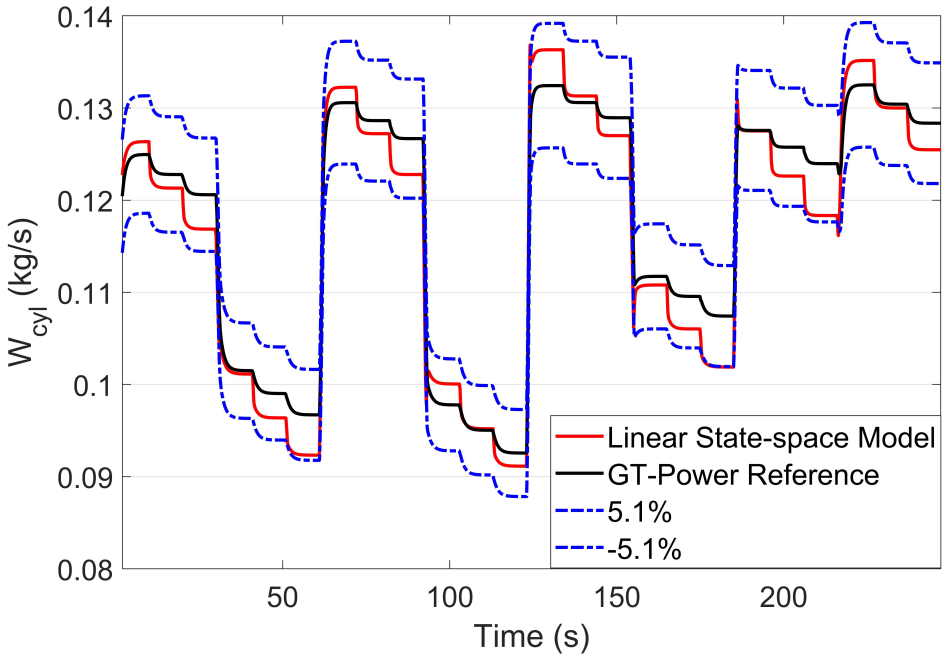

Figure 3.2. : Engine cylinder charge flow rate estimation.

where $\delta x = x - x_{\mathrm{e}}$, $\delta u = u - u_{\mathrm{e}}$, $\delta u_d = u_d - u_{d\mathrm{e}}$, $\delta y = y - y_{\mathrm{e}}$.

An observer is designed from the linear model:

$$\hat{\dot{x}} = A\delta\hat{x} + B\delta u + F\delta u_d + L(\delta y - \delta\hat{y})$$

$$\delta\hat{y} = C\delta\hat{x} + D\delta u + G\delta u_d$$

In simulation results that follow, the commanded engine throttle angle and number of firing cylinders are fixed as their linearization points. As studied in[57], a 11.5% brake-specific fuel consumption (BSFC) reduction and 4.5% absolute indicated efficiency improvement can be achieved by introducing 10% cooled EGR in a 2L, 4-cylinder, turbo-charged, direct injected SI engine at 3000 RPM part load conditions. Considering the fact that EGR tolerance decreases with the increasing engine speed[58], for an engine operation speed range of 2400 to 4000 RPM, the waste-gate and LP EGR valve are operated as shown in Fig. 3.3 and Fig. 3.4, to vary the EGR ratio within 1.5% to 11%.

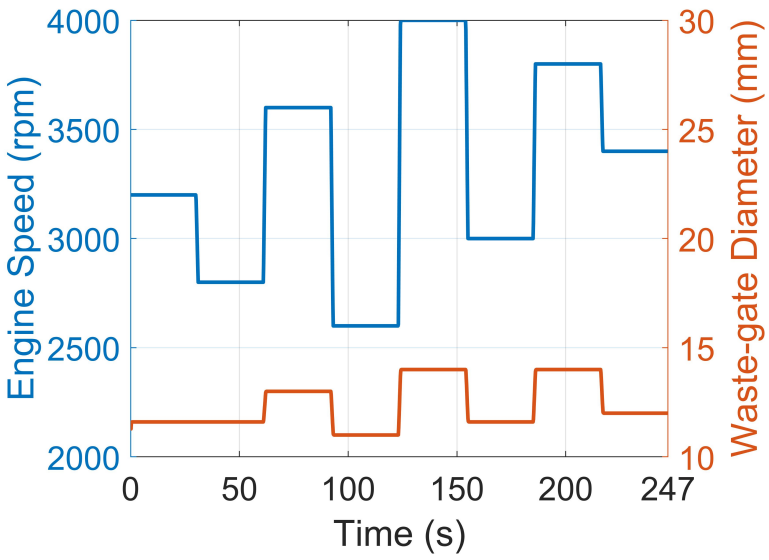

Figure 3.3. : Engine operation conditions: engine speed and waste-gate.

3.3.2 Unknown Disturbance

The process noise $B_w w$ and measurement noise Hv (per equation (3.1)) are two necessary parameters to describe model and sensor errors. Incorrect description of the noise could result in significant worsening of estimation performances[59] and even the failure of the proposed sensor selection framework. Typically, the noise error covariance can be estimated by experimental tuning or computational methods[59][60][61][62]. The purpose of this section is to provide a simple and quick noise estimation method for the engine system based on experimental data to avoid repeated tuning work or complex computations. The sensor selection framework works well for the engine system with the diagonal noise covariance matrix estimated by the proposed method.

To implement the proposed sensor selection algorithm, the actual system is expressed as a linear state-space model with uncertainty represented by additive errors:

$$\dot{x} = \delta\dot{x} = A\delta x + B\delta u + F\delta u_d + B_w w \tag{3.20}$$

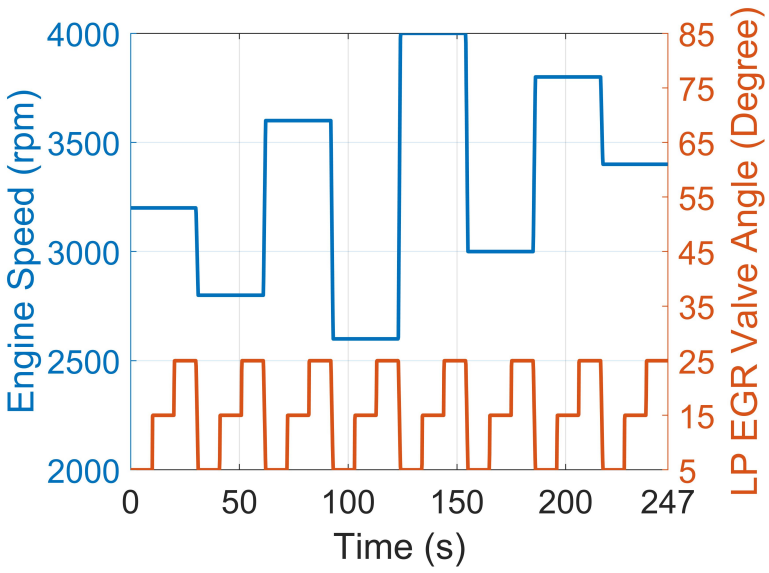

Figure 3.4. : Engine operation conditions: engine speed and LP EGR valve.

where w is zero-mean unitary white noise and ${B_w}^T B_w$ is the process noise covariance matrix. The unknown disturbance $B_w w$ comes from the un-captured dynamics and model linearization errors. In this application, B_w is assumed to be a diagonal matrix.

The modeling error $B_w w$ is estimated by fitting the difference between the actual $\dot{x}$ and the linear model estimated $\dot{x}$ as follows:

$$B_w w = \dot{x}_{GT} - (A\delta x_{GT} + B\delta u_{GT} + F\delta u_{d,GT}) = \Delta\dot{x}_{model} \tag{3.21}$$

where the values of the variables (δx_{GT}, δu_{GT}, $\delta u_{d,GT}$) are from the GT-Power simulation result which is used as the truth-reference, and $\dot{x}_{GT}$ is the derivative of x_{GT}.

Fig. 3.5, 3.6 and 3.7 show the unknown disturbance plots for boost manifold pressure x_1, exhaust manifold pressure x_3 and turbocharger speed x_7, respectively. The errors $\Delta\dot{x}_{model,1}$, $\Delta\dot{x}_{model,3}$, and $\Delta\dot{x}_{model,7}$ are calculated based on equation (3.21) where the data of states x_{GT}, inputs u_{GT} and disturbance inputs $u_{d,GT}$ directly comes from the GT-Power simulation result for the drive cycle in Fig. 3.3 and Fig. 3.4.

An initial estimation of the process noise is the standard deviation of $\Delta\dot{x}_{model}$ in equation (3.21). Considering the fact that non-normal noise (e.g. heavy-tailed or asymmetric)

may not be well-represented by the first two moments (the mean and the standard deviation)[60], the initial estimated process noise is then tuned based on its higher moments, i.e., skewness and kurtosis, to better represent the modeling errors.

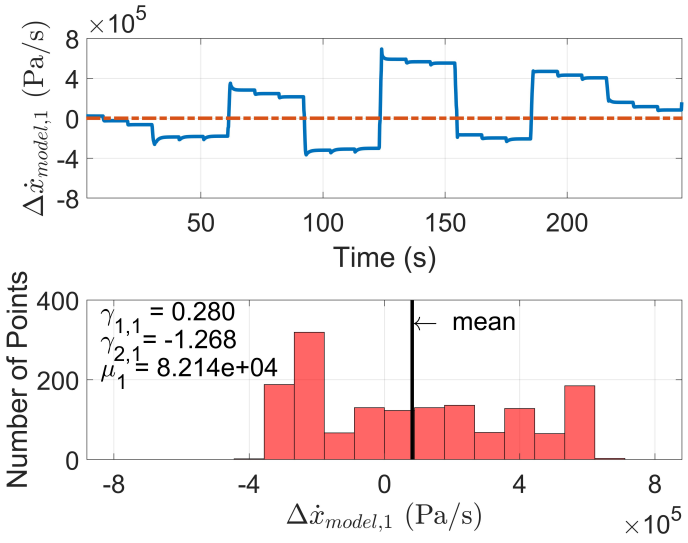

Figure 3.5. : Unknown disturbance estimation for boost manifold pressure: $\Delta\dot{x}_{model,1}$.

Skewness Correction for Unknown Disturbance Estimation

The skewness γ_1 of the error $\Delta\dot{x}_{model}$ is first calculated as follows to evaluate the asymmetry of the distribution and determine which $B_w(\mathrm{i},\mathrm{i})$ estimation equation is used for each state:

$$\gamma_{1,\mathrm{i}} = \frac{\frac{1}{N}\sum_{k=1}^{N}\left(\Delta\dot{x}_{model,\mathrm{i}}(k) - \mu_{\mathrm{i}}\right)}{{\sigma_{\mathrm{i}}}^3} \tag{3.22}$$

where μ_{i} and σ_{i} are the mean value and the standard derivation of $\Delta\dot{x}_{model,\mathrm{i}}$, respectively. μ_{i} and σ_{i} are defined as follows:

$$\begin{aligned}\mu_{\mathrm{i}} &= \frac{1}{N}\sum_{k=1}^{N}\Delta\dot{x}_{model,\mathrm{i}}(k)\\ \sigma_{\mathrm{i}} &= \sqrt{\frac{1}{N}\sum_{k=1}^{N}\left(\Delta\dot{x}_{model,\mathrm{i}}(k) - \mu_{\mathrm{i}}\right)^2}\end{aligned} \tag{3.23}$$

where N is the number of sampled points.

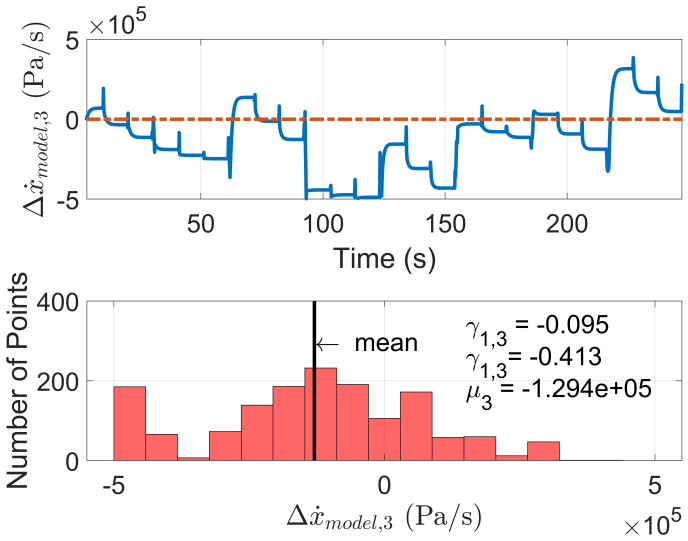

Figure 3.6. : Unknown disturbance estimation for exhaust manifold pressure: $\Delta\dot{x}_{model,3}$.

Positive skewness values mean that the data is skewed to the right (right-tail), and negative values suggest skewing to the left (left-tail)[63]. The larger the absolute skewness value is, the more significant the asymmetry is. For the states where the error $\Delta\dot{x}_{model,7}$ has small skewness (per Fig. 3.6), the asymmetry is neglected and the unknown disturbance term $B_w(\mathrm{i},\mathrm{i})$ is estimated by the following equation:

$$B_w(\mathrm{i},\mathrm{i}) = \sigma(\mathrm{i}) \tag{3.24}$$

For the states where the error $\Delta\dot{x}_{model,\mathrm{i}}$ distributions have large skewness, the asymmetry should not be neglected when estimating the unknown disturbance. If the skewness $\gamma_{1,\mathrm{i}}$ and the mean value μ_{i} have the same sign, the unknown disturbance of the state x_{i} is estimated by the subtraction of the standard deviation σ_{i} and the absolute mean value μ_{i} (per Fig. 3.5), otherwise the unknown disturbance is estimated by the sum (per Fig. 3.7). The condition in equation (3.25) is to account for both of the asymmetry and non-zero mean error distributions. For instance, if the mean is positive and the skewness is negative (per Fig. 3.7), the error has a positive bias and the majority of the errors are even more positive than the bias. In this situation, the standard deviation may under-estimate the error effect

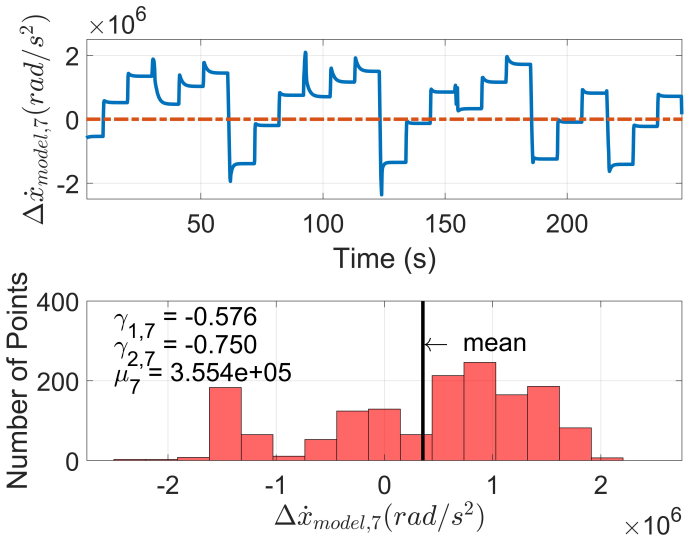

Figure 3.7. : Unknown disturbance estimation for turbocharger speed: $\Delta\dot{x}_{model,7}$.

and thus we re-evaluate by adding the positive bias.

$$B_w(\mathrm{i},\mathrm{i}) = \sigma_\mathrm{i} - |\mu_\mathrm{i}| \quad if \quad \gamma_{1,\mathrm{i}}\mu_\mathrm{i} > 0 \tag{3.25a}$$

$$B_w(\mathrm{i},\mathrm{i}) = \sigma_\mathrm{i} + |\mu_\mathrm{i}| \quad if \quad \gamma_{1,\mathrm{i}}\mu_\mathrm{i} < 0 \tag{3.25b}$$

Kurtosis Correction for Unknown Disturbance Estimation

The excess kurtosis γ_2 of the error $\Delta\dot{x}_{model}$ distribution defined as follows is then calculated to evaluate the outliers of the distribution and determine the correction made to the $B_w(\mathrm{i},\mathrm{i})$ term:

$$\gamma_{2,\mathrm{i}} = \frac{\frac{1}{N}\sum_{k=1}^{N}\left(\Delta\dot{x}_{model,\mathrm{i}}(k) - \mu(\mathrm{i})\right)^4}{\sigma_\mathrm{i}^4} - 3 \tag{3.26}$$

For the states which have negative excess kurtosis, the unknown disturbances have more data distributed outside the region of the peak than a normal distribution. The more negative the excess kurtosis is, the more outliers the distributions will have. When the excess kurtosis

is large, equations (3.24) and (3.25) without considering the extreme error distributions may not be a proper way to estimate the unknown disturbance. Therefore, a correction is made to the unknown disturbance estimations of the states which have excess kurtosis lower than -1 (per Fig. 3.5) by the following equation:

$$B_w(\mathrm{i},\mathrm{i}) = B_{w0}(\mathrm{i},\mathrm{i})\,|\gamma_{2,\mathrm{i}}| \tag{3.27}$$

where B_{w0} is the modeling error estimated by Section 3.2.1.

For the states x_{14} to x_{20} which represent the delayed actuator and sensor responses, the unknown disturbance terms $B_w(\mathrm{i},\mathrm{i})$ are set as 0. The details of $B_w(\mathrm{i},\mathrm{i})$ estimation for each state are listed in Appendix B.

3.3.3 Measurement Noise

The diagonal measurement noise covariance matrix H is defined as:

$$H = \begin{bmatrix} 4\%\delta W_{inlet,max} & 0 & 0 & 0 \\ 0 & 2\%\delta W_{comp,max} & 0 & 0 \\ 0 & 0 & 7\%\delta W_{egrl,max} & 0 \\ 0 & 0 & 0 & 4\%\delta W_{comp,up,max} \end{bmatrix} \tag{3.28}$$

where sensor accuracy data comes from Table 3.1 and δW_{max} is the maximum flow rate deviation with respect to its linearization point.

3.3.4 Sensor Selection Results

The sensor selection algorithm is applied to the scaled linear system. This is to eliminate the effect of magnitude differences of measurements.

Table 3.5 shows the optimal sensor set computed by the sensor selection algorithm (per Section 3.2) for different sensor number constraints. The iterative parameter ϵ is set as $1\mathrm{e}^{-3}$ for single and two-sensor combinations or $1.2\mathrm{e}^{-2}$ for three-sensor combinations. The trace(T), representing the upper power bound of the expected estimation RMSE, is calculated by

equation (3.15) when setting $\alpha = 0$ for the normalized system. The upper bound of the expected RMSE $\mathbb{E}\{RMSE\}_{ub}$ and the expected RMSE $\mathbb{E}\{RMSE\}$ for the actual system can be expressed, and related as follows:

$$\begin{aligned} &\mathbb{E}\{RMSE\}_{ub} \geq \mathbb{E}\{RMSE\} \\ &\mathbb{E}\{RMSE\}_{ub} = \delta x_{11,max}\sqrt{trace(T)} \\ &\mathbb{E}\{RMSE\} = \delta x_{11,max}\sqrt{trace((\tilde{B}_w - L\tilde{H})^T P(\tilde{B}_w - L\tilde{H}))} \end{aligned} \tag{3.29}$$

where $\delta x_{11,max} = max(x_{11} - x_{e,11})$ is the scaling parameter of the intake manifold burnt gas fraction x_{11}. It can be noticed that $\mathbb{E}\{RMSE\}_{ub}$ is a very tight upper bound of $\mathbb{E}\{RMSE\}$ for this application as shown in Table 3.5.

Table 3.5. : Sensor selection results

Sensor Number	Optimal Sensor Set	1000α	$\sum_{j=1}^{n} \mu_j^{(k)} \sum_{i=1}^{m} \lvert S_{ij} \rvert$	trace(T) when $\alpha = 0$	$\mathbb{E}\{RMSE\}_{ub}$	$\mathbb{E}\{RMSE\}$	RMSE (simulation)
0	/	/	/	0.02020	0.894%	0.894%	0.947%
1	EGR DP	1.5	0.9917	0.01552	0.785%	0.785%	0.498%
2	EGR DP, MAFa	0.65	1.9816	0.01290	0.715%	0.715%	0.369%
3	EGR DP, MAFa, MAFh	0.022	2.5922	0.01283	0.713%	0.713%	0.367%
4	EGR DP, MAFa, MAFh,MAF	0	3.9361	0.01283	0.713%	0.713%	0.367%

The algorithm identifies the EGR DP sensor as the best sensor if only one single can be used. When two sensors are used, the optimal sensor set becomes EGR DP and MAFa., which measures the inlet air mass flow rate before the EGR joint (per Fig. 3.1). The optimal three-sensor set combines EGR DP, MAFa and MAFh.

Different sensor sets with their corresponding observers are tested on the reference engine model in GT-Power. The four candidate sensors (per Table 3.1 and Fig. 3.1) are placed in the GT-Power model. Per Table 3.1 data, these four GT-Power outputs are filtered with first-order functions described in equation (3.17) and corrupted by measurement noise before being sent to the observers to account for sensor noise. The GT-Power and observer simulation structure is shown in Fig. 3.8. The observer gain for each sensor set is computed by the optimization (3.15) with $\alpha = 0$. The GT-Power cycle-averaged intake manifold burnt gas fraction is used as the truth-reference to validate the estimation results. RMSE of the

intake manifold burnt gas mass fraction estimation for each sensor set is calculated from 3.3s to the end of the simulation to eliminate the effects of initial conditions.

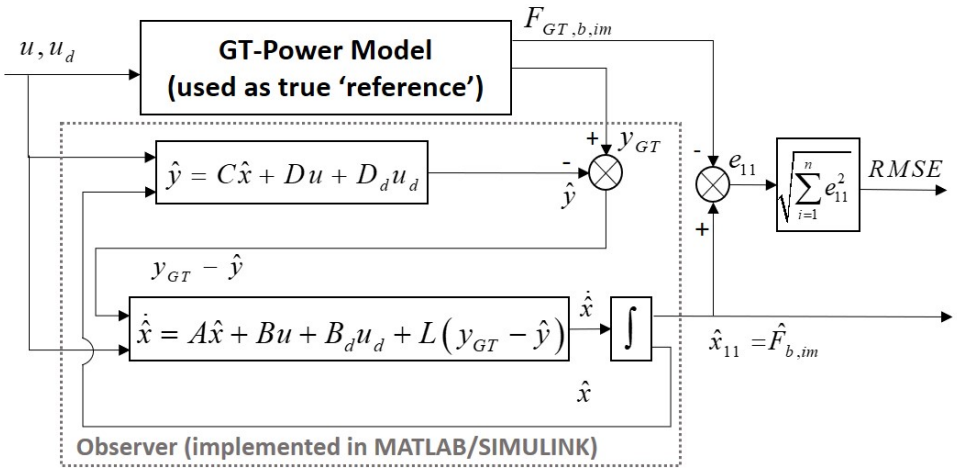

Figure 3.8. : Diagram of GT-Power and observer simulation structure

Single Sensor Sets

Fig. 3.9 shows the estimation results of intake manifold burnt gas mass fraction when using different single sensor sets. As shown in Fig. 3.9, the EGR DP sensor has the most accurate estimation results at every step. Considering the overall estimation performance, the EGR DP sensor is the most accurate single-sensor option since it has the smallest root-mean-square error (RMSE), 0.498%, over the entire simulation. Without using any sensor, the maximum absolute estimation error is 1.744%. With the computed optimal sensor EGR DP, the maximum error is reduced to 1.014%, which is a 42% improvement compared to the model-only estimated result. The maximum errors for single MAFa sensor, MAFh sensor and MAF sensor are 1.684%, 1.724% and 1.724%.

As shown in Table 3.6, the RMSE for a single MAFa sensor, a single MAFh sensor and a single MAF sensor are 0.909%, 0.935% and 0.935%, respectively. This indicates that if the EGR DP sensor fails, the next sensor the engine should select is the MAFa sensor based on their trace (T) and $\mathbb{E}\{RMSE\}_{ub}$ calculations. Though the MAFh sensor has slightly lower trace (T) and $\mathbb{E}\{RMSE\}_{ub}$ than the MAF sensor, their estimation results are the same.

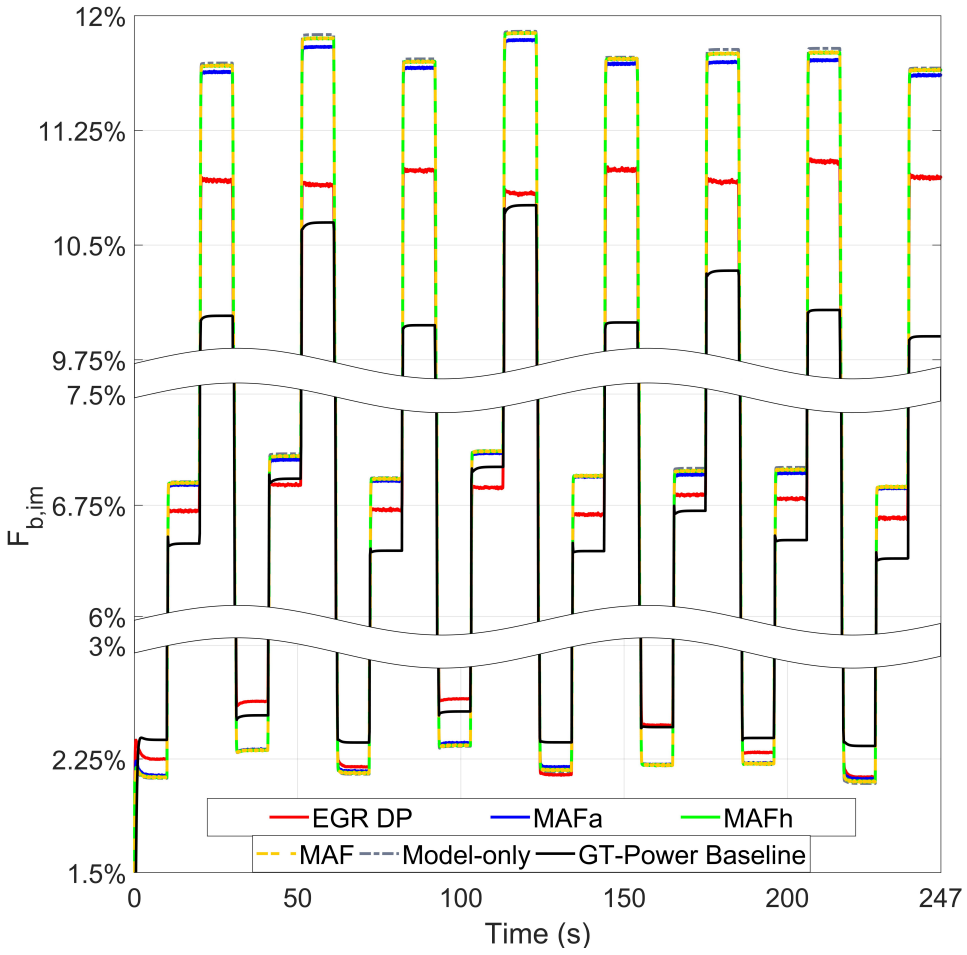

Figure 3.9. : Intake manifold burnt gas mass fraction estimation when only using one sensor

Fig. 3.10 shows the histograms of different single sensor sets' estimation errors. Compared to the optimal sensor EGR DP, the error distributions of the other three sensors are more spread out.

Two-sensor Sets

The optimal two-sensor set computed by the sensor selection algorithm (per Section 3.2) is the combination of the EGR DP and MAFa sensors. This is verified in the coupled GT-Power/Observer simulation (per Fig. 3.8). As shown in Fig. 3.11, the computed optimal

Table 3.6. : Single sensor set

Sensor Set	trace(T) when $\alpha = 0$	$\mathbb{E}\{RMSE\}_{ub}$	$\mathbb{E}\{RMSE\}$	RMSE (simulation)
EGR DP	0.01552	0.785%	0.785%	0.498%
MAFa	0.01870	0.861%	0.861%	0.909%
MAFh	0.01907	0.870%	0.870%	0.935%
MAF	0.01911	0.871%	0.871%	0.935%

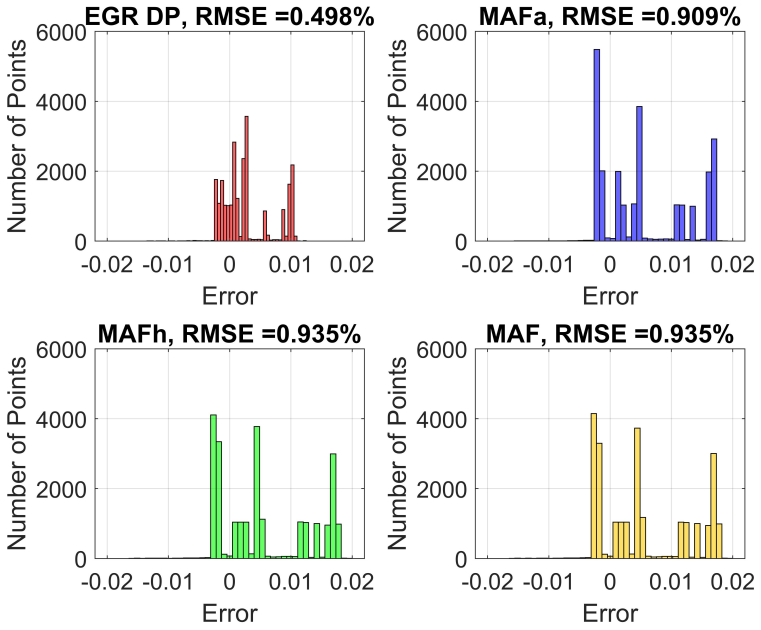

Figure 3.10. : Histograms of Intake manifold burnt gas mass fraction estimation error when only using one sensor.

sensor set has the smallest estimation error for almost every step. Comparing the overall estimation performance of the optimal sensor set with the other five combinations, the optimal one has the lowest RMSE. With the computed optimal sensor set, the maximum error is reduced to 0.754%, which is 57% improvement compared to the model estimated result. The maximum estimation error is 0.794% for the combination of EGR DP sensor and upstream compressor flow sensor MAFh, and is 0.804% for the combination of EGR DP sensor and downstream compressor flow sensor MAF. For the combinations of MAFa sensor + MAFh sensor, MAFa sensor + MAF sensor, the maximum estimation errors are both 1.564% and

1.594%. When only two compressor flow sensors are used, the maximum error is up to 1.724%.

In Table 3.7 and Fig. 3.12, the simulated RMSE for different two-sensor set combinations monotonically increases with increasing $\mathbb{E}\{RMSE\}$, as expected. The sensor sets with the first three lowest $\mathbb{E}\{RMSE\}$ all include the EGR DP sensor. Though the algorithm computes the combination of EGR DP sensor and MAFa sensor as the optimal two-sensor set, the combination of EGR DP sensor + MAFh sensor and EGR DP sensor + MAF sensor have similar estimation performance as the optimal one, as shown in Fig. 3.11. These two combinations have very close $\mathbb{E}\{RMSE\}$ as well as the RMSE as shown in Table. 3.7. When EGR DP is not considered in the two-sensor combination, such as the combination of MAFa sensor and MAFh sensor, there is a large increase in $\mathbb{E}\{RMSE\}$ as well as the simulated RMSE. Additionally the two-sensor sets without the EGR DP sensor even have larger estimation errors than single EGR DP sensor. This indicates that under this operation condition, if only two sensors are allowed, the combination should include EGR DP sensor, and an EGR DP-only strategy would be preferred over a two-sensor strategy which did not include the EGR DP sensor. The optimal selection of the sensor in addition to the EGR DP sensor is MAFa sensor. The MAFh sensor may be considered as a backup selection to the MAFa sensor.

Table 3.7. : Two-sensor combinations

Sensor Set	trace(T) when $\alpha = 0$	$\mathbb{E}\{RMSE\}_{ub}$	$\mathbb{E}\{RMSE\}$	RMSE (simulation)
EGR DP + MAFa	0.01290	0.715%	0.715%	0.369%
EGR DP + MAFh	0.01322	0.724%	0.724%	0.388%
EGR DP + MAF	0.01331	0.727%	0.727%	0.391%
MAFa + MAFh	0.01806	0.847%	0.847%	0.825%
MAFa + MAF	0.01824	0.851%	0.851%	0.849%
MAFh + MAF	0.01905	0.870%	0.870%	0.935%

Fig. 3.13 shows the histograms of different two-sensor combinations estimation errors. As shown, the best three two-sensor combinations have the estimation errors distributions closer to 0.

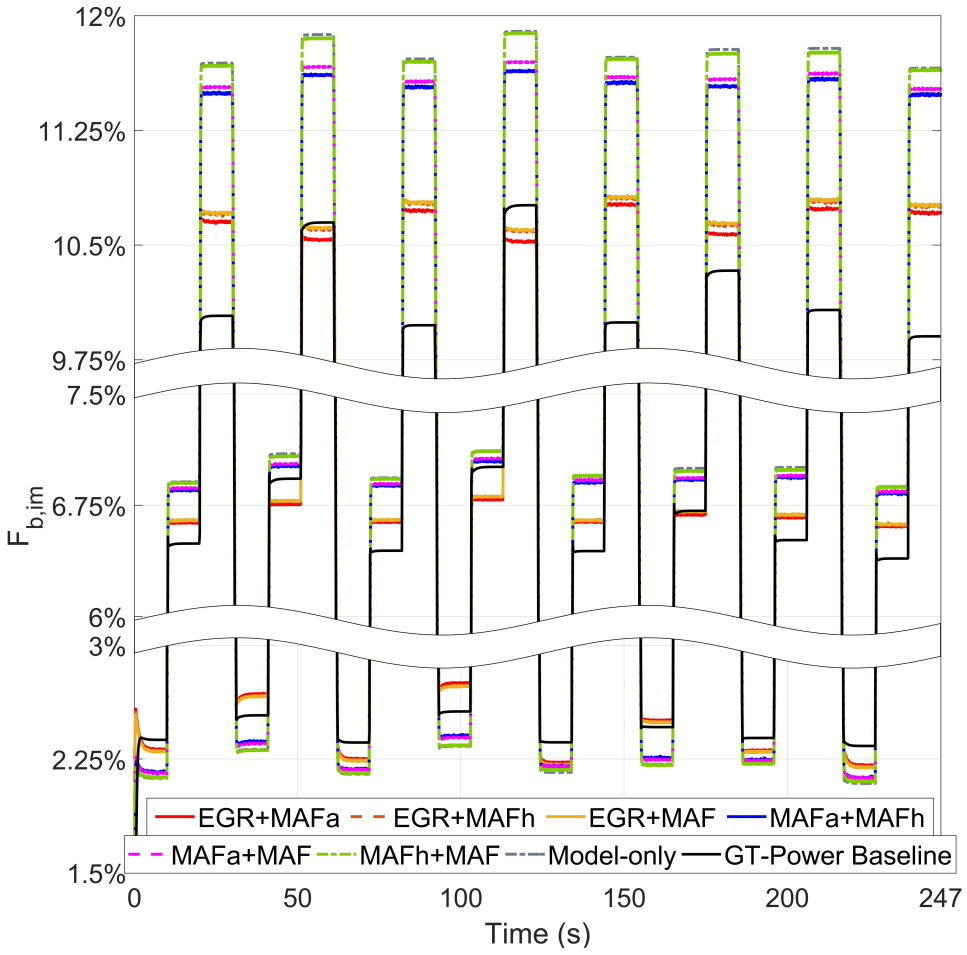

Figure 3.11. : Intake manifold burnt gas mass fraction estimation when using two sensors.

Optimal Sensor Sets

Fig. 3.14 show the estimation results of intake manifold burnt gas mass fraction $F_{b,im}$ when using optimal sensor sets with different sensor numbers. As shown in Fig. 3.14, the optimal two-sensor set has better estimation performance than the optimal single sensor. When more than two sensors can be used, all the optimal sensor set options have very similar estimation performances. Based on the data shown in Table 3.5, the optimal single sensor EGR DP reduces the RMSE by 47.4% compared with model-only estimated results. The optimal two-sensor option further reduces the RMSE by 25.9% based on the optimal single sensor estimation performance. Comparing the RMSE of the optimal three-sensor set, 0.367%, with the RMSE of the optimal two-sensor set, 0.369%, there is only 0.5% accuracy improvement.

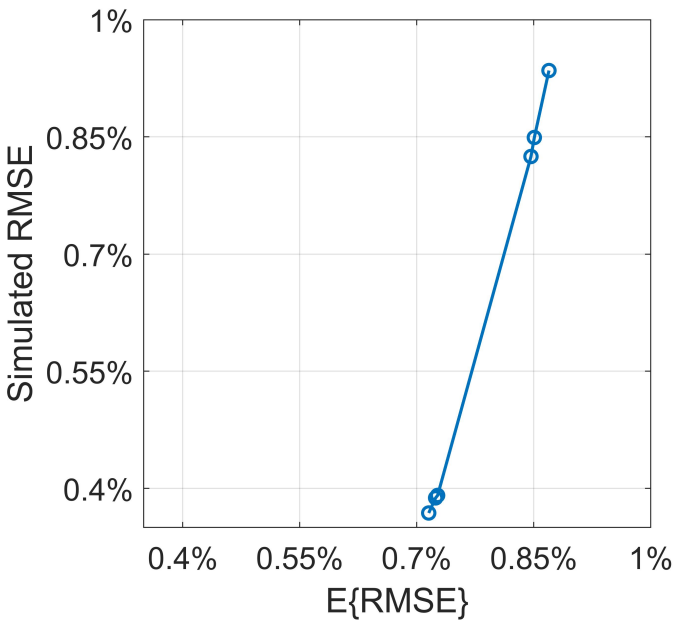

Figure 3.12. : RMSE vs. trace(T) for two-sensor combinations.

When the fourth sensor is added to the optimal three-sensor set, there is no improvement for the RMSE. In Fig. 3.15, the computed $\mathbb{E}\{RMSE\}$ and trace(T) have similar trends. Using the optimal single sensor reduces the trace(T) by 23.2% and $\mathbb{E}\{RMSE\}$ by 12.2% compared with model-only estimation results. From the optimal single sensor to the optimal two-sensor set, the trace(T) and $\mathbb{E}\{RMSE\}$ have 16.9% and 8.9% reductions, respectively. From the optimal two-sensor set to the optimal three-sensor set, the trace(T) is only lowered by 0.5% and $\mathbb{E}\{RMSE\}$ is lowered by 0.3%. From the optimal three-sensor set to the all-sensor set, both trace(T) and $\mathbb{E}\{RMSE\}$ remain the same. Compare the trends of $\mathbb{E}\{RMSE\}$ (or trace(T)) and simulated RMSE, both $\mathbb{E}\{RMSE\}$ (or trace(T)) and simulated RMSE have relatively large reductions from model-only case to single sensor case to two-sensor case and small decreases when adding the third or fourth sensor. In this way, $\mathbb{E}\{RMSE\}$ or trace(T) can be a useful indicator of showing the necessity or redundancy when adding additional sensors.

The sensor selection results indicate that though increasing sensor number reduces RMSE, the added sensor(s) brings in very small improvements of the estimation performance when number of sensors is higher than two. Based on the estimation error requirement, it may

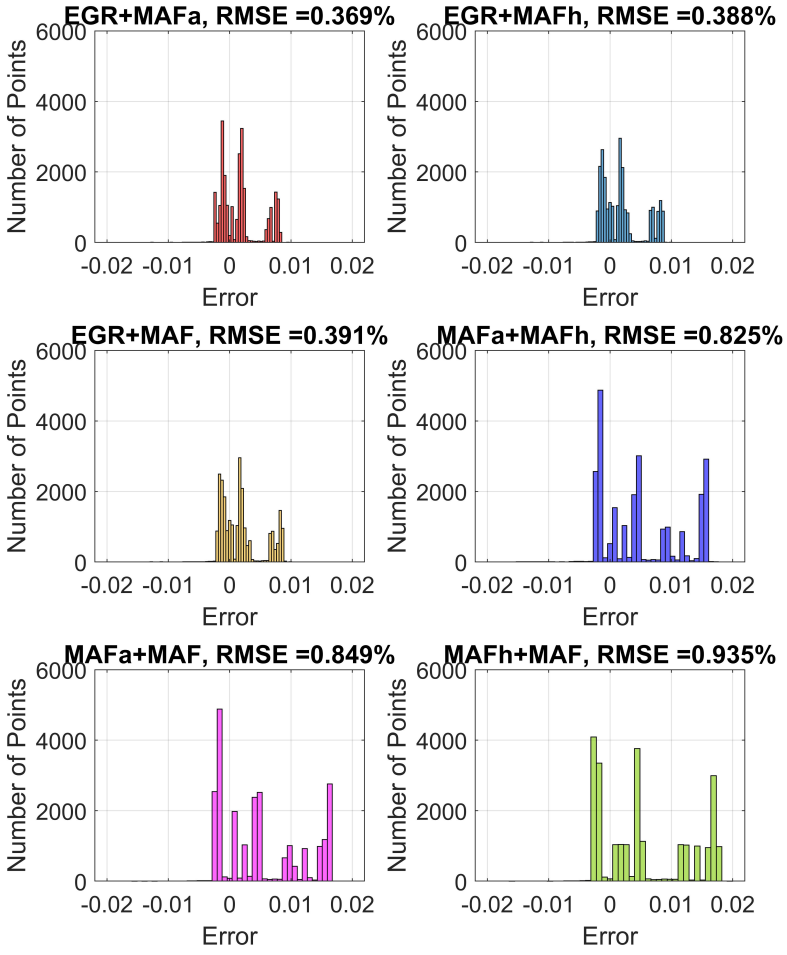

Figure 3.13. : Histograms of intake manifold burnt gas mass fraction estimation error when using two sensors.

be worth using a single EGR DP sensor or adding a second sensor MAFa in addition to a single EGR DP sensor, but it may not be worth spending more money on adding the third or fourth sensor for the intake manifold gas composition estimation.

Fig. 3.16 shows the histograms of different optimal sensor combinations estimation errors. It can be seen that with the increasing of sensor number, the RMSE distribution is narrowed down and has smaller peaks at large errors.

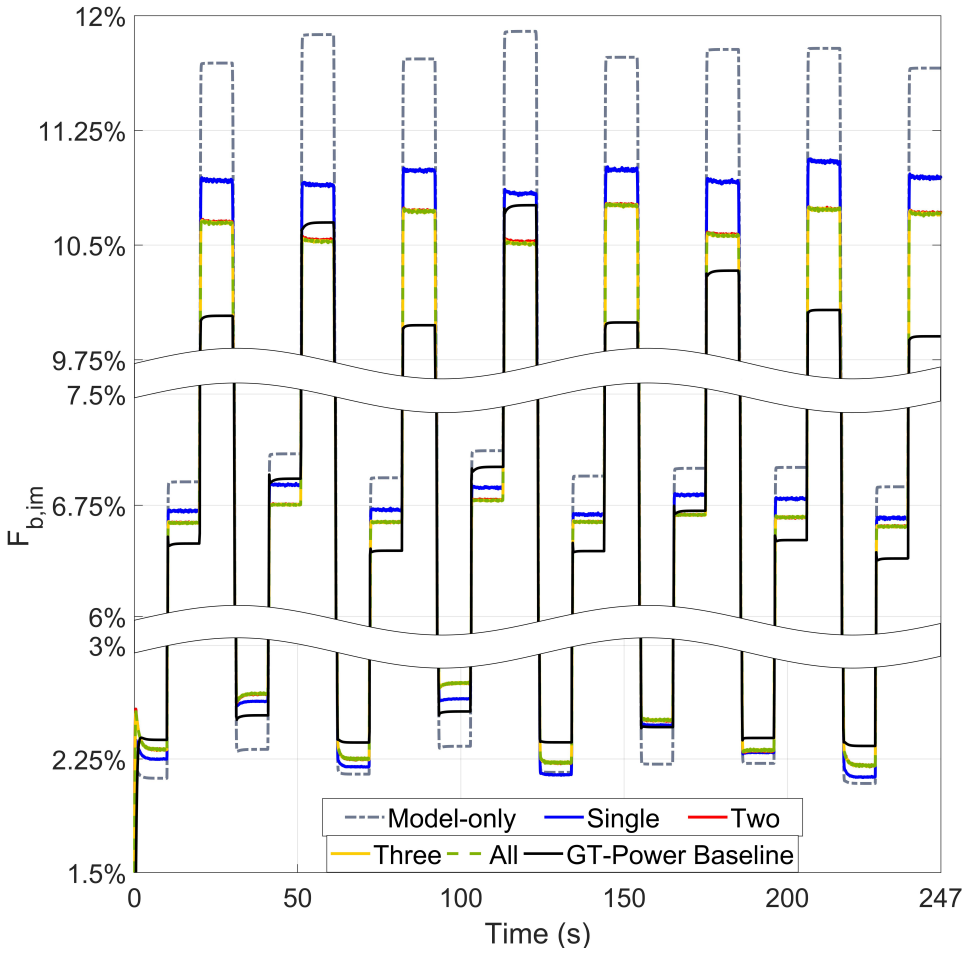

Figure 3.14. : Intake manifold burnt gas mass fraction estimation when using optimal sensor sets.

Additional Discussion

The difference between the expected RMSE $\mathbb{E}\{RMSE\}$ and the simulated RMSE is shown in Table. 3.5 - 3.7, as well as Figures 3.12 and 3.15. This could be explained by: (i) The computation of the expected RMSE, $\mathbb{E}\{RMSE\}$, (via Equation (24)) is based on the assumption that the process noise is zero-mean white noise. However, the actual unknown disturbance term $\dot{x}_{GT}$ is not normally distributed for the example testing cycle. Since this paper focuses on selecting the optimal sensor set among candidate sensors for the engine system rather than studying the differences between the engine model and actual system, a quick and simple approximation method of the process noise described in Section 3.3.2 was

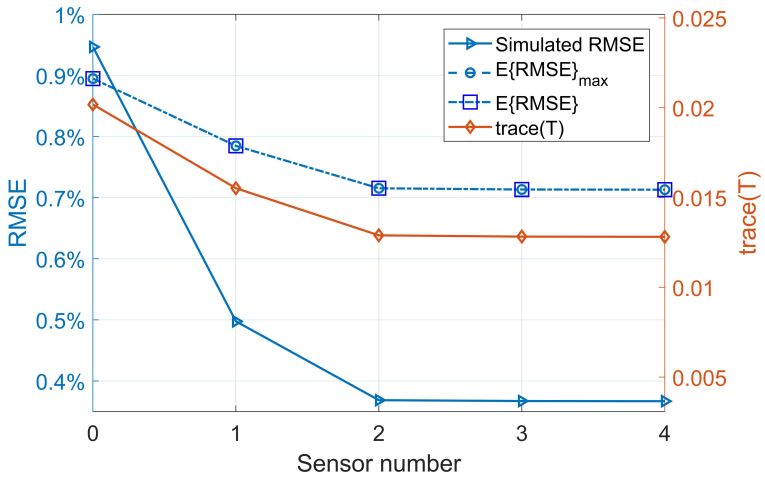

Figure 3.15. : RMSE and trace(T) vs. sensor number for optimal sensor sets.

used. The valuable information provided by the sensor selection algorithm is the sequence and relative increase/decrease among different sensor sets. Further studies could focus on a more appropriate unknown disturbance estimation method, but this would not be expected to change the sensor selection results and thus was not the study purpose; (ii) The measurement noise is approximated by the product of the maximum deviation of the sensor measurement with respect to its linearization point and the accuracy (per Section 3.3.3). This simple approximation would result in some differences between the expected RMSE $\mathbb{E}\{RMSE\}$ and the simulated RMSE due to the reason that the actual sensor measurement deviations are not symmetric about the linearization points, but would not be expected to change the sensor selection results. Further studies could focus on a more appropriate measurement noise estimation method based on analytical approaches.

3.4 Summary

This paper outlines a sensor selection and observer design algorithm based on H_2 optimization while considering process and measurement noise. The approach is (1) implemented to an advanced turbo-charged spark-ignited engine architecture using exhaust gas circulation; and (2) validated on a high fidelity engine simulation in GT-Power. The objective of the sensor selection + observer design algorithm is to minimize the estimation error and the

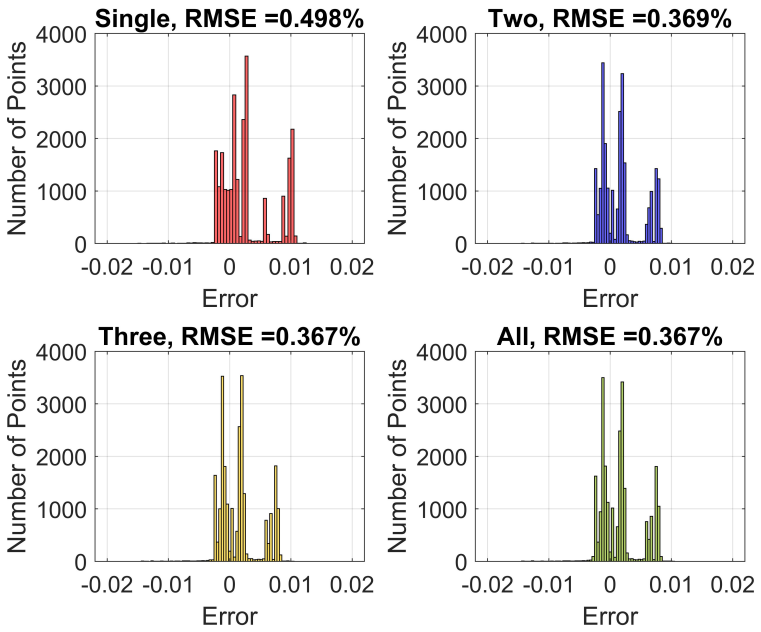

Figure 3.16. : Histograms of intake manifold burnt gas mass fraction estimation error when using optimal sensor sets.

required sensor numbers. The optimization problem is convexified and solved via SDP. A method to estimate the unknown model uncertainties was also developed. The high fidelity simulation results verified that the optimal sensor sets computed by the algorithm had the best estimation performance. Sensor redundancy was also analyzed based on the computation results. This algorithm reduces the computation time and experimental efforts of selecting optimal sensor sets.

4. ROBUST-CONTROL BASED SENSOR SYSTEM AND CONTROLLER CO-DESIGN ALGORITHM

4.1 Motivation

Stoichiometric air-to-fuel ratio (AFR) and air/EGR flow control are essential control problems in today's advanced spark-ignited (SI) engines to enable effective application of the three-way-catalyst (TWC) and generation of required torque. External exhaust gas recirculation (EGR) can be used in SI engines to help mitigate knock, reduce enrichment and improve efficiency[1]. However, the introduction of the EGR system increases the complexity of stoichiometric engine-out lambda and torque management, particularly for high BMEP commercial vehicle applications, in the following way: (1) measurement proximity - through transient operations, the flow measured at the air filter (point-of-measurement) is not representative of what actually goes into the cylinder (point-of-interest). The rapid changes in EGR flow are also not seen immediately by the air flow sensors owing to the transport delays and volume filling effects[64]. This will result in AFR and torque control errors if uncompensated; (2) variation across OEM vehicle configuration - The methods relating the point-of-measurement to the point-of-interest are challenged by a proliferation of configurations of the air handling piping in commercial vehicles. Due to the variation of inlet air flow configurations and sensors in different OEM vehicles, the estimation methods and their accuracies can be very different and thus brings additional uncertainties and disturbances to the controller design problem; (3) limited EGR rate at high loads - During engine tip-out events, slow low-pressure (LP) EGR response may delay the reduction of EGR concentration in the intake manifold despite EGR valve closure. The resulting elevation in EGR concentration at low load conditions may lead to combustion instability and misfire due to lower external EGR tolerance at low load conditions. This effectively constrains the maximum LP EGR rate that can be sustained at high load prior to a tip-out[65].

Previous research work focuses on air-path or EGR flow control. As a result of air/EGR-path dynamics and measurement inaccuracy, there are always some flow control errors during steady-state or transient conditions. Considering the interactions between the air/EGR-path control performance and the AFR control performance, the flow control inaccuracy

will further result in errors in AFR control, which has a very tight control target for the stoichiometric SI engines. Some researchers have studied the air-path and AFR control strategies for other types of engines with EGR. However, considering the different AFR control accuracy requirements and significant combustion differences, these control strategies are not expected to be suitable for stoichiometric SI engines.

Proper sensor selection is critical for successful engine and control system designs. The most appropriate candidate control algorithms will depend on the sensing strategy selected. Ideally, sensor characteristics including noise, accuracy, dynamics, and delays would be taken into account when designing the controllers to achieve desired control performance. In the SI engine control problem, feedforward-feedback control is usually used for fast transient response and steady-state tracking performance. The sensor measurements can be used by the feedback controller or/and the feedforward controller. Experimental testing is one way to select sensor configurations and calibrate controller parameters. However, this method can be expensive and time-consuming, and may need to be redone even when there are minor changes to the engine system or the sensor/actuator characteristics. Therefore, a co-design strategy for both the sensing approach and control algorithm is desired to effectively select the acceptable sensor configurations and robustly design the controllers.

In this chapter, a framework is developed for selecting candidate sensor suites and designing a corresponding robust controller to ensure stoichiometric operation with desired torque production of a turbocharged SI engine using low pressure EGR, wastegate turbo-charging, intake throttling, and VVT.

4.2 Control Problem Formulation

The target engine architecture is shown in Fig. 4.1 and is modeled per Section 4.3. A two-loop control structure (per Fig. 4.2) is proposed for the engine. The flow loop is to control the air and EGR flows while the AFR loop is to control the cylinder AFR. Both control loops use the signals from the same sensor set. To handle the interactions between the two loops, the actuators' commands generated by the flow loop controller are used as inputs of the AFR loop controller, and vice versa.

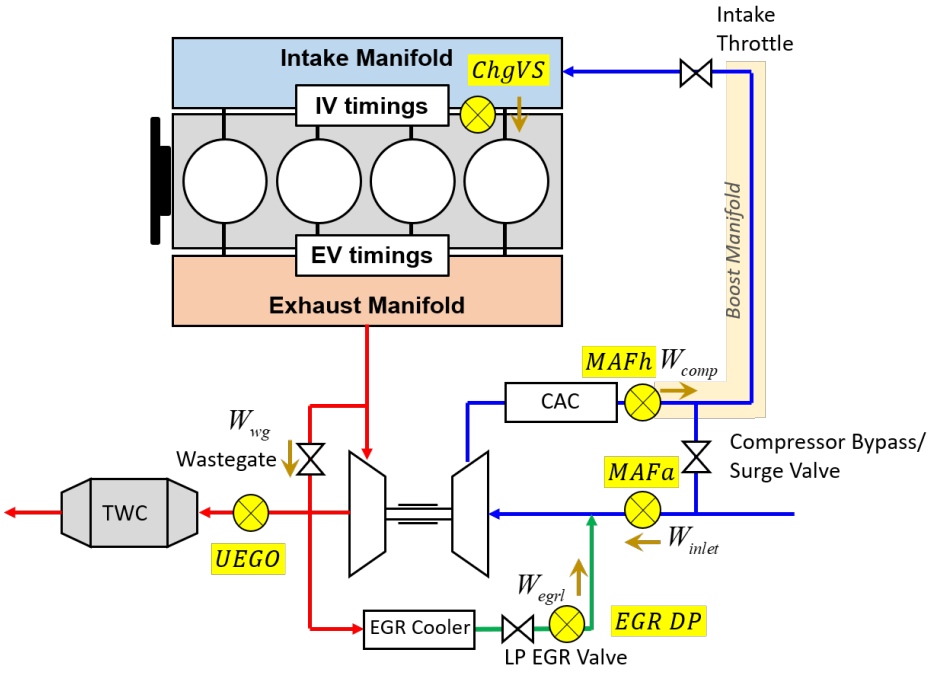

Figure 4.1. : Engine architecture and candidate sensor placements.

For illustrative purposes, four available sensors are considered as candidates as shown in Table 4.1. A mass air flow sensor for inlet air (MAFa) can be placed upstream of the air and low pressure (LP) EGR confluence point, to measure the inlet air mass flow rate (W_{inlet}). A mass air flow sensor for high pressure flow (MAFh) can be placed downstream of the charge air cooler (CAC) to measure the cooled compressor mass flow rate (W_{comp}). An EGR delta pressure sensor (EGR DP) can be located in the LP EGR valve to measure the LP EGR mass flow rate (W_{egrl}). A virtual charge flow sensor (ChgVS) based on the speed-density equation is also available for estimation of the cylinder charge flow rate (W_{charge}). A UEGO sensor can be placed upstream of the three-way catalyst (TWC) to measure the exhaust AFR (AFR_{exh}). Among these candidate sensors, three different combinations are considered as candidate sensor sets as shown in Fig. 4.3. Case 1 is the combination of MAFa sensor and UEGO sensor. Case 2 is the combination of ChgVS sensor, EGR DP sensor and UEGO sensor. Case 3 is the combination of MAFh sensor, EGR DP sensor and UEGO sensor.

For all three candidate sensor cases, two control loops, the multiple-input single-output (MISO) AFR control loop and multiple-input multiple-output (MIMO)flow control loop are

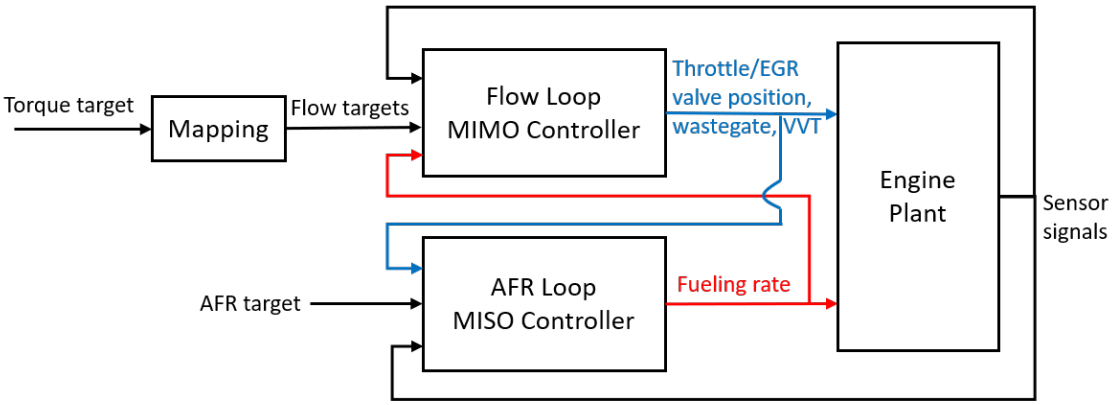

Figure 4.2. : Two-loop control structure.

Table 4.1. : Available sensors

Sensor	Physical Quantity	Accuracy	Response Time
MAFa	Inlet Air Flow (EGR. Up)	4 %	30 ms
MAFh	Comp. Flow (CAC. Dn)	2 %	50 ms
			30ms (1000 rpm)
EGR DP	EGR Flow	7 %	20ms (2000 rpm)
			10ms (4000 rpm)
ChgVS	Cylinder Charge Flow	4%	30 ms
UEGO	Exhaust λ	0.01 (absolute)	200ms

designed to control the fueling rate and the flow actuator inputs (throttle valve effective area, LP EGR valve effective area, waste-gate diameter, intake and exhaust opening/closing timings), respectively.

The principle of this algorithm is to minimize the peak value of the structured singular value μ via synthesis of a linear H_∞ feedback controller for both control loops with a given set of sensors.

(i) If $\mu < 1$ and worst-case gain < 1, then a linear controller exists for a given sensor set that satisfies the performance objective. In this case, the candidate sensor set is accepted. Among all of the acceptable sensor sets, select the optimal one based on the μ value (the lower μ is, the more robust the system will be), sensor costs, lifetime and other economy factors.

(ii) If $\mu > 1$ or worst-case gain > 1, the controller cannot be found with the given sensor set to satisfy the performance objective. Either the given sensor set is rejected or the performance requirement is relaxed, or the sensor/actuator characteristics are improved.

4.3 Control-oriented State-space Model

A mean-value engine model based on [32][44][45] [46] was developed for the robust control design analysis. The model had 8 inputs, 1 disturbance input and 16 states as shown in

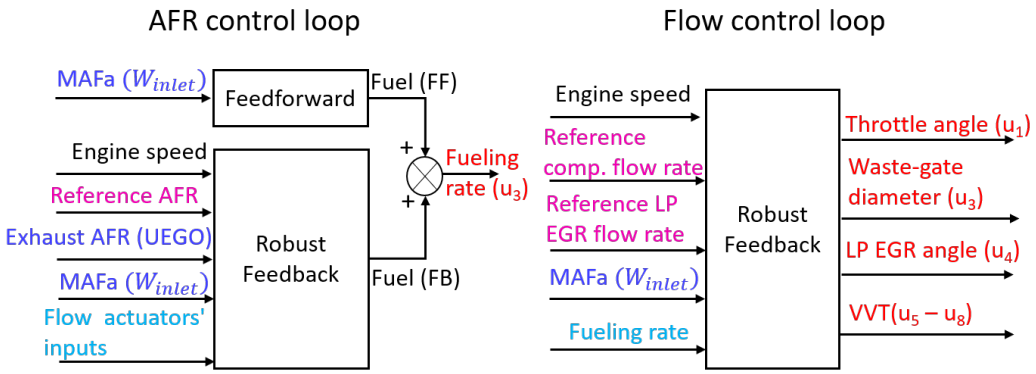

(a) Case 1

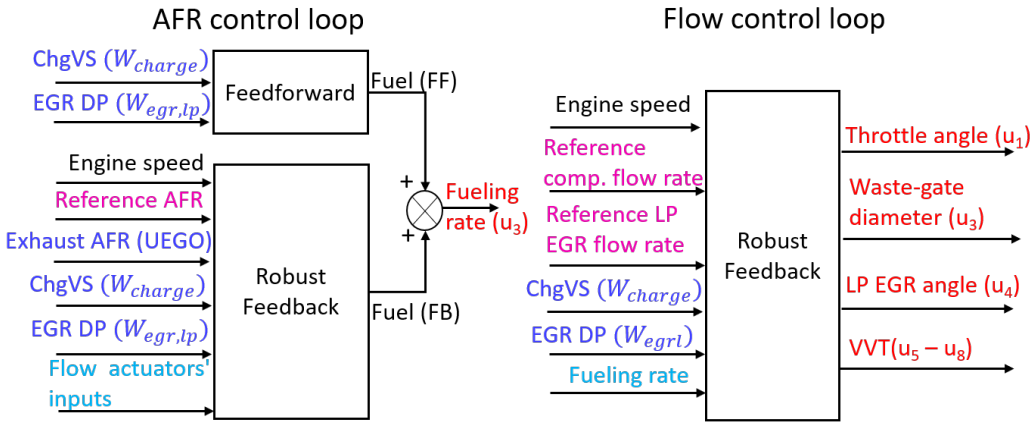

(b) Case 2

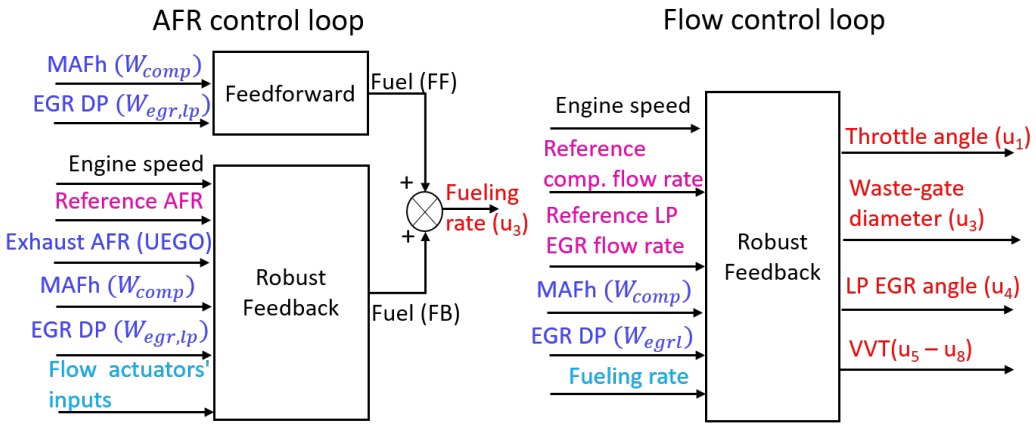

(c) Case 3

Figure 4.3. : Three candidate sensor sets

Table 4.2, 4.3 and 4.4, respectively. The nonlinear dynamic model equations can be written as follows and the detailed governing equations are listed in Appendix A:

$$\dot{x} = f(x, u, u_d) \tag{4.1}$$

Table 4.2. : State variables for the engine model

State	Variable	Description	Units
x_1	P_{bm}	Boost Manifold Pressure	Pa
x_2	P_{im}	Intake Manifold Pressure	Pa
x_3	P_{em}	Exh. Manifold Pressure	Pa
x_4	T_{bm}	Boost Manifold Temperature	K
x_5	T_{im}	Intake Manifold Temperature	K
x_6	T_{em}	Exh. Manifold Temperature	K
x_7	ω_{tc}	Turbo-charger Speed	rpm
x_8	$F_{ub,bm}$	Boost Manifold Unburnt Gas Fraction	/
x_9	$F_{b,bm}$	Boost Manifold Burnt Gas Fraction	/
x_{10}	$F_{ub,im}$	Intake Manifold Unburnt Gas Fraction	/
x_{11}	$F_{b,im}$	Intake Manifold Burnt Gas Fraction	/
x_{12}	$F_{ub,em}$	Exh. Manifold Unburnt Gas Fraction	/
x_{13}	$F_{b,em}$	Exh. Manifold Burnt Gas Fraction	/
x_{14}	A_{thr}	Effective Throttle Valve Area	m^2
x_{15}	A_{egrl}	Effective LP EGR Valve Area	m^2
x_{16}	D_{wg}	Waste-gate Diameter	m

Taking the actuator response times into consideration, states x_{14} to x_{16} were added. First-order actuator responses were considered for the throttle valve, LP EGR valve and waste-gate.

The five model outputs, $y_1 = W_{inlet}$, $y_2 = W_{comp}$, $y_3 = W_{egrl}$, $y_4 = W_{charge}$ and $y_5 = AFR_{cyl}$, were modeled as nonlinear functions of states, inputs and disturbance input.

The nonlinear model was linearized at the steady-state (x_e, u_e, u_{de}, y_e) of 3200 RPM engine speed, 60° throttle valve angle, 0° bypass valve angle, 11.6mm waste-gate diameter and 10° LP EGR valve angle. All of the valves are butterfly valves. The VVT positions (IVO, IVC, EVO, EVC) were (322°, 583°, 131°, 384°). The equilibrium points of system states x_1 to x_{16} were directly obtained from GT-Power simulation results.

Table 4.3. : Input variables for the engine model

Input	Variable	Description	Units
u_1	$A_{cmd,thr}$	Cmd. Effective Throttle Area	m^2
u_2	W_{fuel}	Fueling Rate	kg/s
u_3	$D_{cmd,wg}$	Cmd. Waste-gate Diameter	m
u_4	$A_{cmd,egrl}$	Cmd. Effective LP EGR Valve Area	m^2
u_5	IVO	Intake Valve Open	CAD
u_6	IVC	Intake Valve Close	CAD
u_7	EVO	Exh.Valve Open	CAD
u_8	EVC	Exh.Valve Close	CAD

Table 4.4. : Disturbance input variables for the engine model

Disturbance Input	Variable	Description b	Units
u_d	N	Engine Speed	rpm

The nominal model was linearized into the following format:

$$\begin{aligned} \dot{x} &= A\delta x + B\delta u + F\delta u_d \\ \delta y &= C\delta x + D\delta u + G\delta u_d \end{aligned} \tag{4.2}$$

where $\delta x = x - x_{\mathrm{e}}$, $\delta u = u - u_{\mathrm{e}}$, $\delta u_d = u_d - u_{d\mathrm{e}}$, $\delta y = y - y_{\mathrm{e}}$.

The linear state-space model was normalized as follows for control analysis:

$$\begin{aligned} \dot{\bar{x}} &= \bar{A}\delta\bar{x} + \bar{B}\delta\bar{u} + \bar{B}_d\delta\bar{u}_d \\ \delta\bar{y} &= \bar{C}\delta\bar{x} + \bar{D}\delta\bar{u} + \bar{D}_d\delta\bar{u}_d \end{aligned} \tag{4.3}$$

The normalized state $\delta\bar{x}$ can be expressed as follows:

$$\begin{aligned} \delta\bar{x} &= G_u\delta\bar{u} + G_d\delta\bar{u}_d \\ G_u &= \left(sI - \bar{A}\right)^{-1}\bar{B} \\ G_d &= \left(sI - \bar{A}\right)^{-1}\bar{B}_d \end{aligned} \tag{4.4}$$

where G_u is the transfer function matrix between the normalized state and the normalized input, G_d is the transfer function matrix between the normalized state and the normalized disturbance input.

4.4 General Control Configuration

The general control configuration for the AFR loop can be first expressed as in Fig. 4.4a where Δ denotes the model uncertainties, P_{eng} is the generalized engine model plant, P_{flow} represents the flow sensor model, K_{FF} is the feedforward controller and K_{FB} is the feedback controller. Two different types of inputs, exogenous inputs w (commands, disturbances and noise) and control signals u are fed into the plant P_{eng}. The plant output z denotes the exogenous outputs, which are the errors to be minimized. v_{eng} is the feedback controller inputs for the general configuration, e.g. commands, measured plant outputs, measured disturbances. The measurements of flow sensor(s), v_{flow} are used by the feedforward controller K_{FF} as well as the feedback controller K_{FB}. The total plant control input u consists of the feedforward command u_{FF} and feedback command u_{FB}. y_Δ and u_Δ are output and input perturbations, respectively.

By integrating the flow sensor model P_{flow} and feedforward controller K_{FF} into P_{eng}, and augmenting the measured output v_{eng} to $v = (v_{eng}, v_{flow})$, the general control configuration for AFR loop can be further expressed as in Fig. 4.4b. The new nominal open-loop plant is denoted by P. For the flow loop, the general configuration can also be expressed as Fig. 4.4b. As such, the general configuration in Fig. 4.4b can be used for both loops' feedback controller synthesis.

$N\Delta$-structure The general control configuration (per Fig. 4.4b) can be rearranged into $N\Delta$-structure (per Fig. 4.5b) through lower linear fractional transformations (LFTs) as following equations[66]:

$$N = F_l(P, K) \triangleq P_{11} + P_{12}K(I - P_{22}K)^{-1}P_{21} \tag{4.5}$$

where N is the nominal closed-loop system, w is the exogenous input, z is exogenous output, the subscript l denotes lower.

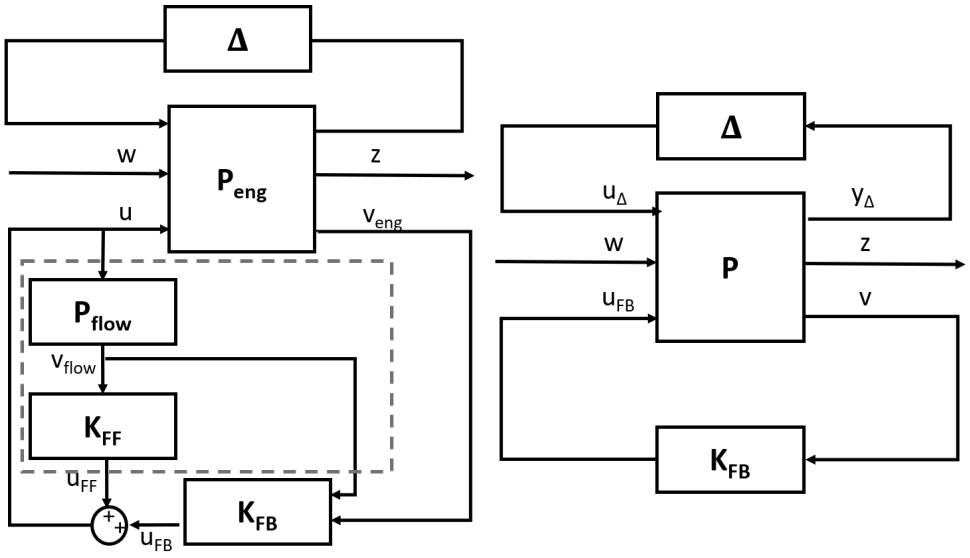

(a) Feedforwad-feedback structure for AFR loop (b) Feedback controller synthesis for both loops

Figure 4.4. : General control configuration

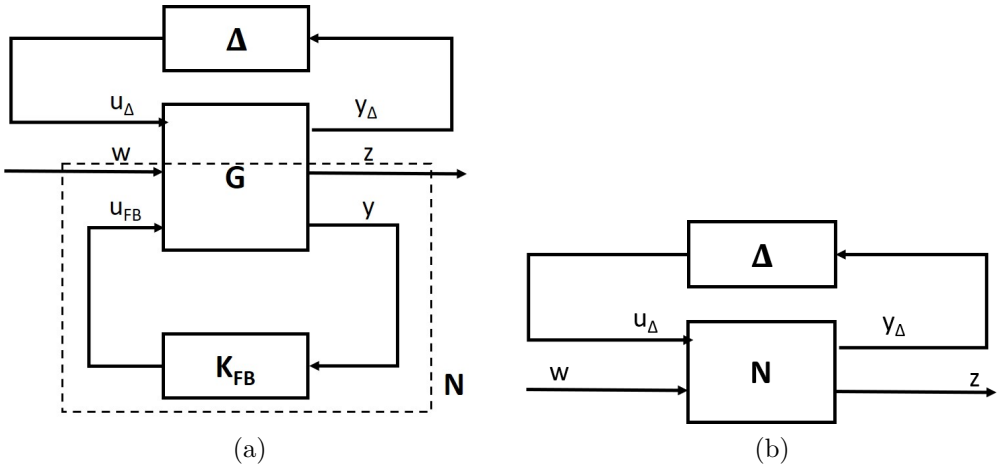

(a) (b)

Figure 4.5. : $N\Delta$-structure

***F*-structure** The $N\Delta$-structure (per Fig. 4.5b) can be rearranged into F-structure (per Fig. 4.6b) through upper LFTs as following equations[66]:

$$F = F_u\left(N, \Delta\right) \triangleq N_{22} + N_{21}\Delta(I - N_{11}\Delta)^{-1}N_{12} \tag{4.6}$$

where F is the uncertainty closed-loop transfer function from the exogenous input w to the exogenous output z and the subscript u denotes upper.

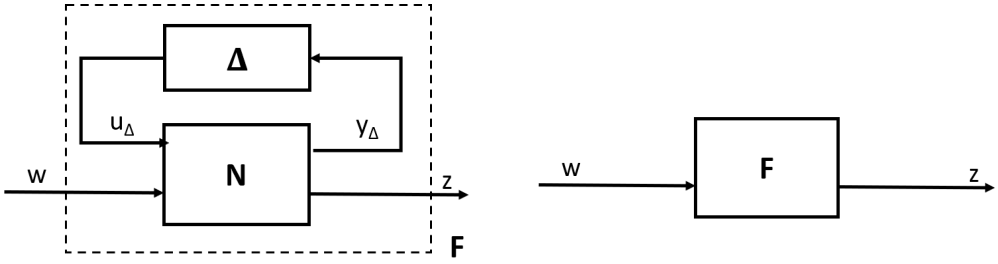

(a) (b)

Figure 4.6. : F-structure

$M\Delta$-structure The general control configuration (per Fig. 4.4b) can also be rearranged into $M\Delta$-structure (per Fig. 4.7b):

$$M = N_{11} \tag{4.7}$$

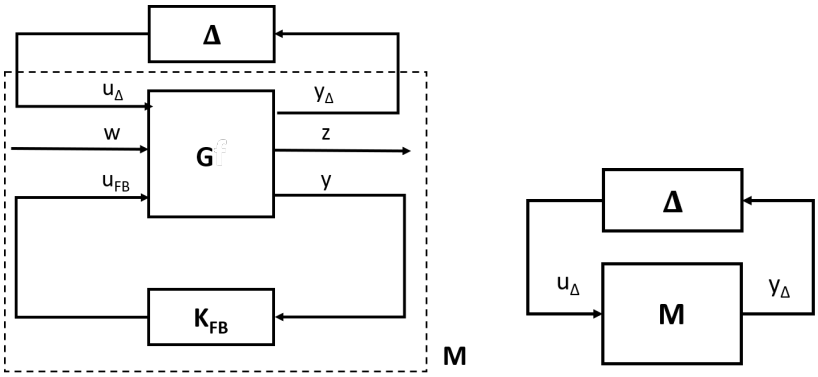

(a) (b)

Figure 4.7. : $M\Delta$-structure

Fig. 4.8 shows the detailed general control configurations of the proposed two control loops. The feedback controller for each control loop is synthesized independently.

4.4.1 The Structured Singular Value

Robust Stability

Robust stability (RS) is the ability of the system to remain stable for all plants in the uncertainty sets with a given controller.

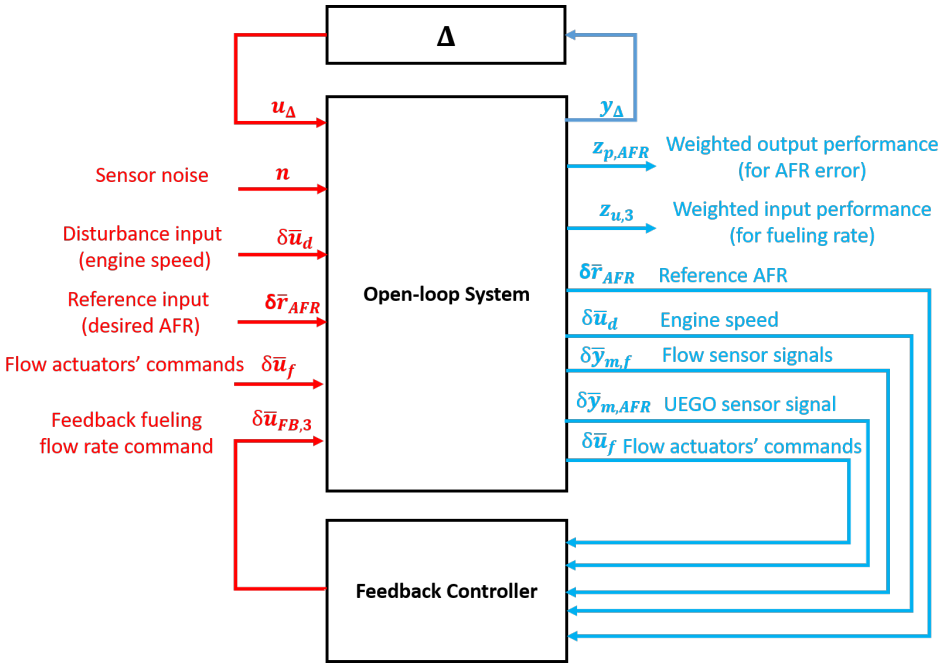

(a) AFR control loop

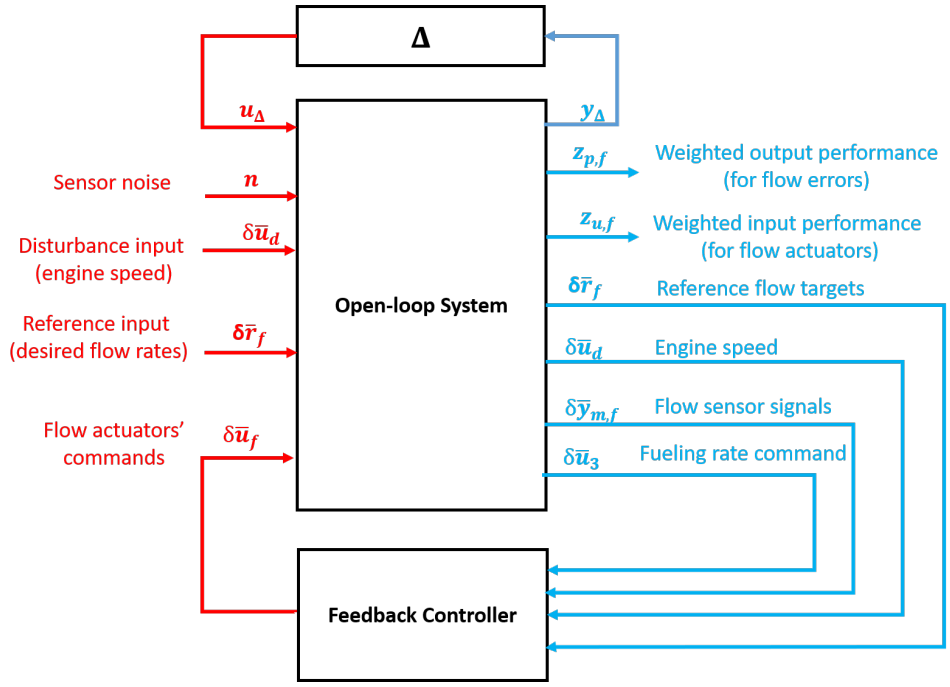

(b) Flow control loop

Figure 4.8. : General control configuration of closed-loop system

The mathematical definition of RS for a nominal stable (NS) system is:

$$RS \quad \overset{def}{\Leftrightarrow} \quad \|F\|_\infty = F_u\left(N, \Delta\right) \quad \text{is} \quad \textit{stable}, \quad \forall \|\Delta\|_\infty \leq 1 \tag{4.8}$$

From equation (4.6), if the system is nominally stable, i.e. N is internally stable (and thus $M = N_{11}$ is stable), the stability of the uncertain system depends on $(I - N_{11}\Delta)^{-1} = (I - M\Delta)^{-1}$ (suppose Δ is also stable).

Recall the spectral radius condition for complex perturbations, the system is RS if and only if:

$$\rho\left(M\Delta\left(\mathrm{j}\omega\right)\right) = \max_{\Delta} \rho\left(M\Delta\left(\mathrm{j}\omega\right)\right) < 1, \quad \forall \omega \tag{4.9}$$

where ρ denotes the spectral radius.

Recall the Lemma in [66]

$$\max_{\Delta} \rho\left(M\Delta\left(\mathrm{j}\omega\right)\right) = \bar{\sigma}\left(M\left(\mathrm{j}\omega\right)\right) \tag{4.10}$$

where $\bar{\sigma}$ denotes the maximum singular value.

For the unstructured complex uncertainty $\Delta = \Delta_{full}$, i.e., full-block perturbation uncertainty, which satisfies $\|\Delta_{full}\|_\infty \leq 1$, the sufficient and necessary RS condition is that:

$$RS \quad \Leftrightarrow \quad \bar{\sigma}\left(M\left(\mathrm{j}\omega\right)\right) < 1, \quad \forall \omega \quad \textit{and} \quad NS \tag{4.11}$$

However, for the structured uncertainty where the uncertainty is block-diagonal, the condition (4.11) is sufficient but not necessary[67]. A tighter RS-condition needs to be defined for the structured uncertainty.

Recall the Generalized (MIMO) Nyquist theorem and apply it to a positive feedback system with a stable open-loop transfer function $M\Delta$ (M and Δ are both stable)[66], the uncertain system F is stable if and only if:

$$det\left(I - M\Delta\right) \neq 0, \quad \forall \omega, \quad \forall \Delta \tag{4.12}$$

For the structured uncertainty $\Delta = \Delta_{diag}$ where the uncertainty is block-diagonal, i.e.,

$$\Delta_{diag} = diag\left\{\Delta_{\mathrm{i}}\right\} \tag{4.13}$$

the structured singular value μ is used to indicate the robust stability of the uncertain system by finding out the smallest structured Δ_{diag} (measured in terms of $\bar{\sigma}\left(\Delta_{diag}\right)$)[66] which makes

$$\det\left(I - M\Delta_{diag}\right) = 0 \tag{4.14}$$

then

$$\mu\left(M\right) = \frac{1}{\bar{\sigma}\left(\Delta_{diag}\right)} \tag{4.15}$$

where $\bar{\sigma}\left(\Delta_{diag}\right)$ denotes the maximum singular value of Δ_{diag}.

Instead of varying $\bar{\sigma}\left(\Delta_{diag}\right)$, another definition of μ is more widely used based on pre-scaled Δ_{diag}[66]:

$$\mu\left(M\right) \triangleq \frac{1}{\min\{k_m | \det\left(I - k_m M\Delta_{diag}\right) = 0\}} \quad for \quad \Delta = \Delta_{diag}, \quad \bar{\sigma}\left(\Delta_{diag}\right) \leq 1 \tag{4.16}$$

$\mu = 1$ indicates that there exists a boundary perturbation with $\bar{\sigma}\left(\Delta_{diag}\right) = 1$ which makes the system unstable. $\mu < 1$ means that the system can remain stable with $\bar{\sigma}\left(\Delta_{diag}\right)$ increasing by a factor $\frac{1}{\mu} = k_m$. $\mu > 1$ means that a small perturbation $\bar{\sigma}\left(\Delta_{diag}\right) < 1$ will cause the system becoming unstable.

Therefore, the sufficient and necessary RS condition for all allowed structured uncertainty $\bar{\sigma}\left(\Delta_{diag}\right) \leq 1$ is that:

$$RS \quad \Leftrightarrow \quad \mu\left(M\right) \leq 1, \quad ,\forall\omega \quad and \quad NS \tag{4.17}$$

For the unstructured uncertainty Δ_{full}, $\mu(M)$ can also be defined as the inverse of the smallest $\bar{\sigma}\left(\Delta_{full}\right)$ which results in the singularity of $\left(I - M\Delta_{full}\right)$:

$$\mu(M) = \frac{1}{\bar{\sigma}\left(\Delta_{full}\right)} = \bar{\sigma}\left(M\right) \tag{4.18}$$

For the structured uncertainty Δ_{diag},

$$\mu\left(M\right) \leq \bar{\sigma}\left(M\right) \tag{4.19}$$

Robust Performance

If a system with RS can achieve the performance objectives for all plants in the uncertainty sets with a given controller, then the system has robust performance.

The mathematical definition of RP for an NS system is[66]:

$$RP \quad \overset{def}{\Leftrightarrow} \quad \left\|F\right\|_{\infty} = \left\|F_u\left(N,\Delta\right)\right\|_{\infty} < 1, \quad \forall \left\|\Delta\right\|_{\infty} \leq 1 \tag{4.20}$$

which means that the H_{∞} norm of the closed-loop transfer function from exogenous input to output is less than 1 for all allowed perturbations (structured or/and unstructured) $\left\|\Delta\right\|_{\infty} \leq 1$.

For an H_{∞} performance objective, the robust performance condition is identical to a RS-condition for the structured uncertain system with additional perturbation block Δ_P[66]. Δ_P is the uncertainty block from performance specifications, and thus Δ_P is always a full matrix. Therefore, the sufficient and necessary condition for an NS uncertain system with all allowed perturbations

$$RP \quad \Leftrightarrow \quad \mu_{\tilde{\Delta}}\left(N\right) < 1, \quad \forall\omega, \quad \tilde{\Delta} = \begin{bmatrix} \Delta_{diag} & 0 \\ 0 & \Delta_P \end{bmatrix} \quad and \quad NS \tag{4.21}$$

4.4.2 μ-synthesis and DK-Iteration

The structured singular value μ is a useful indicator to analyze the robust performance of the uncertain system with a given controller. Besides, it can also be used in the μ-synthesis problem which computes the controller to minimize the μ value. However, it is currently not possible to synthesize a truly μ-optimal controller[68]. The approximation approach, DK-iteration, is an available practical method for the μ-synthesis problem.

Instead of directly minimizing $\mu(N)$, the DK-iteration approach optimizes the variables D_f and K iteratively to minimize the upper bound of $\mu(N)$ across the frequency range:

$$\mu(N) \leq \min\left\{\bar{\sigma}\left(D_f N {D_f}^{-1}\right) | D \in \mathcal{D}\right\} \tag{4.22}$$

where D_f is the designed matrix which commutes with the uncertainty Δ, i.e. $D_f\Delta = \Delta D_f$, $\mathcal{D}$ is the set of all matrices commute with Δ, and K is the controller.

The DK-iteration approach involves two minimization steps in sequence[66]. The first step optimizes the H_∞ controller K with the D variable fixed to minimize the maximum $\bar{\sigma}\left(D_f N {D_f}^{-1}\right)$ over the frequency range:

$$\min_K \quad \left\| D_f N(K) {D_f}^{-1} \right\|_\infty \tag{4.23}$$

The second step optimizes the D variable with the controller K fixed to minimize $\bar{\sigma}\left(D_f N {D_f}^{-1}\right)$ at each frequency:

$$\min_{D_f(\mathrm{j}\omega)\in\mathcal{D}} \bar{\sigma}\left(D_f(\mathrm{j}\omega) N {D_f}^{-1}(\mathrm{j}\omega)\right) \tag{4.24}$$

and fits the magnitude of each element of $D_f(\mathrm{j}\omega)$ to create a stable and minimum-phase transfer matrices $D_f(s)$. Then go back to the first step for the next iteration.

The iteration can be terminated if the upper bound is lower than 1 or it no longer decreases. One problem with the D-K iteration procedure is that it is not guaranteed to converge to the global minimum μ value, but it often works well in practice.

Convenient toolbox "dksyn" for performing DK-iteration method in MATLAB has been developed and is used in this thesis for the controller synthesis.

4.4.3 Worst-case Analysis

The structured singular value μ indicates if the uncertain system can achieve desired performance objective or not. By the definition of (4.16), μ is the maximum amount of uncertainty which can be tolerated by the system. It doesn't tell the worst-case peak gain

of the system over a specific uncertainty range or where the worst-case occurs. For MIMO systems, the worst-case peak gain is:

$$\max \left\{ \bar{\sigma} \left(F_u \left(N, \Delta \right) \left(\mathrm{j}\omega \right) \right) | \bar{\sigma} \left(\Delta \right) \leq 1 \right\} \tag{4.25}$$

which is the maximum singular value of the closed-loop system F.

Since μ quantifies the maximum allowed uncertainty while worst-case gain quantifies the worst peak of the uncertain system, both of them are useful tools for analyzing the system robust performance and thus for sensor selection problem. Worst-case can be used as a syntax check of μ tool after computing the robust controller.

The worst-case analysis is performed by MATLAB command "wcgain".

4.4.4 AFR Control Loop

For the AFR control loop, both feedforward and feedback controllers are used. The feedforward controller calculates the basic fueling rate command based on flow sensor measurements. It does not have to "wait" for the feedback signal from the exhaust λ sensor. Therefore, it can quickly respond to the engine transient operations. However, due to flow sensor noise, delay and/or unmodeled flow dynamics, the feedforward controller will cause control errors in AFR tracking performance. For this reason, it is typical to implement a feedforward controller together with the feedback controller.

Three feedforward controllers corresponding with different candidate sensor sets (per Fig. 4.3 and Table 4.1) are considered for this application. The feedback controller is the synthesized robust controller. The total fueling rate W_{fuel} is the sum of the feedforward command $W_{FF,fuel}$ and the feedback command $W_{FB,fuel}$:

$$W_{fuel} = W_{FF,fuel} + W_{FB,fuel} \tag{4.26}$$

In Case 1 (per Fig. 4.3a), only the MAFa and UEGO sensors are used. The feedforward fueling command is:

$$W_{FF,fuel} = \frac{W_{inlet}}{14.7} \tag{4.27}$$

In Case 2 (per Fig. 4.3b), the ChgVS, EGR DP and UEGO sensors are used. The feedforward fueling command is:

$$W_{FF,fuel} = \frac{W_{charge} - W_{egrl}}{14.7} \tag{4.28}$$

In Case 3 (per Fig. 4.3c), the MAFh, EGR DP and UEGO sensors are used. The feedforward fueling command is:

$$W_{FF,fuel} = \frac{W_{comp} - W_{egrl}}{14.7} \tag{4.29}$$

The flow actuators' commands δu_f are treated as exogenous inputs for the AFR loop. That is to say, the AFR loop controls the injected fueling rate to keep the cylinder AFR at the stoichiometric value with any given air flow. Fig. 4.8a shows the detailed control diagram of AFR control loop and the parameters shown in the diagram are listed in Table 4.5.

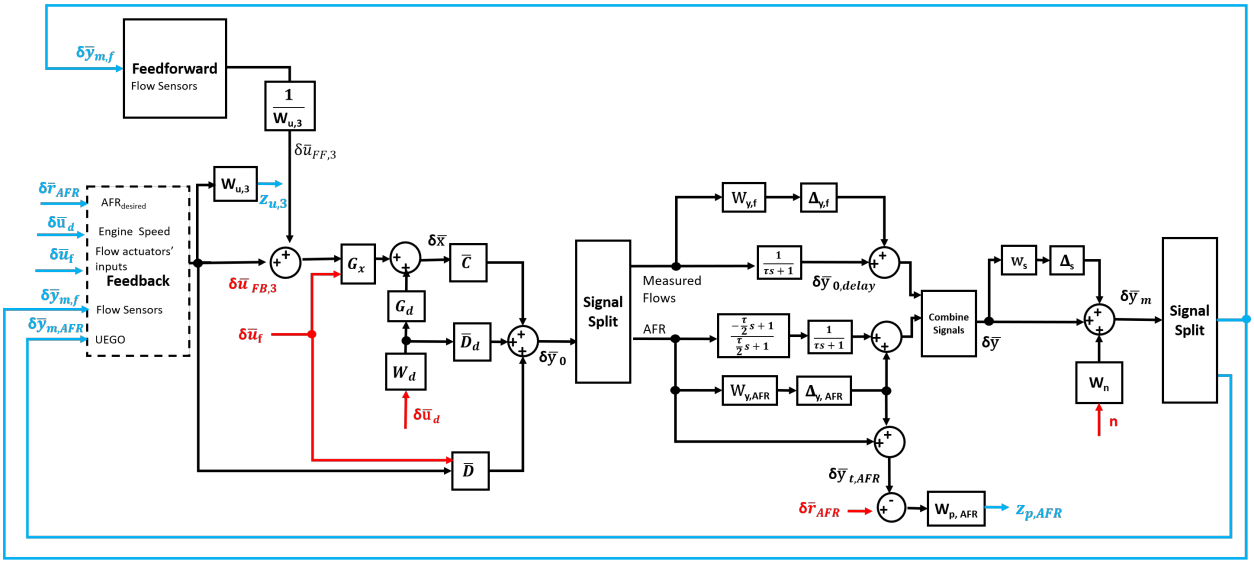

Figure 4.9. : Detailed control diagram of AFR control loop.

4.4.5 Flow Control Loop

The flow control loop manages the inlet air and EGR paths to enable torque and EGR fraction control. The tracking targets for this control loop are compressor mass flow rate

W_{comp} and LP EGR mass flow rate W_{egrl}. The inlet air flow is directly associated with the torque and the controlled EGR flow is used to suppress knock and reduce pumping loses[1].

Only a feedback controller is used for the flow control loop. Fig. 4.3 shows the inputs and outputs of the feedback controller for the three sensor suite cases considered. In all three cases, the flow controller manipulates the throttle valve, LP EGR valve, waste-gate, and cylinder intake and exhaust valves.

Fig. 4.8b shows the detailed block diagram of flow control loop and the parameters shown in the diagram are listed in Table 4.5. The total fueling command is known to the feedback flow controller and is not treated as an exogenous input to the closed-loop system. That is to say, the robust feedback flow controller is synthesized around stoichiometric combustion conditions. When the controller is implemented for the real-time control, the actual fueling command generated by the AFR controller is used as one of the inputs of the flow loop controller to account for changing fueling dynamics.

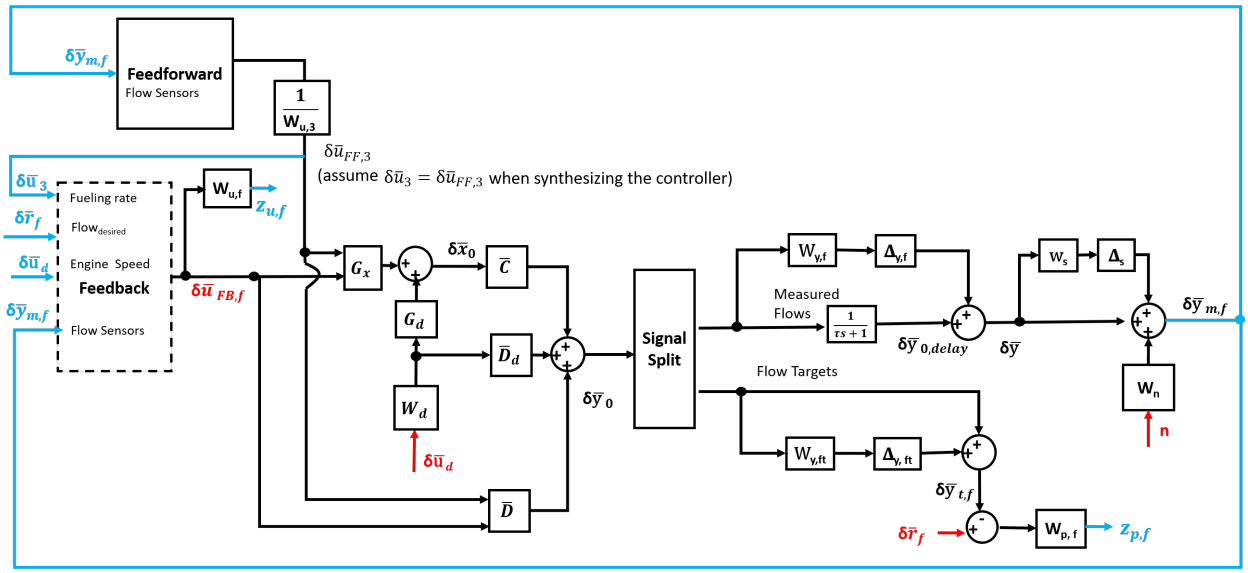

Figure 4.10. : Detailed control diagram of flow control loop.

Table 4.5. : Variables in the detailed control diagram

Symbol	Parameter
$\delta\bar{r}_{AFR}$	Nominalized AFR reference
$\delta\bar{r}_f$	Nominalized Flow reference
$\delta\bar{u}_d$	Nominalized Engine Speed
$\delta\bar{u}_{FB,3}$	Feedback Fueling Command
$\delta\bar{u}_{FF,3}$	Feedforward Fueling Command
$\delta\bar{u}_3$	Total Fueling Command
$\delta\bar{u}_f$	Flow Actuators' Commands
n	Sensor Noise
$Z_{p,AFR}$	Weighted Control Output of AFR
$Z_{p,f}$	Weighted Control Output of Flows
$Z_{u,f}$	Weighted Flows Actuators' Commands
$Z_{u,3}$	Weighted Fueling Rate Command
$\delta\bar{y}_m$	Normalized Sensor Measurements
$\delta\bar{y}_{m,f}$	Normalized Flow Sensor Measurements
$\delta\bar{y}_{m,AFR}$	Normalized UEGO Sensor Measurement
$\delta\bar{y}_{t,AFR}$	Normalized AFR Control Target
$\delta\bar{y}_{t,f}$	Normalized Flow Control Target
$\delta\bar{W}_{u,3}$	Normalized Feedforward Fueling Command
$\delta\bar{u}$	Normalized Total Actuator Input
$\delta\bar{x}_0$	Normalized Model States (Nominal)
$\delta\bar{y}_0$	Normalized Model Output (Nominal)
$\delta\bar{y}$	Normalized Model Output (With Uncertainty)
G_u, G_d	Normalized System Plants
W_d	Disturbance Weighting Function
W_{y_f}	Shaping Function of Measured Flow Modeling Uncertainty
$W_{y_f t}$	Shaping Function of Target Modeling Uncertainty
$W_{y_A FR}$	Shaping Function of AFR Modeling Uncertainty
$\Delta_{y,f}$, $\Delta_{y,AFR}$, $\Delta_{y,ft}$	Modeling Uncertainty
Δ_s	Sensor Bias Error

4.5 Performance Objectives and Uncertainties

In this framework, the tracking error requirements and the actuator physical limits are mathematically expressed as error and input performance weights, respectively. The model uncertainty, delays, sensor dynamics and errors are all expressed as transfer functions in the frequency domain.

4.5.1 Tracking Error Performance Weighting

The control target of the AFR control loop was set to keep cylinder AFR within 14.7±0.3 at low frequencies to enable a good conversion efficiency of TWC. For the flow control loop, the targets were to track reference compressor flow rate within 11.2g/s error ($6.5\% - 12.9\%$ for the interested engine operation range) and EGR flow rate within 1g/s error ($9.5\% - 40\%$ for the interested engine operation range). Three different error performance weights W_p are used to specify the requirements of the tracking errors in the frequency domain.

Let $\delta\bar{y}_t$ denote the control target and $\delta\bar{r}$ denote the tracking reference. The tracking error e can be expressed as:

$$\mathrm{e} = \delta\bar{r} - \delta\bar{y}_t \tag{4.30}$$

The exogenous output z_p is defined as:

$$z_p = W_p \mathrm{e} = Fw \tag{4.31}$$

Recall the definition of robust performance (RP)[66]:

$$\|F\|_\infty \leq 1 \tag{4.32}$$

For a scaled system with exogenous input bounded by $\|w\|_\infty < 1$, the following conditions should hold to achieve RP[66]:

$$\begin{aligned} &\|z_p\|_\infty = \|Fw\|_\infty \leq \|F\|_\infty \|w\|_\infty < 1 \\ &\Leftrightarrow \|W_p \mathrm{e}\|_\infty < 1 \Leftrightarrow |W_p \mathrm{e}| < 1, \quad \forall\omega \end{aligned} \tag{4.33}$$

Table 4.6. : Parameters of Weighting Function W_p

Control Target	M^*	A^*	ω^* (rad/s)
AFR	5	0.3	3.2
Comp. Mass Flow Rate	5	0.26	2
ERG Mass Flow Rate	5	0.25	2

Therefore, W_p^{-1} can be used to shape the upper bound of the error at every frequency. The following second-order W_p was used in this application[66]:

$$W_P = \left(\frac{\frac{s}{\sqrt{M^*}} + {\omega^*}_B}{s + {\omega^*}_B \sqrt{A^*}} \right)^2 \tag{4.34}$$

where M^* is the maximum error at high frequencies, A^* is the steady-state error and ω^* is the frequency where error reaches 100%. These parameters for three control targets are listed in Table 4.6.

Fig 4.11 shows the bode plot of ${W_p}^{-1}$ which is also the upper bound of the controlled error for three control targets.

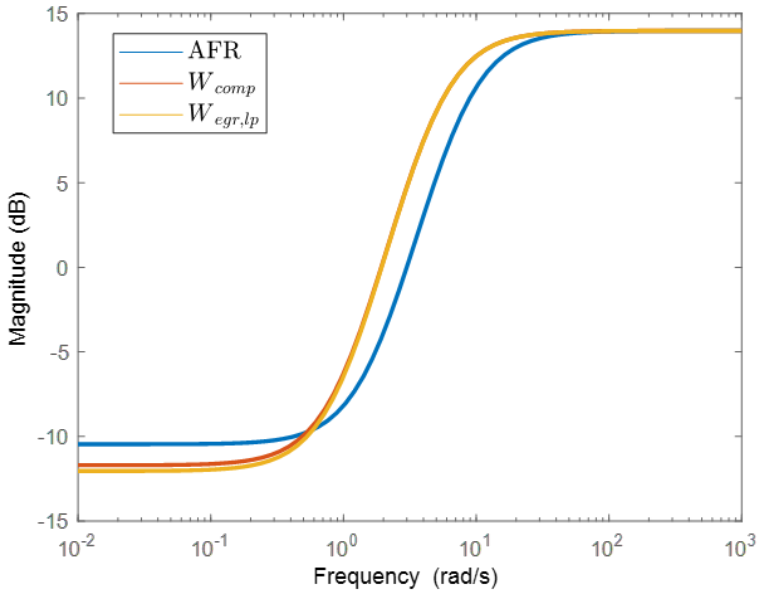

Figure 4.11. : Bode plot of error weight performance inverse.

4.5.2 Actuator Effect Weighting

The input performance weights W_u are used to account for the physical limits of the actuators (per Table 4.7).

Table 4.7. : Actuator characteristics

Actuator	Physical Quantity	Response Time
Valves	Flow Rate	30 ms
Injector	Fuel Flow Rate	30 ms
Electrical Waste-gate	Exhaust Flow	93 ms

The exogenous output z_u is defined as:

$$z_u = W_u u \tag{4.35}$$

Similar to W_p, ${W_u}^{-1}$ is the upper bound of the actuator (command) input. Due to the physical limitations, the actuators cannot respond infinitely fast. Therefore, ${W_u}^{-1}$ is formulated as a low-pass filter (thus W_u is a high-pass filter) to penalize the control action at high frequencies.

W_u is modeled as a first-order high-pass filter in the following format:

$$W_u = \frac{\tau s + 1}{\frac{\tau s}{100} + 1} \tag{4.36}$$

where τ is the actuator response time.

Fig 4.12 shows the bode plot of ${W_u}^{-1}$ for different actuators. As shown, once the frequency exceeds the cut-off frequency ($\frac{1}{\tau}$) of the actuators, the actuators' control actions are penalized.

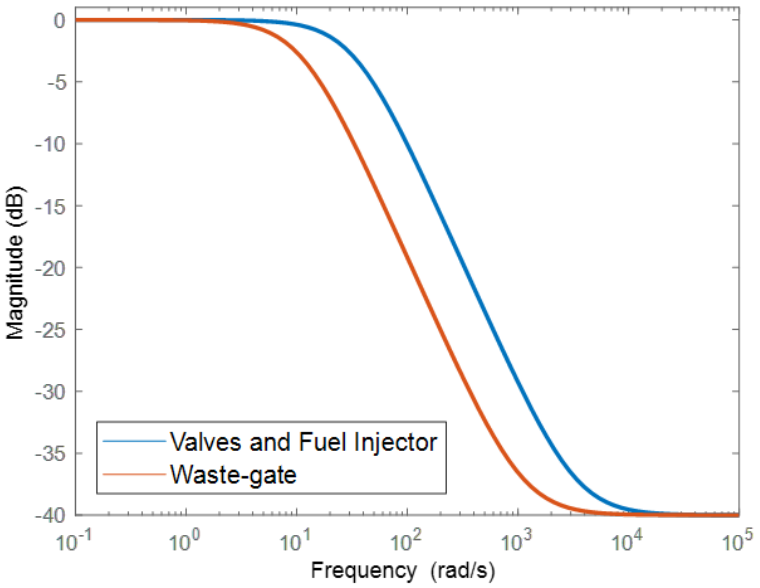

Figure 4.12. : Bode plot of input weight performance inverse.

4.5.3 Disturbance Shaping Function

A low-pass filter W_d is added (per Fig. 4.9 and Fig. 4.10) to specify the frequency of the engine speed change. In this application, the cutoff frequency was selected as 5 rad/s to focus on rejecting the disturbance input at low frequencies.

$$W_d = \frac{1}{\frac{s}{5} + 1} \tag{4.37}$$

4.5.4 Sensor Characteristics

Three sensor characteristics, delay, precision error and bias error, are considered in this framework.

Sensor Delay

The sensor delay is modeled as the first order approximation based on the response time listed in Table 4.1:

$$\delta\bar{y}_{0,delay} = \frac{\delta\bar{y}_0}{\tau s + 1} \tag{4.38}$$

where τ is the response time.

For the EGR DP sensor, the response time varies with the engine speed (per Table 4.1). In this application, the response time was assumed to be 15ms for the speeds of (2400 − 3500 RPM).

Sensor Error

Two different sensor error types, precision error n_p and bias error n_b, are modeled in this framework, as following:

$$y_m = y + n_b + n_p \tag{4.39}$$

Fig 4.13 shows the block diagram of sensor error modeling. The bias error is modeled as a perturbation. w_s is the diagonal weight function matrix of uncertainty which is defined as identity matrix I, and Δ_s is the scaled diagonal uncertainty block, i.e. $\Delta_s = diag\{\delta_{s1}, \delta_{s2}, ..., \delta_{s5}\}$ and $\delta_{si} \in [-1, 1]$. The percent bias error δ_{si} is given as accuracy in Table 4.1 .

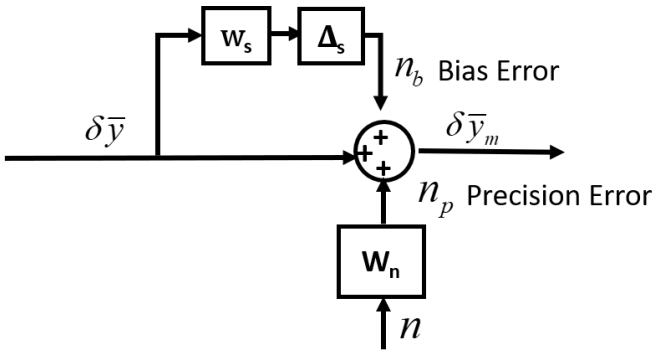

Figure 4.13. : Sensor error modeling.

The sensor precision error is estimated based on the Fast Fourier Transform (FFT) analysis of real-time UEGO sensor measurements. Fig 4.14 shows the FFT analysis of ΔAFR (Reference ΔAFR) which is the difference between every point and the average of the measurements at stoichiometric conditions.

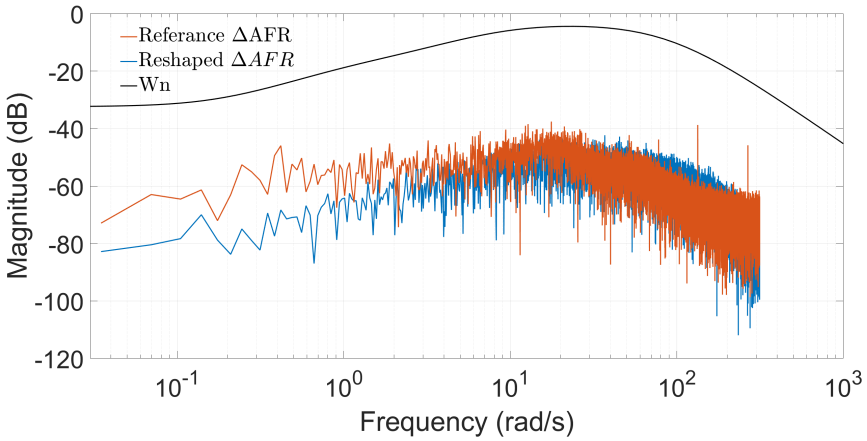

Figure 4.14. : FFT analysis of AFR measurements.

A noise shaping function W_n is used to approximate the frequency component of the precision error. Assuming the input of W_n is Gaussian noise with 0.1 variance, the precision error can be expressed as:

$$n_p = W_n n \tag{4.40}$$

and

$$W_n = 0.024 \frac{\left(\frac{1}{0.18}s+1\right)\left(\frac{1}{2.1}s+1\right)}{\left(\frac{1}{1.2}s+1\right)\left(\frac{1}{9}s+1\right)\left(\frac{1}{80}s+1\right)\left(\frac{1}{100}s+1\right)} \tag{4.41}$$

The reshaped AFR precision error is shown in Fig. 4.14 (Reshaped ΔAFR), which has similar frequency components as the actual measurement.

The noise shaping function of flow sensors is formulated as a second-order high pass filter:

$$W_n = \left(\frac{s + 37.7 \times \sqrt{0.001}}{\frac{s}{\sqrt{0.02}} + 37.7}\right)^2 \tag{4.42}$$

which indicates that the low-frequency error is 0.1%, the high frequency error is 2%, and the frequency where the error reaches 2% is 6Hz (37.7rad/s).

4.5.5 Model Uncertainty

Shaped model uncertainty is used to approximate the unmodeled dynamics and linearization errors. The diagonal multiplicative output uncertainty is selected in this application since it can be easily estimated by comparing the model outputs and the reference outputs.

Fig. 5.40 shows the multiplicative output uncertainty block of the nominal output $\delta\bar{y}_0$ (per equation (4.2)).

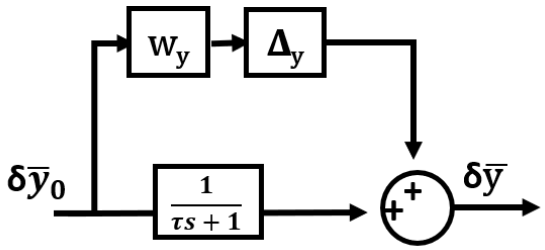

Figure 4.15. : Multiplicative output uncertainty for outputs.

The actual output with first-order sensor dynamics can be expressed as follows:

$$\delta\bar{y} = \frac{\delta\bar{y}_0}{\tau s + 1} + w_y \Delta_y \delta\bar{y}_0 \tag{4.43}$$

where τ is the sensor response time, w_y is the diagonal weight function matrix of uncertainty in the frequency domain, and Δ_y is the scaled diagonal uncertainty block, i.e. $\Delta_y = diag\{\delta_{y1}, \delta_{y2}, ..., \delta_{y5}\}$ and $\delta_{yi} \in [-1, 1]$. If the output is used as the control target, the delay block should be removed.

The diagonal element in w_y is defined as:

$$w_{y,\mathrm{i}} = w_y(\mathrm{i},\mathrm{i}) = \frac{\frac{s}{\omega_{yB,\mathrm{i}}} + \mathrm{e}_{y,\mathrm{i}}}{\frac{s}{2\mathrm{e}_{y,\mathrm{i}}\omega_{yB,\mathrm{i}}} + 1} \tag{4.44}$$

where $\mathrm{e}_{y,\mathrm{i}}$ is the relative error at steady state of output y_i, $\omega_{yB,\mathrm{i}}$ is the approximate frequency where the relative uncertainty reaches $2\mathrm{e}_{y,\mathrm{i}}$.

The steady-state relative error value $e_{y,i}$ is estimated by the following multiplicative output uncertainty:

$$e_{y,i} = \max\left(\frac{\delta y_{\ GT,i} - \delta y_{0,i}}{\delta y_{\ 0,i}}\right) = \max\left(\frac{y_{\ GT,i} - y_{0,i}}{y_{\ 0,i} - y_{e,i}}\right) \tag{4.45}$$

where $y_{0,i}$ is the ith nominal model output, $y_{\ GT,i}$ is the ith GT-Power cycle averaged output and $y_{e,i}$ is the equilibrium point value of the ith output. δ donates the difference between the value and its equilibrium point.

One problem with this uncertainty estimation is that when the nominal state y_0 is close to the equilibrium point y_e, the denominator becomes very small, which results in a large relative steady-state error. The numerical issue brought by the small denominator results in an improper estimation of the perturbation for these points. Therefore, the peak $y_{0,i}$ at the points that are close to the equilibrium points should be neglected. In this application, the maximum steady-state relative value which occurs outside the speed range 3200±300RPM is used as the error value $e_{y,i}$.

Fig. 4.16 shows the relative steady-state error of the compressor mass flow rate (W_{comp}) modeling based on equation (4.45). The error value was estimated by 0.19, which occurred at 2900RPM (1250s). The relative steady state error $e_{y,i}$ and frequency $\omega_{yB,i}$ for different output y_i are listed in Table 4.8.

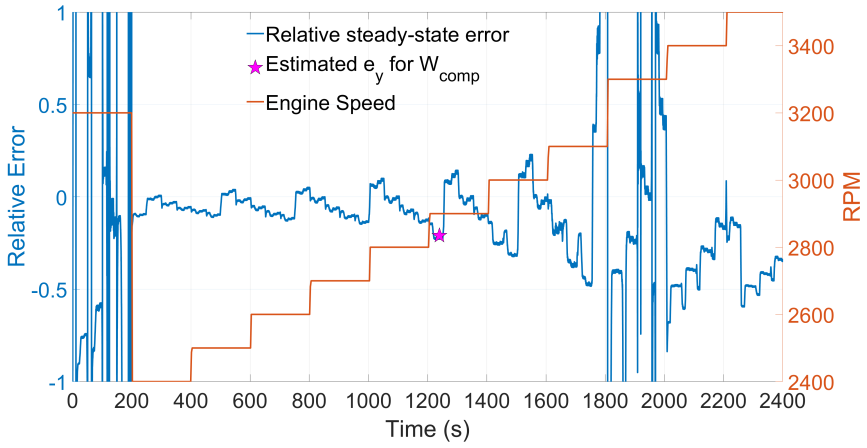

Figure 4.16. : Relative steady-state error of the compressor mass flow rate W_{comp} modeling at different engine speeds.

Table 4.8. : Model Output Uncertainty

Output	Symbol	$e_{y,i}$	$\omega_{yB,i}$ (rad/s)
y_1	W_{inlet}	0.23	20
y_2	W_{comp}	0.19	20
y_3	W_{egrl}	0.18	20
y_4	W_{charge}	0.15	20
y_5	AFR_{cyl}	0.2	20

The Pade approximation is used to model the transport delay between the cylinder AFR (AFR_{cyl}) and the exhaust AFR (AFR_{exh}):

$$AFR_{exh}(s) = \frac{-\frac{\tau_d}{2}s + 1}{\frac{\tau_d}{2}s + 1} AFR_{cyl}(s) \tag{4.46}$$

and the time constant τ_d can be estimated by[32]:

$$\tau_d = \frac{180 + 180 + 180}{360 N_e} s \tag{4.47}$$

where N_e is the engine speed. τ_d used in this application was approximated by 30ms (N_e = 3200RPM).

4.6 Sensor Selection Results

4.6.1 Operating Conditions

Desired Engine Operation Points

In order to generate reasonable compressor and LP EGR flow rate targets, 240 steady-state operating conditions were tested in the high fidelity engine GT-Power model. The operating conditions included twelve engine speeds varying from 2400 to 3500 RPM at every 100 RPM, four throttle valve angles (40°, 60°, 75°, fully-open 90°), and five LP EGR valve angles (fully-closed 0°, 5°, 10°, 15°, 20°). The AFR was maintained at the stoichiometric value.

The desired torque curve is shown in Fig. 4.17a. For each desired torque point, the corresponding compressor mass flow rate and LP EGR flow rate were selected as flow tracking targets (per Fig. 4.17b and 4.17c). By controlling the compressor and LP EGR mass flow rates, the inlet air flow rate, EGR ratio and the torque can be controlled.

Sensor Working Conditions

Three sensor working conditions were considered for testing the control performance:

Condition 1: All four flow sensors worked at their maximum bias error which pushed the feedforward command towards leaner combustion, i.e. -4% for MAFa, -2% for MAFh, 7% for EGR DP, -5.1% for ChgVS. The UEGO sensor was set as 0.1 bias error for measured AFR which made the feedback fueling command towards richer combustion. The precision errors for all flow sensors were ignored. For the UEGO sensor, the precision error was the shaped Gaussian noise by equation (4.41). All sensor delays were considered.

Condition 2: All four flow sensors worked at their maximum bias error which pushed the feedforward command towards richer combustion, i.e. 4% for MAFa, 2% for MAFh, -7% for EGR DP, 5.1% for ChgVS. The UEGO sensor was set as -0.1 bias error for measured AFR which made the feedback fueling command towards leaner combustion. The precision errors for all flow sensors were ignored. For the sensor, the precision error was the shaped Gaussian noise by equation (4.41). All sensor delays were considered.

Ideal condition: All four flow sensors as well as the UEGO sensor, perfectly measured the flows and AFR. No bias error or precision error was added. All sensor delays were considered.

Engine Operating Scenarios

Two operating scenarios (per Fig. 4.18) were performed for testing the control performance: (1) operating scenario 1 was the step engine speed change within 2400 to 3500 RPM at every 100 RPM for 82s; (2) operating scenario 2 was the ramp engine speed change within 2400 to 3500 RPM for 42s.

4.6.2 Computation Results

The synthesis of the H_∞ controller and the calculation of the structured singular value μ were based on the DK-iteration method. The MATLAB function dksyn was used for controller synthesis. Table 4.9 shows the sensor selection results for both AFR and air/EGR flow control loops.

For the AFR control loop, only Case 2 had $\mu < 1$ and the worst-case gain lower than 1. In Case 3, μ was very close to 1. Case 1 had the highest μ as well as the highest worst-case gain. These results indicated that Case 2, the combination of ChgVS sensor, EGR DP sensor and UEGO sensor, was the most robust sensor set for AFR control. Considering the μ values in both Case 2 and Case 3 were close to 1, their robustness of AFR control performance would not have significant differences. Case 1, the combination of MAFa sensor and UEGO sensor, was the least robust sensor set. Compared with Cases 2 and 3, the worst-case peak of Case 1 occurred at higher frequencies, indicating that larger oscillations would occur during transient operations when Case 1 was used.

For the flow control loop, Case 3 was the most robust sensor set and it was the only case with μ lower than 1. Case 3 had much lower μ compared with the other two cases. This indicated that Case 3 could still achieve robust performance even with a stricter objective requirement whereas the other two cases cannot. In Case 2, μ and the worst-case gain were very close to 1, which indicated that the flow control objective could be achieved if the requirements were slightly relaxed or the sensor set performance was slightly improved. Case 1 was the least robust sensor set for flow control targets. The worst-case gains for both Case 1 and Case 2 occurred at relatively low frequencies, which indicated the flow control difficulties of the uncertain system near steady states.

4.6.3 Testing Results

The synthesized robust AFR, EGR flow and air flow controllers were applied to a high fidelity SI engine GT-Power model. A co-simulation harness block was used to connect the controllers in SIMULINK and the GT-Power model. The desired compressor and LP EGR

Table 4.9. : Sensor selection results for robust-control based framework

Case	Sensor(s)	Feedforward controller	AFR Control Loop				Flow Control Loop			
			μ	Worst-case Performance			μ	Worst-case Performance		
				Lower Bound	Upper Bound	Critical Frequency (rad/s)		Lower Bound	Upper Bound	Critical Frequency (rad/s)
1	MAFa, λ	$\frac{W_{inlet}}{14.7}$	1.0193	1.0525	1.0547	10	1.0468	1.0717	1.0743	0.0588
2	ChgVS, EGR DP, λ	$\frac{W_{charge}-W_{egrl}}{14.7}$	0.9927	0.9876	0.9898	2.2855	1.0008	1.0003	1.0025	0.2572
3	MAFh(50ms), EGR DP, λ	$\frac{W_{comp}-W_{egrl}}{14.7}$	1.0054	1.0081	1.0102	1.4251	0.9114	0.8825	0.8844	1.6318

mass flow rates at each speed (per Fig. 4.17) were used as the flow control targets. The desired AFR was set as 14.7.

The cycle averaged cylinder AFR, cooled compressor mass flow rate and LP EGR flow rate from GT-Power model were used as the truth-references. Four candidate flow sensors and the UEGO sensor were placed in the GT-Power model. The cycle averaged outputs were corrupted by the first-order dynamics, bias and precision errors before the controllers accept the signals. Actuator delays were implemented directly in the GT-Power model as first-order responses.

Five tests with different sensor working conditions and operating scenarios were performed (per Table 4.10) and the results are listed in Table 4.11. In all five tests, Case 1 (MAFa sensor + UEGO sensor) failed the LP EGR tracking requirement (per Table 4.11), which was consistent with $\mu > 1$ in Table 4.9. Though in Case 2 (ChgVS sensor + EGR DP sensor + UEGO sensor) μ was slightly greater than 1 (per Table 4.9), it could satisfy the compressor and LP EGR flow tracking requirements in all five tests (per Table 4.11). For Case 3 (MAFh sensor + MAF sensor + UEGO sensor), the compressor and LP EGR control errors were much lower than the requirements, which was consistent with $\mu < 1$ (per Table 4.11). Per Table 4.11, Case 3 had smaller compressor and LP EGR flow control errors than Case 2 in all tests, which was consistent with the fact that μ in Case 3 was lower than μ in Case 2 per Table 4.9.

Table 4.10. : Operating scenarios and sensor working conditions

Test case	Operating Scenario	Sensor Working Condition
1	Ramp	Ideal Condition
2	Step	Condition 1
3	Step	Condition 2
4	Ramp	Condition 1
5	Ramp	Condition 2

Table 4.11. : Flow Control Loop Tracking Errors

Test	Maximum Error of W_{comp} (g/s) Requriement: <11.2g/s			Maximum Error of W_{egrl} (g/s) Requriement: <1g/s			Maximum Error of Torque (Nm)			Maximum Error of EGR Ratio		
	Case 1	Case 2	Case 3	Case 1	Case 2	Case 3	Case 1	Case 2	Case 3	Case 1	Case 2	Case 3
Test 1	5.5 (6.6%)	5.3 (6.4%)	4 (6.8%)	1.50	0.62 (8.1%)	0.50 (7.0%)	32 (8.6%)	28 (7.5%)	22 (5.9%)	2.0%	1.04%	0.84%
Test 2	5.1(6.1%)	5.7(6.9%)	3.8 (4.5%)	1.36 (19.1%)	0.55 (7.7%)	0.55 (7.7%)	33 (8.8%)	36 (9.5%)	25 (6.7%)	1.8%	1.1%	0.9%
Test 3	6.1 (4.3%)	7 (4.9%)	4.4 (3.1%)	1.53 (21.5%)	0.52 (17.3%)	0.40 (13.3%)	30 (6.8%)	32 (7.2%)	24 (5.5%)	1.8%	0.55%	0.40%
Test 4	7.0 (8.4%)	7.4 (8.9%)	5.2 (6.3%)	1.52	0.80 (11.3%)	0.77 (10.8%)	46 (12.4%)	46 (12.4%)	34 (8.2%)	2.03%	1.36%	1.18%
Test 5	5.8 (4.0%)	6.6 (4.6%)	4.2 (2.9%)	1.68 (23.6%)	0.79 (27.5%)	0.62 (21.6%)	27 (6.1%)	29 (6.6%)	23 (5.2%)	1.99%	1.04%	0.84%

Test 1

Fig. 4.19 shows the ramp test for three sensor sets. In this test, all sensors worked at their ideal conditions without bias or precision errors. The sensor delay was considered in this test. Case 2 had the best AFR control performance while Case 1 was the worst one. For all three sensor sets, AFR was controlled to remain within 14.7±0.1 when the engine speed changed within 2400 to 3500 RPM rapidly. The objective requirement of AFR control loop was satisfied for all three sensor cases.

Fig. 4.20 shows the compressor mass flow rate tracking performance. At 20s when the transient engine speed change occurred, Case 3 had the smallest tracking error among the three sensor sets. At higher engine speeds, Case 3 also had better tracking performance than Case 1 and 2. The maximum tracking errors of Case 1, 2, 3 were 5.5kg/s, 5.3g/s and 4.0g/s, respectively. The corresponding percent errors were 6.6%, 6.4% and 4.8%.

Fig. 4.21 shows the LP EGR mass flow rate tracking performance. The maximum tracking error in Case 1 reached 1.5g/s at 22s. Case 3 had the best LP EGR flow tracking performance. Case 2 was slightly worse than Case 3. In Case 2, the controlled EGR flow had slower responses to the transient target change. At low EGR flow rate levels, Case 2 had the worst

tracking performance. The largest LP EGR tracking errors of Case 2 and Case 3 were 0.62g/s (8.7%) and 0.50g/s (7.0%).

Fig. 4.22 and 4.23 show the inlet air flow rate and EGR ratio control performance of three sensor cases. Case 3 achieved the best control performance of these two variables. For inlet air flow, the maximum tracking errors of Case 1, 2 and 3 were 6.1g/s (7.8%), 5.1g/s (6.5%) and 3.8g/s (4.8%), respectively. Case 1 had a reverse EGR ratio drop during 10 to 20s due to the large EGR flow tracking error (per Fig. 4.21). The maximum EGR ratio tracking errors of Case 1, 2, 3 were 2.0%, 1.04% and 0.85%, respectively.

Fig. 4.24 shows the torque tracking performance. Case 3 achieved the best torque control performance with the maximum transient tracking error lower than 22Nm (5.9%). The maximum torque tracking errors of Case 1 and Case 2 were 32Nm (8.6%) and 28Nm (7.5%). A torque tracking delay was observed in all three sensor cases. The delays of Case 1, 2, and 3 were 1.6s, 1.4s and 1.2s, respectively. The error bar plot (per Fig. 4.25) shows a detailed comparison of the torque control performance. For each sensor case, the average torque error was calculated every 0.5s and the envelope was the standard deviation of the error. In this ideal test, the envelop in all three sensor cases was small. Case 3 had the lowest torque tracking error over the entire test. Case 2 had better torque control performance than Case 1 before 25s.

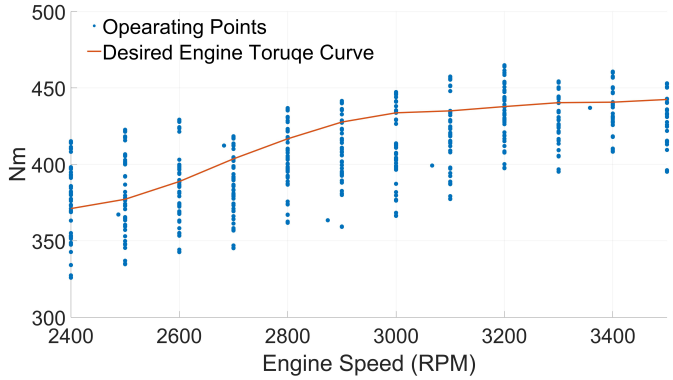

(a) Brake torque vs. engine speed.

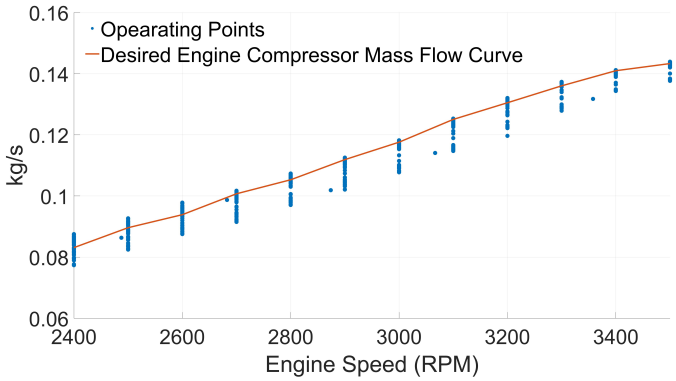

(b) Compressor mass flow rate vs. speed.

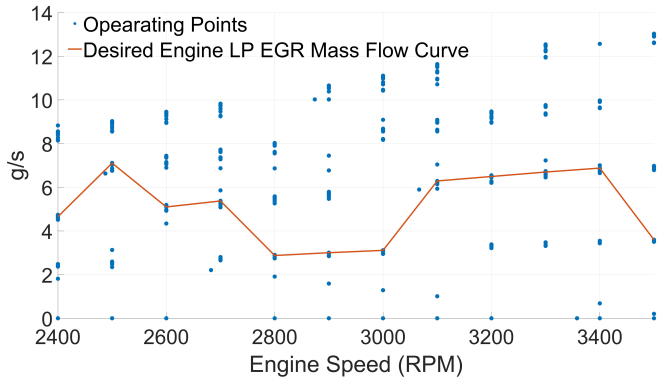

(c) LP EGR mass flow rate vs. engine speed.

Figure 4.17. : Engine Operation Conditions

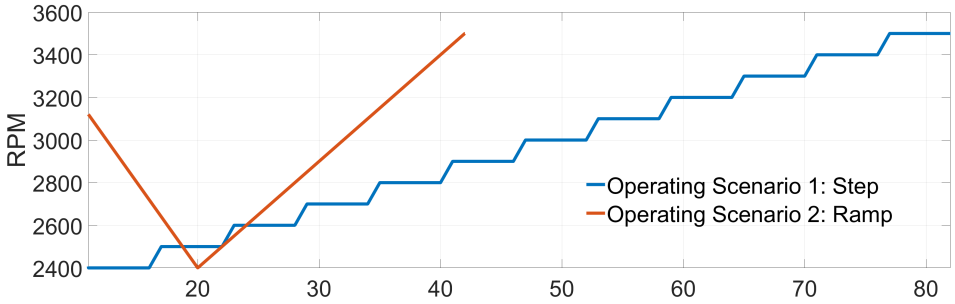

Figure 4.18. : Engine speed profiles

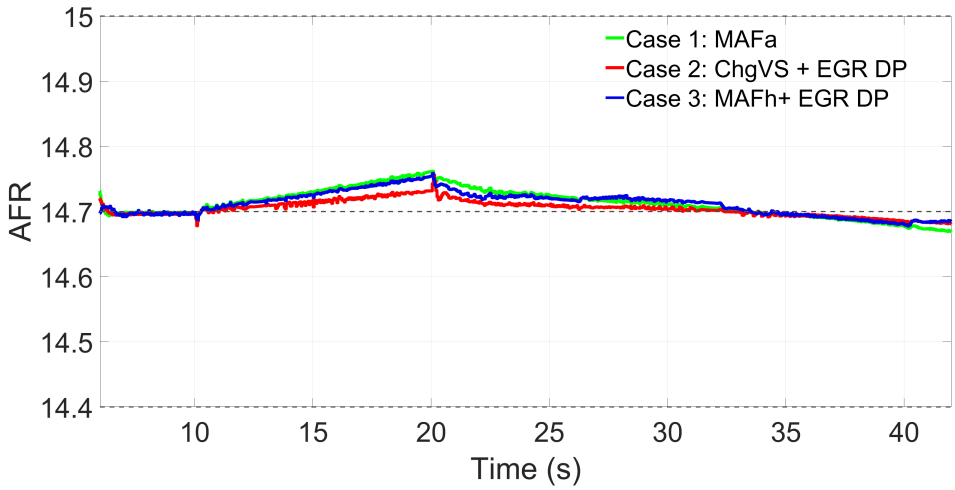

Figure 4.19. : Test 1: AFR tracking performance.

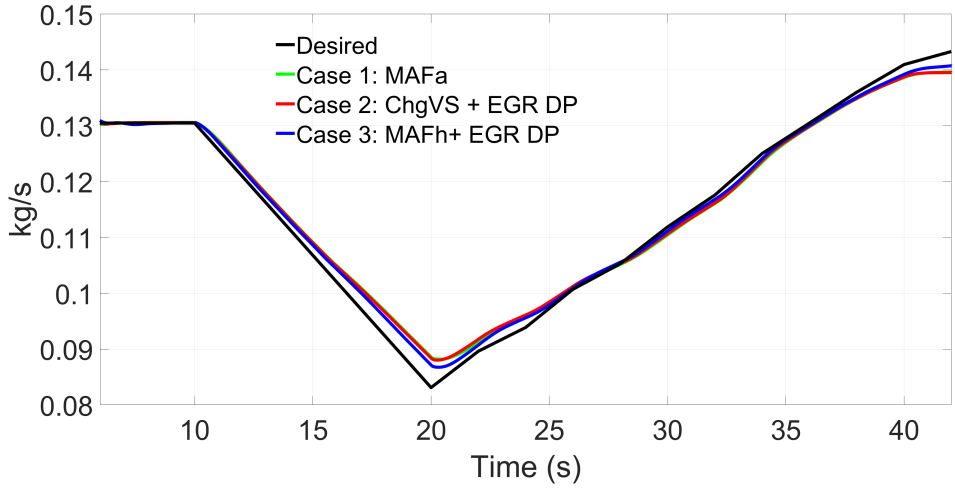

Figure 4.20. : Test 1: compressor mass flow rate tracking performance.

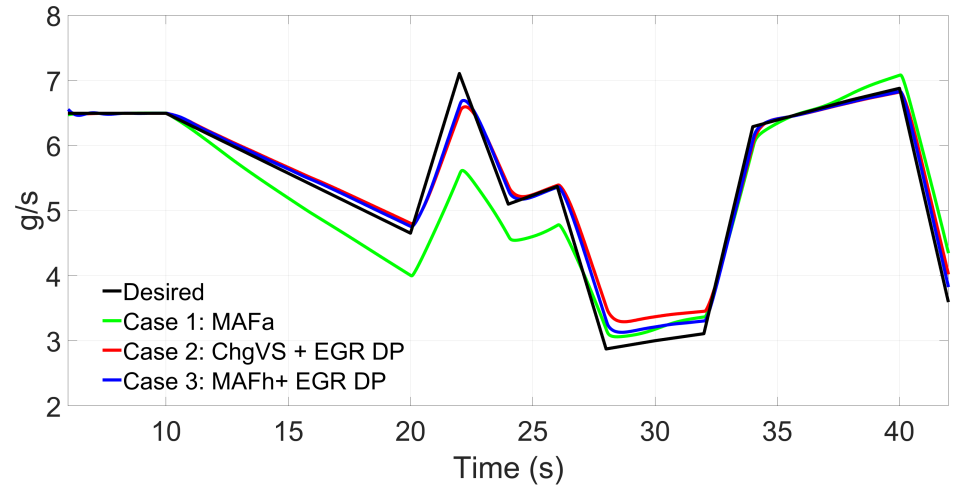

Figure 4.21. : Test 1: LP EGR mass flow rate tracking performance.

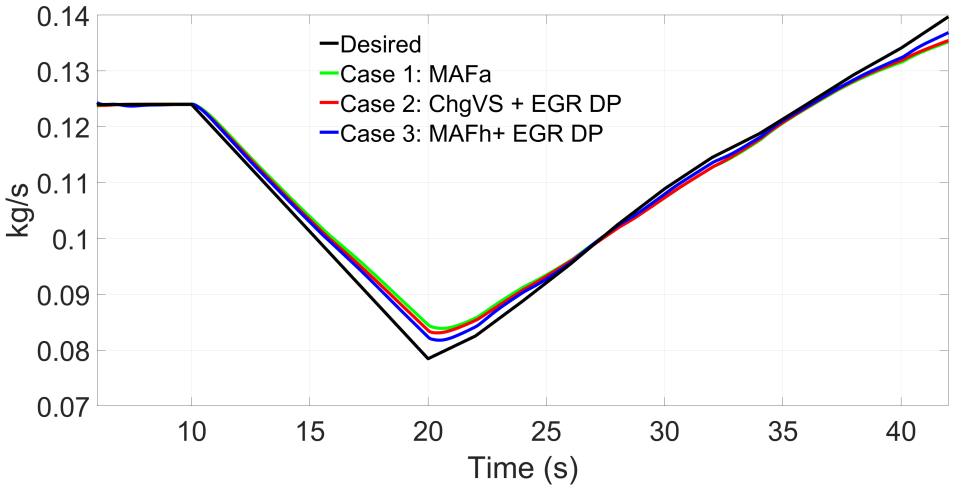

Figure 4.22. : Test 1: inlet air mass flow rate control performance.

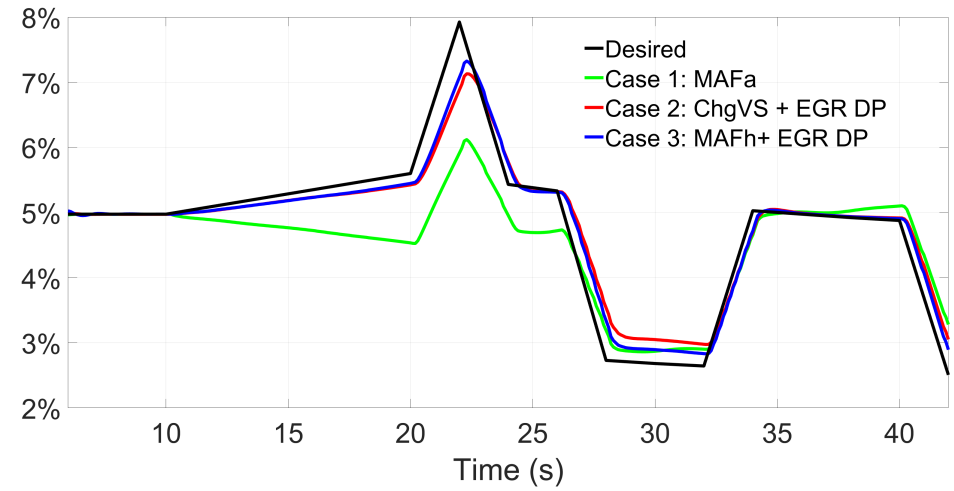

Figure 4.23. : Test 1: EGR ratio control performance.

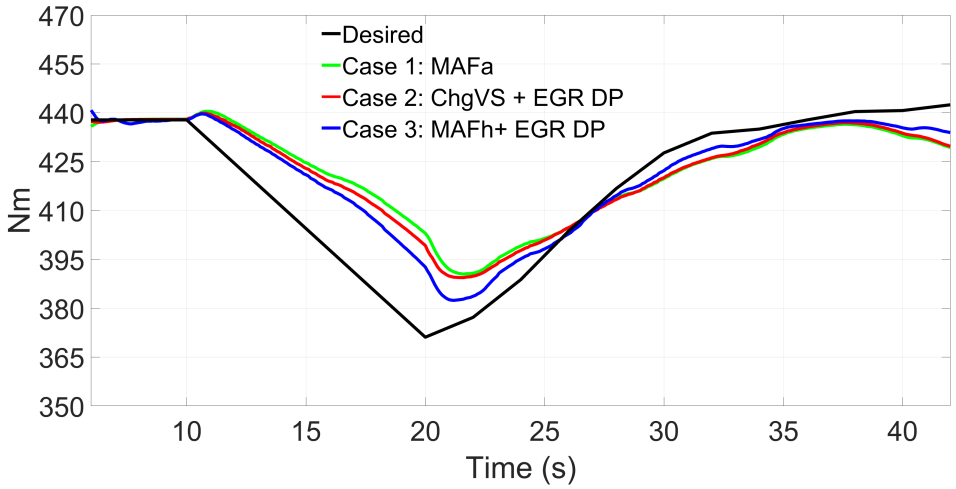

Figure 4.24. : Test 1: Torque control performance.

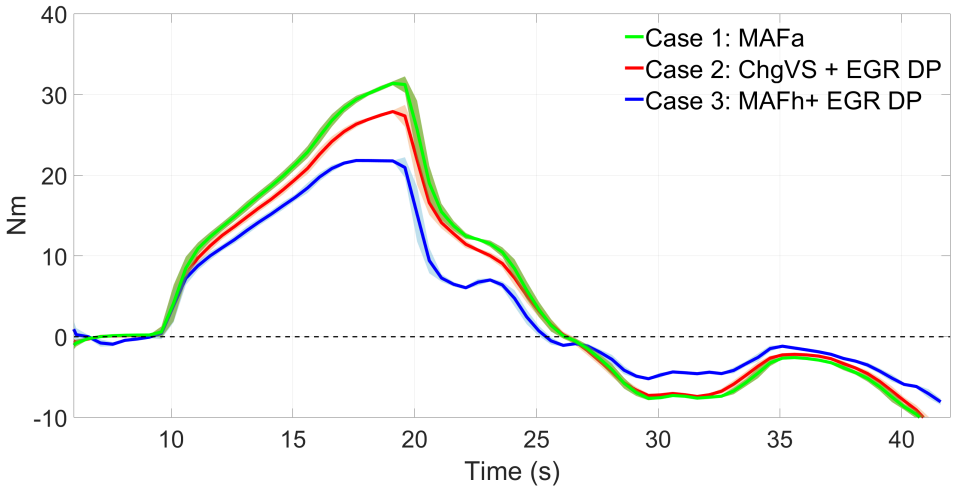

Figure 4.25. : Test 1: Error bar of torque.

Test 2

Fig. 4.26 shows the AFR tracking performance of three sensor cases. All four flow sensors worked at their maximum bias error which pushed the feedforward fueling command towards leaner combustion and the UEGO sensor was with 0.1 bias error as well as precision errors. All sensor cases had noisy AFR control performance due to the UEGO sensor noise. Large oscillations occurred during 10 to 20s when the engine was run at the lowest speed 2400RPM. For the entire test, all three sensor cases could maintain cylinder AFR within 14.7±0.3 for most of the time. Among the three sensor sets, Case 1 had the largest oscillation peak whereas Case 2 had the smallest (per Fig. 4.27). When the engine was operated at high speeds from 3300 to 3500 RPM, the AFR in Case 2 stayed closer to the stoichiometric value 14.7 than in Case 1 or Case 3, where the combustion was towards richer.

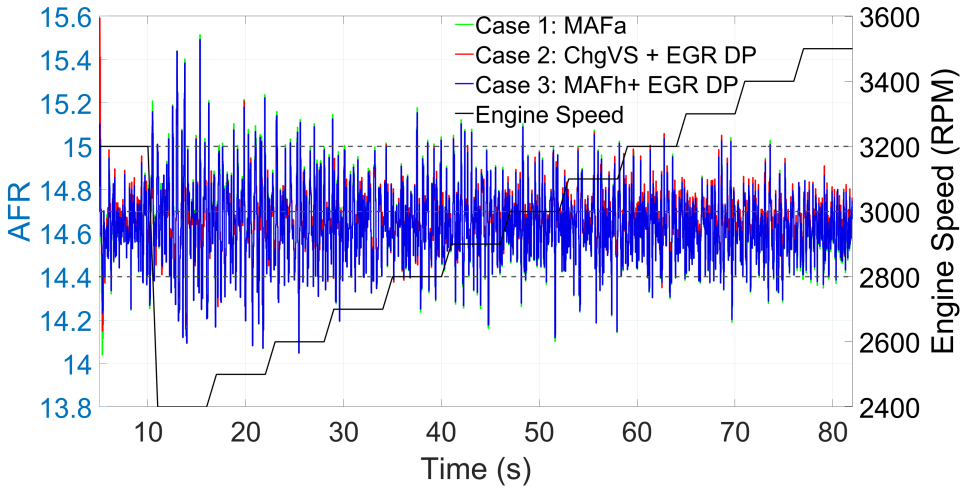

Figure 4.26. : Test 2: AFR tracking performance.

Fig. 4.29 and 4.30 show the control performance of the compressor and LP EGR flow. For the controlled compressor flow (per Fig. 4.29), Case 3 had the lowest tracking error at every step. The largest steady-state tracking errors of all three cases occurred during 11 − 16s when the engine was operated at 2400 RPM. The maximum steady-state error in Case 3 was 3.8g/s (4.5%) at 15s. The maximum absolute errors in Case 1 and Case 2 were 5.1g/s (6.1%) and 5.7g/s (6.9%). All three sensor cases met the compressor flow rate error requirement 11.2g/s. For the LP EGR flow (per Fig. 4.30), Case 3 was better than Case

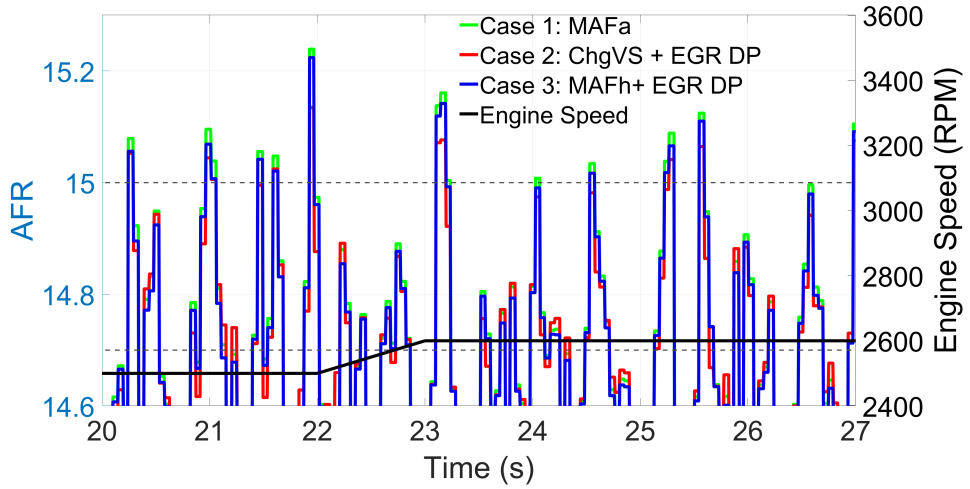

Figure 4.27. : Test 2: AFR tracking performance (20−27s).

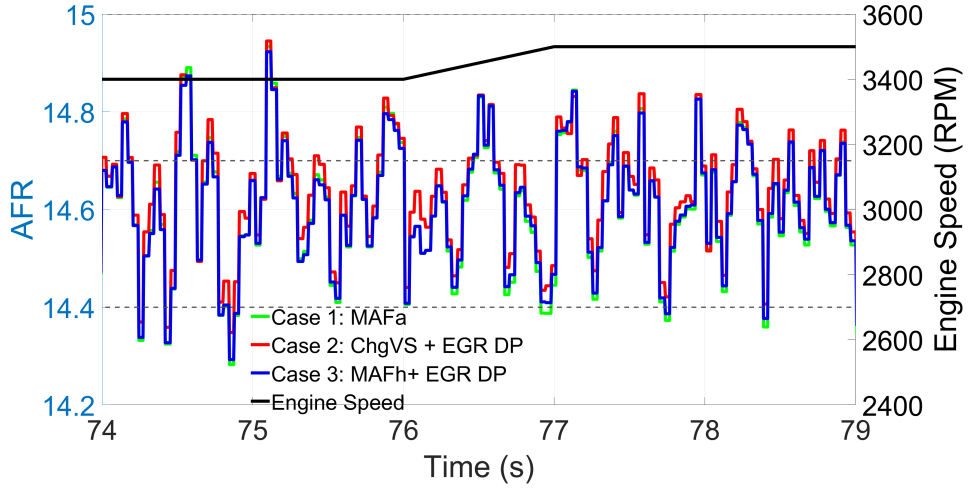

Figure 4.28. : Test 2: AFR tracking performance (74−79s).

2 at low EGR levels whereas Case 2 was slightly better than Case 3 at higher EGR levels. Case 1 was the worst sensor set for LP EGR tracking. The largest error in Case 1 was up to 1.36g/s (19.1%) at 21s. The largest errors of Case 2 and Case 3 were both 0.55g/s (7.7%) at 21s. Both Case 2 and Case 3 met the LP EGR flow error requirement 1g/s while Case 1 failed.

Fig. 4.31 and 4.32 show the inlet air flow rate and EGR ratio control performance of three sensor cases. Case 3 achieved the best control performance of these two variables at every step. The maximum inlet air flow control errors for Case 1, 2, 3 were 6.1g/s (7.4%), 6.5g/s (7.9%), and 4.4g/s (5.3%), respectively. Per Fig. 4.31, the maximum air flow errors for all

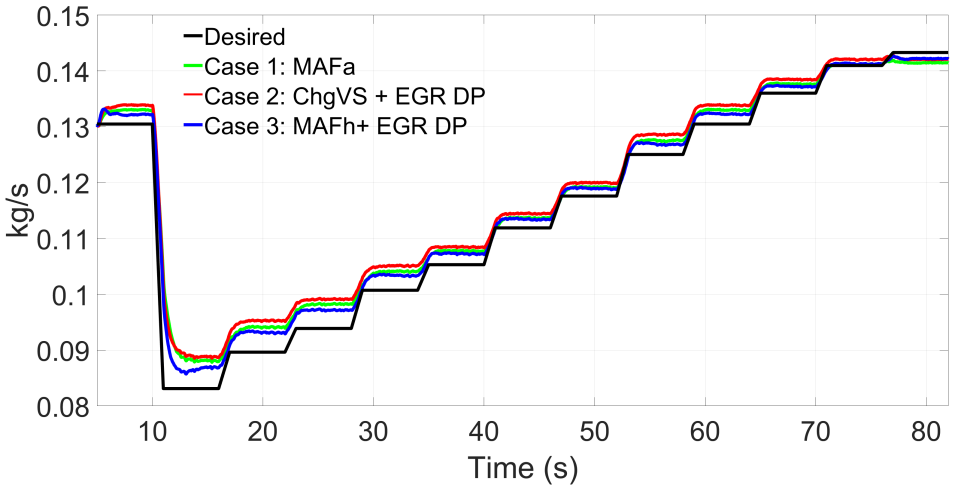

Figure 4.29. : Test 2: compressor mass flow rate tracking performance.

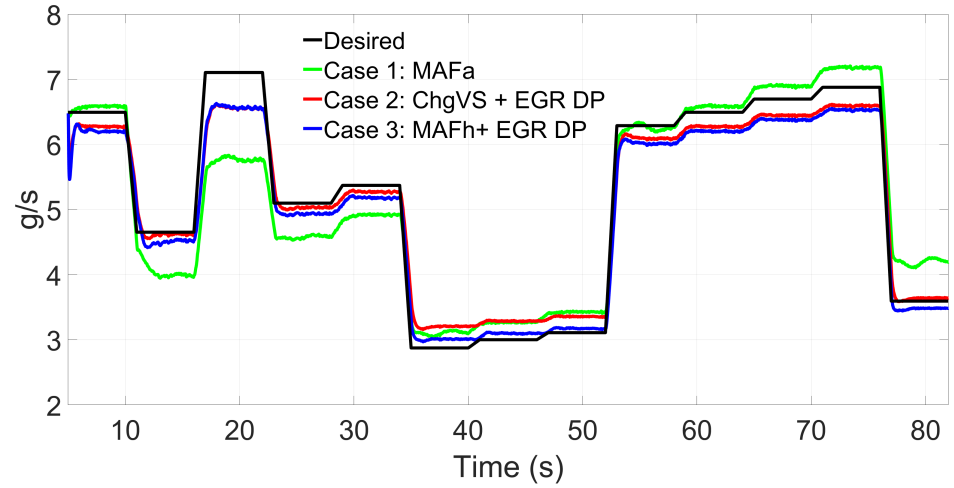

Figure 4.30. : Test Case 2: LP EGR mass flow rate tracking performance.

three cases occurred during 17 to 22s, the second step. For EGR ratio control performance (per Fig. 4.32), Case 1 cannot achieve the desired increase during 11 to 16s and 53 to 78s. The maximum EGR ratio control errors for Case 1, 2, 3 were 1.8%, 1.1% and 0.9%, at 21s.

Fig. 4.33 shows the torque tracking performance. Case 3 achieved the best torque control performance for both steady-state and transient changes. The worst steady-state torque tracking performance of all these cases occurred at 20s. The maximum error values for Case 1, 2 and 3 were 33Nm (8.8%), 36Nm (9.5%) and 25Nm (6.7%), respectively. The error bar plot (per Fig. 4.34) shows a detailed comparison of the torque control performance. For each sensor case, the average torque error was calculated every 0.5s and the envelope was

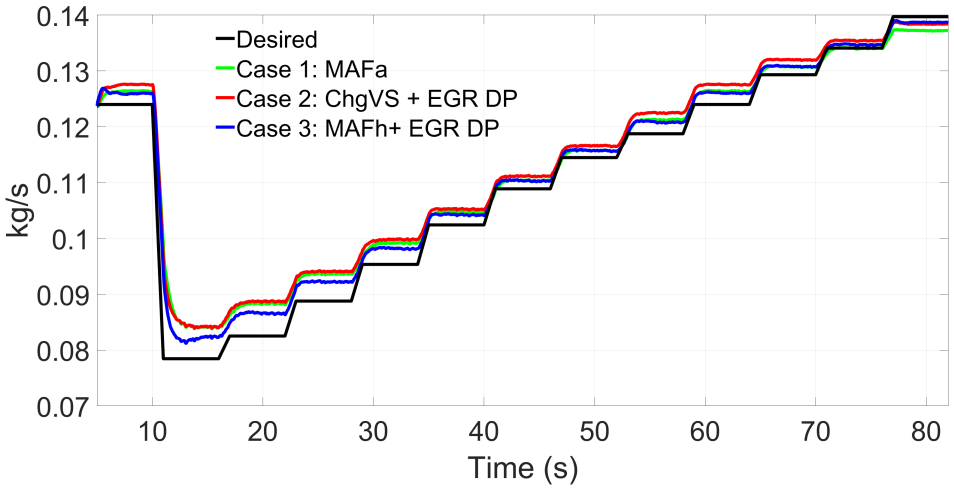

Figure 4.31. : Test 2: inlet air mass flow rate control performance.

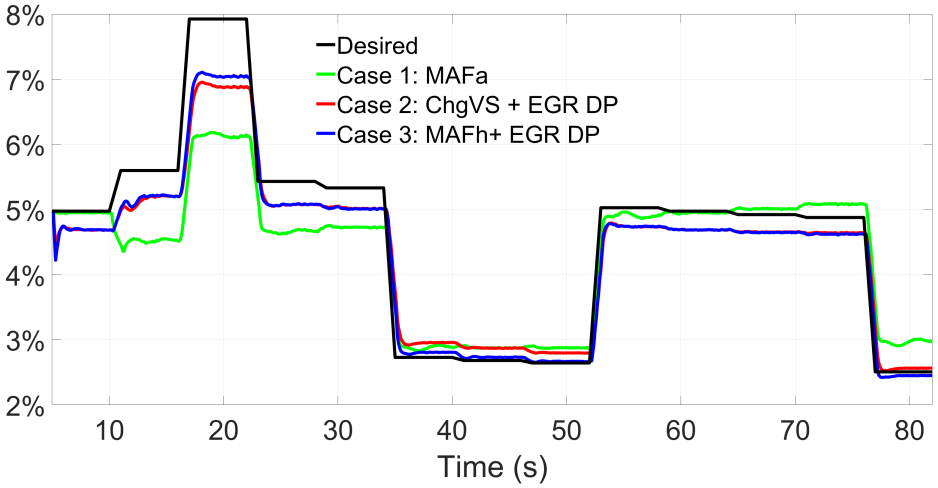

Figure 4.32. : Test 2: EGR ratio control performance.

the standard deviation of the error. When the engine was run at low speeds ($10 - 30$s), small steady-state errors with large oscillations were observed in all three sensor cases (per Fig. 4.34). During the entire test, Case 3 always had the lowest torque tracking error.

Fig. 4.35 shows the exhaust λ sensor working condition in each of the three sensor cases. The GT-Power cycle-averaged exhaust AFR is used as the truth-value. The simulated sensor measured AFR is the GT-Power output AFR corrupted with 200ms first-order delay, 0.1 absolute bias error and random precision errors.

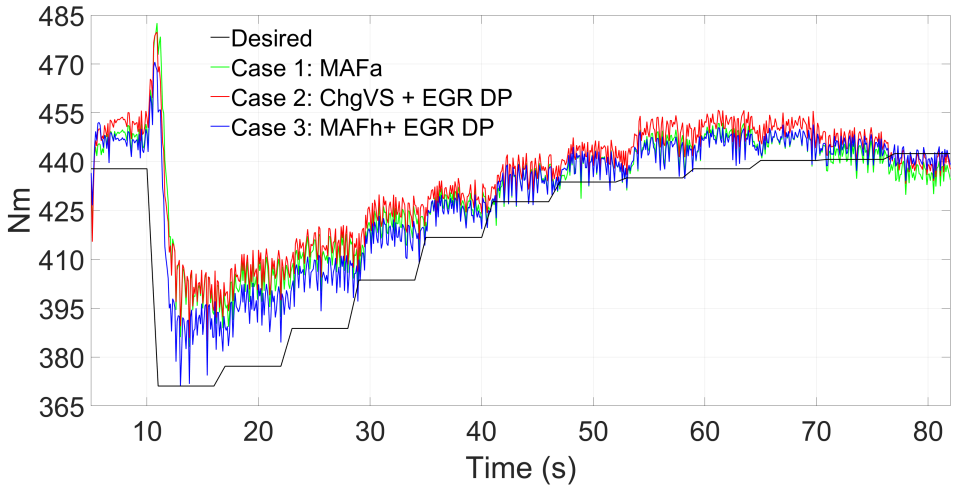

Figure 4.33. : Test 2: Torque control performance.

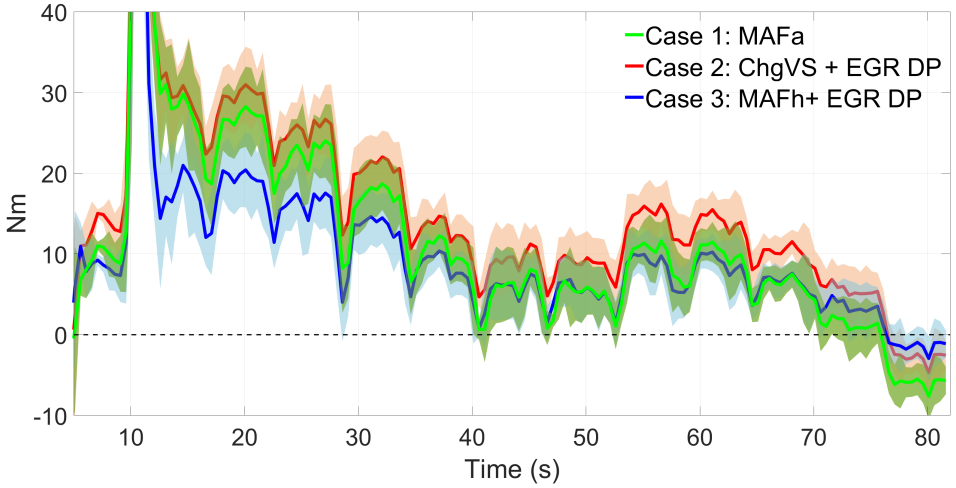

Figure 4.34. : Test 2: Error bar of torque.

Fig. 4.36a, 4.36b and 4.36c show the working conditions of flow sensors in different sensor cases. The GT-Power cycle-averaged flow rates W_{GT} are used as the true values. The simulated sensor measurement W_{sim} is calculated as following:

$$W_{sim} = \frac{W_{GT}}{1+\tau s} \times (1+n_b) \tag{4.48}$$

where τ is the sensor delay and n_b is the maximum sensor bias error in percent.

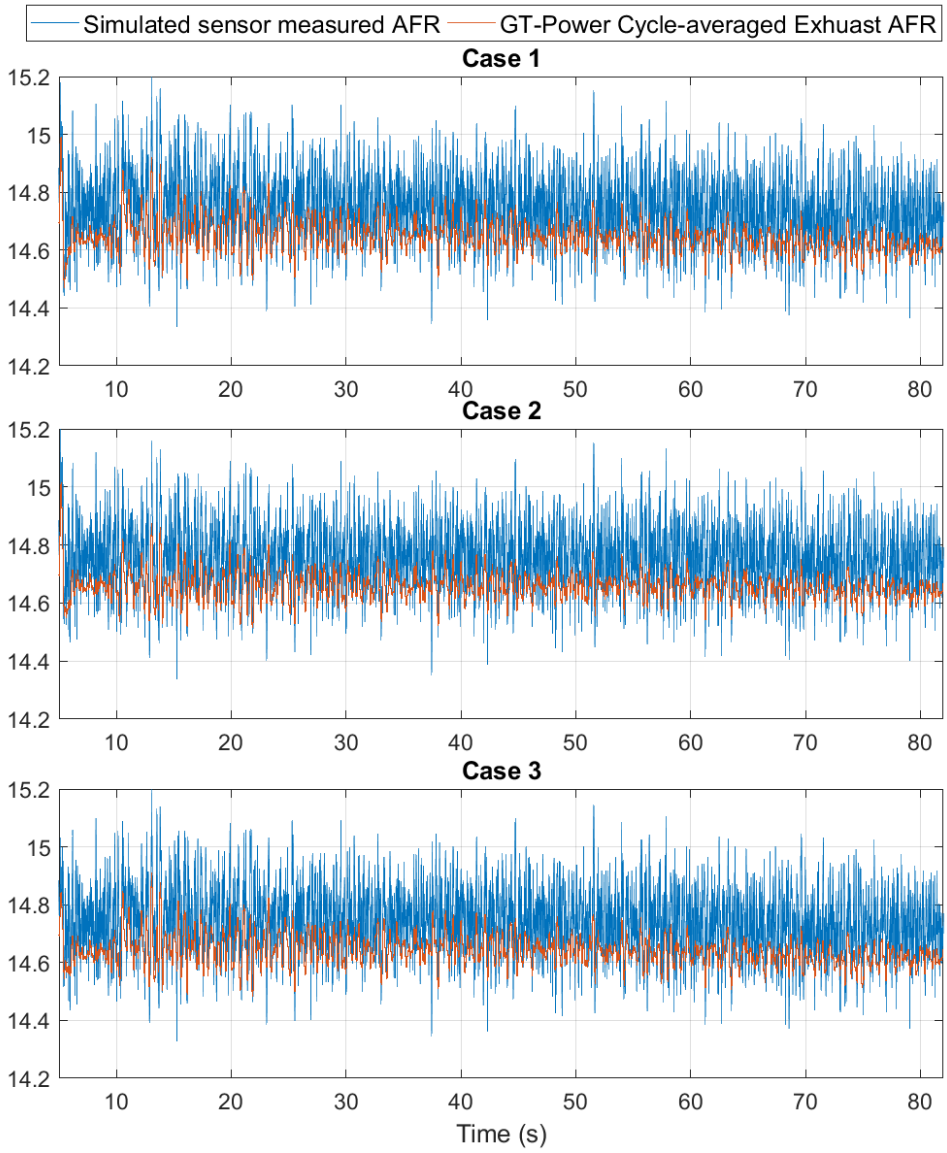

Figure 4.35. : Test 2: exhaust lambda sensor measurement.

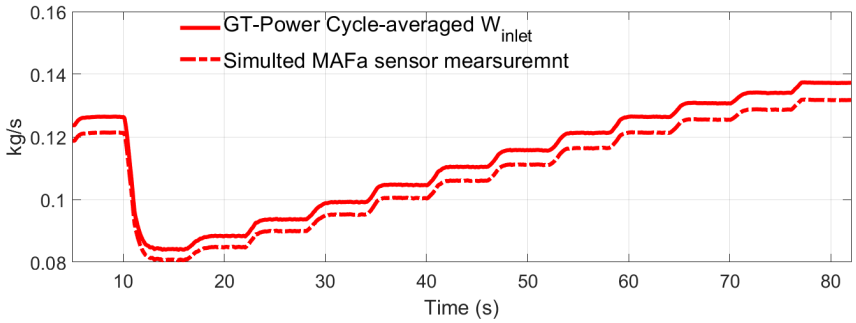

(a) Case 1: MAFa sensor's working condition.

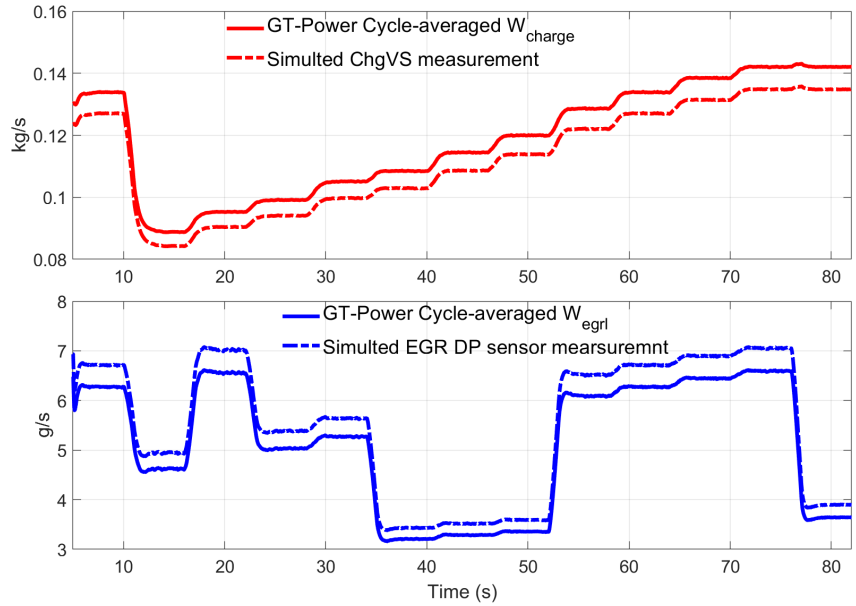

(b) Case 2: ChgVS and EGR DP sensors' working conditions.

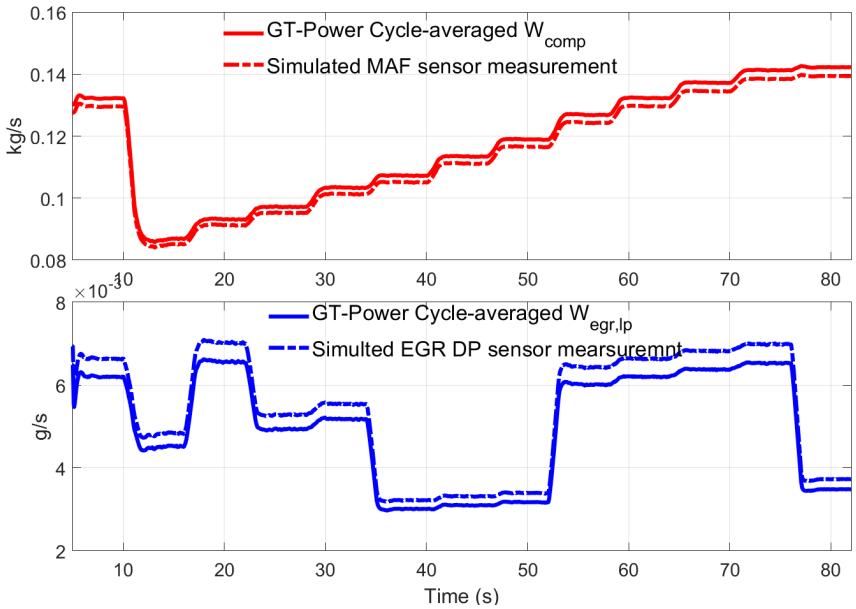

(c) Case 3: MAFh and EGR DP sensors' working conditions.

Figure 4.36. : Test 2: flow sensor working conditions.

Test 3

Fig. 4.37 shows the AFR tracking performance of three sensor cases. In this 82s step test, the sensors worked at condition 2. Similar to Test 2, large oscillations occurred during 10 to 20s when the engine was operated at the lowest speed 2400 RPM. All three sensor had more oscillations outside the required AFR control range compared with Test Case 2 (per Fig. 4.26).

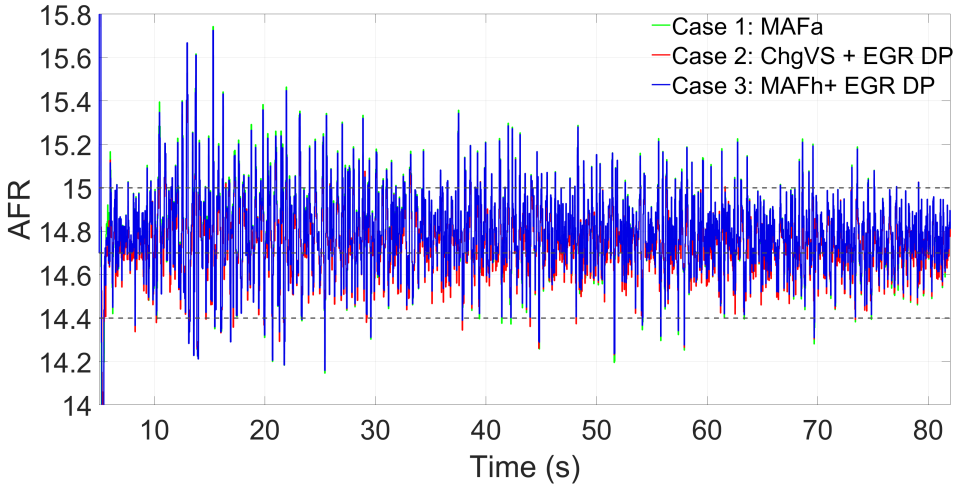

Figure 4.37. : Test 3: AFR tracking performance.

Fig. 4.38 shows the detailed AFR control performance during 20 to 27s. Case 1 had the largest oscillation peak. Fig. 4.39 shows the detailed AFR control performance during 74 to 79s. During this time, the engine was operated at high speeds from 3300 to 3500 RPM. In Case 2, AFR was closer to the stoichiometric value 14.7 than in Case 1 and 3, where the combustion was leaner.

Fig. 4.40 shows the compressor mass flow rate tracking performance. Case 3 had the lowest tracking error at every step. With increasing engine speed, the tracking errors in all three sensor cases became larger. The largest steady-state error in Case 3 was 4.4kg/s (3.1%) at 80s, and it was lower than the requirement 11.2g/s. The largest steady-state tracking errors of Case 1 and Case 2 also occurred at 80s. The maximum absolute errors in Case 1 and Case 2 were 6.1g/s (4.3%) and 7g/s (4.9%), respectively.

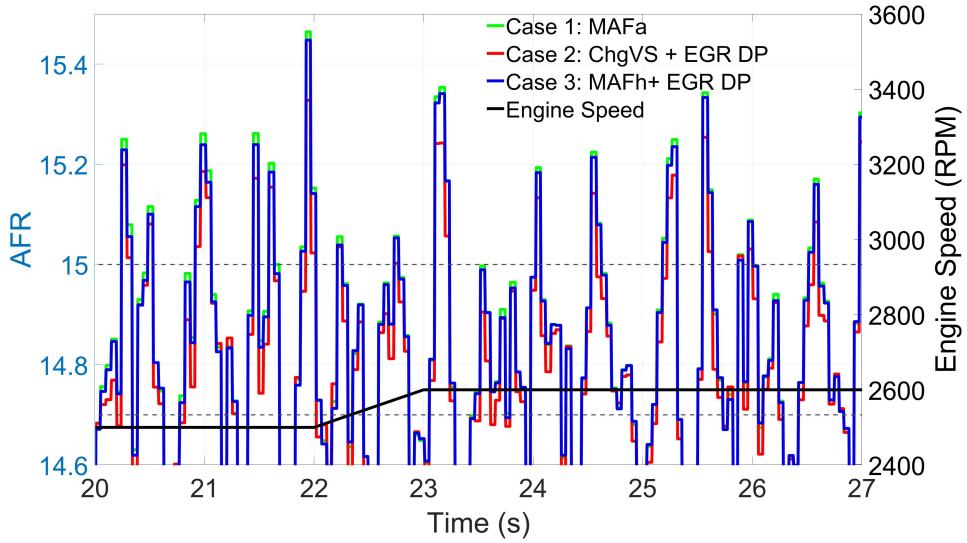

Figure 4.38. : Test 3: AFR tracking performance (20−27s).

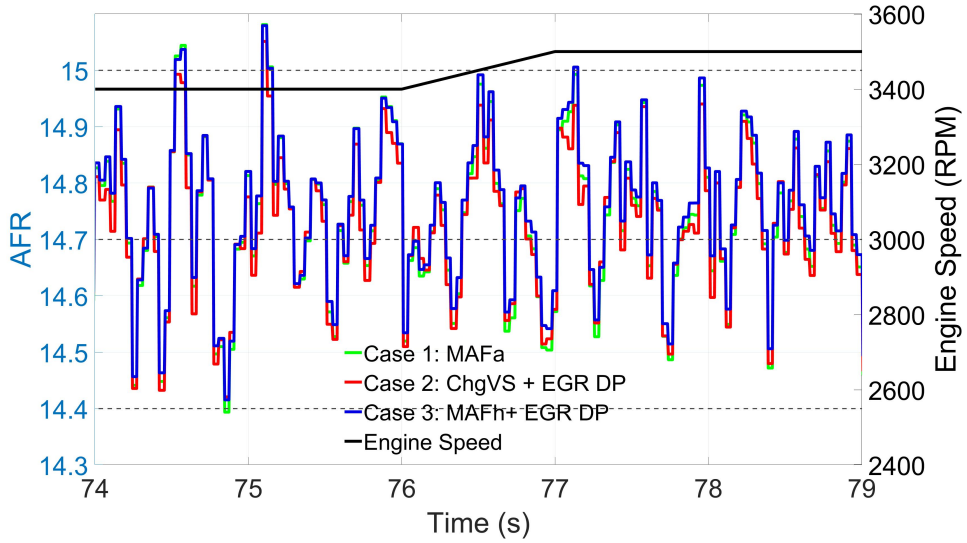

Figure 4.39. : Test 3: AFR tracking performance (74−79s).

Fig. 4.41 shows the LP EGR mass flow rate tracking performance. Case 2 and Case 3 had similar good EGR tracking performance. Case 1 was the worst sensor set for the LP EGR flow tracking. The largest error in Case 1 was 1.53g/s (21.5%) at 20s, which was greater than the requirement. The largest error was 0.52g/s (17.3%) for Case 2 and 0.40g/s (13.3%) for Case 3, both at 45s .

Fig. 4.42 and 4.43 show the inlet air flow rate and EGR ratio control performance of three sensor cases. Case 3 achieved the best control performance of these two variables at

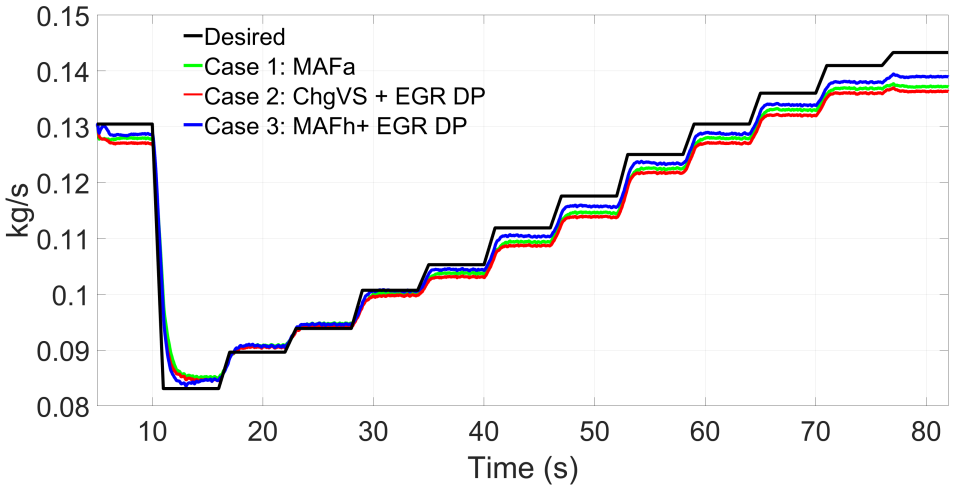

Figure 4.40. : Test 3: compressor mass flow rate tracking performance.

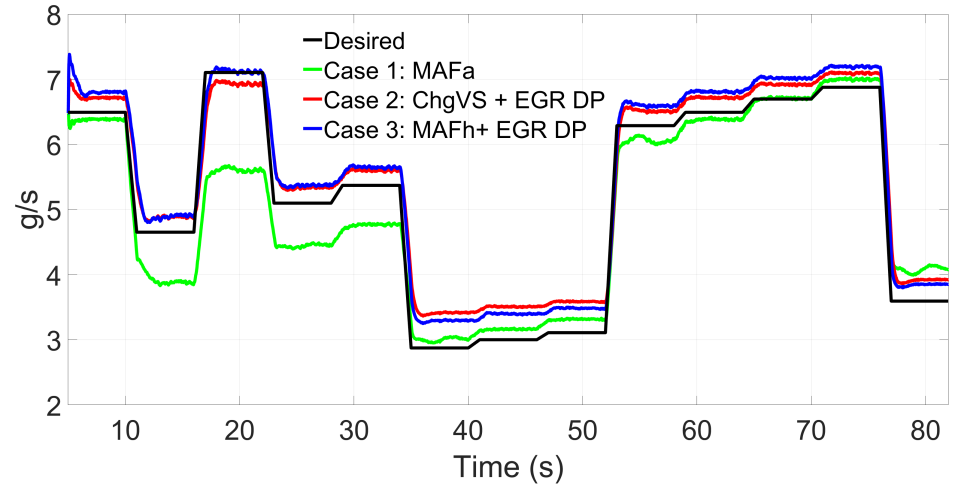

Figure 4.41. : Test 3: LP EGR mass flow rate tracking performance.

every step. Per Fig. 4.42, all three sensor cases reached the maximum inlet air flow control error at 80s. The maximum errors for Case 1, 2 and 3 were 6.6g/s (5.0%), 7.3g/s (5.5%) and 4.6g/s (3.5%), respectively. For the EGR ratio control performance (per Fig. 4.43), Case 1 cannot track the desired increase during 11 to 16s or 53 to 78s. The maximum EGR ratio control error for Case 1 was 1.8% at 21s. The worst EGR ratio control performance for Case 2 and 3 occurred at 45s. The maximum error values were 0.55% for Case 2 and 0.40% for Case 3.

Fig. 4.44 shows the torque tracking performance. Case 3 achieved the best torque control performance. The maximum error in Case 3 was 24Nm (5.5%) at 78s. All three sensor sets

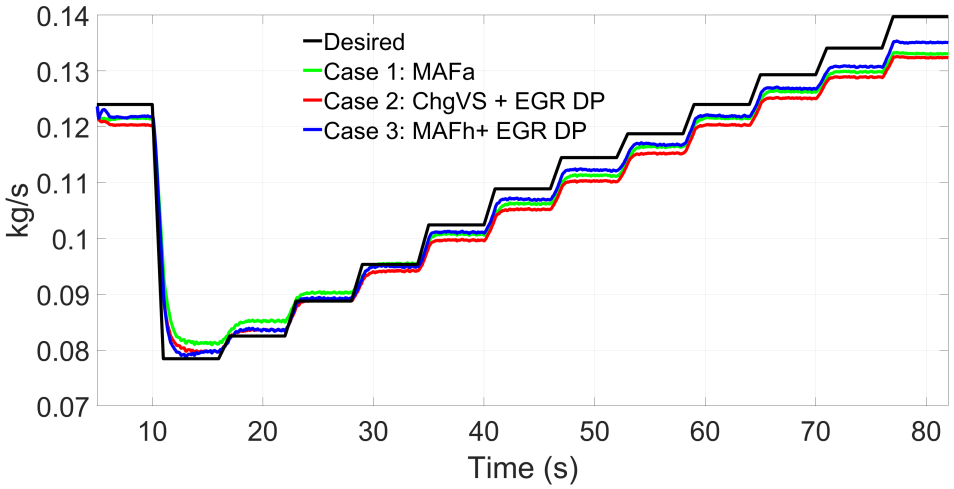

Figure 4.42. : Test 3: inlet air mass flow rate control performance.

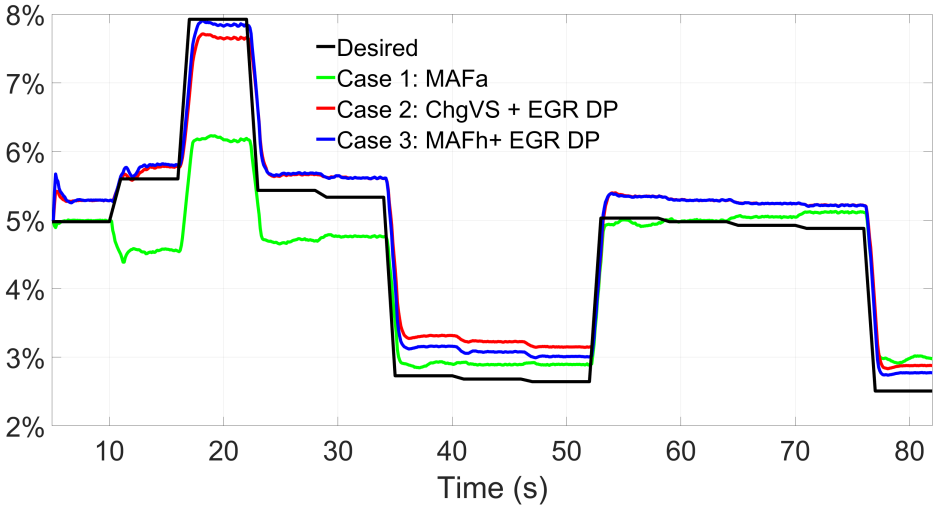

Figure 4.43. : Test 3: EGR ratio control performance.

failed to track the increasing torque target at the last step. Compared with Case 1, Case 2 had smaller tracking errors for the first 34s when the desired torque was lower while Case 1 became better with the increasing of the target torque. The largest error was 30Nm (6.8%) for Case 2 and 32Nm (7.2%) for Case 3, both at 78s. The error bar plot (per Fig. 4.45) shows a detailed comparison of the torque control performance. For each sensor case, the average torque error was calculated every 0.5s and the envelope was the standard deviation of the error. Similar to Test 2, small steady-state errors with large oscillations were observed

in all three sensor cases when the engine was run at low speeds (10 − 30s) (per Fig. 4.45). During the entire test, Case 3 always had the lowest torque tracking error.

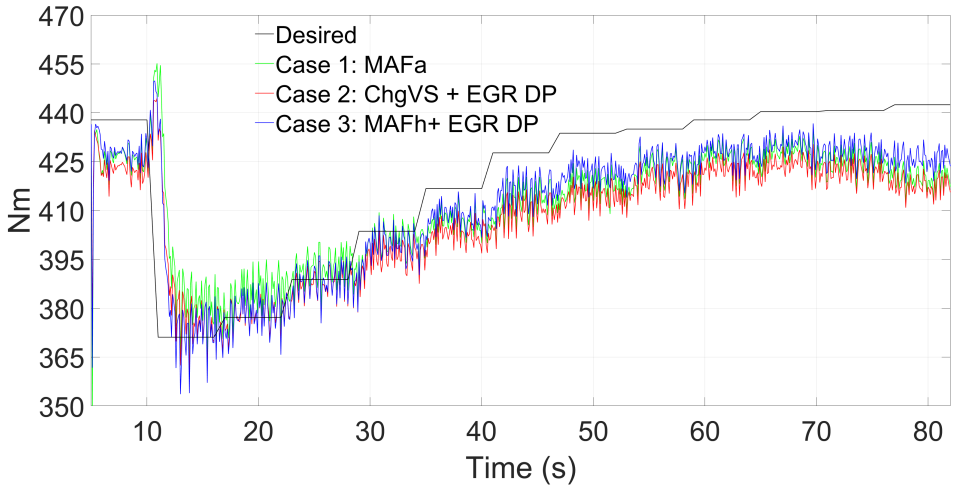

Figure 4.44. : Test 3: Torque control performance.

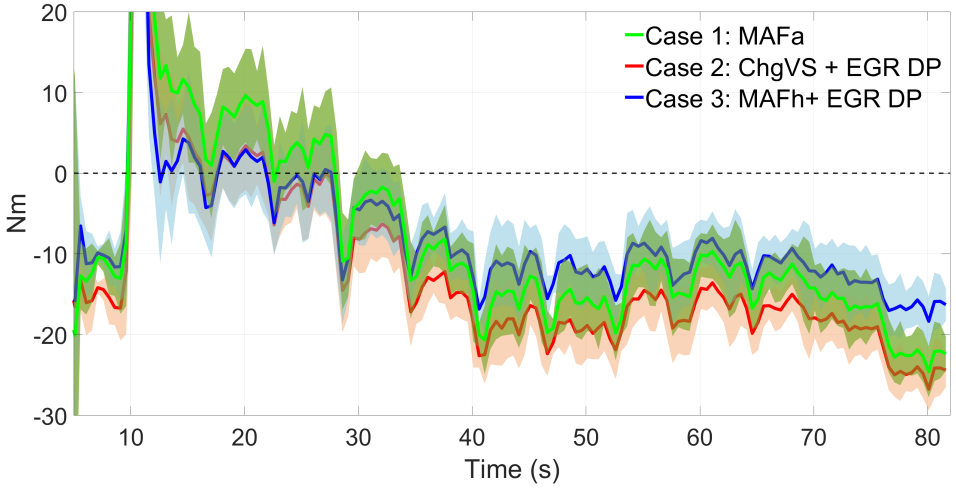

Figure 4.45. : Test 3: Error bar of torque.

Test 4

Fig. 4.46 shows the ramp test for the three sensor sets. In this ramp test, all sensors worked in condition 1. For all three sensor sets, AFR was controlled to remain within 14.7±0.3 for most of the time. Large oscillations occurred during 20 to 25s due to the transient change of the engine speed.

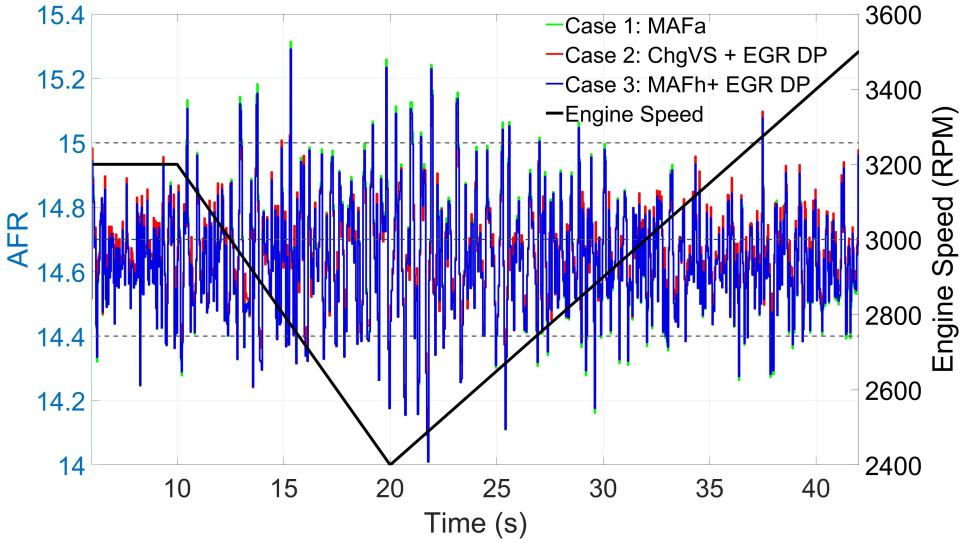

Figure 4.46. : Test 4: AFR tracking performance.

Fig. 4.47 shows the detailed AFR control performance during 18 to 22s. Case 1 had the largest positive error peak and Case 3 had the largest negative error peak. Case 2 had the smallest oscillation among the three sensor sets.

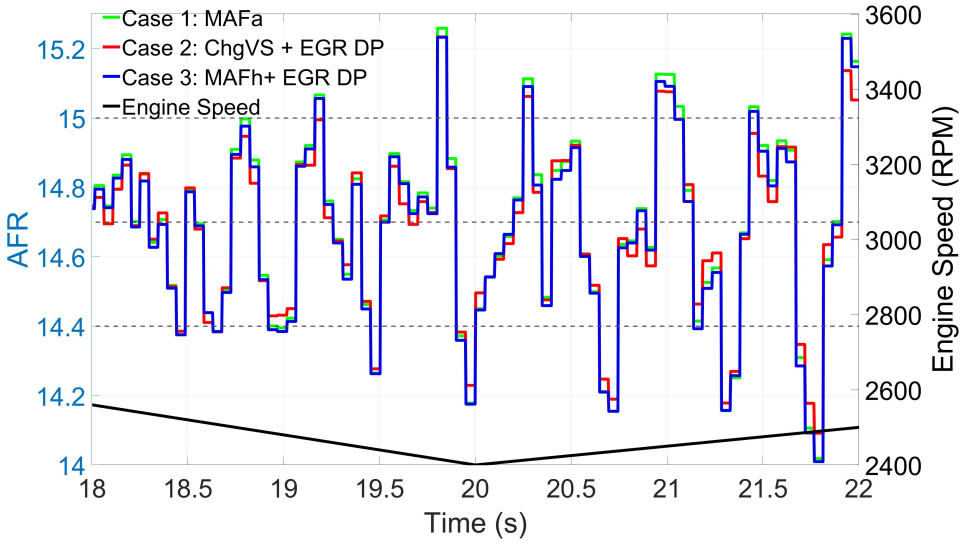

Figure 4.47. : Test 4: AFR tracking performance (18−22s).

Fig. 4.48 shows the compressor mass flow rate tracking performance. Case 3 had the best tracking performance during the entire test. The maximum tracking error in Case 3 was 5.2 g/s (6.3%) at 20s. Case 2 was the worst sensor set for compressor mass flow tracking in

this test and its maximum tracking error reached 7.4g/s (8.9%) at 20s. Case 1 had similar tracking performance as Case 3 after 20s when the engine speed started to increase. The maximum flow tracking error in Case 1 was 7.0g/s (8.4%).

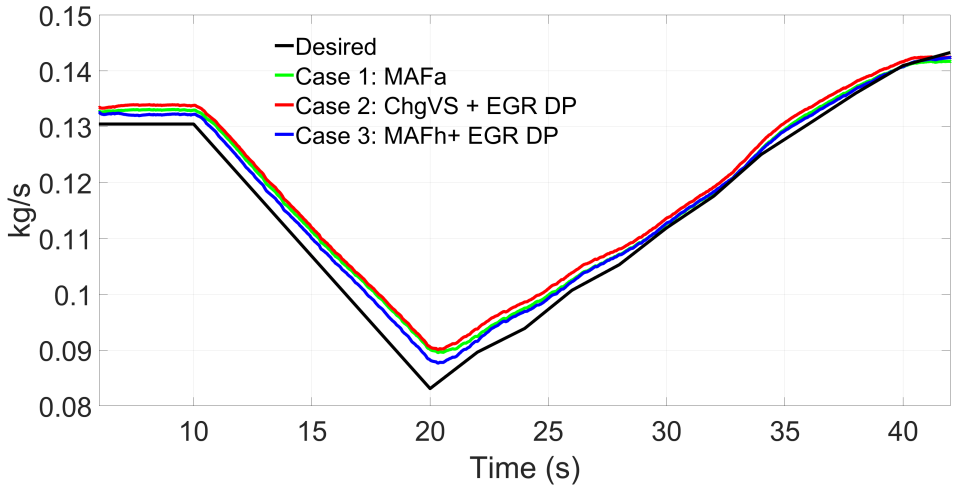

Figure 4.48. : Test 4: compressor mass flow rate tracking performance.

Fig. 4.49 shows the LP EGR mass flow rate tracking performance. Case 1 had very large tracking error 1.52 g/s at 22s. Case 3 had the best LP EGR flow tracking performance. The largest LP EGR tracking errors were 0.80g/s (11.3%) for Case 2 and 0.77g/s (10.8%) for Case 3, both at 22s.

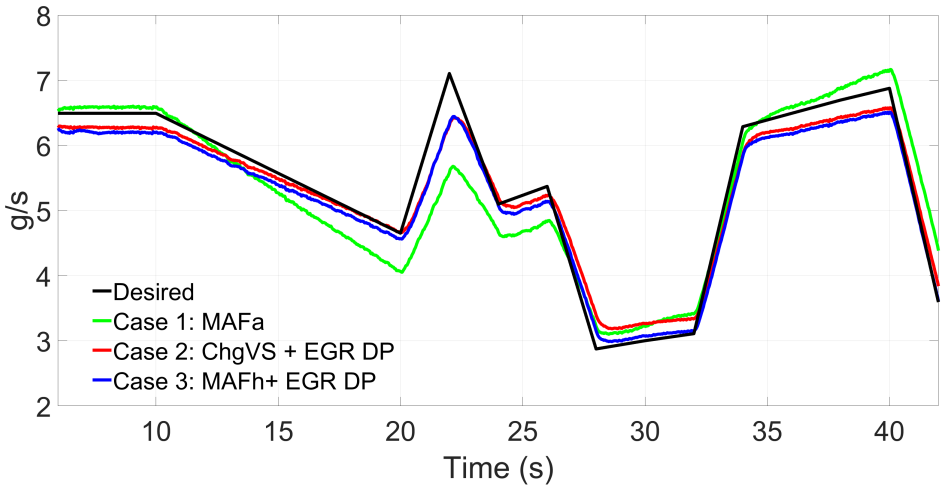

Figure 4.49. : Test 4: LP EGR mass flow rate tracking performance.

Fig. 4.50 and 4.51 show the inlet air flow rate and EGR ration control performance of all three sensor cases. Case 3 achieved the best control performance of these two variables. For the inlet air flow control, the largest errors for all three sensor cases all occurred at 22s. The maximum errors were 7.6g/s (9.7%) for Case 1, 7.4kg/s (9.4%) for Case 2 and 5.2g/s (6.6%) for Case 3, all within the required range. Per Fig. 4.51, the worst EGR ratio control performance occurred at 22s for all three cases. The largest errors for Case 1, 2 and 3 were 2.03%, 1.36% and 1.18%, respectively.

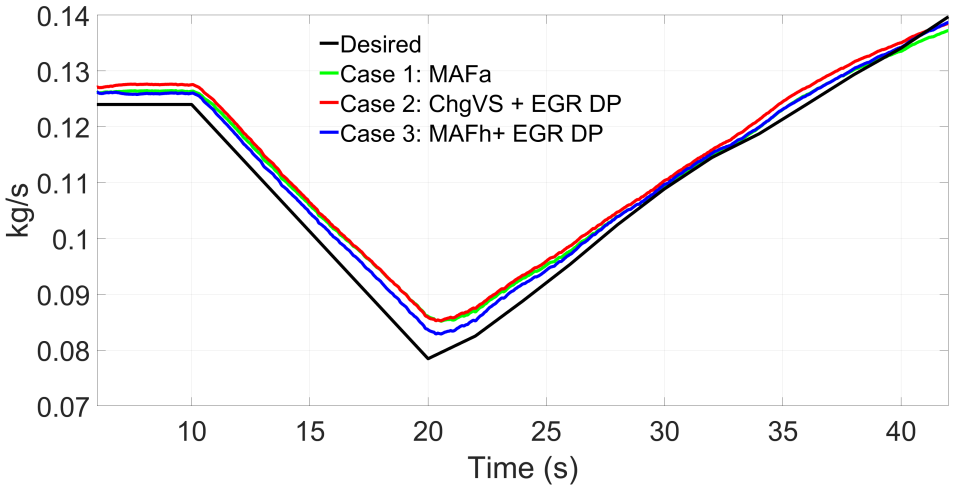

Figure 4.50. : Test 4: inlet air mass flow rate control performance.

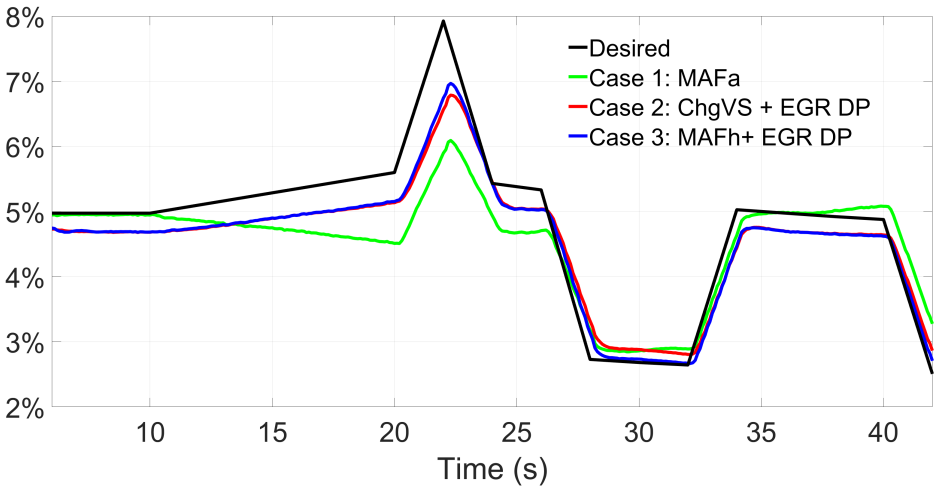

Figure 4.51. : Test 4: EGR ratio control performance.

Fig. 4.52 shows the torque tracking performance. Case 3 achieved the best torque control performance for this ramp test. During 20 to 23s, there was about 1.5s torque tracking delay in all three sensor cases. Case 3 achieved the lowest transient tracking error among the three cases. At 20s, the maximum tracking errors for Case 1, 2 and 3 were 46Nm (12.4%), 46Nm (12.4%) and 34Nm (8.2%), respectively. The error bar plot (per Fig. 4.53) shows a detailed comparison of the torque control performance. For each sensor case, the average torque error was calculated every 0.5s and the envelope was the standard deviation of the error. Per Fig. 4.53, Case 1 achieved lower tracking error than Case 2 during the entire ramp test even though the maximum error values in Case 1 and Case 2 were the same.

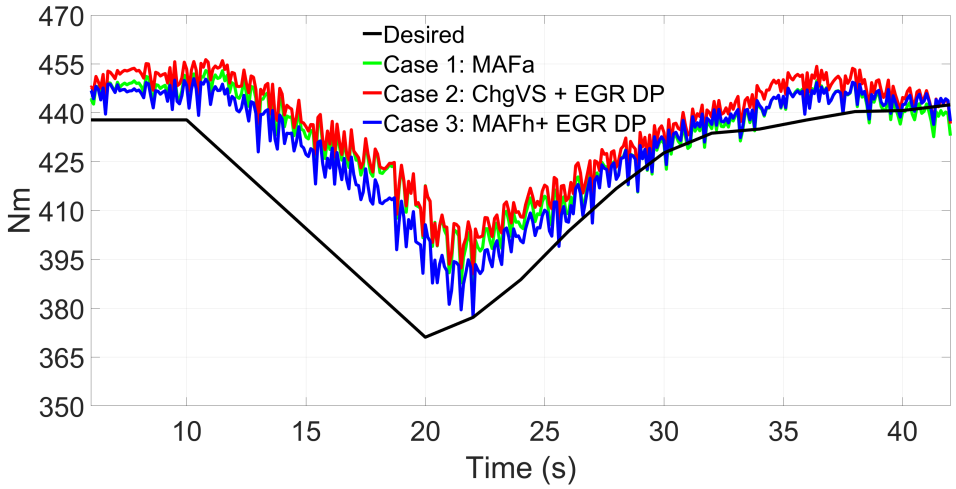

Figure 4.52. : Test 4: Torque control performance.

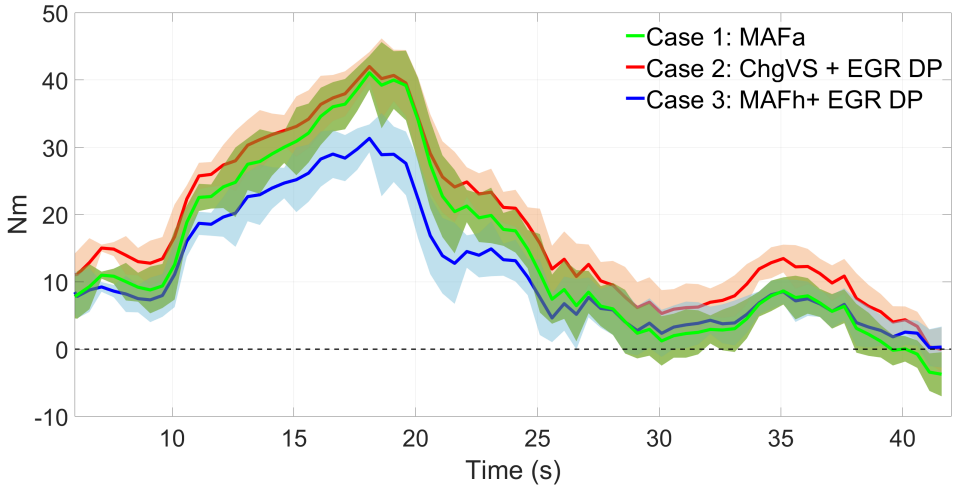

Figure 4.53. : Test 4: Error bar of torque.

Test 5

Fig. 4.54 shows the ramp test for three sensor sets. In this ramp test, the sensors worked at condition 2. For all three sensor sets, AFR was controlled to remain within 14.7±0.3 for most of the time. Large oscillations occurred during 20 to 25s due to the transient change of engine speed. Due to the negative bias error of the exhaust λ sensor, the controlled AFR was towards leaner during the transient engine speed change in all three cases.

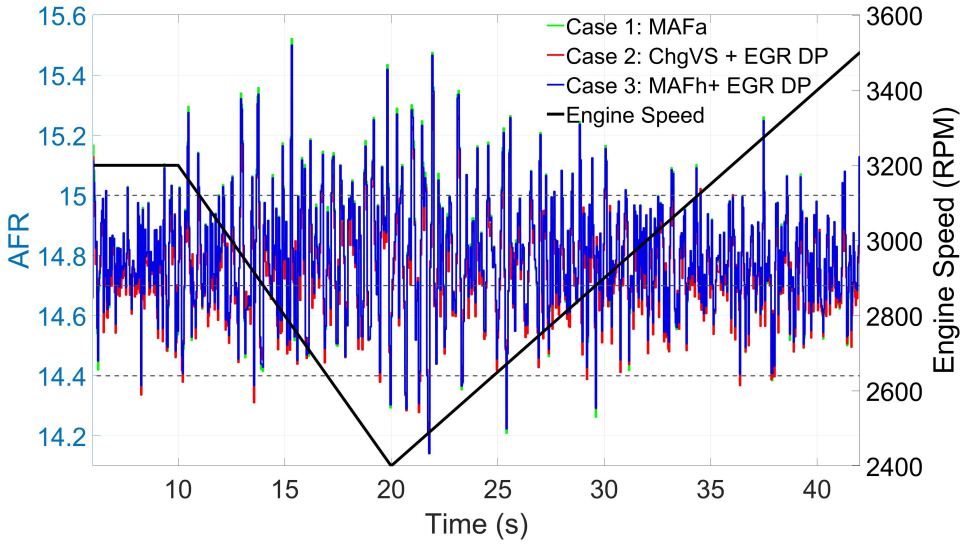

Figure 4.54. : Test 5: AFR tracking performance.

Per Fig. 4.55, AFR in Case 2 stayed closer to 14.7, whereas Case 1 and Case 3 had larger error peaks during 18 to 22s.

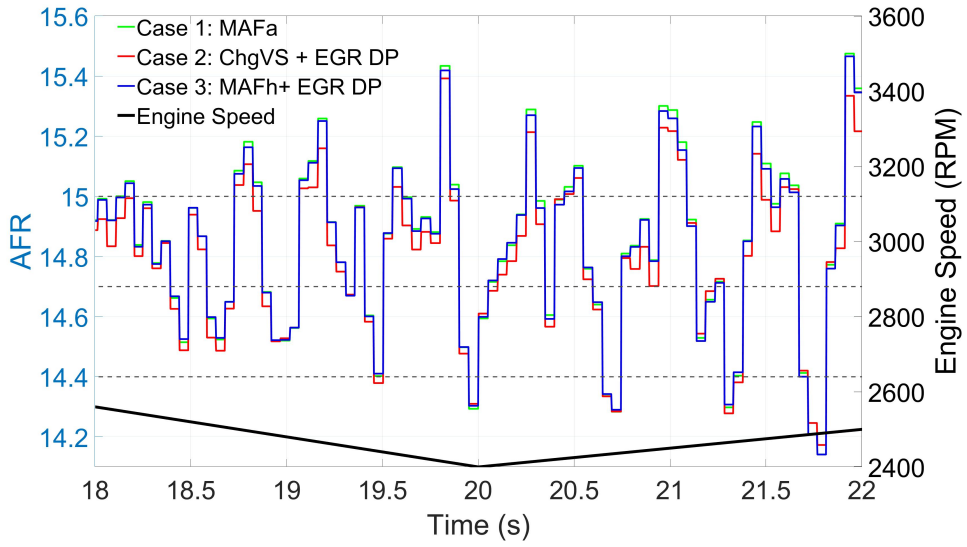

Figure 4.55. : Test Case 5: AFR tracking performance (18−22s).

Fig. 4.56 and 4.57 show the compressor mass flow rate and LP EGR mass flow rate tracking performance. Case 3 had the best tracking performance over the entire test and was the best sensor set for the control of air/EGR paths. Per Fig. 4.56, Case 3 was closer to the target compressor mass flow rate than the other two cases during 20 to 42s when the engine speed kept increasing. The maximum tracking error for Case 1, 2, 3 was 5.8g/s (4.0%), 6.6g/s (4.6%) and 4.2g/s (2.9%), respectively. Per Fig. 4.57, the maximum LP EGR flow tracking error in Case 1 occurred at 22s and was 1.68g/s (23.6%). The error peaks of Case 2 and 3 both occurred at 28s, which were 0.79g/s (27.5%) and 0.62g/s (21.6%), respectively.

Fig. 4.58 and 4.59 show the inlet air flow rate and EGR ratio control performance. Per Fig. 4.58, all three sensor cases had larger tracking errors with the increasing of the target air flow rate. Among the three sensor cases, Case 3 had the best control performance. The maximum air flow tracking errors for Case 1, 2 and 3 were 6.6g/s (4.7%), 7.3g/s (5.2%) and 4.7g/s (3.4%), respectively. Per Fig. 4.59, Case 2 and Case 3 had similar EGR ratio control performance except 27 to 33s when the target EGR ratio was low. Case 1 was the worst for EGR ratio control. The maximum EGR ratio tracking error in Case 1 was 1.99% at 22s.

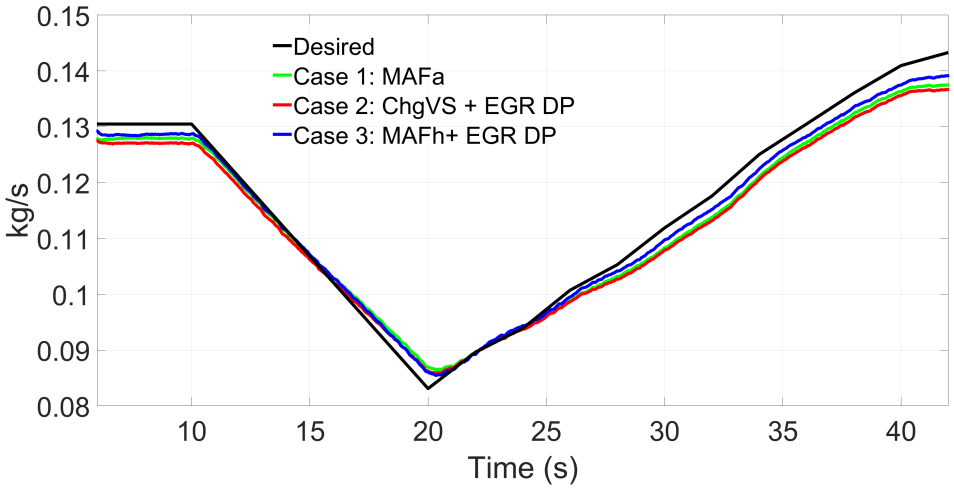

Figure 4.56. : Test 5: compressor mass flow rate tracking performance.

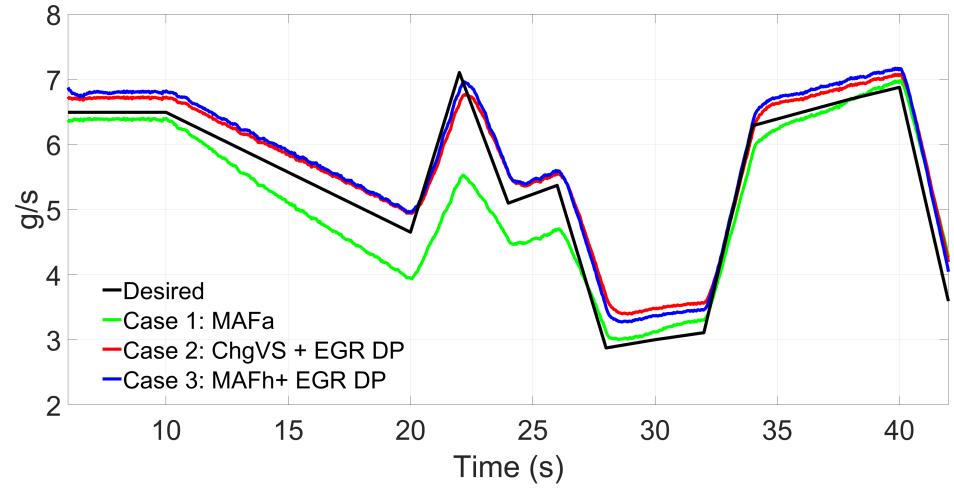

Figure 4.57. : Test 5: LP EGR mass flow rate tracking performance.

The largest transient EGR ratio control errors were 1.04% for Case 2 and 0.84% for Case 3, both at 28s.

Fig. 4.60 shows the torque tracking performance. There were larger control errors when the desired torque was higher in all three cases. Case 3 was better than the other two cases to track the dynamic torque target during 10 to 42s. The maximum tracking errors occurred at 42s for all three sensor cases. The maximum error values for Case 1, 2 and 3 were 27Nm (6.1%), 29Nm (6.6%) and 23Nm (5.2%), respectively. The error bar plot (per Fig. 4.61) shows a detailed comparison of the torque control performance. For each sensor case, the average torque error was calculated every 0.5s and the envelope was the standard deviation

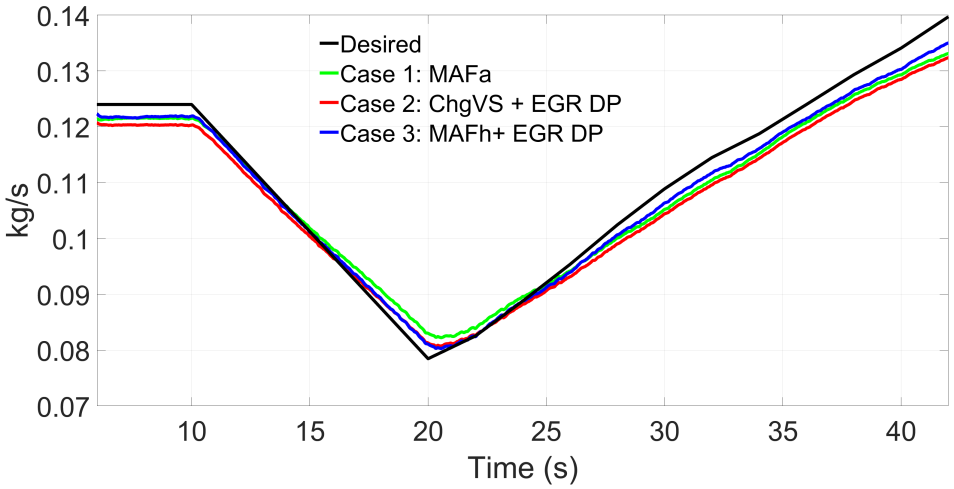

Figure 4.58. : Test 5: inlet air mass flow rate control performance.

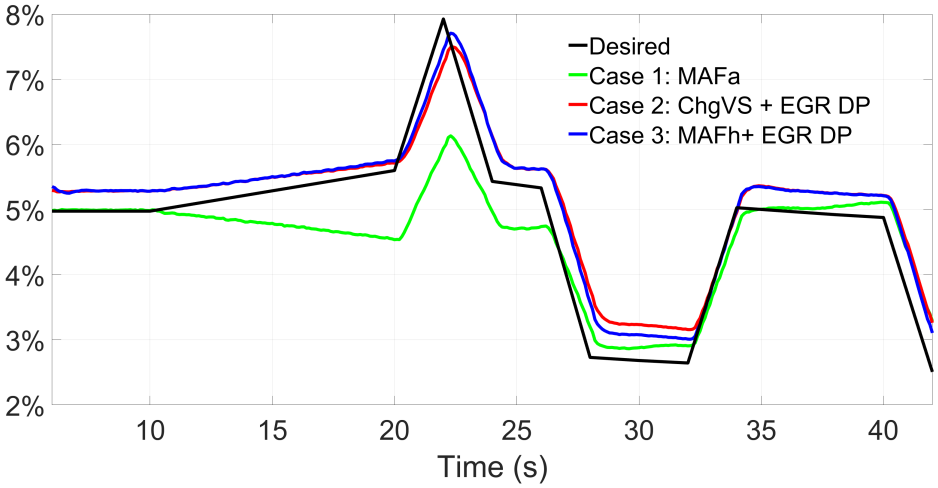

Figure 4.59. : Test 5: EGR ratio control performance.

of the error. Per Fig. 4.61, Case 2 had the lowest torque tracking error during 12 to 20s when the engine speed kept decreasing while Case 3 had advantages over the other two sensor sets during 25 to 42s when the engine speed kept increasing.

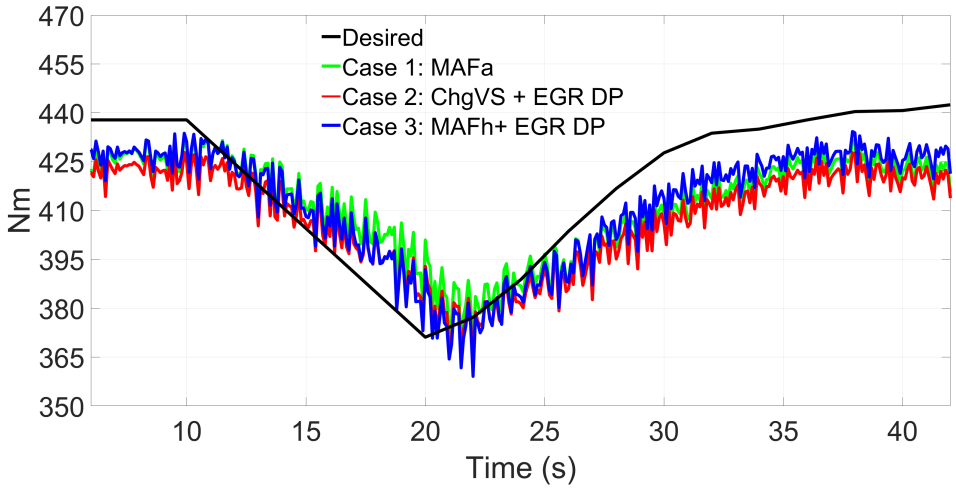

Figure 4.60. : Test 5: Torque control performance.

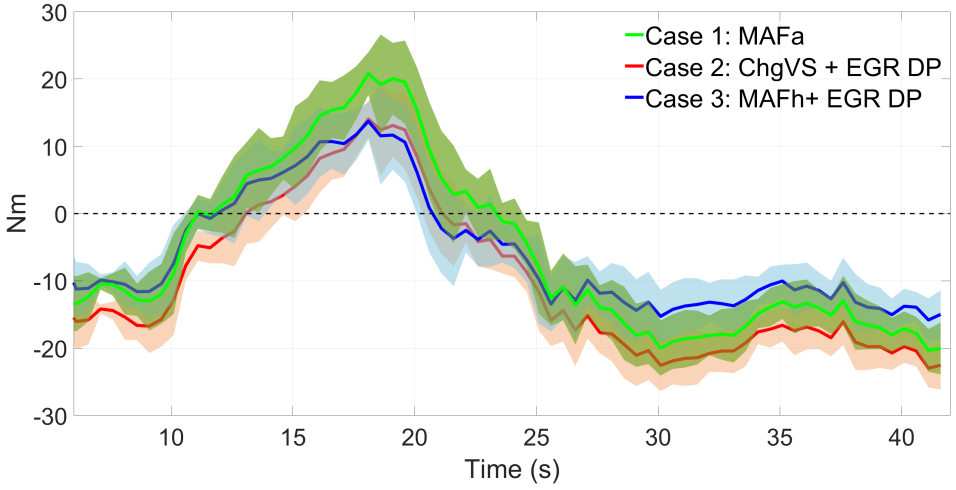

Figure 4.61. : Test 5: Error bar of torque.

4.7 Summary

A robust control based sensor system and controller co-design framework is developed in this work. The framework uses the μ-synthesis method to compute the structured singular value μ while synthesizing a linear H_∞ controller. The worst-case analysis is also performed as an additional robust performance evaluation. The μ value and the worst-case gain are compared with 1 to determine the acceptable sensor sets and controllers. The framework was applied to a high fidelity GT-Power turbocharged SI engine model utilizing LP EGR for stoichiometric AFR and flow controls.

Two independent control loops, flow control loop and AFR control loop, are designed to control the compressor flow, the EGR flow and maintain the cylinder AFR. The performance objectives of the flow control loop are to track the compressor mass flow rate within 11.2g/s absolute error and the LP EGR flow rate within 1g/s at low frequencies, via manipulating the throttle valve, LP EGR valve, waste-gate and VVT. The performance requirement of the AFR control loop is to maintain the AFR within 14.7±0.3 at low frequencies by controlling the fueling rate. Feedforwad controllers are used in the AFR control loop to improve the AFR control performance.

For AFR control, the computational results indicated that all three candidate sensor sets had similar control performance. The most robust AFR control was expected for Case 2 (the combination of ChgVS sensor, EGR DP sensor and UEGO sensor). The simulation results showed that all three sensors could keep the AFR within 14.7±0.3 for most of the time. Larger AFR oscillations were observed at low engine speeds and during transient operations. Case 2 had the lowest oscillation peak while Case 1 had the largest peak. At higher engine speeds, AFR in Case 2 could stay closer to 14.7 while the combustion in Case 1 and 3 (the combination of MAFh sensor, EGR DP sensor and UEGO sensor) became richer.

For the control of air/EGR paths, the computational results indicated that the desired robust performance could be achieved in Case 3 whereas Case 1 would be the least robust sensor suite for the flow control. The simulation results showed that all three cases met the compressor flow control requirement whereas only Case 2 and 3 could satisfy the LP EGR control requirement. As a consequence, Case 3 had the best torque control performance and EGR ratio control performance.

Based on the computation and high fidelity simulation results, Case 3 (MAFh sensor + EGR DP sensor + UEGO sensor) should be selected as the most robust sensor set for the control of air/EGR paths while Case 2 (ChgVS sensor + MAF sensor + UEGO sensor) should be selected as the most robust sensor set for AFR control. Considering the similar AFR control performance of Case 2 and Case 3 as well as the significant flow control improvements in Case 3, Case 3 (MAFh sensor + MAF sensor + UEGO sensor) should be selected if only one sensor set can be used.

5. ESTIMATION AND CONTROL OF THREE-WAY CATALYST OXYGEN STORAGE LEVEL

5.1 Motivation

The three-way catalyst (TWC) works as a buffer to store or release oxygen and increases the operating window about the stoichiometric air-fuel-ratio (AFR). The fractional oxidation state (FOS) of TWC is a key control parameter for emission reductions. By manipulating the desired engine AFR, the TWC oxygen storage can be kept at the desired level to reduce emissions. Due to the lack of sensors, FOS is typically estimated by models. The model-based estimation could result in inaccurate estimations and thus limits the control performance. Some detailed chemical and thermodynamic-based models have been developed to describe the complex TWC chemical reactions by set of partial differential equations (PDEs) in time and space[6][7]. Though such models could provide good estimates of FOS, they are not well-suited for controller designs. Moreover, the pre-existing discrepancy between the AFR command and the actual AFR brings additional difficulties to the FOS controller. Considering all the challenges, this chapter proposes a robust control strategy for the TWC FOS based on closed-loop FOS estimation. A simple first-order model capturing the TWC oxygen storage/depletion dynamics is corrected by an extended Kalman-filter (EKF) and used as the FOS estimator. A robust controller considering model uncertainties, disturbances and sensor/actuator inaccuracies is used to control the desired FOS by manipulating the desired engine AFR.

5.2 Oxygen Storage and Release in TWC

The three major pollutants in the engine-out exhaust are carbon monoxide (CO), unburnt hydrocarbons (HC) and nitrogen oxides (NO_x). Three-way-catalyst (TWC) can be used to simultaneously reduce NO_x and oxidize HC and CO for SI engines. The chemical reactions for emission reductions in TWC can be described by (5.1) - (5.3). The reductants HC and CO can be oxidized into carbon dioxide (CO_2) and water (H_2O) by oxygen while the oxidant NO can be converted into nitrogen (N_2) and CO_2 by CO. However, the relative AFR window for achieving both oxidation and reduction simultaneously is very narrow (per Fig. 5.1), bringing difficulties to the engine AFR control system.

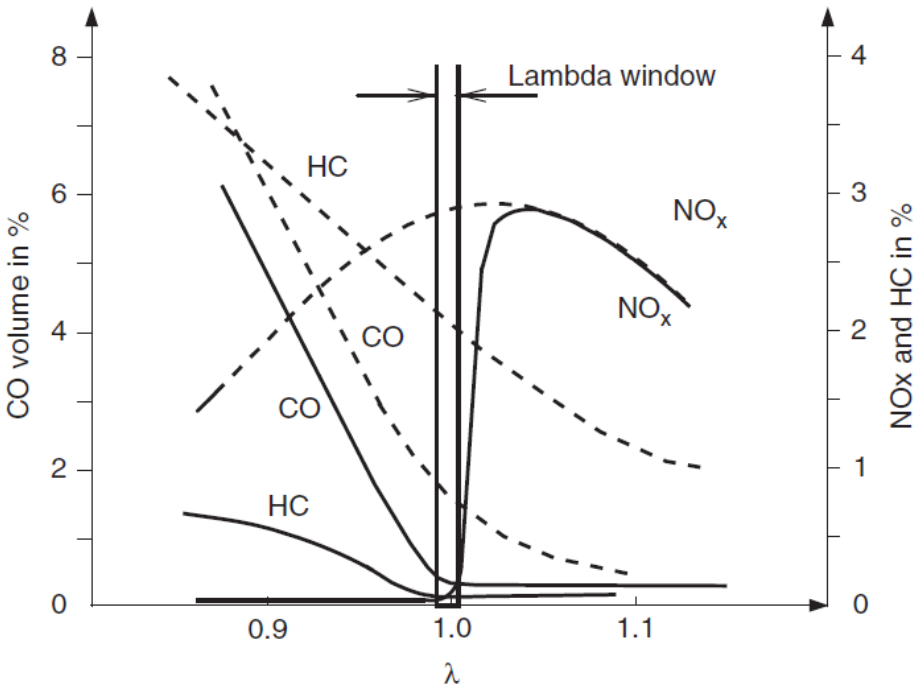

Figure 5.1. : Emissions before (dashed) and after (solid) the catalyst[32].

The TWC consists of Cerium oxides and precious metals[32]. The precious metals make the reactions happen and Cerium oxidize CeO_2 (ceria) provides the TWC with an ability to store oxygen in lean conditions and release oxygen in rich conditions. By maintaining the TWC oxygen storage capacity in a state where oxygen can always be released or absorbed in response to AFR variation in the engine-out exhaust, the narrow AFR window within which all three pollutants are effectively removed, is widened substantially[69]. The chemical reactions (5.4) and (5.5) describe the oxygen storage and release processes in the TWC, respectively. Under rich conditions, all NO is converted whereas the removal of CO and HC is incomplete due to the lack of oxygen in the engine-out exhaust[40]. If there is pre-stored oxygen in the TWC, it can be released through (5.5) and oxidize HC and CO to water and CO_2. To remove NO under slightly lean conditions, TWC must react CO with NO rather than with O_2. However, the reaction (5.2) is dominant over (5.3) in the presence of excess oxygen[70] and thus the reduction of NO is inhibited[40]. If there is a capacity for the TWC to store the excess oxygen, NO can be reduced to N_2 through reaction (5.3). Therefore, TWC works as a buffer to store or release oxygen when there is extra oxygen or insufficient oxygen, respectively, in the engine-out exhaust. Keeping the TWC in a proper oxidation state is important for emission reductions.

$$C_xH_y + \left(x + \frac{y}{4}\right) O_2 \rightarrow xCO_2 + \frac{y}{2}H_2O \tag{5.1}$$

$$CO + \frac{1}{2}O_2 \rightarrow CO_2 \tag{5.2}$$

$$CO + NO \rightarrow CO_2 + \frac{1}{2}N_2 \tag{5.3}$$

$$2Ce_2O_3 + O_2 \rightarrow 4CeO_2 \tag{5.4}$$

$$4CeO_2 \rightarrow 2Ce_2O_3 + O_2 \tag{5.5}$$

The fractional oxidation state (FOS) is used to describe the current oxidation state of TWC and is defined as:

$$FOS = \frac{\text{stored amount of } O_2}{\text{total TWC } O_2 \text{ storage capacity}} = \frac{2\,[CeO_2]}{[CeO_2] + [Ce_2O_3]} \tag{5.6}$$

where [ ] denotes the mole fraction.

5.3 Control Structure

Fig. 5.2 shows the dual-loop control structure for the engine and its aftertreatment system. The outer loop robust controller controls the TWC FOS to track the desired FOS by manipulating the desired engine lambda ($\lambda_{desired}$) based on the measured exhaust flow rate (W_{exh}), desired FOS ($FOS_{desired}$) and estimated TWC FOS ($FOS_{estimated}$). The inner loop AFR controller controls the actual engine lambda (λ_{up}) to track the desired engine lambda. The actual engine lambda is measured by a wide-band universal exhaust gas oxygen (UEGO) sensor placed upstream of the TWC. A secondary narrow-band exhaust gas oxygen (EGO) sensor is placed downstream the TWC and the voltage signal is mapped to the lambda value (λ_{dn}). The FOS estimator consists of a TWC model and an extended Kalman-filter. The FOS estimator predicts the current TWC FOS which is an input of the robust controller based on the mapped λ_{dn} and the measured W_{exh} and λ_{up}. The inner loop controller is a pre-existing AFR controller. The work described in this chapter focuses on the development of the outer loop controller which can be coupled with the inner loop controller.

5.4 Control-oriented TWC Model

5.4.1 Model Formulation

The control-oriented model is developed based on the model proposed in [71] for FOS estimator and robust controller designs.

$$\frac{dFOS}{dt} = \begin{cases} 0.21 \times f_{sat}(W_{air}) \times \left(1 - \frac{1}{\lambda_{up}}\right) \times \rho\left(\lambda_{up}, FOS\right) \times \frac{1}{C} & 0 < FOS < 1 \\ 0 & otherwise \end{cases} \tag{5.7}$$

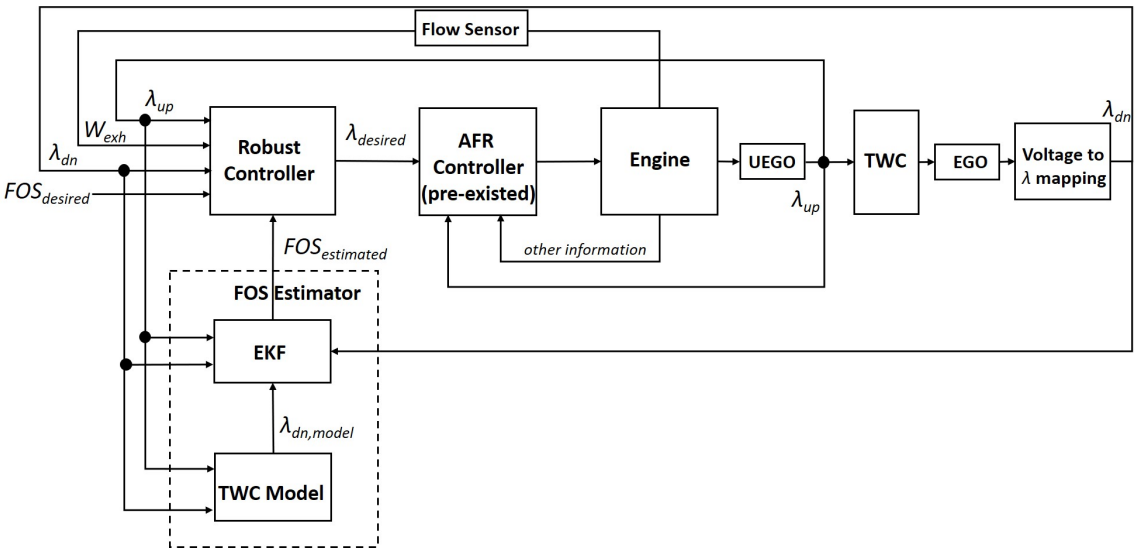

Figure 5.2. : Control structure of TWC fractional oxidation state (FOS)

where W_{air} is the engine-out mass air flow rate (approximated by the mixture mass flow rate), f_{sat} is the saturation function of W_{air}, C is the effective TWC oxygen capacity (the total mass of oxygen which can be stored in the TWC), λ_{up} is the TWC upstream λ (engine-out λ) and ρ describes the exchange of oxygen between the engine-out exhaust and the TWC. The saturation function f_{sat} is used to describe the phenomenon that the effective TWC oxygen capacity C increases as flow rate increases past a certain point[71] (thus $\frac{W_{air}}{C}$ is limited). ρ is modeled as a function of λ_{up} and FOS:

$$\rho\left(\lambda_{up}, FOS\right) = \begin{cases} \alpha_L f_L\left(FOS\right) & \lambda_{up} > 1 \\ \alpha_R f_R\left(FOS\right) & \lambda_{up} < 1 \end{cases} \tag{5.8}$$

where α_L and α_R are the adsorption and desorption rate of oxygen, respectively. $0 \leq f_L \leq 1$ represents the fraction of oxygen from the engine-out exhaust gas sticking to a site in the TWC, and $0 \leq f_R \leq 1$ represents the fraction of oxygen being released by the TWC and recombining with the engine-out exhaust gas. f_L and f_R are defined as:

$$\begin{aligned} f_L\left(FOS\right) &= \frac{\mathrm{e}^{\left(a_L \times FOS^2 + b_L \times FOS\right)} - \mathrm{e}^{(a_L + b_L)}}{\mathrm{e}^{(a_L + b_L)} - 1} \\ f_R\left(FOS\right) &= \frac{\mathrm{e}^{\left(a_R \times FOS^2 + b_R \times FOS\right)} - 1}{\mathrm{e}^{(a_R + b_R)} - 1} \end{aligned} \tag{5.9}$$

where a_L, b_L, a_R and b_R are tuning parameters. f_L is monotonically decreasing with FOS while f_R is monotonically increasing with FOS. When FOS $= 0$, $f_L = 1$ and $f_R = 0$. When FOS $= 1$, $f_L = 0$ and $f_R = 1$.

In equation (5.7), FOS is bounded by 0 and 1. The term $0.21 \times f_{sat}(W_{air}) \times \left(1 - \frac{1}{\lambda_{up}}\right)$ is the differential total mass of O_2 in the engine-out exhaust gas with respect to stoichiometry. The product $0.21 \times f_{sat}(W_{air}) \times \left(1 - \frac{1}{\lambda_{up}}\right) \times \rho\left(\lambda_{up}, FOS\right)$ represents the mass flow rate of O_2 that is absorbed or released by the TWC. Under the lean condition ($\lambda_{up} > 1$), TWC absorbs oxygen from the engine-out exhaust gas and $\frac{dFOS}{dt} > 0$. During the rich operation ($\lambda_{up} < 1$), TWC releases oxygen to the engine-out exhaust gas and $\frac{dFOS}{dt} < 0$.

The TWC-out λ (λ_{dn}) can expressed as:

$$\lambda_{dn} = \lambda_{up} - (\lambda_{up} - 1) \times \rho\left(\lambda_{up}, FOS\right) \tag{5.10}$$

By defining the state x as:

$$x = FOS \tag{5.11}$$

the input u and the disturbance input u_d as:

$$\begin{aligned} u &= \lambda_{up} \\ u_d &= W_{air} \end{aligned} \tag{5.12}$$

the output as:

$$\begin{aligned} y_1 &= FOS \\ y_2 &= \lambda_{dn} \end{aligned} \tag{5.13}$$

the system can be expressed as:

$$\begin{aligned} \dot{x} &= \begin{cases} 0.21 \times \frac{1}{C} \times f_{sat}(u_d) \times \left(1 - \frac{1}{u}\right) \times \alpha_L \times f_L\left(x\right) & 0 < x < 1 \quad and \quad u > 1 \\ 0.21 \times \frac{1}{C} \times f_{sat}(u_d) \times \left(1 - \frac{1}{u}\right) \times \alpha_R \times f_R\left(x\right) & 0 < x < 1 \quad and \quad u \leq 1 \\ 0 & otherwise \end{cases} \\ y_1 &= x_1 \\ y_2 &= \begin{cases} u - (u-1) \times \alpha_L \times f_L\left(x\right) & u > 1 \\ u - (u-1) \times \alpha_R \times f_R\left(x\right) & u \leq 1 \end{cases} \end{aligned} \tag{5.14}$$

5.4.2 Model Calibration

The parameters a_L, b_L, a_R, b_R, α_L, α_R, f_{sat} and C can be calibrated based on the experimental data. In this work, a high fidelity aftertreatment model built in AVL BOOST was used as the truth reference. The reference model was a dual-site TWC model developed for an aged TWC consisting of two TWCs connected in-series (per Fig 5.3) based on[7][72]. The reference model was calibrated with test bench data and was able to correctly predict the TWC dynamics. Due to the computation complexity, the reference model is not suitable

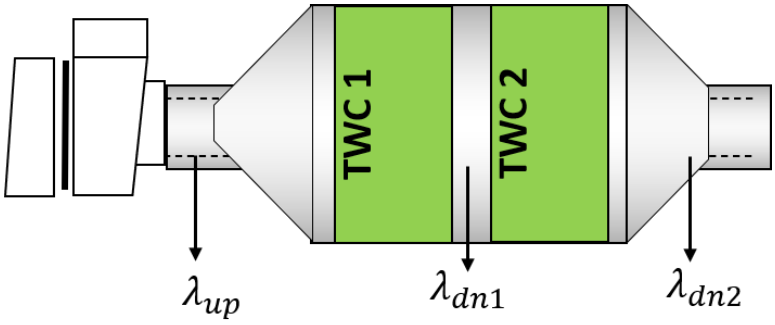

Figure 5.3. : TWC structure

for control analysis, but can be a good reference to provide necessary information for the control-oriented model (per equation (5.14)) calibration and serve as a virtual test bench. In the reference model, each TWC is divided into four equal pieces and modeled piece-wisely. The average TWC surface Ce_2O_4 mole fraction is used as the reference FOS.

The developed control-oriented model (equation (5.14) was first calibrated for TWC1 (per Fig 5.3) by the following three steps:

1. Find the saturation point of the air flow rate W_{air}: operate the TWC at the same λ_{up} profile for different flow rate conditions and find out at which flow rate point the TWC breakthrough time starts to have few changes.

2. Calculate the effective TWC1 oxygen capacity C_1: calculate O_2 mass difference between the TWC upstream and downstream exhaust gas at low air flow rate (below the saturation rate) conditions.

3. Find out a_L, b_L, a_R, b_R, α_L and α_R: use the least-square fitting method to minimize the ρ error for both lean and rich conditions. The reference ρ is calculated by the measured TWC1 upstream λ ($\lambda_{up,measure}$) and downstream λ ($\lambda_{dn1,measure}$) based on equation (5.10). The optimization problem can be expressed as follows and solved by MATLAB function "lsqcurvefit".

$$\begin{aligned} &\min_{\alpha_L,a_L,b_L} \sum \left(\rho_{model} - \rho_{measure}\right)^2 \quad \lambda_{up,measure} > 1 \\ &\min_{\alpha_R,a_R,b_R} \sum \left(\rho_{model} - \rho_{measure}\right)^2 \quad \lambda_{up,measure} \leq 1 \end{aligned} \tag{5.15}$$

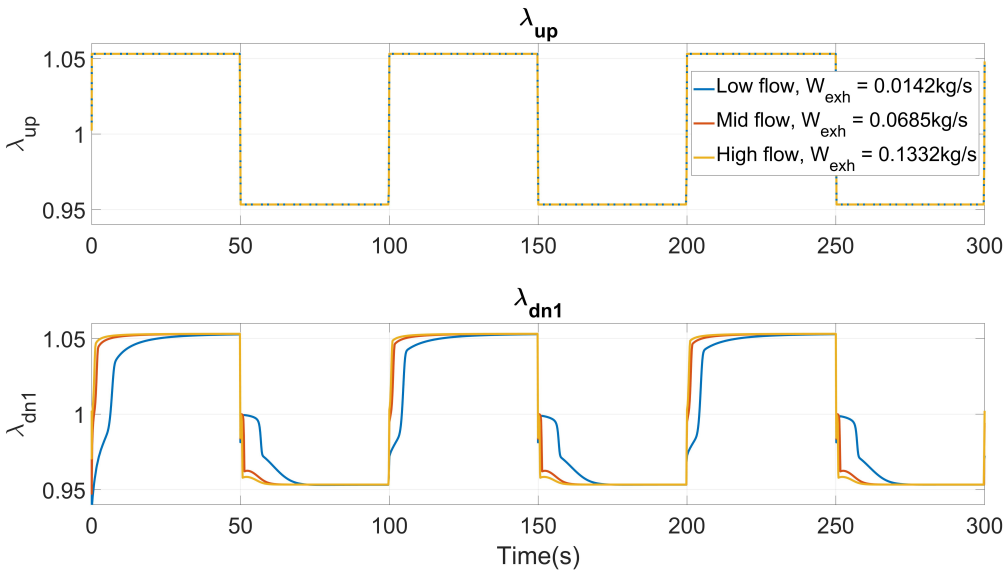

Figure 5.4. : Measured λ_{up} and λ_{dn1} for TWC1

Recall equation(5.10), ρ can be calculated by:

$$\rho = \frac{\lambda_{up} - \lambda_{dn}}{\lambda_{up} - 1} \tag{5.16}$$

By substituting ρ_{model} and $\rho_{measure}$, the optimization problem can be expressed as:

$$\begin{aligned} \min_{\alpha_L, a_L, b_L} \sum \left(\alpha_L \times \frac{e^{\left(a_L \times FOS^2 + b_L \times FOS\right)} - e^{\left(a_L + b_L\right)}}{e^{\left(a_L + b_L\right)} - 1} - \frac{\lambda_{up,measure} - \lambda_{dn1,measure}}{\lambda_{up,measure} - 1} \right)^2 & \quad \lambda_{up,measure} > 1 \\ \min_{\alpha_R, a_R, b_R} \sum \left(\alpha_R \times \frac{e^{\left(a_R \times FOS^2 + b_R \times FOS\right)} - 1}{e^{\left(a_R + b_R\right)} - 1} - \frac{\lambda_{up,measure} - \lambda_{dn1,measure}}{\lambda_{up,measure} - 1} \right)^2 & \quad \lambda_{up,measure} \leq 1 \end{aligned} \tag{5.17}$$

Fig. 5.4 shows the TWC1 upstream λ_{up} profiles and measured downstream λ_{dn1} in the reference AVL Boost Model for three different engine-out flow rate cases. The same square wave excitation signal is set for λ_{up} for all cases. Fig 5.5 shows the zoomed plot of λ_{up} and λ_{dn1}. It can been seen that the dependency of the TWC1 breakthrough time on the flow rate is more significant at low flow rate 0.0142kg/s. There is about 0.5s breakthrough time difference between the low and mid flow rate cases. The saturation point of the W_{air} is approximated by 0.1332kg/s.

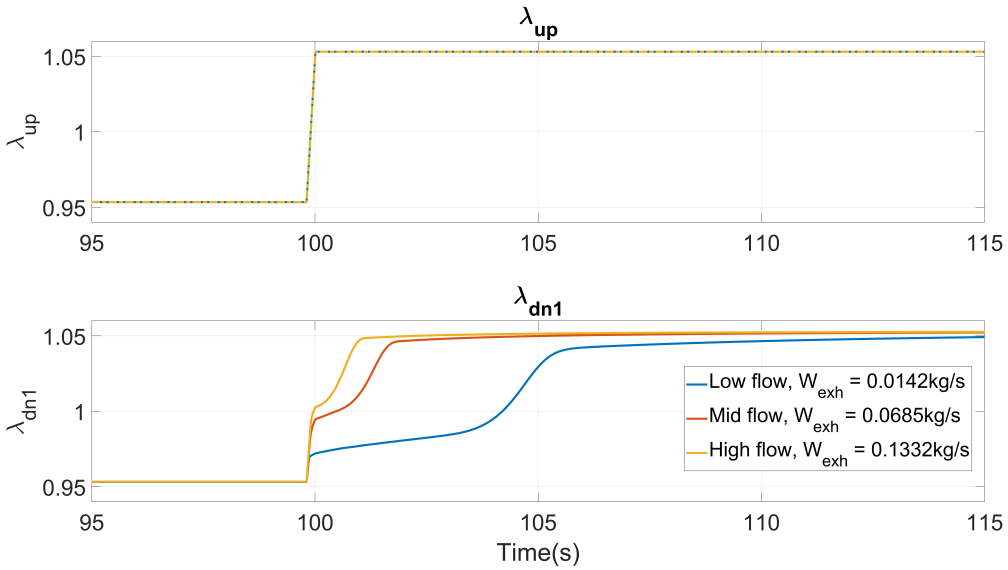

Figure 5.5. : Measured λ_{up} and λ_{dn1} for TWC1 (zoomed)

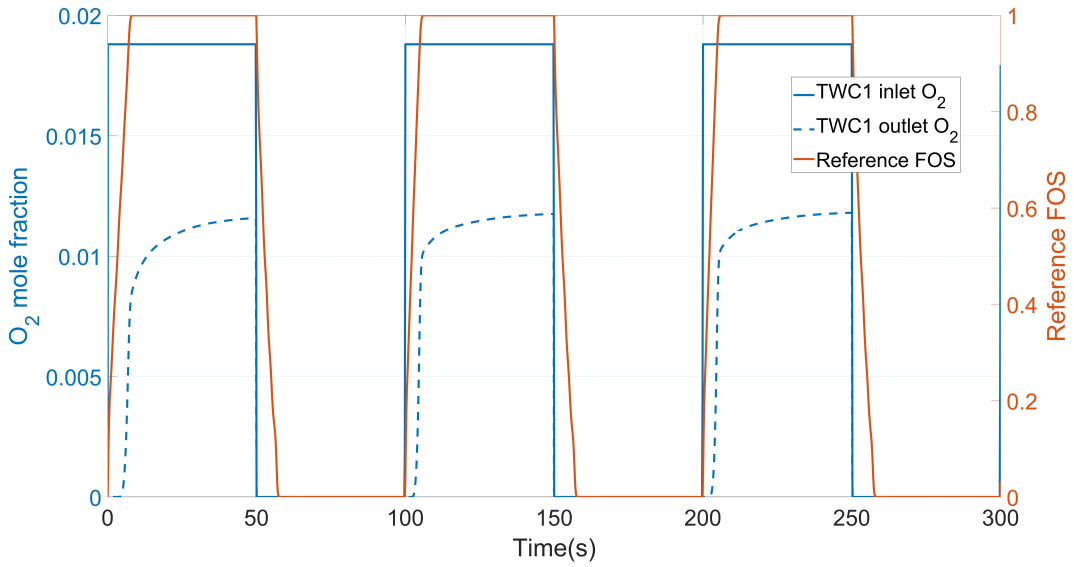

Figure 5.6. : TWC1 inlet and outlet O_2 mole fraction and reference FOS

Table 5.1. : C_1 calculation for TWC1

Transition	t_1	t_2	C_1 (kg)
1	0	8.8	0.0023
2	99.8	106.7	0.0016
3	199.8	206.7	0.0016

Fig 5.6 shows the O_2 mole fraction in the TWC1 inlet and outlet flow as well as the reference FOS. The TWC1 effective oxygen capacity C_1 is calculated by the following integral over a complete FOS increasing period ($FOS(t_1) = 0$, $FOS(t_2) = 1$):

$$C_1 = \frac{M_{O_2}}{M_{exh}} \int_{t_1}^{t_2} W_{exh} \left(C_{O_2,\text{in}} - C_{O_2,out} \right) \tag{5.18}$$

where M_{O_2} denotes the molar mass of O_2 and M_{exh} denotes the molar mass of the engine-out exhaust gas (approximated by the molar mass of air), W_{exh} denotes the engine-out mass flow rate, $C_{O_2,\text{in}}$ and $C_{O_2,out}$ denote the O_2 mole fraction in the TWC inlet and outlet flow, respectively.

Table 5.1 shows the C_1 calculation for the three transitions in Fig 5.6. Due to the effects of the initial condition, transition 1 is very different from transition 2 and 3. Therefore, C_1 is estimated by the average of transition 2 and 3, which is 0.0016kg.

Fig. 5.7 shows $\rho_{measure}$ (in equation (5.15)) for rich conditions. α_R is approximated by the maximum value of $\rho_{measure}$ ($\alpha_R = 1$). For the fitted ρ_{model}, a_R is 13.45 and b_R is -20.63.

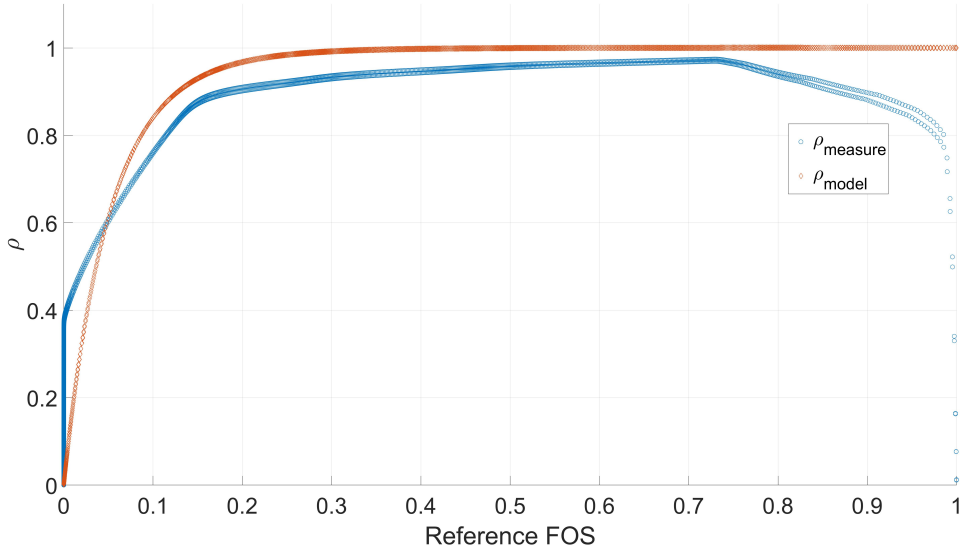

Figure 5.7. : Rich condition: $\rho_{measure}$ vs. reference FOS

Fig. 5.8 shows $\rho_{measure}$ (in equation (5.15)) for lean conditions. α_L is approximated by the maximum value of $\rho_{measure}$ ($\alpha_L = 1.527$). For the fitted ρ_{model}, a_L is 2.55 and b_L is 1.2.

5.4.3 Model Validation

Fig. 5.9 and 5.10 show the TWC model validation for square and triangle excitation λ_{up}. Three different exhaust flow conditions, low flow ($W_{exh} = 0.0142$kg/s), mid flow ($W_{exh} = 0.0685$kg/s), and high flow ($W_{exh} = 0.1332$kg/s), are considered. Compared with the mid flow and high flow conditions, low flow case has larger FOS and λ_{dn1} estimation errors.

Fig. 5.11 - 5.14 show the detailed zoomed plots for the rich-lean and lean-rich transitions for both excitation signals. Per Fig. 5.11 and Fig. 5.12, both of the mid flow and high flow cases have good FOS estimation performance during the rich-lean transition whereas the low flow case has about 0.5s delay. All three cases have delayed λ_{dn1} estimations during the rich-lean transition. A possible explanation could be that the estimated FOS in the control-oriented model started to increase after λ_{up} crosses the switching point 1 whereas the average TWC1 FOS in the complex reference model started to increase before the crossover point.

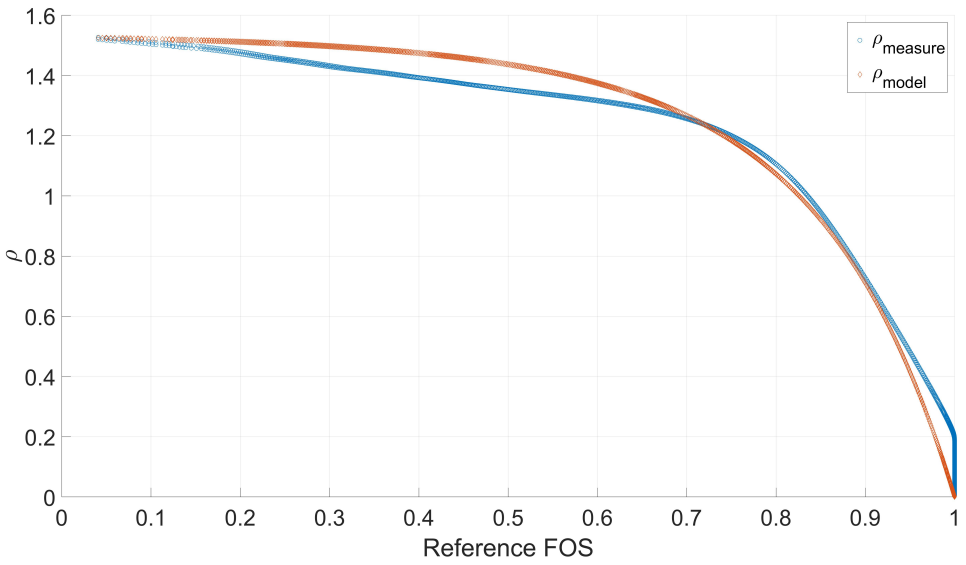

Figure 5.8. : Lean condition: $\rho_{measure}$ vs. reference FOS

This results in a delayed estimation of FOS in the control-oriented model, especially when the flow rate is low. The delayed FOS estimation would result in a delayed ρ and thus a delayed λ_{dn1} estimation. Another thing should be noticed here is that the control-oriented model is a lumped system and does not consider the internal interactions of TWC1, which could bring some estimation errors. During the rapid lean-rich transition (per Fig. 5.13), the estimation delays of FOS and λ_{dn1} could be found for all three flow conditions. During the slow lean-rich transition (per Fig 5.14), the model has better FOS and λ_{dn1} estimation performance compared to the rapid transition.

5.5 Extended Kalman-filter

In a manner similar to the approach taken in [73], an extended Kalman-filter (EKF) is designed to correct the open-loop model estimation results.

For the nonlinear discrete-time system:

$$\begin{aligned} x_{k+1} &= f_k(x_k, u_k) + w_k \\ y_k &= h_k(x_k) + v_k \end{aligned} \tag{5.19}$$

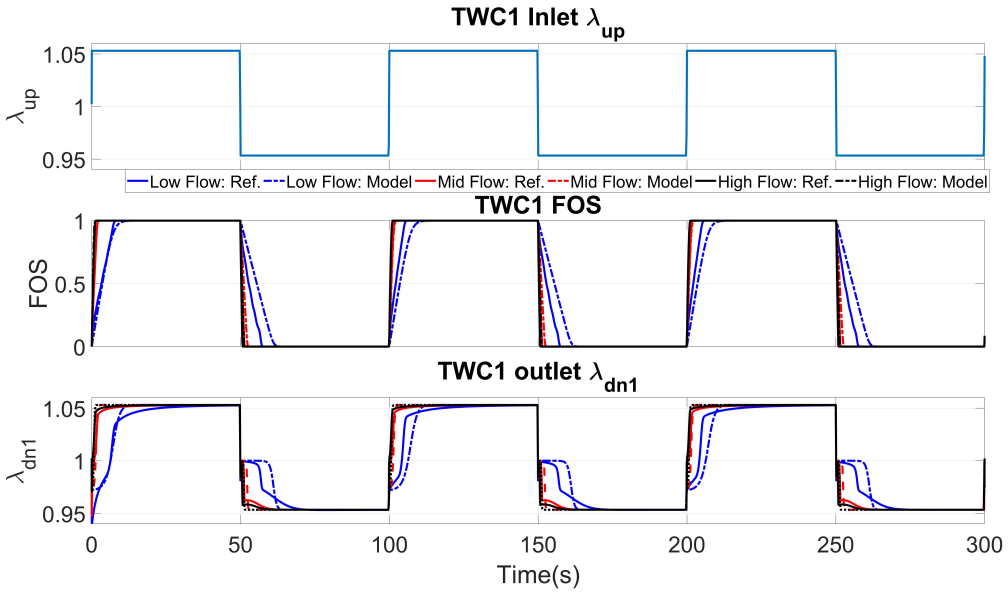

Figure 5.9. : Model validation for square waves

where w_k and v_k are white Gaussian, independent random processes with zero mean and covariance matrix:

$$\begin{aligned} E\left[w_k {w_k}^T\right] &= N_k \\ E\left[v_k {v_k}^T\right] &= R_k \end{aligned} \tag{5.20}$$

The extended Kalman-filter (EKF) algorithm can be stated as[74]:

Prediction Cycle:

$$\begin{aligned} \text{Predicted state estimate: } \hat{x}_{k+1|k} &= f_k\left(\hat{x}_{k|k}\right) \\ \text{Forecast error covariance: } P_{k+1|k} &= A_k P_k A_k^T + N_k \end{aligned} \tag{5.21}$$

Filtered Cycle:

$$\begin{aligned} \text{EKF gain: } L_{k+1} &= P_{k+1|k} C_{k+1}^T \left(R_{k+1} + C_{k+1}^T P_{k+1|k} C_{k+1}\right) \\ \text{Updated state estimation: } \hat{x}_{k+1|k+1} &= \hat{x}_{k+1|k} + L_{k+1}\left(y_{k+1} - h_{k+1}\left(\hat{x}_{k+1|k}\right)\right) \\ \text{Posterior error covariance: } P_{k+1} &= \left(I - L_{k+1} C_{k+1}\right) P_{k+1|k} \end{aligned} \tag{5.22}$$

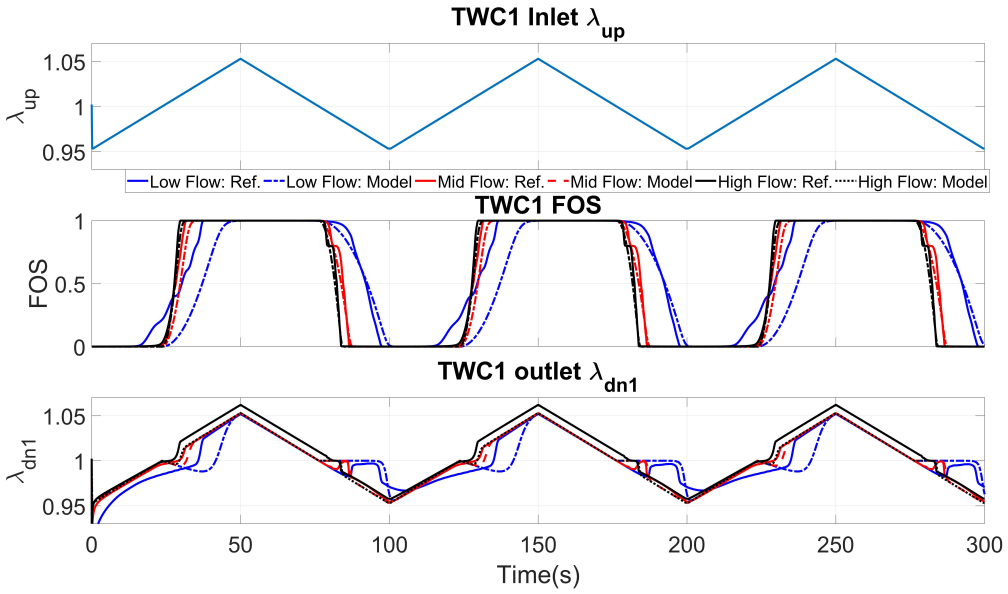

Figure 5.10. : Model validation for triangle waves

where A_k, C_{k+1} are Jacobian matrices of f and h:

$$\begin{aligned} A_k &= \nabla f_k|_{\hat{x}_k} \\ C_{k+1} &= \nabla h_k|_{\hat{x}_{k+1|k}} \end{aligned} \tag{5.23}$$

5.5.1 Extended Kalman-filter Design

To implement the extended Kalman-filter, the TWC model in equation (5.14) is augmented as follows:

$$\begin{aligned} u &= \lambda_{up} \\ u_d &= Wair \\ \hat{x} &= \begin{bmatrix} FOS & \lambda_{dn,\tau} & \alpha_L & \alpha_R & \frac{1}{C} \end{bmatrix}^T \\ \hat{y} &= \lambda_{dn,\tau} \end{aligned} \tag{5.24}$$

where $\lambda_{dn,\tau}$ is the modeled TWC outlet λ sensor measurement. The sensor response time is assumed as 0.3s.

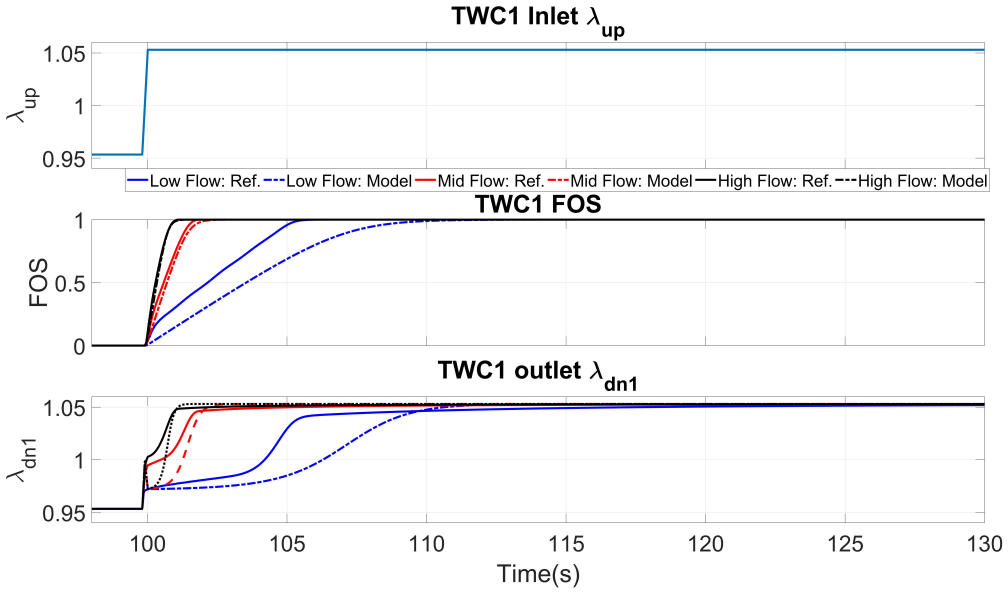

Figure 5.11. : Model validation for square waves (zoomed plot for the rich-lean transition)

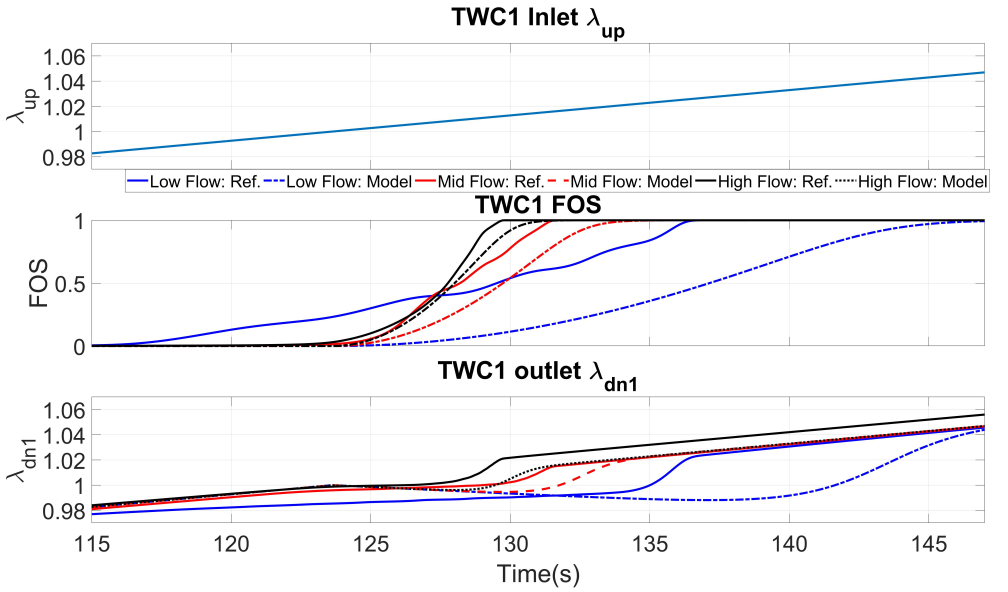

Figure 5.12. : Model validation for triangle waves (zoomed plot for the rich-lean transition)

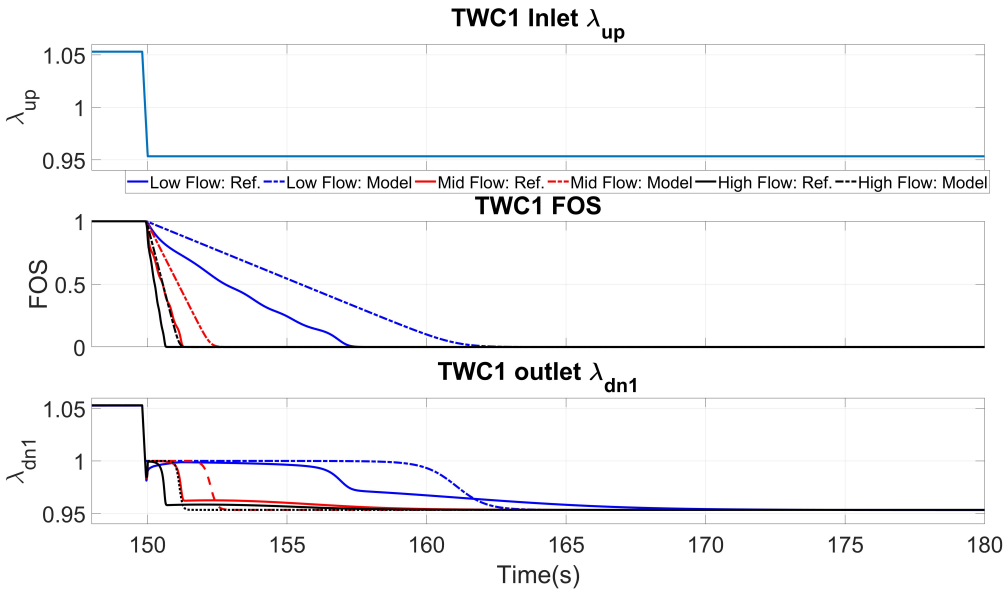

Figure 5.13. : Model validation for square waves (32s zoomed plot for the lean-rich transition)

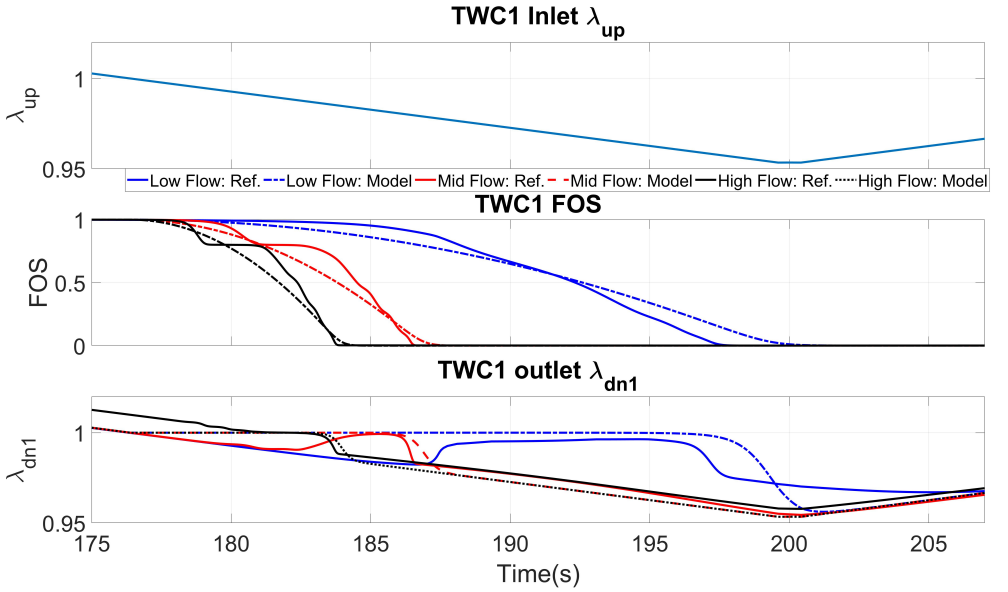

Figure 5.14. : Model validation for triangle waves (32s zoomed plot for the lean-rich transition)

The augmented system is expressed as follows:

$$
\begin{aligned}
\dot{\hat{x}}_1 &= \begin{cases} 0.21 \times \hat{x}_3 \times f_{sat}\left(u_d\right) \times \left(1 - \frac{1}{u}\right) \times \hat{x}_5 \times f_L\left(x_1\right) & u > 1, \hat{x}_1 < 1 \\ 0.21 \times \hat{x}_4 \times f_{sat}\left(u_d\right) \times \left(1 - \frac{1}{u}\right) \times \hat{x}_5 \times f_R\left(x_1\right) & u \leq 1, \hat{x}_1 > 0 \\ 0 & otherwise \end{cases} \\
\dot{\hat{x}}_2 &= \begin{cases} \frac{1}{0.3} \times \left[-\hat{x}_2 + u - (u-1) \times \hat{x}_3 \times f_L\left(\hat{x}_1\right)\right] & u > 1 \\ \frac{1}{0.3} \times \left[-\hat{x}_2 + u - (u-1) \times \hat{x}_4 \times f_R\left(\hat{x}_1\right)\right] & u \leq 1 \end{cases} \\
\dot{\hat{x}}_3 &= 0 \\
\dot{\hat{x}}_4 &= 0 \\
\dot{\hat{x}}_5 &= 0
\end{aligned}
\tag{5.25}
$$

The Jacobian matrices of the continuous-time system is expressed as:

$$
A = \frac{d\dot{\hat{x}}}{dt} = \begin{bmatrix} A_{11} & 0 & A_{13} & A_{14} & A_{15} \\ A_{21} & A_{22} & A_{23} & A_{24} & 0 \\ 0 & 0 & 0 & 0 & 0 \\ 0 & 0 & 0 & 0 & 0 \\ 0 & 0 & 0 & 0 & 0 \end{bmatrix}
\tag{5.26}
$$

$$
C = \begin{bmatrix} 0 & 1 & 0 & 0 & 0 \end{bmatrix}
$$

where

$$
\begin{aligned}
A_{11} &= \begin{cases} 0.21 \times \hat{x}_3 \times f_{sat}(u_d) \times \left(1 - \frac{1}{u}\right) \times \hat{x}_5 \times \frac{(5.1\hat{x}_1 + 1.2)\mathrm{e}^{2.55 \times \hat{x}_1^2 + 1.2 \times \hat{x}_1}}{41.66} & u > 1, \hat{x}_1 < 1 \\ 0.21 \times \hat{x}_4 \times f_{sat}(u_d) \times \left(1 - \frac{1}{u}\right) \times \hat{x}_5 \times \frac{(26.9\hat{x}_1 - 20.63)\mathrm{e}^{13.45 \times \hat{x}_1^2 - 20.63\hat{x}_1}}{-0.9992} & u \leq 1, \hat{x}_1 > 0 \\ 0 & otherwise \end{cases} \\
A_{13} &= \begin{cases} 0.21 \times f_{sat}(u_d) \times \left(1 - \frac{1}{u}\right) \times \hat{x}_5 \times f_L(\hat{x}_1) & u > 1, \hat{x}_1 < 1 \\ 0 & otherwise \end{cases} \\
A_{14} &= \begin{cases} 0.21 \times f_{sat}(u_d) \times \left(1 - \frac{1}{u}\right) \times \hat{x}_5 \times f_R(\hat{x}_1) & u \leq 1, \hat{x}_1 > 0 \\ 0 & otherwise \end{cases} \\
A_{15} &= \begin{cases} 0.21 \times \hat{x}_3 \times f_{sat}(u_d) \times \left(1 - \frac{1}{u}\right) \times f_L(\hat{x}_1) & u > 1, \hat{x}_1 < 1 \\ 0.21 \times \hat{x}_4 \times f_{sat}(u_d) \times \left(1 - \frac{1}{u}\right) \times f_R(\hat{x}_1) & u \leq 1, \hat{x}_1 > 0 \\ 0 & otherwise \end{cases} \\
A_{21} &= \begin{cases} -\frac{1}{0.3} \times (u-1) \times \hat{x}_3 \times \frac{(5.1\hat{x}_1 + 1.2)\mathrm{e}^{2.55 \times \hat{x}_1^2 + 1.2 \times \hat{x}_1}}{41.66} & u > 1 \\ -\frac{1}{0.3} \times (1-u) \times \hat{x}_4 \times \frac{(26.9\hat{x}_1 - 20.63)\mathrm{e}^{13.45 \times \hat{x}_1^2 - 20.63\hat{x}_1}}{0.9992} & u \leq 1 \end{cases} \\
A_{22} &= -\frac{1}{0.3} \\
A_{23} &= \begin{cases} -\frac{1}{0.3} \times (u-1) \times f_L(\hat{x}_1) & u > 1, \hat{x}_1 < 1 \\ 0 & otherwise \end{cases} \\
A_{24} &= \begin{cases} \frac{1}{0.3} \times (1-u) \times f_R(\hat{x}_1) & u \leq 1, \hat{x}_1 > 0 \\ 0 & otherwise \end{cases}
\end{aligned}
\tag{5.27}
$$

The above continuous-time system can be discretized via Euler discretization as follows. The step size T_s is set as 0.01s.

$$
\begin{aligned}
A_k &= I + T_s A \\
B_k &= T_s B \\
C_k &= C
\end{aligned}
\tag{5.28}
$$

Therefore, the extended Kalman-filter for the TWC model is implemented as: **Prediction Cycle:**

$$
\begin{aligned}
&\text{Predicted state estimate: } \hat{x}_{k+1|k} = \hat{x}_k + T_s \dot{\hat{x}}_{k|k} \\
&\text{Forecast error covariance: } P_{k+1|k} = A_k P_k A_k^T + N_k
\end{aligned}
\tag{5.29}
$$

Filtered Cycle:

$$\begin{aligned} \text{EKF gain: } & L_{k+1} = P_{k+1|k} C_{k+1}^T \left(R_{k+1} + C_{k+1}^T P_{k+1|k} C_{k+1} \right) \\ \text{Updated state estimation: } & \hat{x}_{k+1|k+1} = \hat{x}_{k+1|k} + L_{k+1} \left(y_{k+1} - C_{k+1} \hat{x}_{k+1|k} \right) \\ \text{Posterior error covariance: } & P_{k+1} = \left(I - L_{k+1} C_{k+1} \right) P_{k+1|k} \end{aligned} \tag{5.30}$$

Per Fig. 5.2, the EKF is used in the FOS estimator. The input signal engine-outlet λ_{up} and disturbance input signal W_{air} (approximated by W_{exh}) are known to both of the TWC model and the EKF. The EKF corrects the FOS estimation based on the difference between the modeled $\lambda_{dn,\tau}$ and the actual sensor measurement $\lambda_{dn,\tau}$.

5.5.2 Extended Kalman-filter Tuning

To tune the extended Kalman-filter, a drive cycle shown in Fig. 5.15 was run in the reference model and the data was collected. The engine was operated at 1500 RPM and 300Nm torque. In the first 3000s, TWC1 inlet λ_{up} was set as a sinusoidal signal with 0.04 amplitude, 0.4 rad/s frequency and 1 offset, i.e., $\lambda_{up} = 1 + 0.04sin(0.4t)$. Under this large λ_{up} oscillation, the TWC1 FOS kept varying within 0 to 1. This operation provided the EKF with sufficient information to get converged model parameter estimations (α_L, α_R, and $1/C$) based on the initial guess from the model calibration. A simple PI controller was implemented in the reference model to track the FOS set points after the 3000s calibration procedure finished.

Two different EKF implementation modes were considered. In EKF Mode 1, the EKF used the same N_k for the entire drive cycle. In EKF Mode 2, the parameter updates of α_L,

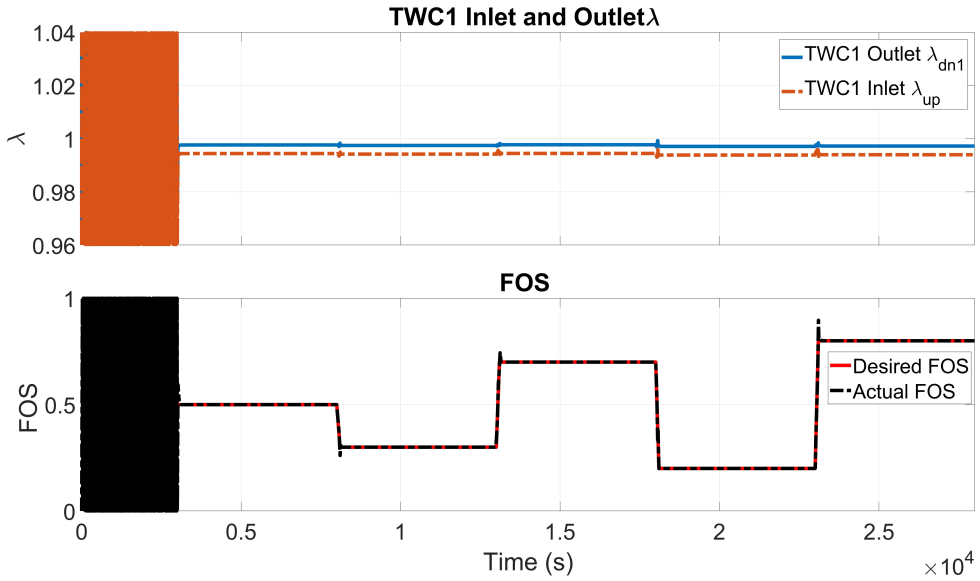

Figure 5.15. : Drive cycle for EKF calibration (0 - 3000s for EKF calibration, 3000 - 28000s for FOS estimation test)

α_R, and $1/C$ turned off after the calibration was finished. For both of these two modes, $R_k = 0.1$ during the entire drive cycle.

$$\text{EKF Mode 1: } N_{k1} = \frac{1}{100^2}\begin{bmatrix} 0.1 & 0 & 0 & 0 & 0 \\ 0 & 0.3 & 0 & 0 & 0 \\ 0 & 0 & 0.1 & 0 & 0 \\ 0 & 0 & 0 & 0.1 & 0 \\ 0 & 0 & 0 & 0 & 50 \end{bmatrix}^2$$

$$\text{EKF Mode 2: } N_{k2} = \begin{cases} N_{k1} & t \leq 3000s \\ \frac{1}{100^2}\begin{bmatrix} 0.1 & 0 & 0 & 0 & 0 \\ 0 & 0.3 & 0 & 0 & 0 \\ 0 & 0 & 0 & 0 & 0 \\ 0 & 0 & 0 & 0 & 0 \\ 0 & 0 & 0 & 0 & 0 \end{bmatrix}^2 & t > 3000s \end{cases} \tag{5.31}$$

Fig. 5.16 shows the FOS estimation performance for the drive cycle. Both the EKFs and the model failed to estimate the FOS. Tuning the parameter N_k made few effects on the

estimation result. This issue was caused by an improper setting of the switching points of λ_{up} and λ_{dn} in the control-oriented model. Per Fig 5.15, neither of these two λ values crossed 1 during the FOS estimation test. The crossover point was 0.9944 for λ_{up} and 0.9978 for λ_{dn}. Therefore, the model is revised as follows:

$$
\begin{aligned}
\dot{x} &= \begin{cases} 0.21 \times \frac{1}{C} \times f_{sat}(u_d) \times \left(1 - \frac{0.9944}{u}\right) \times \alpha_L \times f_L(x) & 0 < x < 1 \quad and \quad u > 0.9944 \\ 0.21 \times \frac{1}{C} \times f_{sat}(u_d) \times \left(1 - \frac{0.9944}{u}\right) \times \alpha_R \times f_R(x) & 0 < x < 1 \quad and \quad u \leq 0.9944 \\ 0 & otherwise \end{cases} \\
y_1 &= x_1 \\
y_2 &= \begin{cases} u - (u - 0.9978) \times \alpha_L \times f_L(x) & u > 0.9944 \\ u - (u - 0.9978) \times \alpha_R \times f_R(x) & u \leq 0.9944 \end{cases}
\end{aligned}
\tag{5.32}
$$

and the augmented system (per equation (5.24)) is revised to:

$$
\begin{aligned}
\dot{\hat{x}}_1 &= \begin{cases} 0.21 \times \hat{x}_3 \times f_{sat}(u_d) \times \left(1 - \frac{0.9944}{u}\right) \times \hat{x}_5 \times f_L(x_1) & u > 0.9944, \hat{x}_1 < 1 \\ 0.21 \times \hat{x}_4 \times f_{sat}(u_d) \times \left(1 - \frac{0.9944}{u}\right) \times \hat{x}_5 \times f_R(x_1) & u \leq 0.9944, \hat{x}_1 > 0 \\ 0 & otherwise \end{cases} \\
\dot{\hat{x}}_2 &= \begin{cases} \frac{1}{0.3} \times [-\hat{x}_2 + u - (u - 0.9978) \times \hat{x}_3 \times f_L(\hat{x}_1)] & u > 0.9944 \\ \frac{1}{0.3} \times [-\hat{x}_2 + u - (u - 0.9978) \times \hat{x}_4 \times f_R(\hat{x}_1)] & u \leq 0.9944 \end{cases} \\
\dot{\hat{x}}_3 &= 0 \\
\dot{\hat{x}}_4 &= 0 \\
\dot{\hat{x}}_5 &= 0
\end{aligned}
\tag{5.33}
$$

The Jacobian matrix A (per equation (5.27)) is also re-calculated based on the revised model. This tuning operation could be used to deal with the λ sensor offset.

Fig. 5.17 shows the FOS estimation performance after resetting the crossover points of λ_{up} and λ_{dn}. Same N_k and R_k were used for the EKF. It can be seen that both the model and the EKF started to work after this revision.

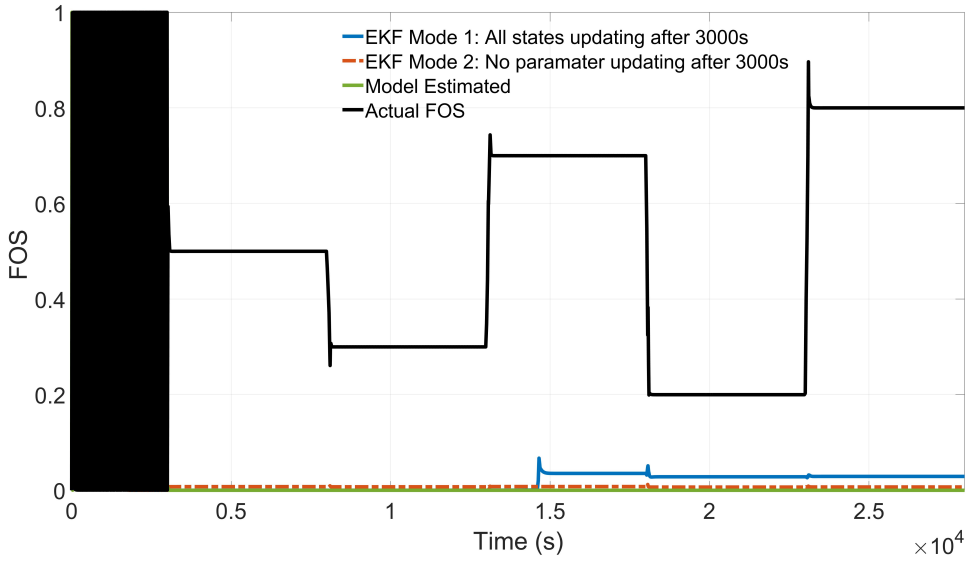

Figure 5.16. : FOS estimation performance

5.5.3 Extended Kalman-filter Testing

To test the EKF estimation performance, a drive cycle (per Fig. 5.18) with oscillated FOS set points was performed on the reference model and the data was collected. A PI controller was implemented to control the TWC1 FOS by manipulating the commanded engine λ_{up}. The engine was operated at 1500 RPM and 300Nm. Fig. 5.19 and 5.20 show the operating points on the model plant. With a larger FOS oscillation, the commanded and actual TWC1 inlet λ_{up} oscillations are greater.

Fig. 5.21 shows the estimation performance of the EKF and the model. Compared to the model estimation, both EKF Mode 1 and EKF Mode 2 have some improvements. EKF Mode 1 has a better overall estimation performance than EKF Mode 2. Fig. 5.22 shows a 100s zoomed plot of the estimation performance for each FOS amplitude. During 14900 - 15000s when the desired FOS oscillates within 0.4 to 0.6, EKF Mode 2 fails to estimate the FOS while EKF Mode 1 still has a good prediction. However, EKF Mode 1 tends to have some divergence issues for the parameter $1/C$ estimation at the last step when the desired FOS is a fixed point (per Fig. 5.23). Considering the fact that the change of TWC capacity is a long-term aging issue, the update of the parameter $1/C$ is turned off after the calibration

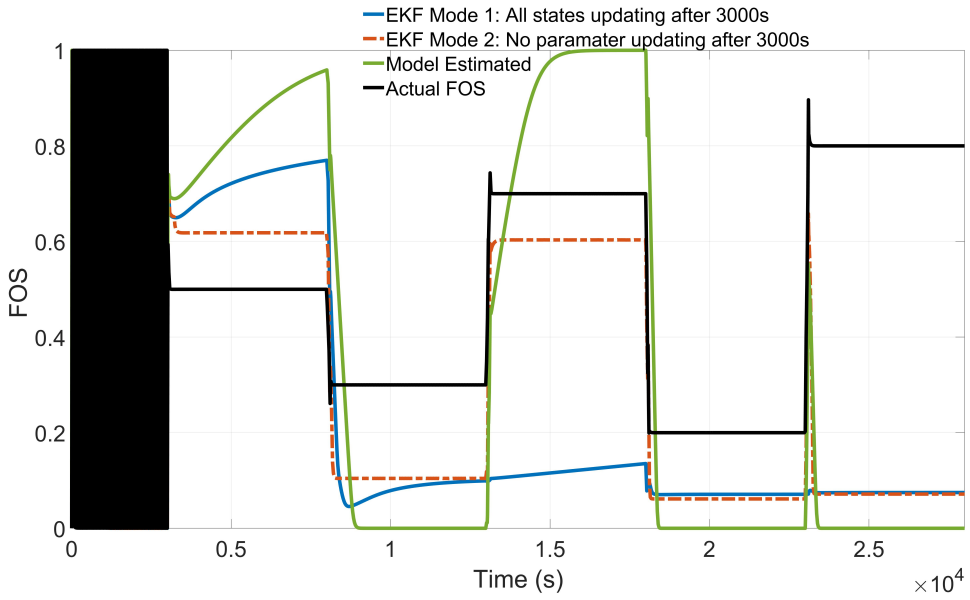

Figure 5.17. : FOS estimation performance after resetting the λ crossover points

finishes for the EKF implementation. That is to say, $N_k(5,5)$ is set as 0 after the calibration procedure.

5.6 Robust Controller Design

A robust MISO controller is designed for the TWC to control the FOS by manipulating the desired engine λ. Fig. 5.24 shows the control block for the robust controller. The robust controller is designed based on the framework developed in Chapter 4. The robust controller has five inputs, the desired FOS (FOS_{des}), EKF estimated FOS (FOS_{est}), measured TWC downstream λ ($\lambda_{dn,m}$), measured engine-out air flow rate W_{air} (approximated by the exhaust flow rate W_{exh}), and measured TWC upstream (engine-out) λ ($\lambda_{up,m}$). Four error/uncertainty blocks, inner AFR control error, upstream λ sensor error, TWC model uncertainty, and output measurement errors, are considered in the robust controller. Fig. 5.25 shows the general control configuration for the TWC FOS control. The perturbed closed-loop system has three exogenous inputs, the sensor noise n (including the TWC upstream λ sensor noise n_{u0} and downstream sensor noise n_0), the disturbance input (W_{air}) and the reference input (FOS_{des}). The two exogenous outputs of the closed-loop system are the weighted output performance (FOS control error) and the weighted input performance (desired engine λ).

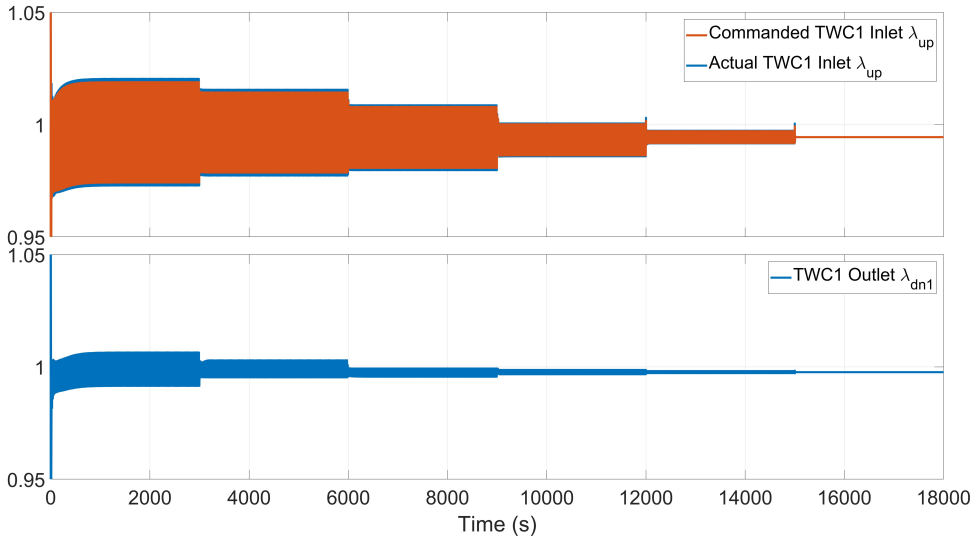

Figure 5.18. : FOS estimation performance after resetting the λ crossover points

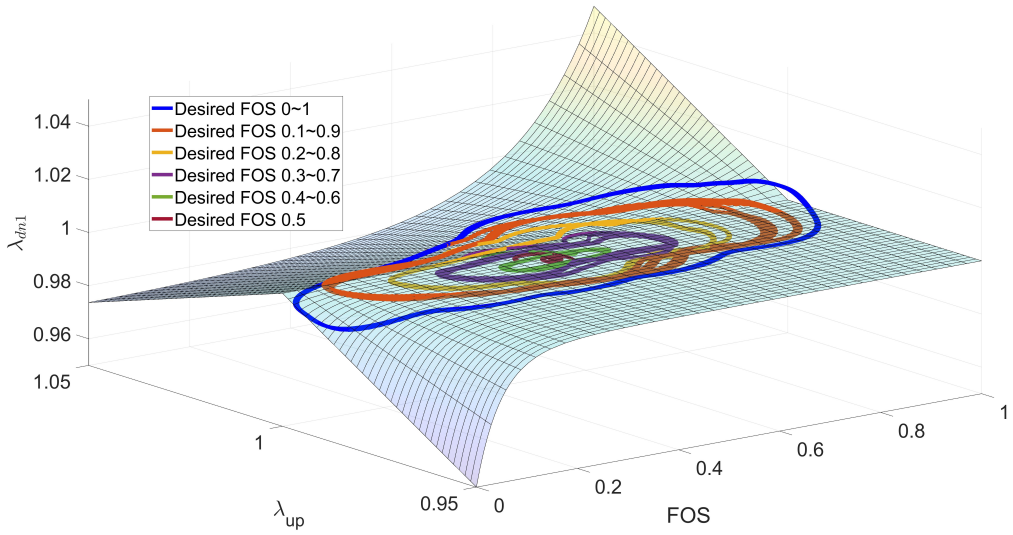

Figure 5.19. : Operating points for EKF testing (3D)

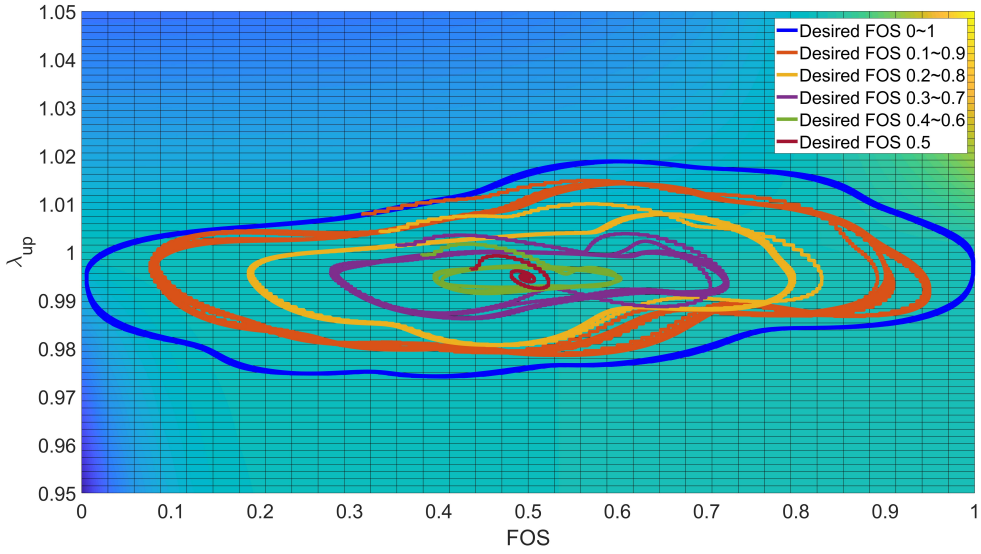

Figure 5.20. : Operating points for EKF testing (2D)

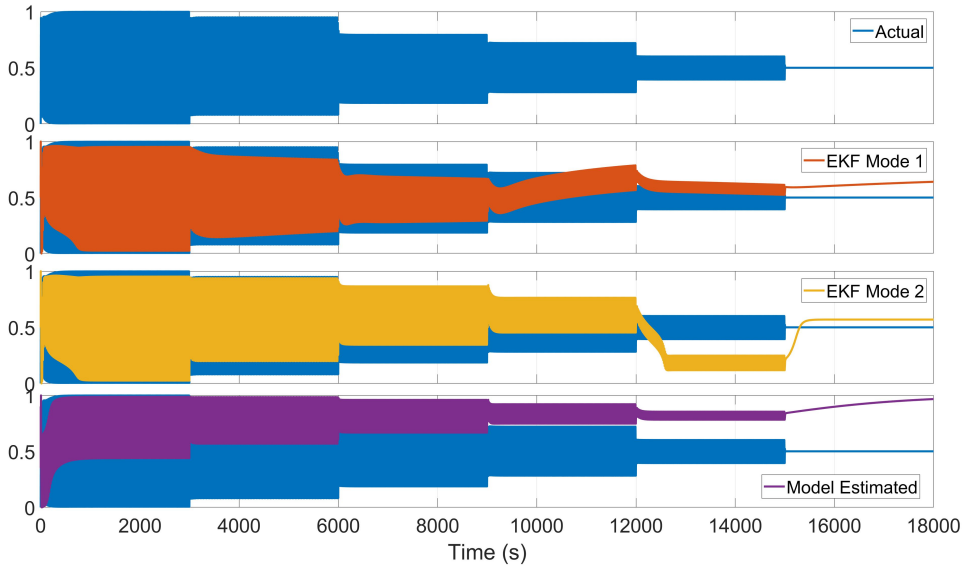

Figure 5.21. : FOS estimation performance for oscillated FOS set points

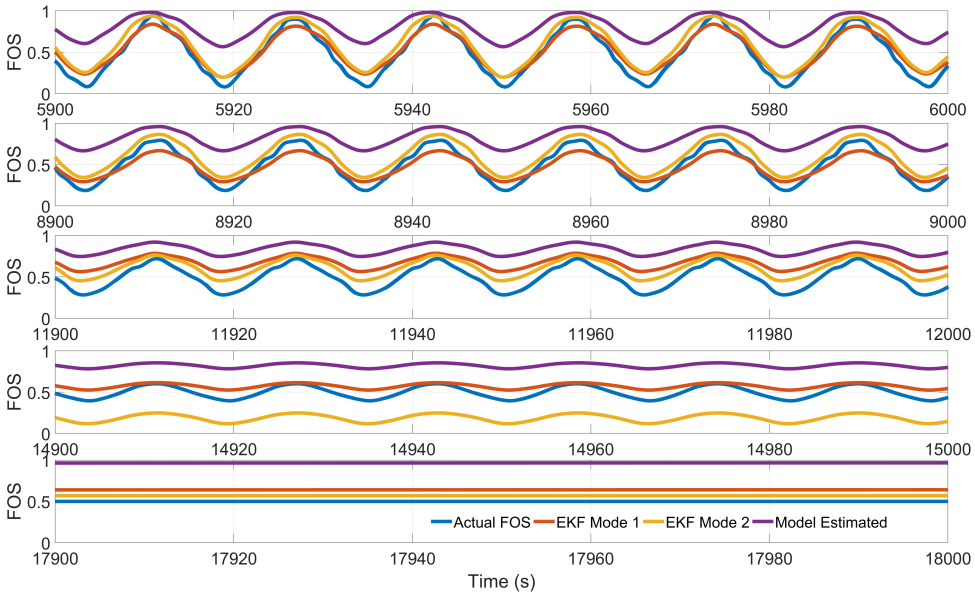

Figure 5.22. : FOS estimation performance for oscillated FOS set points (100s zoomed)

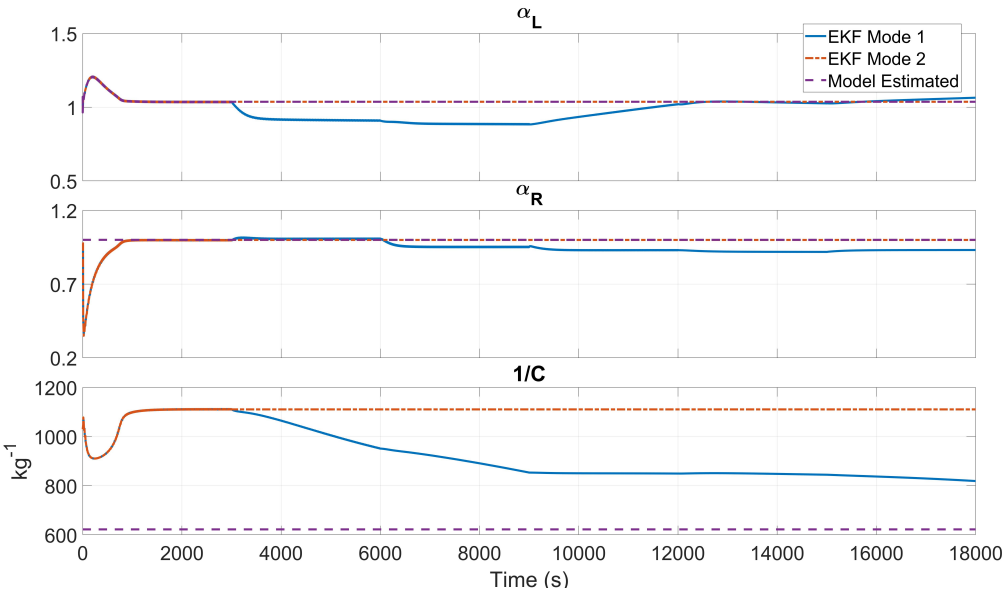

Figure 5.23. : Parameter estimation performance for oscillated FOS set points

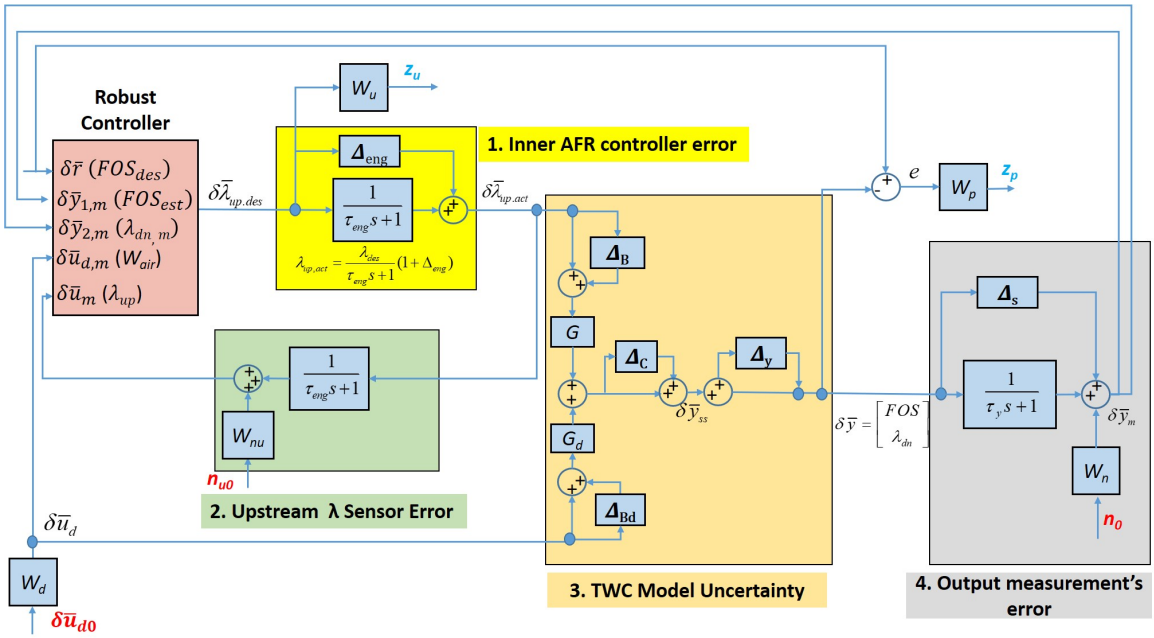

Figure 5.24. : Robust control block for TWC FOS

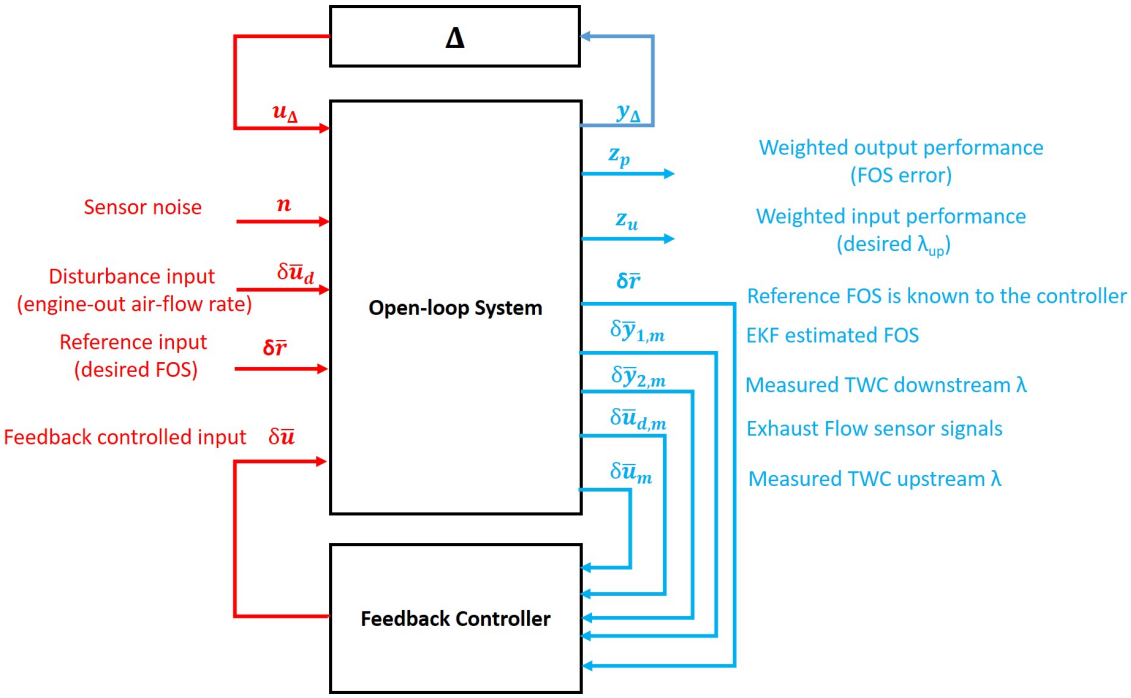

Figure 5.25. : General control configuration for TWC FOS

5.6.1 Inner AFR Control Error

The inner loop AFR control error is modeled by a first-order approximation:

$$\delta\bar{\lambda}_{up,act} = \frac{\delta\bar{\lambda}_{des}}{\tau_{eng}s+1}(1+\Delta_{eng}) \tag{5.34}$$

where the time constant τ_{eng} is approximated by 0.05s and the frequency-shaped uncertainty Δ_{eng} is:

$$\Delta_{eng} = \frac{\frac{1}{20}s+0.001}{\frac{1}{20\times 0.01}s+1}\delta, \text{ where} -1<\delta<1 \tag{5.35}$$

where the engine λ control error is within 0.001 at steady-state and is 0.01 when the frequency is higher than 20rad/s.

5.6.2 Upstream λ Sensor Error

The upstream λ sensor dynamics is modeled by a first-order approximation:

$$\delta\bar{u}_m = \frac{\delta\bar{\lambda}_{up,act}}{\tau_{\lambda_{up}}s+1} + W_{nu}n_{u0} \tag{5.36}$$

where the time constant $\tau_{\lambda_{up}}$ is 0.3s and the noise shaping function W_{nu} is:

$$W_{nu} = 0.024\frac{\left(\frac{1}{0.18}s+1\right)\left(\frac{1}{2.1}s+1\right)}{\left(\frac{1}{1.2}s+1\right)\left(\frac{1}{9}s+1\right)\left(\frac{1}{80}s+1\right)\left(\frac{1}{100}s+1\right)} \tag{5.37}$$

5.6.3 TWC Model Uncertainty

The model uncertainty block includes the parametric state-space uncertainty (Δ_B,Δ_{B_d} and Δ_C) and multiplicative output uncertainty. The parametric uncertainty is to account for the uncertain parameters in the state space model and is expressed as:

$$\delta\bar{y}_{ss} = \bar{C}_p(sI-A)^{-1}\bar{B}_p\delta\bar{u} + \bar{C}_p(sI-A)^{-1}\bar{B}_{pd}\delta\bar{u}_d \tag{5.38}$$

where $\bar{B}_{pd}$, $\bar{B}_p$ and $\bar{C}_p$ are the normalized perturbed state space matrices derived from the model in equation (5.14):

$$\begin{aligned}\bar{B}_p &= \bar{B}(x_{\mathrm{e},}u_{\mathrm{e}} + \Delta u, u_{de} + \Delta u_d)\\ \bar{B}_{pd} &= \bar{B}_d(x_{\mathrm{e},}u_{\mathrm{e}} + \Delta u, u_{de} + \Delta u_d)\\ \bar{C}_p &= \bar{C}(x_{\mathrm{e},}u_{\mathrm{e}} + \Delta u, u_{de} + \Delta u_d)\end{aligned} \tag{5.39}$$

The multiplicative output uncertainty Δ_y is to account for the uncaptured dynamics of the state-space model:

$$\delta\bar{y} = (1 + \Delta_y)\,\delta\bar{y}_{ss} \tag{5.40}$$

5.6.4 Output Measurement Errors

The output measurement errors are expressed as:

$$\delta\bar{y}_m = \frac{\delta\bar{y}}{\tau_y s + 1} + \delta\bar{y}\Delta_s + W_n n_0 \tag{5.41}$$

where τ_y is the time constant, Δ_s is the measurement bias error, W_n is the noise shaping function and n_0 is noise.

For the FOS estimator, the first-order dynamics and the shaped noise are ignored, i.e., $\tau_{y_1} = 0$ and $W_{n_1} = 0$:

$$\begin{aligned}\delta\bar{y}_{1,m} &= (1 + \Delta_{s_1})\,\delta\bar{y}_1\\ \Delta_{s_1} &= 0.1\delta,\ \text{where} - 1 < \delta < 1\end{aligned} \tag{5.42}$$

For the TWC downstream λ sensor, the measurement bias error is ignored, i.e., $\Delta_{s_2} = 0$:

$$\begin{aligned}\delta\bar{y}_{2,m} &= \frac{\delta\bar{y}_2}{\tau_{y_2} s + 1} + W_{n_2} n_2\\ W_{n_2} = W_{nu} &= 0.024\frac{\left(\frac{1}{0.18}s + 1\right)\left(\frac{1}{2.1}s + 1\right)}{\left(\frac{1}{1.2}s + 1\right)\left(\frac{1}{9}s + 1\right)\left(\frac{1}{80}s + 1\right)\left(\frac{1}{100}s + 1\right)}\\ \tau_{y_2} &= 0.3s\end{aligned} \tag{5.43}$$

5.6.5 Weighting Function

Output Weighting Function

The following second-order output weighting function is used to shape the FOS control error in the frequency domain:

$$W_p = \left(\frac{\frac{s}{\sqrt{M^*}} + {\omega^*}_B}{s + {\omega^*}_B \sqrt{A^*}} \right)^2 \tag{5.44}$$

where M^* is the maximum error at high frequencies, A^* is the steady-state error and ω^* is the frequency where error reaches 100%. The values of these three parameters are listed as follows:

$$\begin{aligned} M^* &= 1 \\ A^* &= 0.3 \\ \omega^* &= 1 \quad rad/s \end{aligned} \tag{5.45}$$

The inverse of W_p (${W_p}^{-1}$) shown in Fig 5.26 represents the shaped upper bound of the FOS control error.

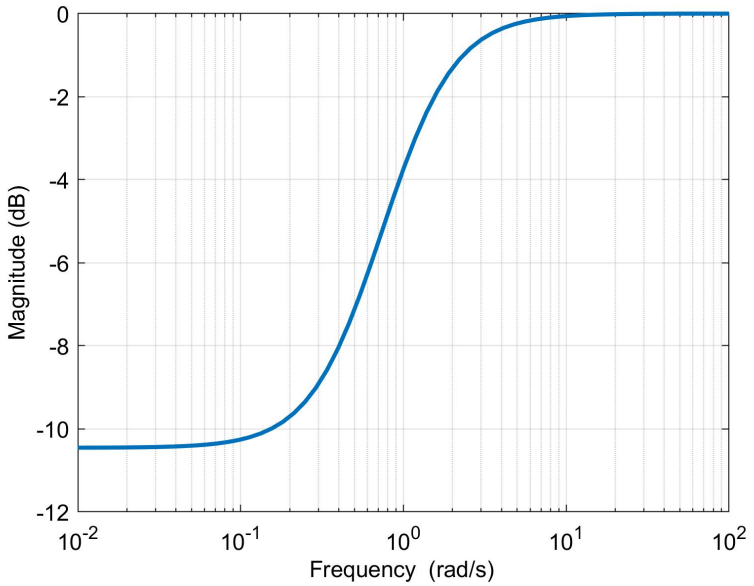

Figure 5.26. : Bode plot of the output weighting function inverse

Input Weighting Function

The input weighting function W_u is used to set the physical limits of the controlled input. W_u is modeled as a first-order high-pass filter in the following format:

$$W_u = \frac{\tau_u s + 1}{\frac{\tau_u s}{100} + 1} \tag{5.46}$$

where τ_u is the actuator response time.

For the commanded engine λ, W_u is:

$$W_u = \frac{\frac{s}{33} + 1}{\frac{s}{3300} + 1} \tag{5.47}$$

The inverse of W_u (${W_u}^{-1}$) is shown in Fig 5.27. The commanded engine λ is penalized by a factor of 0.01 at high frequencies.

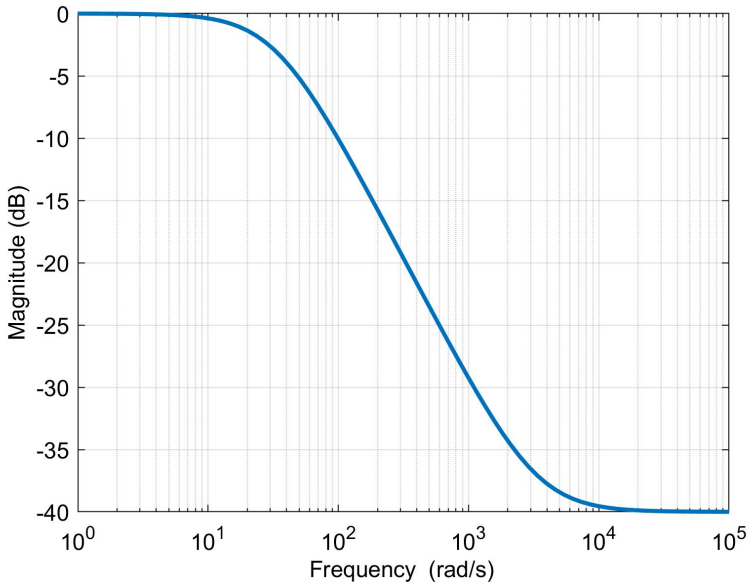

Figure 5.27. : Bode plot of the input weighting function inverse

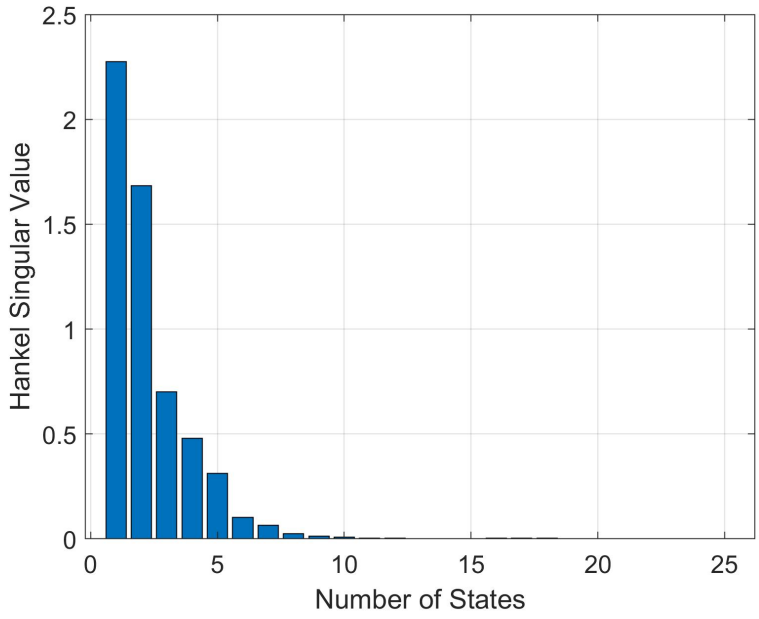

Figure 5.28. : The Hankel singular values of the original synthesized controller

Disturbance Weighting Function

A disturbance shaping function W_d is used to identify the bandwidth of the disturbance input W_{air}:

$$\delta\bar{u}_d = \frac{\delta\bar{u}_{d0}}{\tau_{u_d}s + 1} \tag{5.48}$$

where $\delta\bar{u}_{d0}$ denotes the normalized disturbance input. The time constant τ_{u_d} is 0.05s.

5.6.6 Transfer Function of the Robust Controller

The robust controller is computed based on the μ-synthesis method. The toolbox "dksyn" for performing DK-iteration in MATLAB is used for the controller synthesis.

Fig 5.28 shows the Hankel singular values of the original synthesized MISO controller. The Hankel singular values can be used to quantify the importance of each state in the corresponding input–output map and it is a useful tool for model reduction of the linear system[75]. For the robust controller, 8 states are selected to reduce the controller order. Fig. 5.29 shows the comparison of the original high-order controller and the simplified controller.

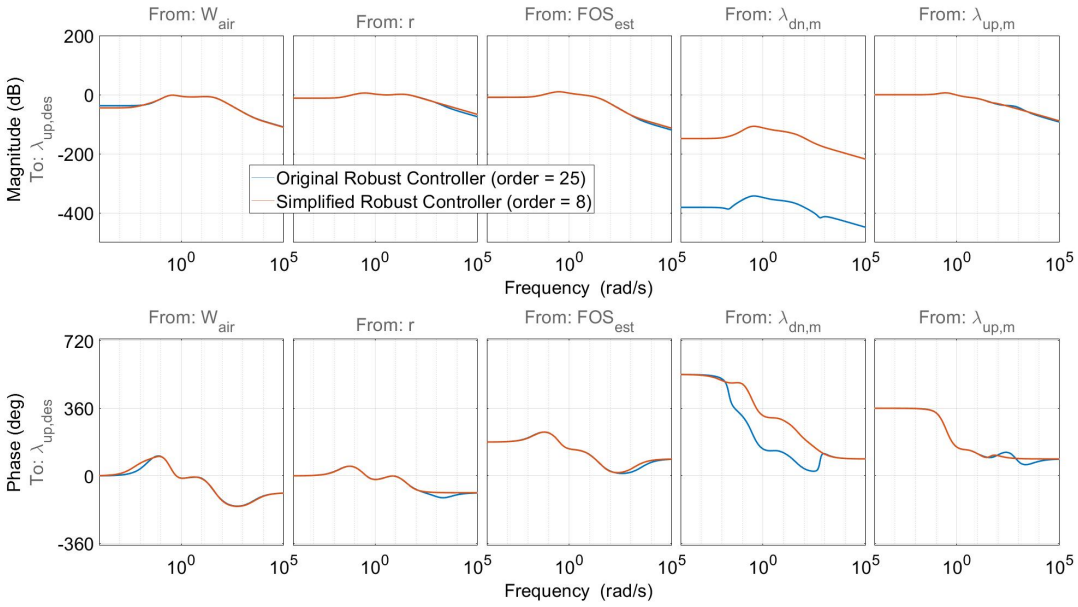

Figure 5.29. : Bode plot comparison of original robust controller and simplified robust controller

5.7 Otto FTP Cycle Emission Testing

A cold start and a warm start Otto FTP cycle tests (per Fig. 5.30) are performed on the reference model in SIMULINK to evaluate the emission reduction performance of the proposed algorithm. The reference SIMULINK model has a pre-existed AFR controller and incorporates the AVL TWC model. It is calibrated based on the experimental data and serves as a virtual test benth. Per Fig. 5.30, the lower bound of the torque command is 0. That is to say, the fuel cut-off events are not included in this test.

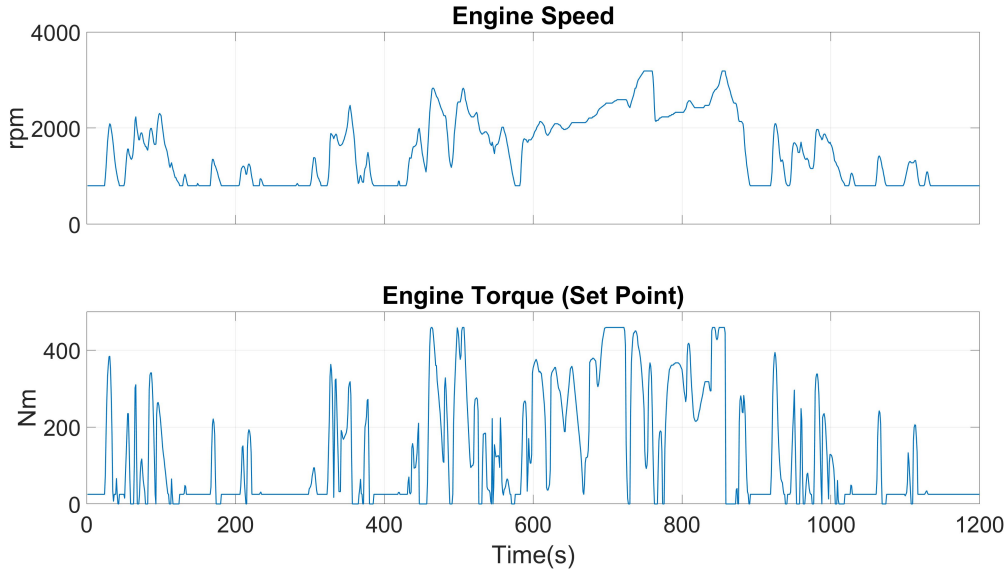

Figure 5.30. : Otto FTP cycle

5.7.1 Simulation Setups

The pre-existing inner loop AFR controller is used to control the engine λ based on the commanded engine λ. A UEGO sensor is placed upstream of the TWC1 and an EGO sensor is placed downstream of the TWC1. The response times of both the UEGO and EGO sensors is 0.3s. The TWC2 is not controlled and used as a passive TWC. The emissions are measured at the TWC2 outlet.

A first-order dynamics block is added to the engine-out (TWC upstream) λ measurement to simulate the UEGO sensor dynamics. A λ-voltage conversion table block converts the

TWC1 downstream λ to voltage based on the sensor voltage curve (per Fig. 5.31). The voltage signal is filtered by a first-order transfer function block to simulate the sensor dynamics.

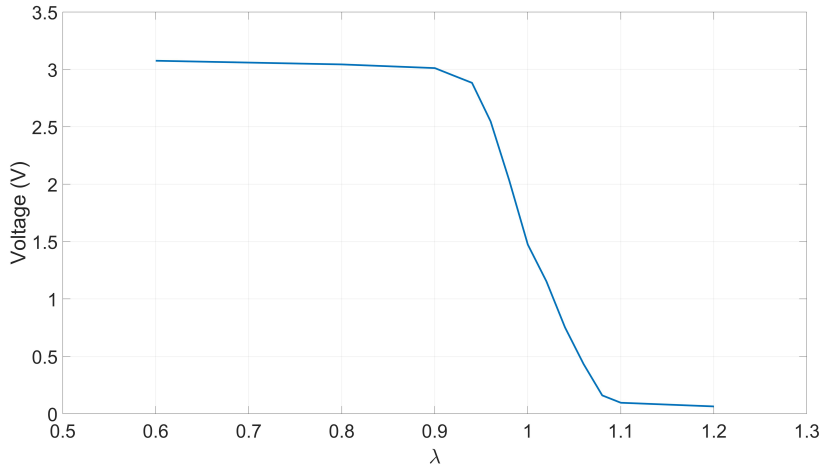

Figure 5.31. : HEGO voltage vs. λ

Three different control strategies are tested for emission comparisons. **Strategy 1: Constant λ Control** For the constant λ control strategy (per Fig. 5.32), only the inner loop AFR controller is used. Three different λ set points, 0.99, 0.9944 and 1, are tested. This control strategy is used as the baseline for the emission comparison.

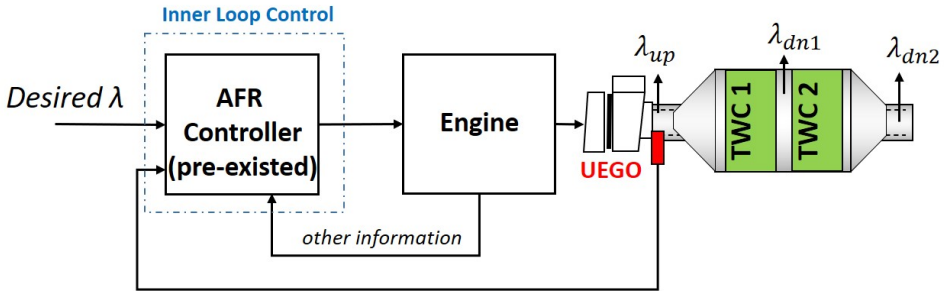

Figure 5.32. : Constant λ Control Strategy Diagram

Strategy 2: Inner Loop AFR Control + Binary Outer Loop Control In this control strategy, both the inner loop AFR controller and the switch-type λ sensor-based outer loop controller are used (per Fig. 5.33). The inner loop controller is the same controller used in Strategy 1. Instead of a constant λ set point, the desired λ is controlled by the outer

loop controller. The TWC1 downstream HEGO sensor voltage is mapped to the λ value via reverse table look-ups. The outer loop controller switches the output command based on the mapped TWC1 downstream HEGO signal and the set point. If the mapped HEGO signal is less than the set point ($\Delta_{dn1} > 0$), the outer loop controller reduces the constant engine command λ_{ref} set point by K_p, otherwise it increases λ_{ref} by K_p. This control strategy is used as an advanced baseline for emission comparison.

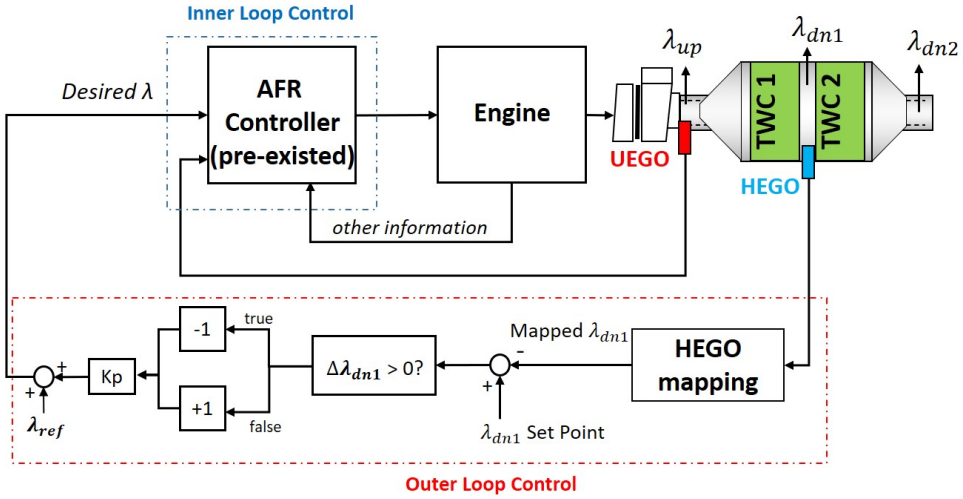

Figure 5.33. : Inner AFR Control + Binary Outer Loop Control Strategy Diagram

Strategy 3: Inner AFR Control + Robust Outer loop Control with EKF Similar to Strategy 2, the two-loop control structure is also used in this control strategy (per Fig 5.34). In this control strategy, the outer loop controller consists of the FOS estimator and the robust controller. The FOS estimator consists of the TWC model and the EKF. The robust controller controls the TWC1 FOS by manipulating the desired engine λ. The same HEGO signal mapping method as Strategy 2 is used in this control strategy. The engine-out exhaust air flow rate is approximated by the exhaust flow rate.

5.7.2 Cold Start Otto FTP Cycle

Strategy 1

Fig. 5.35 shows the emission comparison for different desired λ set points in Strategy 1. It can be seen that the richest λ set point ($\lambda_{des} = 0.99$) has the lowest NO whereas it

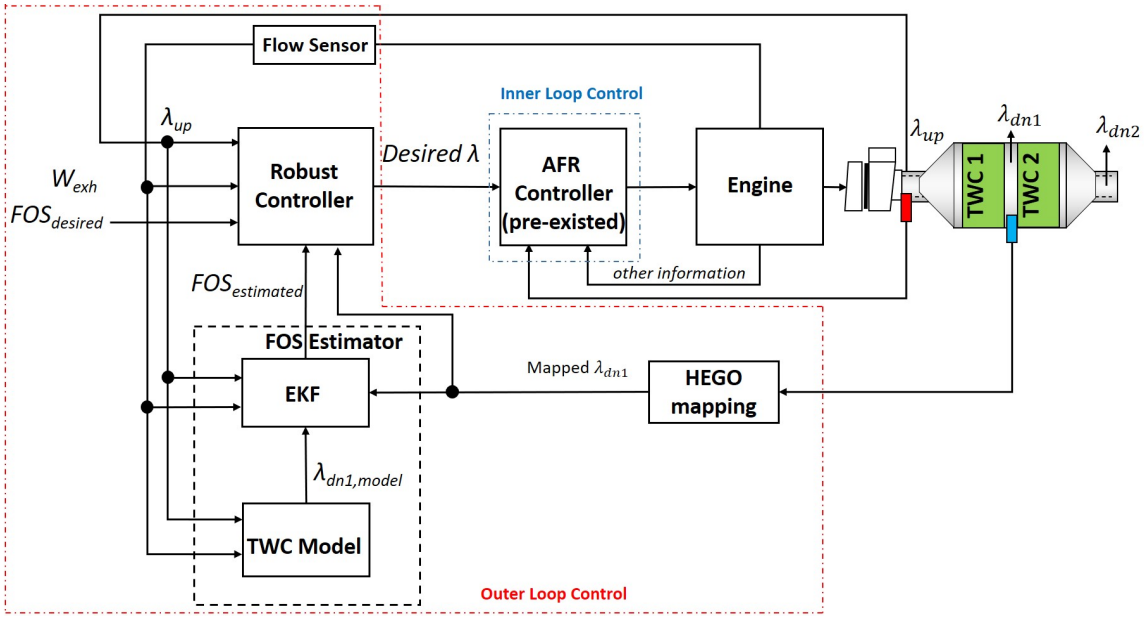

Figure 5.34. : Inner AFR Control + Binary Outer Loop Control Strategy Diagram

results in the highest CO emission. On the contrary, the stoichiometric set point ($\lambda_{des} = 1$) has the lowest CO emission whereas it results in the highest NO emission. Considering the overall performance, 0.9944 is the best set point for λ_{des} and this case is used as the emission baseline.

Fig. 5.36 shows the TWC1 temperature, λ, and TWC1 average FOS for setting $\lambda_{des} = 0.9944$ during the cold start Otto FTP cycle test. The desired engine λ is fixed at 0.9944 for the entire drive cycle. For the first 350s, the TWC1 temperature is lower than 700K and the TWC1 FOS remains around 1. When the TWC1 is warmed-up, the TWC1 FOS starts to oscillate. Fig 5.37 shows the instantaneous emissions for Strategy 1. For the first 350s, the CH_4 has bad emission reduction performance. Large NO peaks in TWC2 outlet are observed around 350s, 500s, 650s and 700s, when the engine has transient operations (per Fig 5.30).

Strategy 2

Compared with Strategy 1, Strategy 2 has a two-loop control structure. Fig 5.38 shows the emission comparison for different K_p in Strategy 2. $K_P = 0.04$ has the best overall

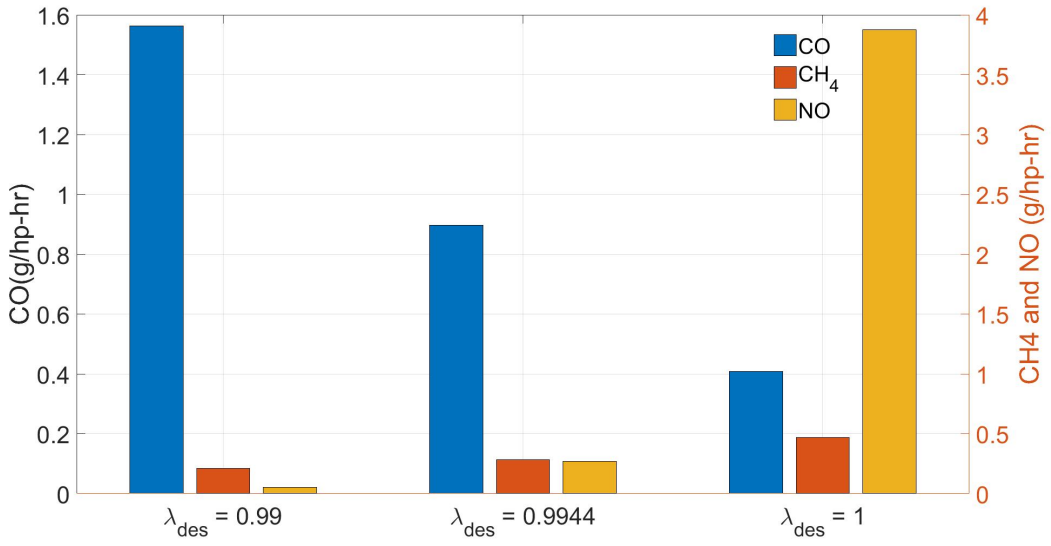

Figure 5.35. : Cold start Otto FTP cycle cumulative emissions for Strategy 1

emission control performance. Therefore, $K_P = 0.04$ in Strategy 2 is used as an advanced baseline for the emission comparison.

Fig. 5.39 shows the temperature, λ and TWC1 average FOS for Strategy 2 when $K_p = 0.04$. For the first 400s, the TWC1 is operated at lean conditions and there is few oxygen stored in TWC1. The controlled engine-out λ (λ_{up}) oscillates more frequently for the first 400s compared to the later time period when TWC1 gets hotter. After 400s, the TWC1 FOS oscillates between 0 and 1 with the controlled λ_{up} excitation.

Fig. 5.39 shows the instantaneous emissions for Strategy 2. For the first 400s, there is almost no emission reduction for CH_4 or NO. Large NO spikes are observed during $400 - 600$s when the engine has transient operations. Per Fig. 5.30, the desired engine torque varies within $0 - 450$Nm and the speed varies within $800 - 3000$ RPM aggressively during this period.

Strategy 3

Fig 5.41 shows the comparison of cumulative emissions for different FOS set points in Strategy 3. When FOS is set within 0.4 to 0.6, better emission reductions can be achieved compared with other FOS set points.

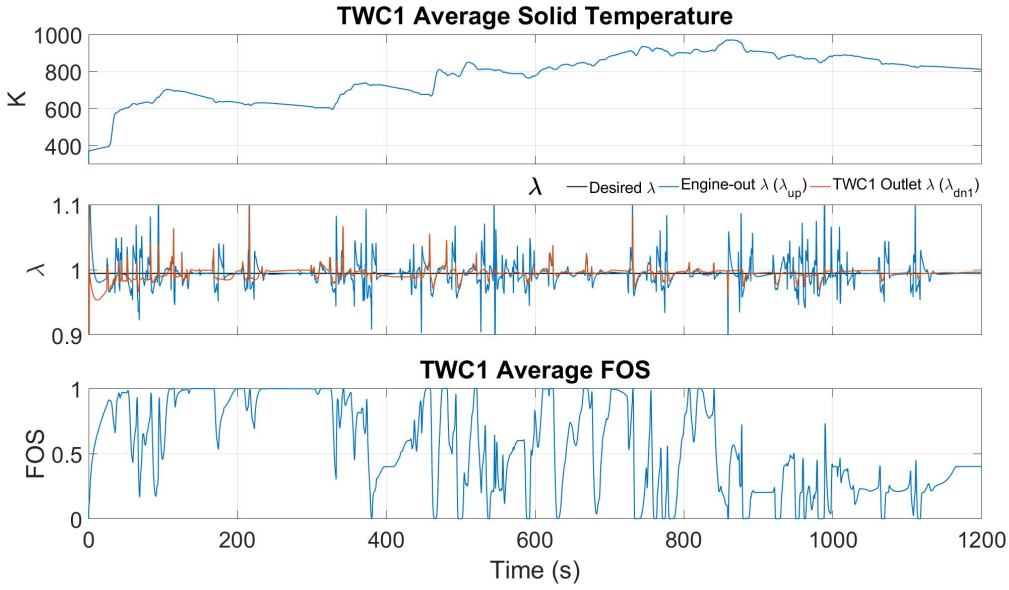

Figure 5.36. : Cold start Otto FTP cycle for Strategy 1 ($\lambda_{des} = 0.9944$)

Fig. 5.42 shows the temperature, λ and TWC1 average FOS for Strategy 3 when desired FOS = 0.4. For the first 50s, the desired λ is set as a constant value 0.9944. The EKF and the robust controller take over at 50s. For the first 400s, the controlled FOS in TWC1 oscillates aggressively between 0 and 1. The output of the outer loop controller, the desired engine λ, has larger oscillations during the first 400s compared to the later time period when TWC1 gets hotter.

Fig. 5.43 shows the instantaneous emissions for Strategy 3 when desired FOS = 0.4. The NO is immediately reduced after 50s in this control strategy and there are no NO emission spikes observed during the entire Otto FTP cycle even when the engine undergoes transient operations. CH_4 is also reduced during the first 400s.

Comparison for Three Control strategies

Fig 5.44 shows the comparison of cumulative emissions for different control strategies. Compared with the baseline (Strategy 1), the best case in Strategy 2 ($K_p = 0.04$) reduces CO by 27.5% and NO by 19.5% whereas CH_4 increases by 3.8%, respectively. For the best case in Strategy 3 (FOS = 0.4), NO can be greatly reduced by 76.4% and CH_4 can be reduced by 24.1% with a very small increase of CO. Compared with the advanced bassline (Strategy

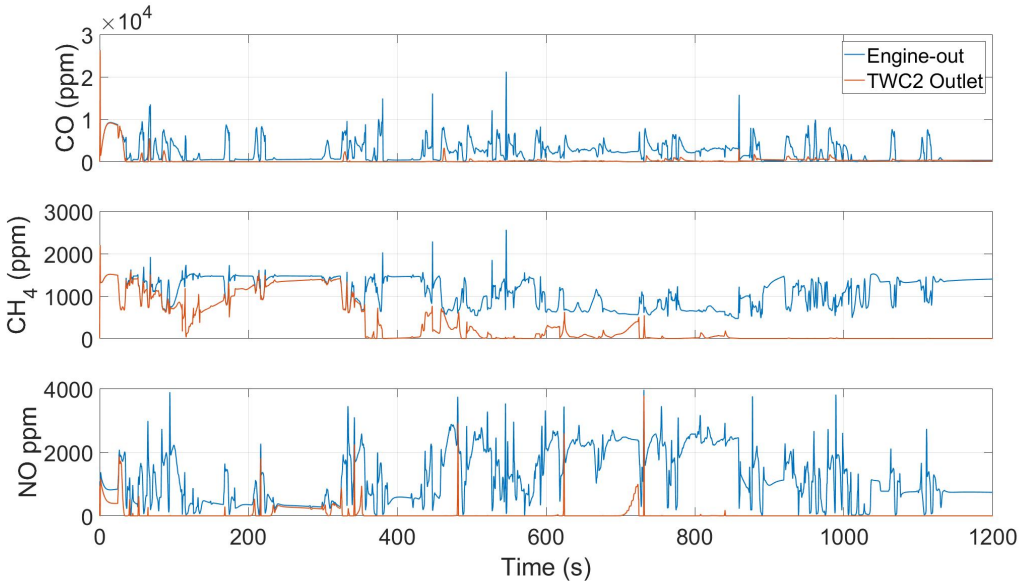

Figure 5.37. : Cold start Otto FTP cycle instantaneous emissions for Strategy 1 ($\lambda_{des} = 0.9944$)

2), the proposed Strategy 3 has 28% and 57% improvements in CH_4 and NO reductions, respectively, for the cold start Otto FTP drive cycle.

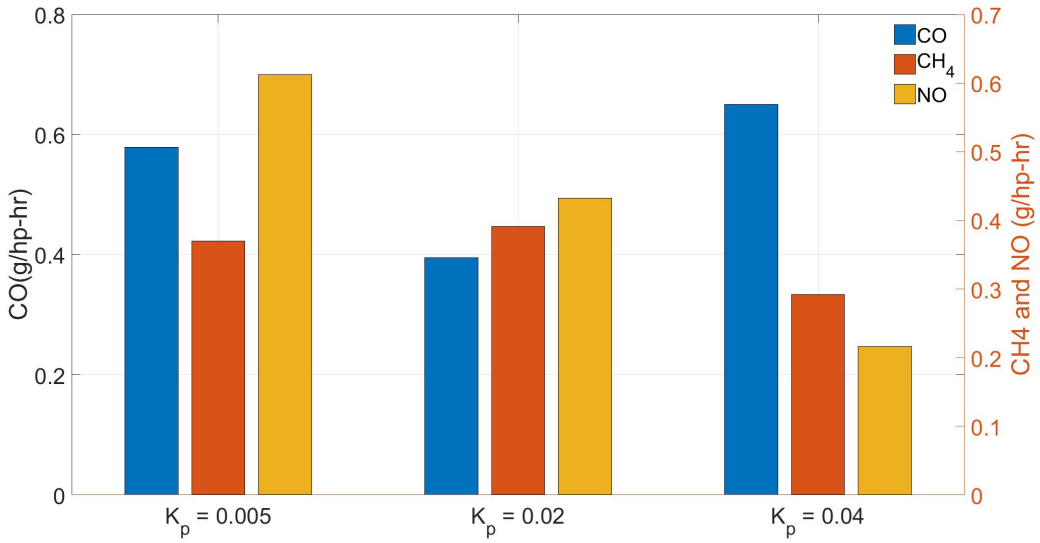

Figure 5.38. : Cold start Otto FTP cycle cumulative emissions for Strategy 2

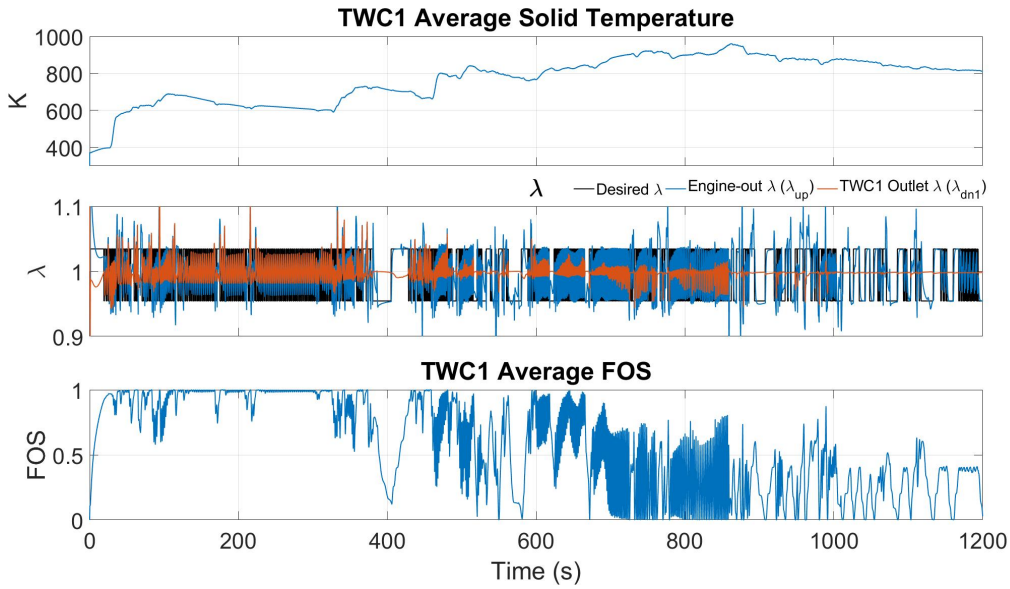

Figure 5.39. : Cold start Otto FTP cycle for Strategy 2 ($K_P = 0.04$)

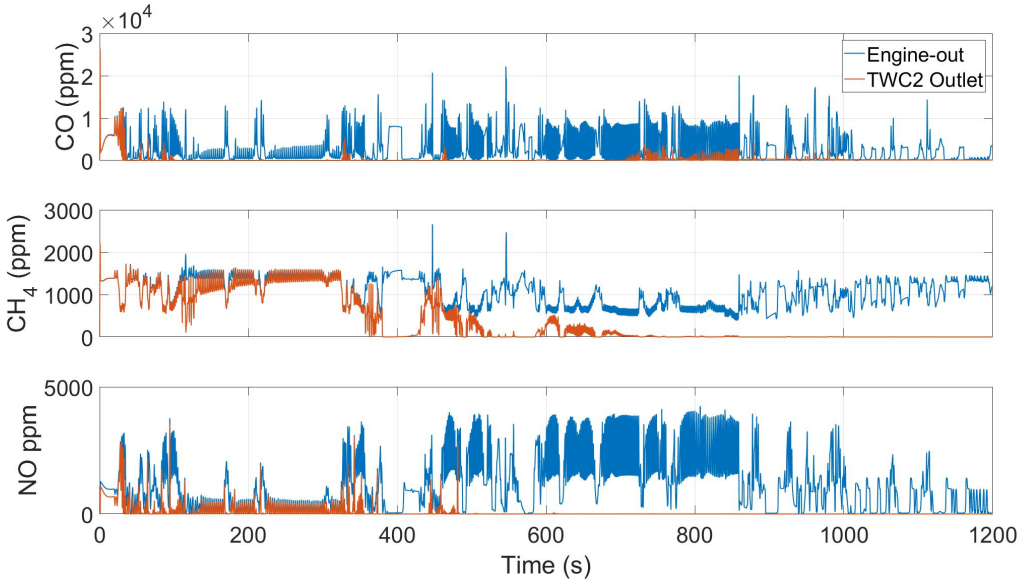

Figure 5.40. : Cold start Otto FTP cycle instantaneous emissions for Strategy 2 ($K_P = 0.04$)

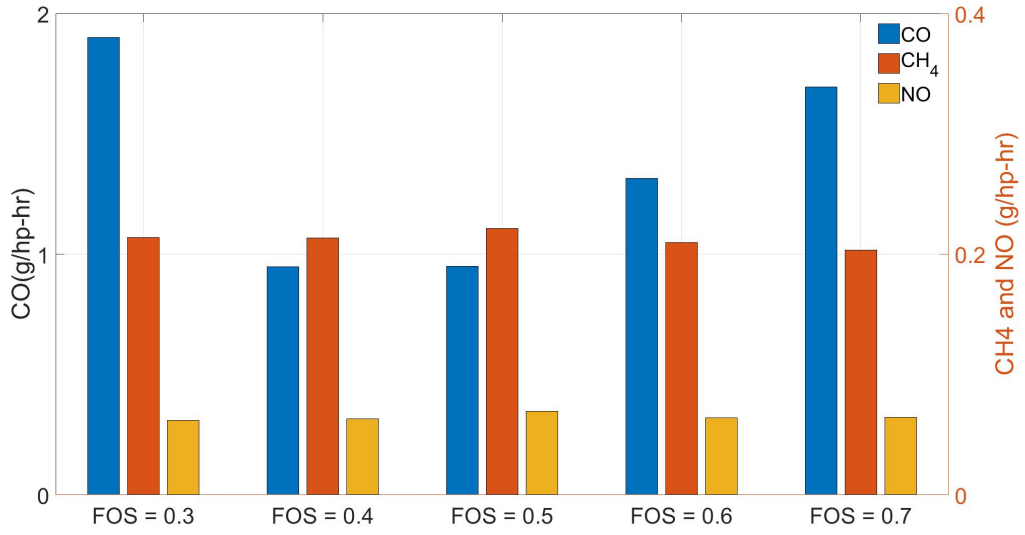

Figure 5.41. : Cold start Otto FTP cycle cumulative emissions for Strategy 3

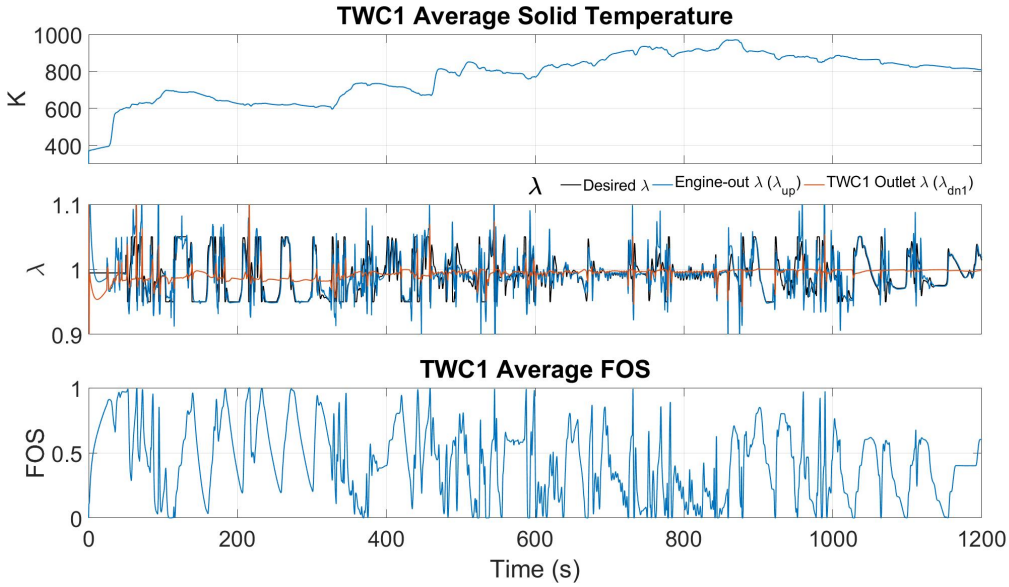

Figure 5.42. : Cold start Otto FTP cycle for Strategy 3 (FOS = 0.4)

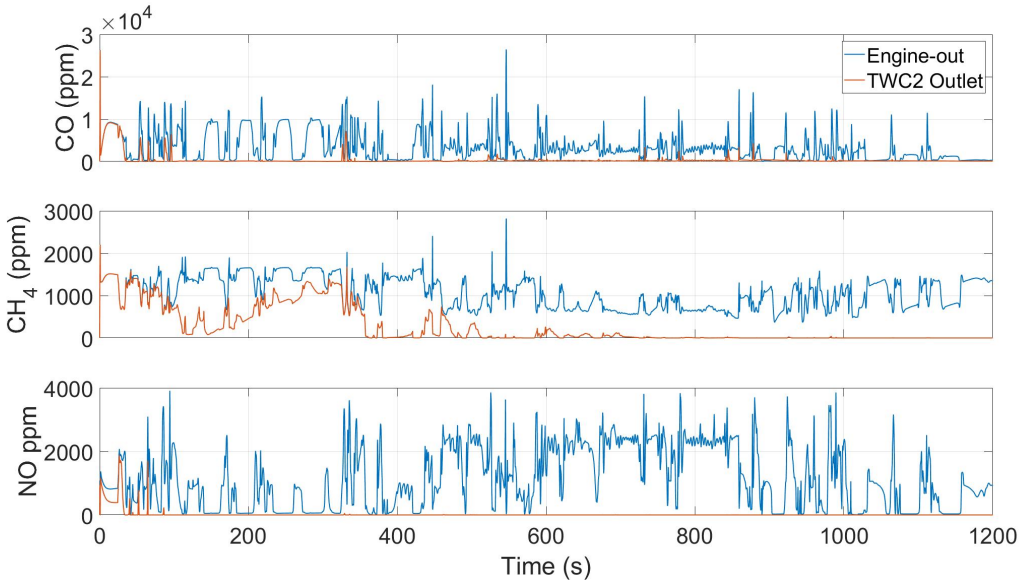

Figure 5.43. : Cold start Otto FTP cycle instantaneous emissions for Strategy 3 (FOS = 0.4)

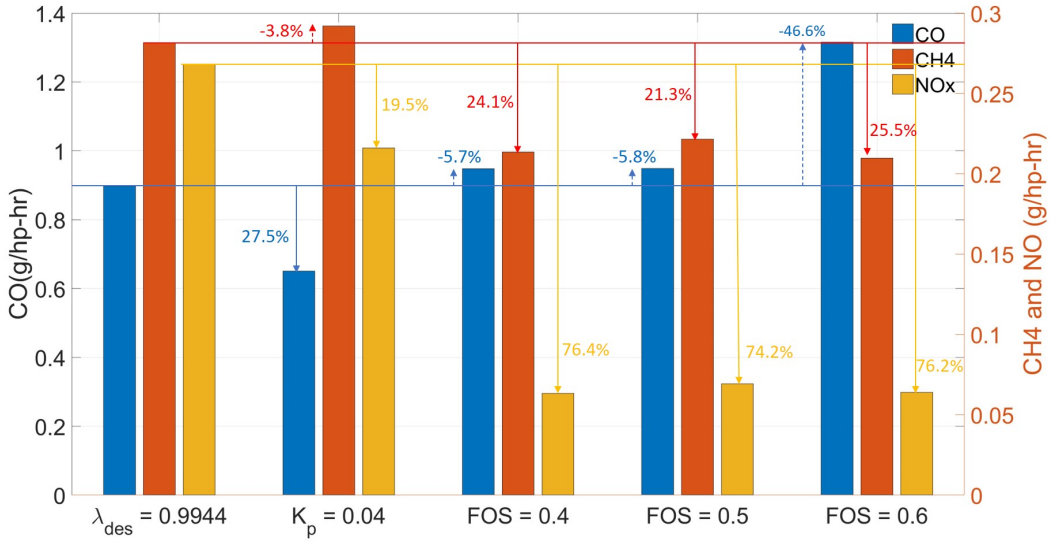

Figure 5.44. : Cold start Otto FTP cycle cumulative emissions for all three strategies

5.7.3 Warm Start Otto FTP Cycle

Strategy 1

Fig. 5.45 shows the emission comparison for different desired λ set points in Strategy 1 for the warm start Otto FTP cycle. Similar to the cold start cycles (per Fig. 5.35), the best overall performance is achieved when the desired engine λ is 0.9944.

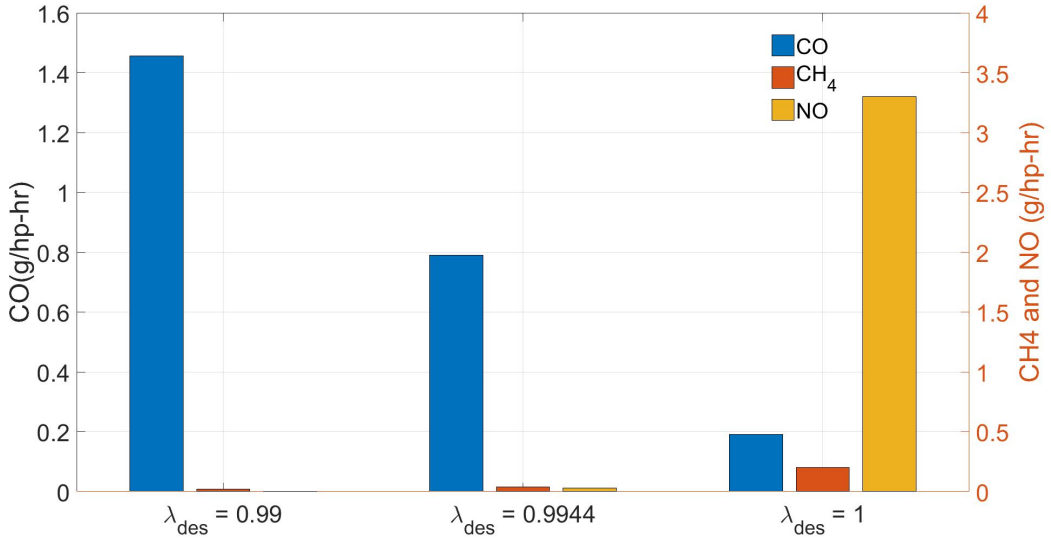

Figure 5.45. : Warm start Otto FTP cycle cumulative emissions for Strategy 1

Fig. 5.46 shows the TWC1 temperature, λ, and TWC1 average FOS for setting $\lambda_{des} = 0.9944$ during the warm start Otto FTP cycle test. The desired engine λ is fixed at 0.9944 for the entire drive cycle. The initial temperature is 800K. Unlike the cold start cycle (per Fig. 5.36), the FOS oscillates around 0.4 for the first 400s. When the engine has transient operations during $500 - 800$s (Per Fig. 5.30), there are large FOS oscillations in TWC1. Fig. 5.47 shows the instantaneous emissions for Strategy 1. Both CH_4 and NO are greatly reduced compared to the cold start cycle.

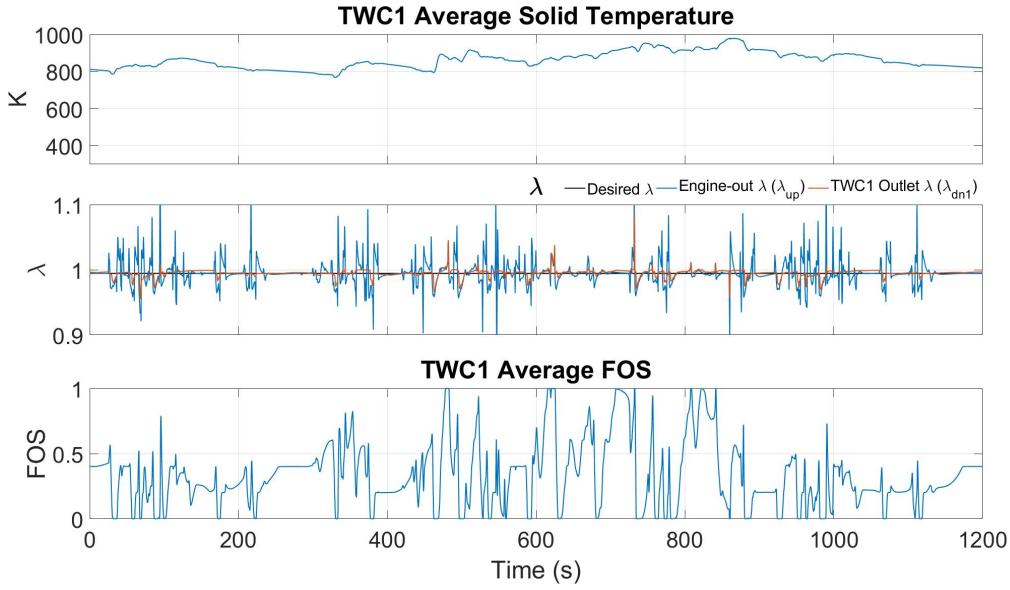

Figure 5.46. : Warm start Otto FTP cycle for Strategy 1 ($\lambda_{des} = 0.9944$)

Strategy 2

Fig 5.48 shows the emission comparison for different K_p in Strategy 2 during the warm start Otto FPT test. Similar to the cold start test (per Fig. 5.38), $K_P = 0.04$ has the best overall emission control performance.

Fig. 5.49 shows the temperature, λ and TWC1 average FOS for Strategy 2 when $K_p = 0.04$. Unlike the cold start test (per Fig. 5.39), the TWC1 FOS oscillates between 0 and 1 during the entire test. The command of the outer loop controller (desired λ) has smaller oscillations in this warm start test compared to the cold start test (per Fig. 5.39). Fig. 5.49 shows the instantaneous emissions for Strategy 2. There are small spikes of TWC2 outlet CH_4 and CO. No spike of TWC2 outlet NO is observed over the entire test.

Strategy 3

Fig. 5.51 shows the comparison of cumulative emissions for different FOS set points in Strategy 3 during the warm start Otto FTPP test. Similar to the cold start test, better emission reductions can be achieved when FOS is set within 0.4 to 0.6.

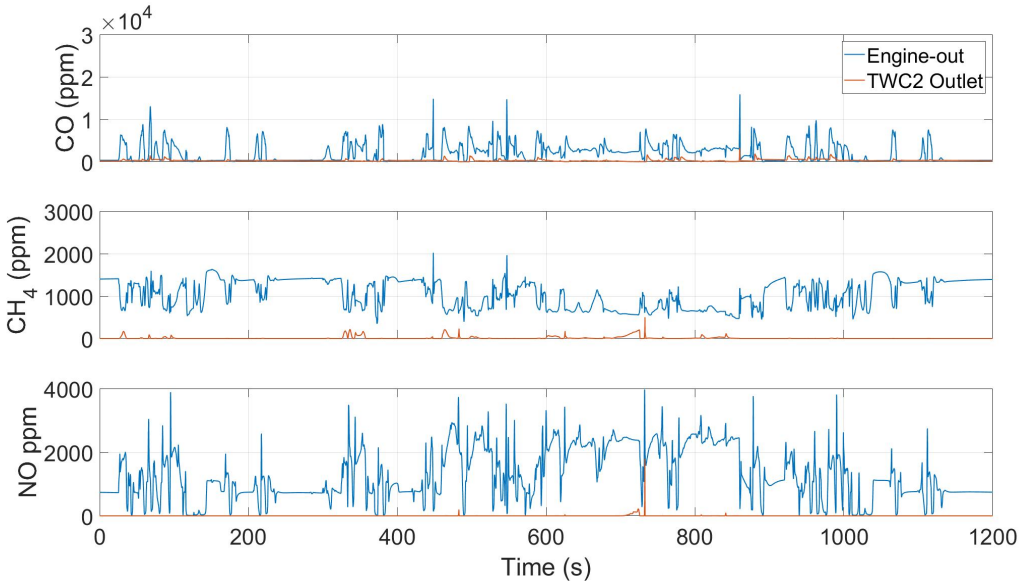

Figure 5.47. : Warm start Otto FTP cycle instantaneous emissions for Strategy 1 ($\lambda_{des} = 0.9944$)

Fig. 5.52 shows the temperature, λ and TWC1 average FOS for Strategy 3 when desired FOS = 0.4. The TWC1 FOS has smaller oscillations for the first 400s compared with the cold start cycle test (per Fig. 5.42). Fig. 5.53 shows the instantaneous emissions for Strategy 3 when desired FOS = 0.4 during the warm start test. The NO emission is greatly reduced for the first 100s compared with the cold start test (per Fig. 5.43). There is also large improvement in the CH_4 emission.

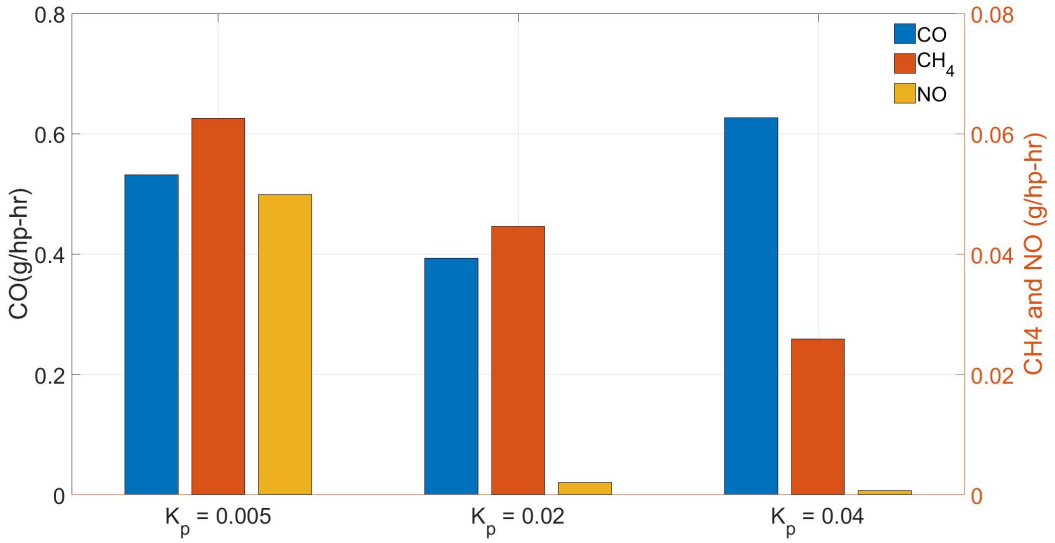

Figure 5.48. : Warm start Otto FTP cycle cumulative emissions for Strategy 2

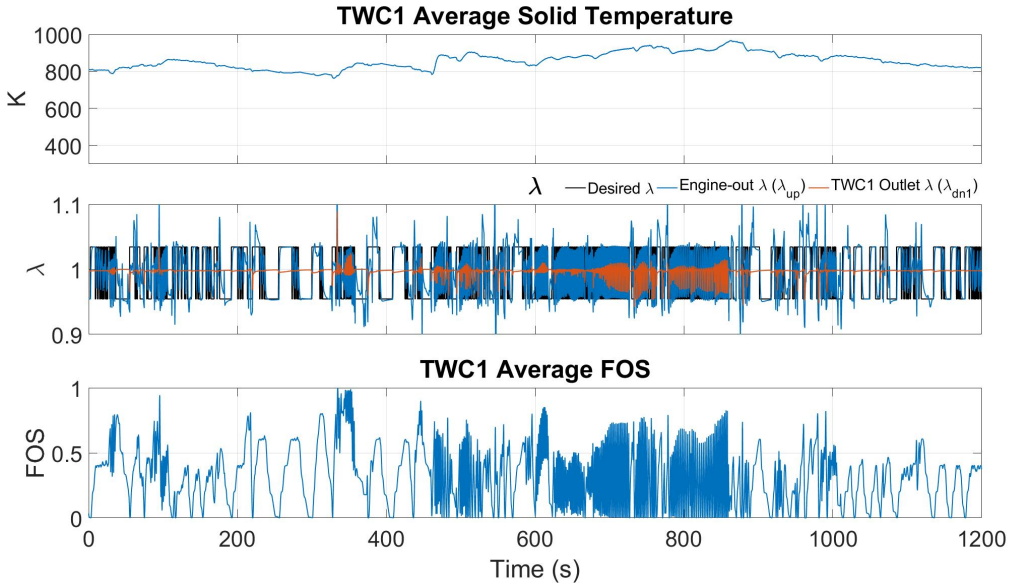

Figure 5.49. : Warm start Otto FTP cycle for Strategy 2 ($K_P = 0.04$)

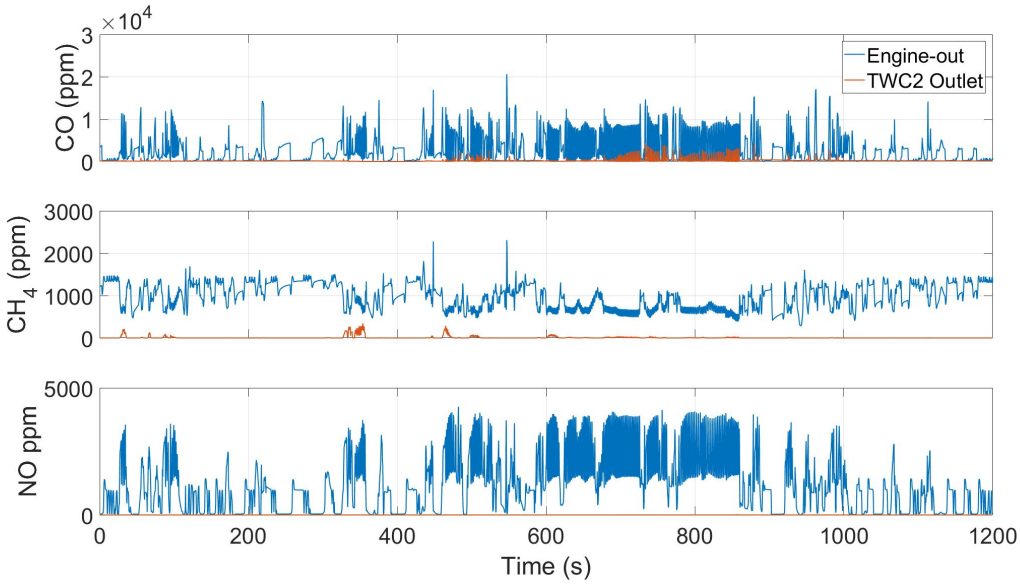

Figure 5.50. : Warm start Otto FTP cycle instantaneous emissions for Strategy 2 ($K_P = 0.04$)

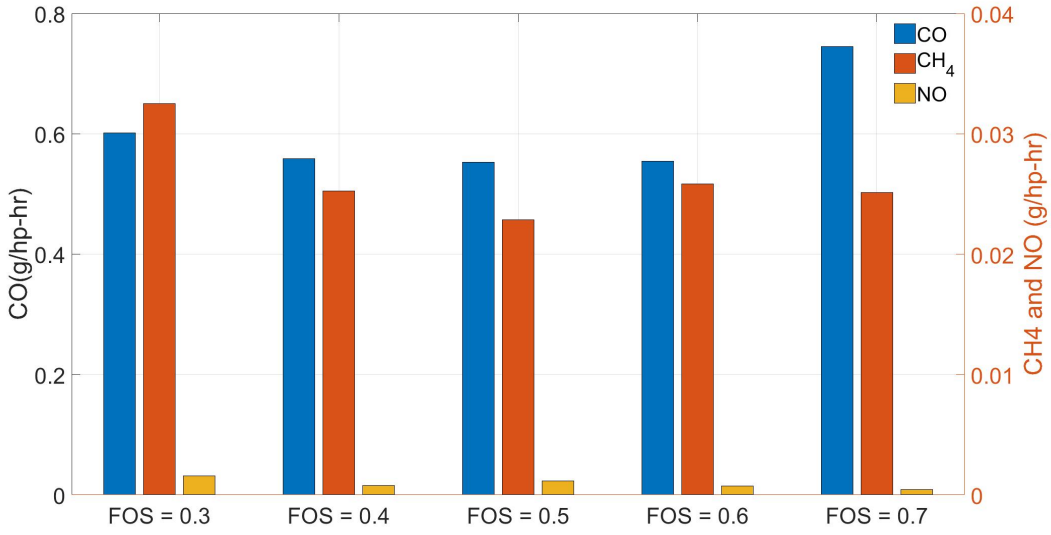

Figure 5.51. : Warm start Otto FTP cycle cumulative emissions for Strategy 3

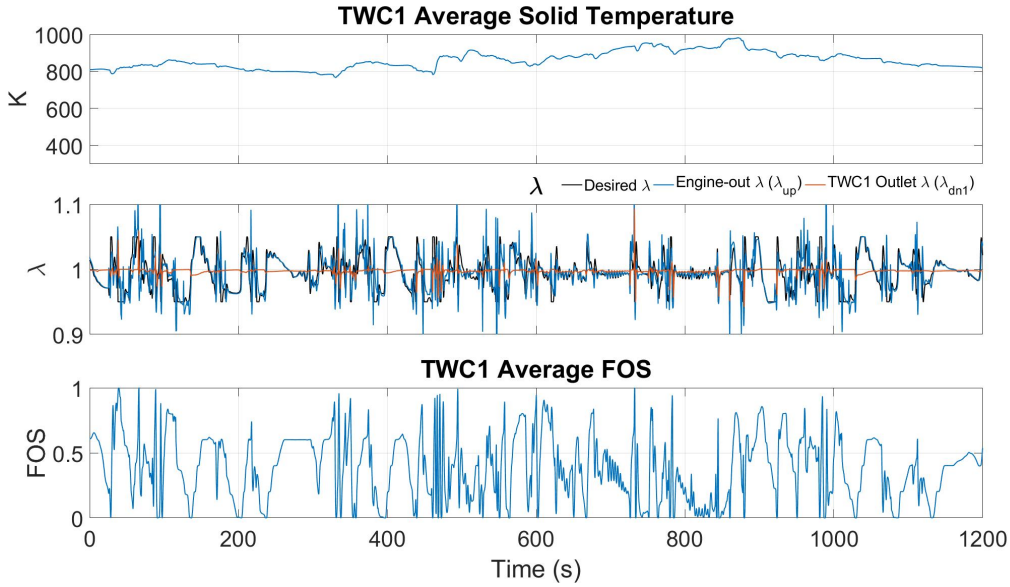

Figure 5.52. : Warm start Otto FTP cycle for Strategy 3 (FOS = 0.4)

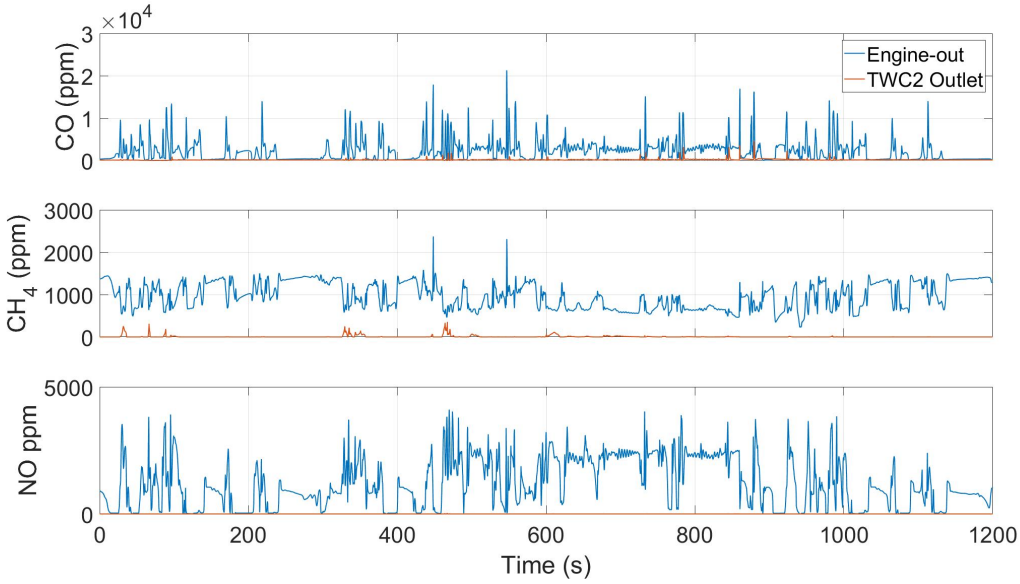

Figure 5.53. : Warm start Otto FTP cycle instantaneous emissions for Strategy 3 (FOS = 0.4)

Comparison for Three Control strategies

Fig. 5.54 shows the comparison of cumulative emissions for different control strategies during the warm start test. Compared with the constant λ control strategy (Strategy 1), the best case in Strategy 2 ($K_p = 0.04$) reduces CO by 20.6%, CH_4 by 35.5% and NO by 97.6%. For the best case in Strategy 3 (FOS = 0.4), there is 29.2% reduction in CO, 37% in CH_4 and 97.5% in NO compared with the baseline. Compared with the advanced baseline (Strategy 2), the proposed Strategy 3 has similar NO reduction performance and further reduces CO and CH_4 by 10% and 1.5%, respectively, for the warm start Otto FTP drive cycle.

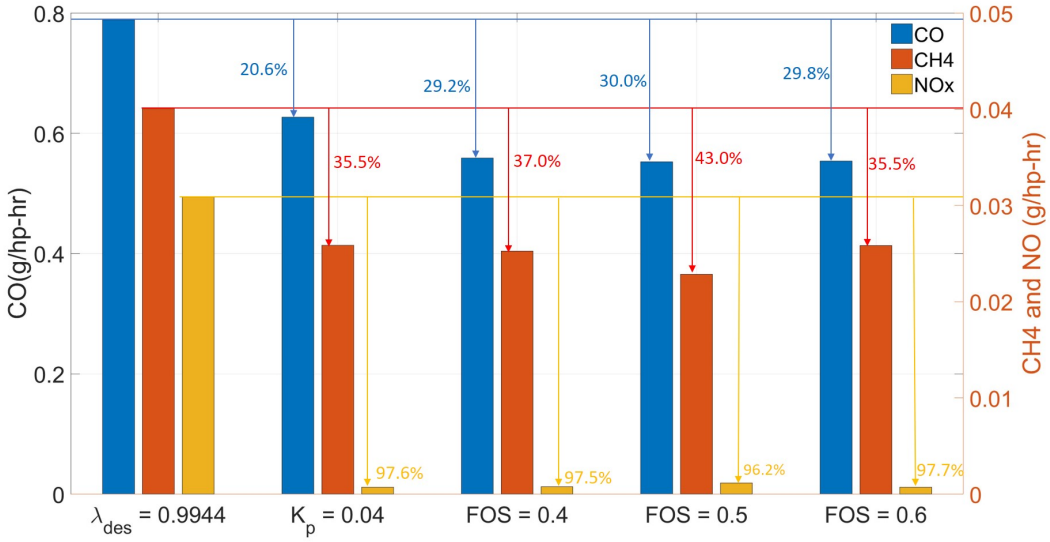

Figure 5.54. : Cold start Otto FTP cycle cumulative emissions for all three strategies

5.7.4 Summary

A two-loop estimation and control strategy is proposed to reduce the emission of the three-way-catalyst (TWC). In the outer loop, an FOS estimator consisting of a TWC model and an extended Kalman-filter is used to estimate the current TWC fractional oxygen state (FOS) and a robust controller is used to control the TWC FOS by manipulating the desired engine λ. The outer loop estimator and controller are combined with an existing inner loop

controller. The inner loop controller controls the engine λ based on the desired λ value and the control inaccuracies are considered and compensated by the outer loop robust controller. This control strategy achieves good emission reduction performance and has advantages over the constant λ control stratagy and the conventional two-loop switch-type control strategy.

6. SUMMARY AND FUTURE WORK

6.1 Summary

In this thesis, a physically-based, control-oriented model was developed for turbo-charged SI engines utilizing cooled EGR and flexible VVA systems. The model includes the impacts of modulation to any combination of 11 actuators, including the throttle valve, bypass valve, fuel injection rate, waste gate, HP EGR valve, LP EGR valve, number of firing cylinders, intake and exhaust valve opening and closing timings. Incorporated with the cylinder-out composition sub-model and the turbine-out pressure sub-model, the control-oriented model is capable of capturing the dynamics of pressure, temperature and gas compositions in manifolds and the cylinder. The control-oriented model supports the development and application of estimation and control strategies to improve engine performance.

A simultaneous, coupled sensor selection and observer design algorithm was developed for the air handling system of turbo-charged SI engines utilizing cooled EGR. The goal of this algorithm is to definitively, and accurately, determine the tradeoff between the necessary sensor number and intake manifold oxygen fraction. The strategy uses H_2 optimization and accounts for both process and measurement noise. The implemented cost function consists of the H_2 norm of the observer error and the weighted l_1 norm of the observer gain. A method to estimate the modeling errors based on the comparison of reference data and modeling data was proposed and allowed to be implemented in the state-space format, enabling the application of the sensor selection framework on actual physical systems.

A co-design algorithm for both sensor system and controller designs was developed. The goal of this algorithm is to evaluate the tradeoff between the performance objective and the sensor characteristics. This algorithm uses the μ-synthesis method to compute the structured singular value μ while synthesizing a linear H_∞ controller, for a given sensor set. The robustness of the closed-loop control performance can be evaluated by the μ value. The algorithm was applied to a turbo-charged SI engine utilizing LP EGR and flexible VVA systems to select proper sensor sets and design robust controllers for controlling stoichiometric AFR and air/EGR paths. A method to estimate the model uncertainty in the frequency domain was developed and implemented for the SI engine in this framework.

A two-loop estimation and control stratagy was proposed to reduce the emission of the three-way-catalyst (TWC). In the outer loop, an FOS estimator consisting of a TWC model and an extended Kalman-filter is used to estimate the current TWC fractional oxygen state (FOS) and a robust controller is used to control the TWC FOS by manipulating the desired engine λ. The outer loop estimator and controller are combined with an existing inner loop controller. The inner loop controller controls the engine λ based on the desired λ value and the control inaccuracies are considered and compensated by the outer loop robust controller. This control strategy achieves good emission reduction performance and has advantages over the constant λ control stratagy and the conventional two-loop switch-type control strategy.

6.2 Future Work

Future work should extend the TWC oxygen storage level estimation and control to include the adaptive updating of the process noise in the EKF to achieve more accurate FOS estimation results. The current process noise in EKF is tuned based on the simulations and remains constant over the entire drive cycle test. A more accurate FOS estimator would assist the robust controller to further reduce the emissions. Additional analysis of the FOS estimator dynamics should be performed and incorporated in the robust controller design to achieve better emission reduction performance. Additional work should also focus on including the fuel cut-off events in the emission test. The current drive cycle test limits the minimum torque as zero and does not consider the motoring period. This work should proceed by improving the reference engine and TWC model to introduce the fuel cut-off events.

REFERENCES

[1] B. Hoepke, S. Jannsen, E. Kasseris, and W. K. Cheng, "EGR effects on boosted SI engine operation and knock integral correlation," *SAE International Journal of Engines*, vol. 5, no. 2, pp. 547–559, 2012.

[2] J. Wang, "Air fraction estimation for multiple combustion mode diesel engines with dual-loop egr systems," *Control Engineering Practice*, vol. 16, no. 12, pp. 1479–1486, 2008.

[3] D. L. Simon and S. Garg, "Optimal tuner selection for kalman filter-based aircraft engine performance estimation," *Journal of Engineering for Gas Turbines and Power*, vol. 132, no. 3, 2010.

[4] P. Chen and J. Wang, "Oxygen concentration dynamic model and observer-based estimation through a diesel engine aftertreatment system," *Journal of Dynamic Systems, Measurement, and Control*, vol. 134, no. 3, p. 031008, 2012.

[5] S. B. Rengarajan, J. Sarlashkar, R. Roecker, and G. Anderson, "Estimation of intake oxygen mass fraction for transient control of egr engines," SAE Technical Paper, Tech. Rep., 2018.

[6] P. Kumar, I. Makki, J. Kerns, K. Grigoriadis, M. Franchek, and V. Balakotaiah, "A low-dimensional model for describing the oxygen storage capacity and transient behavior of a three-way catalytic converter," *Chemical engineering science*, vol. 73, pp. 373–387, 2012.

[7] J. Gong, D. Wang, J. Li, N. Currier, and A. Yezerets, "Dynamic oxygen storage modeling in a three-way catalyst for natural gas engines: A dual-site and shrinking-core diffusion approach," *Applied Catalysis B: Environmental*, vol. 203, pp. 936–945, 2017.

[8] S. Joshi and S. Boyd, "Sensor selection via convex optimization," *IEEE Transactions on Signal Processing*, vol. 57, no. 2, pp. 451–462, 2008.

[9] J. A. Tropp, "Just relax: Convex programming methods for identifying sparse signals in noise," *IEEE transactions on information theory*, vol. 52, no. 3, pp. 1030–1051, 2006.

[10] Z.-Q. Luo, T.-H. Chang, D. Palomar, and Y. Eldar, "Sdp relaxation of homogeneous quadratic optimization: approximation," *Convex Optimization in Signal Processing and Communications*, p. 117, 2010.

[11] M. Kalandros and L. Y. Pao, "Controlling target estimate covariance in centralized multisensor systems," in *Proceedings of the 1998 American Control Conference. ACC (IEEE Cat. No. 98CH36207)*, vol. 5. IEEE, 1998, pp. 2749–2753.

[12] M. Kalandros, L. Y. Pao, and Y.-C. Ho, "Randomization and super-heuristics in choosing sensor sets for target tracking applications," in *Proceedings of the 38th IEEE Conference on Decision and Control (Cat. No. 99CH36304)*, vol. 2. IEEE, 1999, pp. 1803–1808.

[13] A. Hashemi, M. Ghasemi, H. Vikalo, and U. Topcu, "A randomized greedy algorithm for near-optimal sensor scheduling in large-scale sensor networks," in *2018 Annual American Control Conference (ACC)*. IEEE, 2018, pp. 1027–1032.

[14] S. Rao, S. P. Chepuri, and G. Leus, "Greedy sensor selection for non-linear models," in *2015 IEEE 6th International Workshop on Computational Advances in Multi-Sensor Adaptive Processing (CAMSAP)*. IEEE, 2015, pp. 241–244.

[15] M. Fardad, F. Lin, and M. R. Jovanović, "Sparsity-promoting optimal control for a class of distributed systems," in *Proceedings of the 2011 American Control Conference*. IEEE, 2011, pp. 2050–2055.

[16] U. Münz, M. Pfister, and P. Wolfrum, "Sensor and actuator placement for linear systems based on H_2 and H_∞ optimization," *IEEE Transactions on Automatic Control*, vol. 59, pp. 2984–2989, 2014.

[17] A. Zare and M. R. Jovanović, "Optimal sensor selection via proximal optimization algorithms," in *2018 IEEE Conference on Decision and Control (CDC)*. IEEE, 2018, pp. 6514–6518.

[18] N. K. Dhingra, M. R. Jovanović, and Z.-Q. Luo, "An ADMM algorithm for optimal sensor and actuator selection," in *53rd IEEE Conference on Decision and Control*. IEEE, 2014, pp. 4039–4044.

[19] S. P. Chepuri and G. Leus, "Sparsity-promoting sensor selection for non-linear measurement models," *IEEE Transactions on Signal Processing*, vol. 63, no. 3, pp. 684–698, 2014.

[20] J. Pekař, P. Garimella, D. Germann, and G. E. Stewart, "Experimental results for sensor selection and multivariable controller design for a heavy-duty diesel engine," *IFAC Proceedings Volumes*, vol. 45, no. 30, pp. 122–129, 2012.

[21] R. Mushini and D. Simon, "On optimization of sensor selection for aircraft gas turbine engines," in *18th International Conference on Systems Engineering (ICSEng'05)*. IEEE, 2005, pp. 9–14.

[22] R. Suard, C. H. Onder, and L. Guzzella, "Optimal sensor selection and configuration, case study spark ignited engine," *SAE international journal of passenger cars-electronic and electrical systems*, vol. 1, no. 2008-01-0991, pp. 382–392, 2008.

[23] K. A. Palmer, W. T. Hale, and G. M. Bollas, "Active fault diagnosis with sensor selection in a diesel engine air handling system," in *2018 Annual American Control Conference (ACC)*. IEEE, 2018, pp. 4995–5000.

[24] I. Kolmanovsky, J. Sun, M. Druzhinina, and M. Van Nieuwstadt, "Charge control for direct injection spark ignition engines with egr," in *Proceedings of the 2000 American Control Conference. ACC (IEEE Cat. No. 00CH36334)*, vol. 1, no. 6. IEEE, 2000, pp. 34–38.

[25] A. P. Wiese, A. G. Stefanopoulou, A. Y. Karnik, and J. H. Buckland, "Model predictive control for low pressure exhaust gas recirculation with scavenging," in *2017 American Control Conference (ACC)*. IEEE, 2017, pp. 3638–3643.

[26] Q. Zhu, R. Prucka, M. Prucka, and H. Dourra, "A nonlinear model predictive control strategy with a disturbance observer for spark ignition engines with external egr," *SAE International Journal of Commercial Vehicles*, vol. 10, no. 2017-01-0608, pp. 360–372, 2017.

[27] H. Andersson, "Model based control of throttle, egr and wastegate: A system analysis of the gas flows in an si-engine," 2017.

[28] H. Yilmaz and A. Stefanopoulou, "Control of charge dilution in turbocharged diesel engines via exhaust valve timing," 2005.

[29] S. Zentner, E. Schäfer, C. Onder, and L. Guzzella, "Model-based injection and egr adaptation and its impact on transient emissions and drivability of a diesel engine," *IFAC Proceedings Volumes*, vol. 46, no. 21, pp. 89–94, 2013.

[30] C.-J. Chiang and A. Stefanopoulou, "Control of thermal ignition in gasoline engines," in *Proceedings of the 2005, American Control Conference, 2005.* IEEE, 2005, pp. 3847–3852.

[31] B. A. Al-Himyari, A. Yasin, and H. Gitano, "Review of air-fuel ratio prediction and control methods," *Asian Journal of Applied Sciences*, vol. 2, no. 4, 2014.

[32] L. Eriksson and L. Nielsen, *Modeling and control of engines and drivelines.* John Wiley & Sons, 2014.

[33] E. Franceschi, K. R. Muske, J. C. P. Jones, and I. Makki, "An adaptive delay-compensated pid air fuel ratio controller," SAE Technical Paper, Tech. Rep., 2007.

[34] R. Zope, J. Mohammadpour, K. Grigoriadis, and M. Franchek, "Robust fueling strategy for an SI engine modeled as an linear parameter varying time-delayed system," in *Proceedings of the 2010 American Control Conference.* IEEE, 2010, pp. 4634–4639.

[35] C. Wei, H. Selamat, and A. J. Alimin, "Modeling and control of an engine fuel injection system," *Faculty of Electrical Engineering, University Teknologi Malaysia*, 2009.

[36] Y. Yildiz, A. Annaswamy, D. Yanakiev, and I. Kolmanovsky, "Adaptive air fuel ratio control for internal combustion engines," in *2008 American Control Conference*. IEEE, 2008, pp. 2058–2063.

[37] S. Lee, R. Howlett, and S. Walters, "Engine fuel injection control using fuzzy logic," *Intelligent Sistems & Signal Processing Laboratories*, 2004.

[38] H. Hosoya, H. Yoshizawa, S. Ohkuma, S. Watanabe, H. Okada, N. Tomisawa, and K. Abe, "Development of next-generation air-fuel ratio control system,"cosmic"," SAE Technical Paper, Tech. Rep., 2002.

[39] Y.-J. Zhai and D.-L. Yu, "Neural network model-based automotive engine air/fuel ratio control and robustness evaluation," *Engineering Applications of Artificial Intelligence*, vol. 22, no. 2, pp. 171–180, 2009.

[40] L. Guzzella and C. Onder, *Introduction to modeling and control of internal combustion engine systems*. Springer Science & Business Media, 2009.

[41] G. Fiengo, J. W. Grizzle, and J. A. Cook, "Experimental results on dual-uego active catalyst control," *IFAC Proceedings Volumes*, vol. 37, no. 22, pp. 343–348, 2004.

[42] R. W. Schallock, K. R. Muske, and J. C. P. Jones, "Model predictive functional control for an automotive three-way catalyst," *SAE International Journal of Fuels and Lubricants*, vol. 2, no. 1, pp. 242–249, 2009.

[43] P. Kumar and I. Makki, "Model based control of a three-way catalytic converter based on the oxygen storage level of the catalyst," SAE Technical Paper, Tech. Rep., 2017.

[44] L. Kocher, E. Koeberlein, D. Van Alstine, K. Stricker, and G. Shaver, "Physically based volumetric efficiency model for diesel engines utilizing variable intake valve actuation," *International Journal of Engine Research*, vol. 13, no. 2, pp. 169–184, 2012.

[45] D. G. Van Alstine, L. E. Kocher, E. Koeberlein, K. Stricker, and G. M. Shaver, "Control-oriented premixed charge compression ignition combustion timing model for a diesel engine utilizing flexible intake valve modulation," *International Journal of Engine Research*, vol. 14, no. 3, pp. 211–230, 2013.

[46] K. Stricker, L. Kocher, E. Koeberlein, D. Van Alstine, and G. M. Shaver, "Turbocharger map reduction for control-oriented modeling," *Journal of Dynamic Systems, Measurement, and Control*, vol. 136, no. 4, p. 041008, 2014.

[47] J. Heywood, "1988, internal combustion engine fundamentals, mcgraw-hill, new york."

[48] E. Koeberlein, L. Kocher, D. Van Alstine, K. Stricker, and G. Shaver, "Physics based control oriented modeling of exhaust gas enthalpy for engines utilizing variable valve actuation," in *ASME 2011 Dynamic Systems and Control Conference and Bath/ASME Symposium on Fluid Power and Motion Control*. American Society of Mechanical Engineers Digital Collection, 2012, pp. 627–634.

[49] S. Wang, R. Prucka, M. Prucka, and H. Dourra, "Control-oriented residual gas mass prediction for spark ignition engines," *International Journal of Engine Research*, vol. 16, no. 7, pp. 897–907, 2015.

[50] K. Stricker, L. Kocher, E. Koeberlein, D. Van Alstine, and G. Shaver, "Turbocharger map reduction for control-oriented modeling," in *ASME 2011 dynamic systems and control conference and Bath/ASME symposium on fluid power and motion control*. American Society of Mechanical Engineers Digital Collection, 2012, pp. 619–626.

[51] D. ARZELIER, "LMIs in systems control state-space methods performance analysis and synthesis," *Lecture Notes of LAAS Course on LMIs Optimization with Application in Control Part II.2*, 2008.

[52] M. M. Peet, "Lmi methods in optimal and robust control," *Lecture Notes, Department of Mechanical and Aerospace Engineering, Arizona State University*, 2016.

[53] E. K. Chong and S. H. Zak, *An introduction to optimization*. John Wiley & Sons, 2013, vol. 76.

[54] E. J. Candes, M. B. Wakin, and S. P. Boyd, "Enhancing sparsity by reweighted l_1 minimization," *Journal of Fourier analysis and applications*, vol. 14, no. 5-6, pp. 877–905, 2008.

[55] B. Polyak, M. Khlebnikov, and P. Shcherbakov, "An LMI approach to structured sparse feedback design in linear control systems," in *2013 European control conference (ECC)*. IEEE, 2013, pp. 833–838.

[56] M. C. Grant and S. P. Boyd, "The CVX users' guide, release 2.1," *CVX Research Inc*, 2015.

[57] M. E. Rivas Perea, "Assessment of fuel consumption reduction strategies on a gasoline turbocharged direct injection engine with a cooled egr system," Ph.D. dissertation, 2016.

[58] L. Francqueville and J.-B. Michel, "On the effects of egr on spark-ignited gasoline combustion at high load," *SAE International Journal of Engines*, vol. 7, no. 4, pp. 1808–1823, 2014.

[59] J. Duník, O. Straka, O. Kost, and J. Havlík, "Noise covariance matrices in state-space models: A survey and comparison of estimation methods—part i," *International Journal of Adaptive Control and Signal Processing*, vol. 31, no. 11, pp. 1505–1543, 2017.

[60] O. Kost, J. Duník, and O. Straka, "Noise moment and parameter estimation of state-space model," *IFAC-PapersOnLine*, vol. 51, no. 15, pp. 891–896, 2018.

[61] A. Solonen, J. Hakkarainen, A. Ilin, M. Abbas, and A. Bibov, "Estimating model error covariance matrix parameters in extended kalman filtering," *Nonlinear Processes in Geophysics*, vol. 21, no. 5, pp. 919–927, 2014.

[62] S. Miran, J. Z. Simon, M. C. Fu, S. I. Marcus, and B. Babadi, "Estimation of state-space models with gaussian mixture process noise." in *DSW*, 2019, pp. 185–189.

[63] M. J. Blanca, J. Arnau, D. López-Montiel, R. Bono, and R. Bendayan, "Skewness and kurtosis in real data samples," *Methodology*, 2013.

[64] F. Liu, J. M. Pfeiffer, R. Caudle, P. Marshall, and P. Olin, "Low pressure cooled egr transient estimation and measurement for an turbocharged si engine," SAE Technical Paper, Tech. Rep., 2016.

[65] A. Wiese, A. Stefanopoulou, J. Buckland, and A. Y. Karnik, "Modelling and control of engine torque for short-circuit flow and egr evacuation," SAE Technical Paper, Tech. Rep., 2017.

[66] S. Skogestad and I. Postlethwaite, *Multivariable feedback control: analysis and design*. Wiley New York, 2007, vol. 2.

[67] M. Dahleh, M. A. Dahleh, and G. Verghese, "Lectures on dynamic systems and control," *Lecture Notes MIT Course*, vol. 6.24, 2001.

[68] I. Griffin and P. Fleming, "A multiobjective optimization approach to dk-iteration," in *2003 European Control Conference (ECC)*. IEEE, 2003, pp. 360–369.

[69] J. B. Heywood, "Internal combustion engine fundamentals, 2018," *DOI:. Crossref Export Citation*, 1988.

[70] T. S. Auckenthaler, *Modelling and control of three-way catalytic converters*. ETH Zurich, 2005.

[71] E. P. Brandt, Y. Wang, and J. W. Grizzle, "Dynamic modeling of a three-way catalyst for si engine exhaust emission control," *IEEE Transactions on control systems technology*, vol. 8, no. 5, pp. 767–776, 2000.

[72] J. Gong, D. Wang, A. Brahma, J. Li, N. Currier, A. Yezerets, and P. Chen, "Lean breakthrough phenomena analysis for twc obd on a natural gas engine using a dual-site dynamic oxygen storage capacity model," SAE Technical Paper, Tech. Rep., 2017.

[73] E. P. Brandt, "Modeling and diagnostics of three-way catalysts for advanced emissions control systems." 1999.

[74] M. I. Ribeiro, "Kalman and extended kalman filters: Concept, derivation and properties," *Institute for Systems and Robotics*, vol. 43, 2004.

[75] J. M. Scherpen and W. S. Gray, "Nonlinear hilbert adjoints: Properties and applications to hankel singular value analysis," *Nonlinear analysis, theory, methods & applications*, vol. 51, no. 5, pp. 883–901, 2002.

A. NONLINEAR ENGINE MODEL

The nonlinear engine model is developed based on Chapter 2.

$$
\begin{aligned}
\dot{x_1} &= \dot{P}_{bm} = \frac{\gamma_{bm} R_{bm}}{V_{bm}} [W_{comp} T_{cac} - W_{thr} T_{bm} - W_{byp} T_{bm}] \\
\dot{x_2} &= \dot{P}_{\mathrm{im}} = \frac{\gamma_{\mathrm{im}} R_{\mathrm{im}}}{V_{im}} [W_{thr} T_{bm} - W_{cyl} T_{\mathrm{im}}] \\
\dot{x_3} &= \dot{P}_{em} = \frac{\gamma_{em} R_{\mathrm{em}}}{V_{em}} [W_{cylout} T_{cylout} - W_{turb} T_{\mathrm{em}} - W_{wg} T_{\mathrm{em}}] \\
\dot{x_4} &= \dot{T}_{bm} = \frac{R_{bm} T_{bm}}{P_{bm} V_{bm}} [W_{comp} (\gamma_{cac} T_{cac} - T_{bm}) - (W_{thr} + W_{byp}) (\gamma_{bm} T_{bm} - T_{bm})] \\
\dot{x_5} &= \dot{T}_{\mathrm{im}} = \frac{R_{\mathrm{im}} T_{\mathrm{im}}}{P_{\mathrm{im}} V_{\mathrm{im}}} [W_{thr} (\gamma_{bm} T_{bm} - T_{\mathrm{im}}) - W_{cyl} (\gamma_{\mathrm{im}} T_{\mathrm{im}} - T_{\mathrm{im}})] \\
\dot{x_6} &= \dot{T}_{\mathrm{em}} = \frac{R_{\mathrm{em}} T_{\mathrm{em}}}{P_{\mathrm{em}} V_{\mathrm{em}}} [W_{cylout} (\gamma_{cylout} T_{cylout} - T_{\mathrm{em}}) - (W_{turb} + W_{wg}) (\gamma_{\mathrm{em}} T_{\mathrm{em}} - T_{\mathrm{em}})] \\
\dot{x_7} &= \dot{\omega}_{tc} = \frac{Z_{turb} - Z_{comp}}{I_{tc} \omega_{tc}} \\
\dot{x_8} &= \dot{F}_{ub,bm} = \frac{R_{bm} T_{bm}}{P_{bm} V_{bm}} [W_{\mathrm{inlet}} (1 - F_{ub,bm}) + W_{egrl} (F_{ub,\mathrm{em}} - F_{ub,bm})] \\
\dot{x_9} &= \dot{F}_{b,bm} = \frac{R_{bm} T_{bm}}{P_{bm} V_{bm}} [W_{\mathrm{inlet}} (0 - F_{b,bm}) + W_{egrl} (F_{b,\mathrm{em}} - F_{b,bm})] \\
\dot{x_{10}} &= \dot{F}_{ub,\mathrm{im}} = \frac{R_{\mathrm{im}} T_{\mathrm{im}}}{P_{\mathrm{im}} V_{\mathrm{im}}} [W_{thr} (F_{ub,bm} - F_{ub,\mathrm{im}})] \\
\dot{x_{11}} &= \dot{F}_{b,\mathrm{im}} = \frac{R_{\mathrm{im}} T_{\mathrm{im}}}{P_{\mathrm{im}} V_{\mathrm{im}}} [W_{thr} (F_{b,bm} - F_{b,\mathrm{im}})] \\
\dot{x_{12}} &= \dot{F}_{ub,em} = \frac{R_{\mathrm{em}} T_{\mathrm{em}}}{P_{\mathrm{em}} V_{\mathrm{em}}} [W_{cylout} (F_{ub,cylout} - F_{ub,\mathrm{em}})] \\
\dot{x_{13}} &= \dot{F}_{b,\mathrm{em}} = \frac{R_{\mathrm{em}} T_{\mathrm{em}}}{P_{\mathrm{em}} V_{\mathrm{em}}} [W_{cylout} (F_{b,cylout} - F_{b,\mathrm{em}})] \\
\dot{x}_{14} &= \frac{A_{cmd,thr} - A_{thr}}{\tau_{thr}} \\
\dot{x}_{15} &= \frac{A_{cmd,egrl} - A_{egrl}}{\tau_{thr}} \\
\dot{x}_{16} &= \frac{D_{cmd,wg} - D_{wg}}{\tau_{thr}}
\end{aligned}
\tag{A.1}
$$

B. UNKNOWN DISTURBANCE ESTIMATION

Table B.1. : Unknown Disturbance Estimation

State	γ_1	γ_2	μ	σ	Skewness Correction	Kurtosis Correction	$B_w(\mathrm{i},\mathrm{i})$
x_1	0.280	-1.27	8.21e4	2.99e5	eq. (3.25a)	eq. (3.27)	2.73e5
x_2	-0.0745	-1.57	-8.27e4	2.11e5	eq. (3.24)	eq. (3.27)	3.31e5
x_3	-0.0945	-0.413	-1.29e5	1.99e5	eq. (3.24)	/	1.99e5
x_4	-0.309	-1.41	-26.9	276.0	eq. (3.25a)	eq. (3.27)	350.0
x_5	-0.0777	-1.55	-47.1	121.0	eq. (3.24)	eq. (3.27)	187.0
x_6	-1.61e-3	-1.65	-818.0	2011.0	eq. (3.24)	eq. (3.27)	3322.0
x_7	-0.576	-0.75	3.55e5	9.81e5	eq. (3.25b)	/	1.34e6
x_8	0.533	-0.832	0.184	0.249	eq. (3.25a)	/	0.0651
x_9	-0.533	-0.832	-0.184	0.248	eq. (3.25a)	/	0.0636
x_{10}	6.98	76.3	1.05e-4	0.00724	eq. (3.25a)	/	7.14e-3
x_{11}	-6.98	76.3	-1.05e-4	0.00724	eq. (3.25a)	/	7.14e-3
x_{12}	3.06e-3	-0.625	-1.11e-4	5.56e-4	eq. (3.24)	/	5.56e-4
x_{13}	-3.06e-3	-0.625	1.11e-4	5.56e-4	eq. (3.24)	/	5.56e-4
x_{14} - x_{20}	/	/	/	/	/	/	0

VITA

EDUCATION:

Purdue University, West Lafayette, IN, USA:

Ph.D. in Mechanical Engineering, December 2020

Shanghai Jiao Tong University, Shanghai, China:

B.S.M.E. in Mechanical Engineering, July 2016

EMPLOYMENT EXPERIENCE:

Purdue University, Herrick Laboratories:

Graduate Research Assistant, August 2016 - December 2020